Axion direct detection in particle and condensed matter physics

Dissertation
zur Erlangung des Doktorgrades
an der Fakultät für Mathematik, Informatik und Naturwissenschaften
Fachbereich Physik
der Universität Hamburg

vorgelegt von

Jan Schütte-Engel

Hamburg

2020

Gutachter/innen der Dissertation:	Dr. Andreas Ringwald Prof. Dr. Erika Garutti
Zusammensetzung der Prüfungskommission:	Dr. Andreas Ringwald Prof. Dr. Erika Garutti Prof. Dr. Dieter Horns Prof. Dr. Geraldine Servant Prof. Dr. Günter Sigl
Vorsitzender der Prüfungskommission:	Prof. Dr. Dieter Horns
Datum der Disputation:	23.10.2020
Vorsitzender Fach-Promotionsausschusses PHYSIK:	Prof. Dr. Günter Sigl
Leiter des Fachbereichs PHYSIK:	Prof. Dr. Wolfgang Hansen
Dekan der Fakultät MIN:	Prof. Dr. Heinrich Graener

Abstract

The first part of this thesis investigates the direct detection of axions in particle physics. A generalized matrix formalism for describing axion-photon mixing in multi-layer systems to all orders in the axion-photon coupling is developed and applied for studying light shinning through a wall (LSW) experiments with and without dielectric layers. It is found that dielectric layers can be placed into two configurations - a transparent and a resonant one. For the transparent configuration, by tuning the distance between the dielectric layers, the experiment can be made to be more sensitive in specific relatively large axion mass ranges. For the ALPS II setup with dielectric layers it is possible to achieve a sensitivity enhancement for axion masses larger than $10^{-4}\,\mathrm{eV}$. Dielectric layers in the resonant case could be used to replace cavities around the (re)generation regions of existing LSW experiments.

Then we turn to open axion haloscopes, which aim to detect axions from the dark matter halo. Two methods for effectively calculating the emitted electromagnetic fields in 3D are presented. Both methods represent a significant improvement, as they are much more computationally efficient than a straight forward approach based on standard three dimensional finite element computations. We consider the upcoming MADMAX and BRASS axion haloscope experiments. For the BRASS haloscope we study how axion velocity effects could shift the emitted electromagnetic radiation pattern, while for MADMAX we investigate diffraction, disk tiling and waveguide surroundings. None of the studied 3D effects would be a show stopper for the MADMAX experiment.

The second part of the thesis concerns axion quasiparticles (AQs) in topological magentic insulators (TMIs). By AQs we mean quasiparticles, which have the same interaction with the electromagnetic fields as axions from particle physics. AQs in TMIs have not been detected so far. For a future detection via THz transmission spectroscopy a detailed calculation of the expected signal is needed. We present such a calculation and demonstrate that by fitting the future measurements to our signal calculation important material parameters of the TMI can be determined. AQs in TMIs can also be used in order to detect dark matter axions (DAs) since they can resonantly mix with the AQs and photons in TMIs. We present a detailed signal calculation for a DA search with a TMI layer. The calculation takes into account appropriate interface conditions for the electromagnetic and axion field as well as material losses. Analytical expressions for the resonance width and peak values are presented. For a DA search TMI materials with a relatively small refractive index are advantageous. TMIs with a thickness of a few mm and a surface area of $A = 1\,\mathrm{m}^2$ can probe QCD axion models for DA masses between $0.7\,\mathrm{meV}$ and $3.5\,\mathrm{meV}$. Magnon and photon losses need to be less than $10^{-5}\,\mathrm{meV}$ in order not to reduce the emitted signal significantly.

Zusammenfassung

Im ersten Teil dieser Arbeit untersuchen wir, wie Axionen aus der Teilchenphysik direkt detektiert werden können. Es wird ein verallgemeinerter Matrix Formalismus entwickelt, um Axion-Photon mixing in Multilayer Materialien bis zu allen Ordnungen in der Axion-Photon Kopplung zu beschreiben. Dieser wird dann auf light shining through a wall (LSW) Experimente mit und ohne dielektrischen Layern angewendet. Wir finden, dass die dielektrischen Layer in einer transparenten und einer resonanten Konfiguration angeordnet werden können. Im transparenten Fall kann die Sensitivität von LSW Experimenten für relativ große Axion Massen Intervalle gesteigert werden. Mit dielektrischen Layern kann die Sensitivität des ALPS II Experiments für Axion Massen, die größer als $10^{-4}\,\mathrm{eV}$ sind, vergrößert werden. In der resonanten Konfiguration könnten dielektrische Layer dazu verwendet werden, um Hohlraumresonatoren, die um die (Re)Generationsbereiche angeordnet sind, zu ersetzen.

Anschließend wenden wir uns Axion Haloskopen zu, die darauf ausgelegt sind, Axionen aus dem dunkle Materie Halo zu detektieren. Wir stellen zwei Methoden vor, mit denen effektiv die emittierte Strahlung in drei Dimensionen (3D) berechnet werden kann. Beide Methoden sind deutlich effektiver als Standard 3D finite Elemente Simulationen. Wir betrachten dann das MADMAX und BRASS Haloskop. Bezogen auf das BRASS Haloskop berechnen wir den Einfluss von einer endlichen Axion Geschwindigkeit auf die emittierte elektromagnetische Strahlung. Für MADMAX untersuchen wir Diffraktionseffekte und die Auswirkung von zusammengeklebten Discs und Wellenleiter auf die emittierte Strahlung. Keine der untersuchten 3D Effekte stellt ein Showstopper für das MADMAX Experiment dar.

Der zweite Teil dieser Arbeit beschäftigt sich mit Axion Quasiteilchen in topologischen magnetischen Isolatoren (TMI). Axion Quasiteilchen haben die gleichen Wechselwirkungen mit elektromagnetischer Strahlung wie Axionen in der Teilchenphysik, wurden aber auch noch nicht experimentell in TMI nachgewiesen. Um dies in der Zukunft mit THz Spektroskopie zu erreichen, wird eine detaillierte Rechnung des zu erwartenden Signals benötigt. Wir stellen diese Rechnung vor und zeigen, dass durch einen Vergleich unserer Rechnung mit zukünftigen Messungen, wichtige Materialeigenschaften von TMI bestimmt werden können. AQ in TMI können auch dazu benutzt werden, um dunkel Materie Axionen (DA) zu detektieren, was durch ein resonantes Zusammenspiel zwischen Photonen, AQ und DA erreicht werden kann. Wir stellen eine detaillierte Rechnung für das erwartete Signal von einer DA Suche mit TMI vor. Die Rechnung berücksichtigt sowohl geeignete Relationen zwischen den Feldern in und außerhalb des TMI als auch Materialverluste. Wir leiten analytische Formeln für die Resonanzbreite als auch für den Wert des Resonanzpeaks her. Wir finden, dass TMI mit möglichst kleinem Brechungsindex vorteilhaft für eine DA Suche sind. Weiterhin sollte die Layerdicke möglichst einige mm betragen, damit ein ausreichendes Signal erzeugt werden kann. Mit einer TMI Fläche von $A = 1\,\mathrm{m}^2$ können QCD Axion Modelle zwischen $0.7\,\mathrm{meV}$ and $3.5\,\mathrm{meV}$ überprüft werden. Die Magnonen und Photonen Verluste müssen kleiner als $10^{-5}\,\mathrm{meV}$ sein, um das Signal nicht signifikant zu verkleinern.

List of publications

- **S. Knirck and Jan Schütte-Engel et al.**
  "A First Look on 3D Effects in Open Axion Haloscopes"
  JCAP **1908** (2019) 026, Ref. [1]

- **David J. E. Marsh, Alexander J. Millar and Jan Schütte-Engel et al.**
  "Axion Quasiparticles for Axion Dark Matter Detection"
  In preparation for submission to JCAP, Ref. [2]

- **S. Knirck and Jan Schütte-Engel et al.**
  "Dielectric Haloscopes to Search for Axion Dark Matter: 3D Effects"
  In preparation for submission to JCAP, Ref. [3]

Proceedings

- **Jan Schütte-Engel for the MADMAX Collaboration**
  "Simulation studies for the MADMAX axion direct detection experiment"
  Contribution to: PATRAS 2018 and AXION-WIMP 2018
  arxiv:1811.00493, Ref. [4]

Please note: The results and also partly the text that was written by myself in chapter 5 will appear in the upcoming publication Ref. [2].

Notations and Conventions

The following conventions and notations are used in this thesis:

- Naming convention for axions in particle physics: *QCD axions* solve the strong CP problem of the standard model of particle physics. *Axion-like* particles (ALPs) have identical couplings compared to QCD axions, however they do not have the relation between the axion mass and coupling. If there is no need to distinguish directly between QCD axions and axion-like particles we just refer to *axions*. For example in section 2.2 we discuss how axions can account for the dark matter density. In this section we clearly distinguish between QCD axion and axion-like particles.

- Naming convention for axions in condensed matter physics: In chapter 5 we also consider quasiparticles in condensed matter systems, which have the same interactions with electromagnetic radiation as axions from particle physics. To distinguish them from the particle physics axions we always refer to them as axion quasiparticles (AQ).

- We use mainly Heaviside-Lorentz units with $c = 1 = \hbar$. In these units we have $1\,\mathrm{T} = 194\,\mathrm{eV}^2$. In some situations we give certain end results in SI units such that a comparison to measurable quantities is easier.

- Vectors and matrices are written in boldface typesetting.

List of Abbreviations

3D	three dimensional
ALP	**A**xion-**L**ike **P**article
AQ	**A**xion **Q**uasiparticle
CDM	**C**old **D**ark **M**atter
CP	**C**harge **P**arity
DA	**D**ark **A**xion
DM	**D**ark **M**atter
FEM	**F**inite **E**lement **M**ethod
FWHM	**F**ull **W**idth **H**alf **M**aximum
LSW	**L**ight **S**hining **T**hrough a **W**all
PDE	**P**artial **D**ifferential **E**quaitions
PEC	**P**erfect **E**lectric **C**onductor
PML	**P**erfectly **M**atched **L**ayers
PQ	**P**eccei and **Q**uinn
QCD	**Q**uantum **C**hromo**D**ynamics
RAM	**R**andom-**A**ccess **M**emory
RFP	**R**ecursive **F**ourier **P**ropagation
SM	**S**tandard **M**odel of particle physics
TI	**T**opological **I**nsulator
TMI	**T**opological **M**agnetic **I**nsulator
WIMP	**W**eakly **I**nteracting **M**assive **P**article

Contents

Chapter 1

Introduction

It often happens that ideas from one area of physics inspire progress in a completely different area. One example is the concept of spontaneous symmetry breaking (SSB). It was first introduced to explain the spontaneous magnetization in ferromagnets. Soon after the discovery of SSB in condensed matter physics this concept was found to be relevant in the context of particle physics as well, in explaining how the massive vector bosons acquire their mass via the Higgs mechanism [5, 6]. In the case of axions it was the other way around. Axions were first considered in particle physics and were only recently proposed to exist as quasiparticles in condensed matter systems.

Axions in particle physics

In particle physics axions appeared first as a means of solving the *strong CP problem* in the standard model of particle physics (SM). With the neutrinos regarded as massless the SM has 19 parameters. One them denoted as $\bar{\theta}$, has to be extremely small such that the SM is still in agreement with all measurements. The smallness of this parameter is regarded as unnatural since one can show that $\bar{\theta}$ is an angle which can in principle take all values between 0 and 2π. In the SM $\bar{\theta}$ belongs to a charge parity (CP) violating term in quantum chromodynamics (QCD), which describes the strongly interacting sector. Due to the smallness of $\bar{\theta}$ we do not observe any CP violation in the strong interactions although in principle the SM would allow for this by symmetry. A natural solution to the smallness of $\bar{\theta}$ was suggested by Peccei and Quinn (PQ) who introduced a new global $U(1)$ symmetry, $U(1)_{PQ}$ [7]. With the new $U(1)_{PQ}$ symmetry an additional pseudo scalar field, called the axion [8, 9] by Wilczek, is endowed with a shift symmetry. This shift symmetry can be used to shift the $\bar{\theta}$ term away and naturally explains the absence of CP violation in the strong interactions.

Soon after the solution of the strong CP problem it was realized that axions can also account for the relic dark matter density in the universe. In the mass range from $10^{-12}\,\mathrm{eV}$ to $0.1\,\mathrm{eV}$ axions are compatible with all constraints from cosmology and astroparticle physics and are also a dark matter candidate. The upper bound on the axion mass comes from astrophysical constraints, while the lower bound belongs to a $U(1)_{PQ}$ breaking scale that correspond to the Planck scale. Smaller masses (larger breaking scales) would make it necessary to also consider quantum gravity effects. Axions are much lighter than other dark matter candidates such as weakly interacting massive particles (WIMPs) because they are produced non-thermally in the early universe. WIMPs have not been found in direct detection experiments on Earth yet. The WIMP dark matter scenario is not completely ruled out since there is still a parameter space region that is compatible with all experimental constraints. However, the growing sensitivity of WIMP direct dark matter searches will soon reach the neutrino floor past which their sensitivity cannot be increased in a straightforward way. As a consequence other particle dark matter candidates, such as the axion,

are now also being actively investigated. The theoretical motivation for axions as well as the relation to dark matter is described in detail in chapter 2.

An important phenomenological implication of axion models is that axions couple to electromagnetism. The coupling to photons is often used in axion searches, since photons are already well studied particles. The parameter space, where axions can constitute the dark matter density, is still highly unconstrained. In figure 1.1 we show the axion-photon coupling $g_{a\gamma}$ over the axion mass m_a. Axion models in the yellow band solve the strong CP problem and are also referred to as *QCD axions* in this thesis to distinguish them from *axion-like particles* (ALPs), which have no general relationship between mass and coupling. Although ALPs do not solve the strong CP problem, in general they are also well motivated particles which are worth while to study since they can for example arise in string theory [10]. ALPs can also account for the relic dark matter density as will be discussed in more detail in section 2.2. In the case of ALPs there is no lower bound on the mass, since ALPs do not have a relation between the axion mass and PQ breaking scale, i.e. $g_{a\gamma}$.

In this thesis we only distinguish between QCD axions and ALPs if necessary. Otherwise we just refer to axions if an explicit distinction is not relevant. The colored regions in figure 1.1 are already excluded by experiments. ALPS I [11] is a light shining through a wall (LSW) experiment whose working principle is explained in great detail in chapter 3. The CAST experiment [12] looks for axions that have been produced in the sun and can be detected on Earth. ADMX [13, 14], RBF [15] and UF [16], are searching for axions from the dark matter halo.

Figure 1.1 makes very clear that due to the largely non-constrained but well motivated parameter space progress on direct searches for axions is very much needed. However, the axion models over the huge mass range cannot be probed by a single experiment since the corresponding photon wavelength changes by many orders of magnitudes. For example the cavity searches ADMX and RBF+UF cannot be extended in a straightforward way to much larger masses since the cavities have to have a smaller volume to probe larger masses (smaller wavelength) and therefore loose sensitivity since their power output is proportional to the cavity volume. In this thesis we mostly consider approaches which can probe axion models with masses above those which typical cavity searches can probe.

In the first part of this thesis (chapters 3 and 4) we work out novel ideas for the direct detection of axions as well as develop more advanced calculation methods that are needed in order to estimate the sensitivities of future experiments. In chapter 3 a one dimensional matrix formalism is developed to describe the phenomenon of axion-photon mixing. The developed matrix formalism is then applied to ultra relativistic axions in LSW experiments. We consider LSW experiments with and without dielectric layers and point out when these can increase the sensitivity of LSW experiments. In chapter 4 we solve the axion-Maxwell equations in three dimensions. Solving the axion-Maxwell equations in three dimensions with finite element studies is typically a non trivial task, that is computationally very expensive. We introduce two specialized calculation techniques which make the 3D calculations possible. These are then applied to open axion haloscopes. Our developed 3D methods are important for a realistic sensitivity forecast of open axion haloscopes such as MADMAX and BRASS, which can search for axion dark matter in the well motivated axion mass range between 10 µeV and 10 meV.

Axions in condensed matter physics

Only very recently axion quasiparticles (AQ) have been proposed to exist in topological magnetic insulators [17] (TMI). TMIs are antiferromagnetically doped topological insulators in which the AQs can arise as magnetic fluctuations. These correspond to spin waves whose quanta are called magnons. AQs in TMIs have a mass in the meV (THz) range. The quasiparticles in TMIs are also called axions because they have the same interaction with electromagnetic fields as the

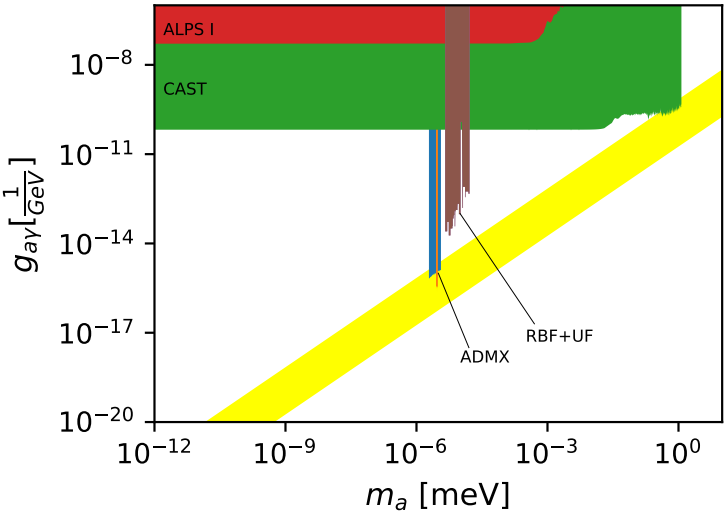

Figure 1.1: Axion-photon coupling $g_{a\gamma}$ over the axion mass m_a. The yellow band represents viable QCD axion models which solve the strong CP problem. Axion models which do not have a relation between $g_{a\gamma}$ and m_a are generically referred to as axion-like particles. Experimental constraints are shown in different colors. A more detailed description of the existing limits can be found in the text.

axions from particle physics. In turn the AQs can also mix with photons. A mixed state of AQs and photons is called an axion polariton, since the mixing phenomenon between both leads to a typical polariton dispersion relation [18].

For particle physicists it is very appealing to also study AQs in TMIs, since this can lead to further insights into axions in particle physics. AQs in TMIs have until now also not been detected. However, several proposals for their detection exist. One way is to detect the AQs via THz transmission spectroscopy [17], where the presence of an AQ would lead to zero transmission around the AQ mass. For a future detection with THz spectroscopy techniques a detailed signal calculation of the expected transmission spectrum is of great relevance. We therefore present such a calculation for a single TMI layer by taking into account the correct interface conditions as well as magnon and photon losses.

In the end we investigate what happens when AQs and DAs coexist together with photons in a TMI. It was shown in Ref. [19] that AQs can be used to detect DAs in the meV range by resonant mixing. In this thesis we perform an explicit signal calculation for the threefold mixing in a layer of TMI. Again we take into account the correct interface conditions for all involved fields as well as magnon and photon losses. A resonant enhancement is needed since otherwise it is very challenging to detect the signal from the weakly interacting DAs.

Chapter 2

Axions and dark matter

In this chapter we discuss the foundations of axions in particle physics. In section 2.1 we review the strong CP problem and show how QCD axions can solve it. Our discussion is mainly based on lecture notes by David Tong [20] and on the review [21]. We discuss the axion as a dark matter candidate together with the corresponding production mechanism in the early universe in section 2.2. Section 2.2 is mainly based on Refs. [21–23].

2.1 Theoretical foundations

The Standard Model (SM) of particle physics is the most successful theory of particle physics up to date. It is a Quantum Field Theory (QFT) which is based on the Poincaré symmetry and the Gauge symmetry group $SU(3) \times SU(2) \times U(1)$.

Although the SM is successful in explaining all kinds of particle physics experiments on Earth there are good reasons to believe that it is not the ultimate theory of everything. One of the reasons is the absence of charge parity violation in the strong interactions. The absence of CP violation in the strong interactions requires a fine tuned relation between two initially independent bare SM parameters. This fine tuning is usually considered as unnatural and is called in the case of the missing CP violation in the strong interactions *strong CP problem*. We discuss the strong CP problem in detail in section 2.1.1. In section 2.1.2 we discuss a possible solution of the strong CP problem with an additional $U(1)$ symmetry and the corresponding pseudo Nambu-Goldstone boson, which is called *axion* (*QCD axion* if an explicit distinction from axion-like particles is necessary).

2.1.1 θ-term and strong CP problem

The SM of particle physics contains the Yang-Mills terms:

$$\mathcal{L}_{\text{SM}} \supset -\frac{1}{4} B_{\mu\nu} B^{\mu\nu} - \frac{1}{4} W^a_{\mu\nu} W^{a,\mu\nu} - \frac{1}{4} G^a_{\mu\nu} G^{a,\mu\nu}, \tag{2.1}$$

where $B_{\mu\nu}$ is the field strength tensor for the gauge group $U(1)$ and $W^a_{\mu\nu}$, $G^a_{\mu\nu}$ are the field strength tensors for $SU(2)$ and $SU(3)$ respectively. In addition to the terms in equation (2.1) one can add at the renormalizable level the following terms:

$$\mathcal{L}_{\text{SM}} \supset \theta_1 \frac{\alpha_Y}{8\pi} B_{\mu\nu} \tilde{B}^{\mu\nu} + \theta_2 \frac{\alpha_W}{8\pi} W^a_{\mu\nu} \tilde{W}^{a,\mu\nu} + \theta_3 \frac{\alpha_s}{8\pi} G^a_{\mu\nu} \tilde{G}^{a,\mu\nu}, \tag{2.2}$$

where α_Y, α_W and α_s are the couplings that describe the electroweak and strong interactions. The dual field strength tensors are defined as $\tilde{B}_{\mu\nu} = \frac{1}{2}\epsilon_{\mu\nu\rho\sigma} B^{\rho\sigma}$, $\tilde{W}^a_{\mu\nu} = \frac{1}{2}\epsilon_{\mu\nu\rho\sigma} W^{a,\rho\sigma}$, $\tilde{G}^a_{\mu\nu} = \frac{1}{2}\epsilon_{\mu\nu\rho\sigma} G^{a,\rho\sigma}$. In equation (2.2) θ_N are constants. All terms in equation (2.2) respect the symmetries of the SM and therefore also have to be consider.

In the SM the θ_1 and θ_2 terms can be rotated away by chiral transformations [24, 25]. However, we cannot do the same with θ_3. In the following we discuss therefore only the θ_3 term and leave out the subscript 3: $\theta_3 \to \theta$.

The θ term can be written as a total derivative $G^a_{\mu\nu}\tilde{G}^{a,\mu\nu} = \partial_\mu K^\mu$ and therefore does not contribute in perturbative calculations. However, it can contribute non-perturbatively and therefore cannot be neglected [26–31].

The QCD Lagrangian is [21]:

$$\mathcal{L}_{\text{QCD}} = \sum_q \bar{q}(i\not{D} - m_q e^{i\theta_q})q - \frac{1}{4}G^{a,\mu\nu}G^a_{\mu\nu} + \theta\frac{g_s^2}{32\pi^2}G^{a\mu\nu}\tilde{G}^a_{\mu\nu}, \tag{2.3}$$

where q is a Dirac spinor, m_q the mass of the quark fields and the sum runs over all quark flavors. The covariant derivative in equation (2.3) is defined as $D_\mu = \partial_\mu - ig_s T^a A^a_\mu$, the $SU(3)$ field strength tensor is given by $G^a_{\mu\nu} = \partial_\mu A^a_\nu - \partial_\nu A^a_\mu + g_s f^{abc} A^b_\mu A^c_\nu$, where $g_s^2 = 4\pi\alpha_s$ is the strong coupling constant T^a are the generators of $SU(3)$, f^{abc} are the structure constants and we use the convention $\epsilon^{0123} = -1$. The θ term in equation (2.3) violates CP invariance. The angle θ_q that appears in the quark mass term has to be considered, because in general the quark mass is not real and has to be made real trough a chiral rotation. Applying a chiral rotation to make the quark mass terms real shifts θ_q to the $G\tilde{G} := G^{a,\mu\nu}G^a_{\mu\nu}$ term because the chiral rotation is anomalous. Therefore after the chiral rotation, which makes the mass term in the QCD Lagrangian real, the QCD Lagrangian becomes:

$$\mathcal{L}_{\text{QCD}} = \sum_q \bar{q}(i\not{D} - m_q)q - \frac{1}{4}G^{a\mu\nu}G^a_{\mu\nu} + \bar{\theta}\frac{g_s^2}{32\pi^2}G^{a\mu\nu}\tilde{G}^a_{\mu\nu}, \tag{2.4}$$

with

$$\bar{\theta} := \theta - \sum_q \theta_q, \tag{2.5}$$

where the sum runs over all quarks. The $\bar{\theta}$-parameter is physical and appears for example in the prediction for the neutron electric dipole moment. A calculation based on QCD sum rules [32] gives:

$$d_n = 2.4\,(1.0) \times 10^{-16}\,\bar{\theta}\,e\,\text{cm} = 1.2\,(0.5) \times 10^{-2}\,\bar{\theta}\,e\,\text{GeV}^{-1}. \tag{2.6}$$

Current experimental bounds [33] on d_n then translate to a bound on $\bar{\theta}$:

$$\bar{\theta} < 3 \times 10^{-10}. \tag{2.7}$$

The smallness of $\bar{\theta}$ is often regarded as a fine tuning problem, since it requires that two independent bare parameters of the SM Lagrangian are fine tuned in order to achieve a cancellation that leads to the smallness of the $\bar{\theta}$ parameter. The fine tuning of two independent bare parameters of the SM is seen as very unnatural and therefore regarded as the *strong CP problem*.

It is a matter of taste if one sees in the smallness of $\bar{\theta}$ as a problem, since one could argue that the SM is not a complete theory of everything and therefore the smallness of $\bar{\theta}$ could be obvious in a more fundamental theory. However, one can also argue that the smallness of the $\bar{\theta}$ parameter can lead us to a more complete theory and therefore it is worth while to investigate how the SM can be extended such that the smallness of $\bar{\theta}$ follows naturally. If this can be achieved then a more complete theory would also try to reproduce the mechanism that makes $\bar{\theta}$ in the SM extension naturally very small.

We have argued that $\bar{\theta}$ is a physical parameter. It appears for example in the QCD vacuum energy density. One can show that the minimum is reached for $\bar{\theta} = 0$ [34]. Furthermore the QCD vacuum energy density is periodic in θ, i.e., $E(\theta) = E(\theta+2\pi)$ and has a the property $E(\theta) = E(-\theta)$.

2.1.2 The axion as a solution of the strong CP problem

It was first noticed by Peccei and Quinn that the smallness of the $\bar{\theta}$ parameter can be explained very naturally if an additional global $U(1)$ symmetry is introduced on top of the SM [7, 35]. In remembrance of its inventors the global symmetry is often called $U(1)_{PQ}$. It was soon realized by Wilczek and Weinberg [8, 9] that the $U(1)_{PQ}$ symmetry therefore predicts a massive pseudo Nambu-Goldstone boson. This new pseudo scalar particle was called *axion* by Wilczek.

After this short historical introduction we first discuss the idea how the axion solves the strong CP problem. This is followed by considering an explicit UV complete axion model. In the end we discuss a more general effective axion Lagrangian which can be matched to all kinds of UV complete axion models.

The idea behind the axion solution of the strong CP problem is that the axion field a obeys a shift symmetry $a \to a + \tilde{\kappa} f_a$, where f_a is the axion decay constant and $\tilde{\kappa}$ is an arbitrary parameter. On the other side the axion couples to $G\tilde{G}$:

$$\frac{g_s^2}{32\pi^2}\frac{a}{f_a}G\tilde{G}. \tag{2.8}$$

The shift symmetry can now be used to get rid of the $\bar{\theta}$ term.

To understand how the coupling in equation (2.8) can be generated one has to construct a UV complete model. Here we discuss the KSVZ axion model [36, 37] that is named after its inventors Kim, Shifman, Vainshtein and Zakharov and which is one of the most minimalistic axion model. In the KSVZ model all SM particles are $U(1)_{PQ}$ singlets. On top of the SM new quarks $Q = (Q_L, Q_R)$ and a complex scalar field φ are introduced. The fields which are introduced on top of the SM transform under $U(1)_{PQ}$ as follows:

$$\varphi \to e^{i\alpha}\varphi, \quad Q_L \to e^{i\alpha/2}Q_L, \quad Q_R \to e^{-i\alpha/2}Q_R. \tag{2.9}$$

The terms on top of the SM, which respect all symmetries, are:

$$\mathcal{L}_{\text{Y, KSVZ}} = -Y_\varphi \bar{Q}_L \varphi Q_R + \text{h.c.}, \tag{2.10}$$

$$\mathcal{L}_{H\varphi}(\Phi, \varphi) = \lambda_\varphi(|\varphi|^2)^2 - \mu_\varphi|\varphi|^2 + \lambda_{\varphi H}|\varphi|^2\Phi^\dagger\Phi, \tag{2.11}$$

$$\mathcal{L}_{\text{kin, KSVZ}} = \bar{Q}_L i\not{D} Q_L + \bar{Q}_R i\not{D} Q_R + (\partial_\mu\varphi)^\dagger\partial^\mu\varphi, \tag{2.12}$$

where Φ is the Higgs doublet and Y_φ is an additional Yukawa coupling.

We now assume that at some scale $U(1)_{PQ}$ is spontaneously broken and the scalar potential acquires a minimum at $|\varphi| = v_{PQ}$. We can then expand φ around v_{PQ}:

$$\varphi(x) = \frac{1}{\sqrt{2}}(v_{PQ} + \rho(x))e^{ia(x)/v_{PQ}}. \tag{2.13}$$

The axion arises in the phase of the scalar field φ. After PQ symmetry breaking the axion a is the massless Nambu-Goldstone boson. The mass of the additional quarks $\sim v_{PQ}Y_\varphi$ is large and at low energies we can integrate them out. The corresponding diagram is shown in figure 2.1, where the heavy quarks are in the loop of the triangle diagram. The QCD anomaly breaks the $U(1)_{PQ}$ symmetry explicitly, making the axion a pseudo Nambu-Goldstone boson. We discuss the axion mass later in this section. Evaluating the diagram in figure 2.1 yields an additional term in the low energy Lagrangian: $\frac{a}{v_{PQ}}\frac{g_s}{32\pi^2}G\tilde{G}$. Since a is shift symmetric we have now shown that we get exactly the term that we need to remove the $\bar{\theta}$ term. In more general axion models one can have more fermions that are in the loop in figure 2.1. To classify this the color anomaly factor $\mathcal{N}$ is introduced. On top that we can also have an electromagnetic anomaly factor $\mathcal{E}$. In the KSVZ model we have $\mathcal{N} = \frac{1}{2}$ and $\mathcal{E} = 0$. The domain wall number

$$N_{\text{DW}} = 2\mathcal{N} \tag{2.14}$$

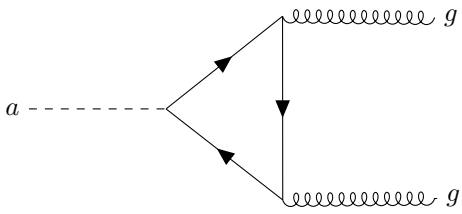

Figure 2.1: Diagram that generates the $aG\tilde{G}$ term that is required to shift away the $\bar{\theta}$ term. In the KSVZ model the heavy quarks Q appear inside the loop.

is important when we consider topological defects that can contribute to the axion dark matter density in the early universe. N_{DW} counts how many degenerate minima in the axion potential exist. In the KSVZ model we have $N_{\mathrm{DW}} = 1$. We discuss the cosmological consequences of N_{DW} further in section 2.2.

In the KSVZ model all SM particles are $U(1)_{PQ}$ singlets and only the added fields carry PQ charges. However, this is not the case for all axion models. In the DFSZ model [38, 39] also SM particles carry PQ charges and the $aG\tilde{G}$ coupling is produced by SM particles in the loop in figure 2.1. In the DFSZ model we get $\mathcal{E} = 8$ and $\mathcal{N} = 3$ and $N_{\mathrm{DW}} = 6$. For a more complete description of the DFSZ model we refer to Ref. [21].

We have now outlined how the $aG\tilde{G}$ coupling in the KSVZ model is produced. However, through mixing with pions this can also result in a $aF\tilde{F}$ coupling. In general the couplings of the axion with SM particles depend on the UV complet axion model. In the following we therefore summarize the most important couplings in an effective Lagrangian. A detailed derivation of the summarized results can be found in Ref. [21].

The axion Lagrangian has a mass and also a kinetic term:

$$\mathcal{L}_a \supset \frac{1}{2}\partial_\mu a \partial^\mu a - \frac{1}{2} m_a^2 a^2. \tag{2.15}$$

With chiral Lagrangian techniques we can derive an expression for the axion mass:

$$m_a^2 = \frac{m_u m_d}{(m_u + m_d)^2} \frac{m_\pi^2 f_\pi^2}{f_a^2} \tag{2.16}$$

where m_u is the up quark mass, m_d the down quark mass, f_π is the pion decay constant, m_π is the pion mass and $f_a = \frac{v_{PQ}}{2\mathcal{N}}$ is the axion decay constant. The pion mass enters in equation (2.16) since the axions acquire their mass via mixing with pions which is described with chiral Lagrangian techniques. The relation for the axion mass in equation (2.16) can be estimated by including QED and NNLO effects. In this case we obtain [40]:

$$m_a = 5.691(51) \left(\frac{10^{12}\,\mathrm{GeV}}{f_a} \right) \mu\mathrm{eV}. \tag{2.17}$$

The estimate of the axion mass based on chiral Lagrangian techniques is valid below the QCD phase transition around $T_C = 160\,\mathrm{MeV}$. One therefore also speaks about that the axion builds up its potential around the QCD phase transition. Chiral Lagrangian techniques can be used below T_C because then QCD is confining. Above the chiral phase transition one can use the dilute instanton gas approximation [41] to estimate the axion mass. Sometimes one refers to this when one says that 'axions acquire their mass by QCD instanton effects'.

For arbitrary temperature the axion mass can only be computed on the lattice. It is given by [42]:

$$m_a^2(T) f_a^2 = \chi^2(T), \tag{2.18}$$

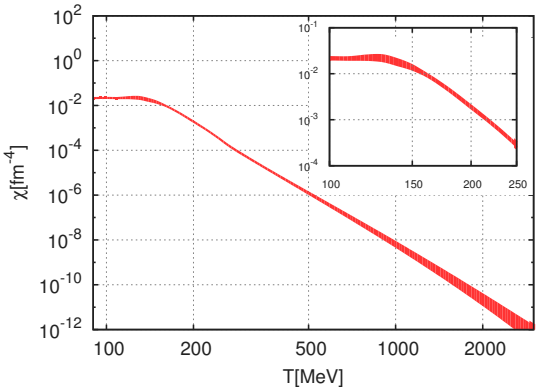

Figure 2.2: Topological susceptibility χ over temperature T from lattice calculations. The figure is taken from [42].

where $\chi(T)$ is the temperature dependent topological susceptibility. In figure 2.2 we show $\chi(T)$ from lattice results [42]. Below T_C the axion mass approaches a constant value that coincides with the chiral Lagrangian computation. However, for $T > T_C$ the axion mass decreases significantly.

The axion photon coupling is described by following effective Lagrangian:

$$\mathcal{L}_a \supset -\frac{g_{a\gamma}}{4} a F^{\mu\nu} \tilde{F}_{\mu\nu}, \tag{2.19}$$

with

$$g_{a\gamma} = \frac{\alpha}{2\pi f_a}\left(\frac{\mathcal{E}}{\mathcal{N}} - \frac{2}{3}\frac{4m_d + m_u}{m_u + m_d}\right). \tag{2.20}$$

The coupling $g_{a\gamma}$ is also sometimes expressed in terms of the dimensionless quantity $C_{a\gamma}$:

$$g_{a\gamma} = \frac{\alpha}{2\pi f_a} C_{a\gamma}, \tag{2.21}$$

with $C_{a\gamma} = \frac{\mathcal{E}}{\mathcal{N}} - \frac{2}{3}\frac{4m_d+m_u}{m_u+m_d}$. Higher order corrections to $C_{a\gamma}$ have been obtained in [43]:

$$C_{a\gamma} = \frac{\mathcal{E}}{\mathcal{N}} - 1.92(4). \tag{2.22}$$

We will always use the $C_{a\gamma}$ from equation (2.22) in this thesis.

The interaction of axions and electrons is described by:

$$\mathcal{L}_a \supset g_{ae} \frac{\partial_\mu a}{2m_e} \bar{e}\gamma^\mu\gamma_5 e, \tag{2.23}$$

where $g_{ae} = C_{ae}\frac{m_e}{f_a}$ and m_e is the electron mass. A similar interaction as in (2.23) can also be derived for the interaction with nuclear spins:

$$\mathcal{L}_a \supset g_{an}\frac{\partial_\mu a}{2m_n}\bar{n}\gamma^\mu\gamma_5 n + g_{ap}\frac{\partial_\mu a}{2m_p}\bar{p}\gamma^\mu\gamma_5 p, \tag{2.24}$$

where $g_{an} = C_{an}\frac{m_n}{f_a}$ and $g_{an} = C_{ap}\frac{m_p}{f_a}$, with the dimensionless constants C_{ap} and C_{an} and m_n and m_p are the mass of the neutron and proton respectively. The interaction of axions and quarks can also be specified, when the axion energies are high enough such that the axion-nucleon coupling is not valid anymore.

There is also an axion-gluon coupling which generates a nuclear electric dipole moment:

$$\mathcal{L}_a \supset -\frac{i}{2} g_d\, a\, \bar{n}\sigma_{\mu\nu}\gamma_5 n F^{\mu\nu} \tag{2.25}$$

where m_n is the mass of the nucleon.

All different axion couplings give rise to detection ideas on Earth and in Space. The chapters 3 and 4 of this thesis are based on the axion-photon mixing. Chapter 5 is also based on the axion-photon mixing but includes a mixing with an axion quasiparticle in a condensed matter system.

Summarized the effective Lagrangian that describes the axion-photon coupling is given by:

$$\mathcal{L}_{a\gamma} = -\frac{1}{4}F^{\mu\nu}F_{\mu\nu} - J^{\mu}A_{\mu} + \frac{1}{2}\partial_{\mu}a\partial^{\mu}a - \frac{1}{2}m_a^2a^2 - \frac{g_{a\gamma}}{4}aF^{\mu\nu}\tilde{F}_{\mu\nu}. \tag{2.26}$$

In the previous discussion we have discussed 'axions', which solve the strong CP problem. From now on in this thesis we will refer to these as *QCD axions*. The more general class of particles, which does not have the relation between m_a and f_a in equation (2.16) (and therefore does not solve in general the strong CP problem) will from now on be referred to as *axion-like* particles (ALP). However, we only make a clear distinction between QCD axions and axion-like particles if there is any fundamental difference between the treatment of both cases. In most cases we will talk about axions with which we refer to QCD axions and also to axion-like particles.

2.2 Axion cosmology

In the previous section we have introduced QCD axions, which solve the strong CP problem, as well as the wider class of axion-like particles. In this section we discuss that either of them can account for the dark matter density in our universe. On top of that we outline the corresponding production mechanism in the early universe. Contrary to weakly interacting massive particles (WIMP), axions are produced non-thermally and can therefore be much lighter as typical WIMP dark matter candidates. In this section we distinguish explicitly between axion-like particles and QCD axions. First we discuss the QCD axion as a dark matter candidate and only at the end of this section we outline that also axion-like particles can account for the dark matter density.

The QCD axion dark matter production depends on the scale $f_a = \frac{v_{PQ}}{2\mathcal{N}}$, where the PQ symmetry was broken in the early universe. We have to distinguish between two scenarios.

In the *pre-inflationary scenario* the PQ symmetry was broken before or during inflation. After inflation the PQ symmetry remains broken. In this case an initial value $a_i = \theta_i f_a$ expanded rapidly during inflation and therefore after inflation the initial axion values a_i is the same in the whole observable universe [23]. The QCD axion dark matter is produced solely via the misalignment mechanism [44–46] in the pre-inflationary scenario. To get the correct relic dark matter abundance a relation between the initial misalignment angle θ_i and the mass of the QCD axion m_a (or equivalently f_a) has to be fulfilled. We show this relation in figure 2.3, which is obtained from lattice calculations. For relatively large QCD axion masses the initail misalignment angel θ_i has to be close to pi in order to explain the relic dark matter abundance. For small axion masses a very small θ_i is required. An initial misalignment angle very close to π or to zero is regarded as fine tuned and therefore masses of the order $10^{-6} - 10^{-4}\,\text{eV}$ can be seen as natural in this scenario. The top row in figure 2.4 shows in yellow the QCD axion mass range which requires no tuning in order to explain the dark matter relic density. The other two regions which are labeled 'tuned' correspond either to a misalignment angle that is very close to π or zero. For axion masses $m_a \gtrsim 1\,\text{meV}$ the misalignment mechanism does not produce enough axions such that the dark matter abundance can be explained.

In the *post-inflationary scenario* the PQ symmetry was also broken before or during inflation. However, it was restored again after inflation and then broken again. In this case the initial QCD axion field can acquire different initial values in the observable universe. The realignment mechanism can still be used to explain the dark matter density. However, one has now to average over all possible initial angles. In figure 2.3 the lower bound of the red solid line, which is at $m_a = 26\,\mu\text{eV}$ corresponds to the case that 100% of the dark matter can be produced through the

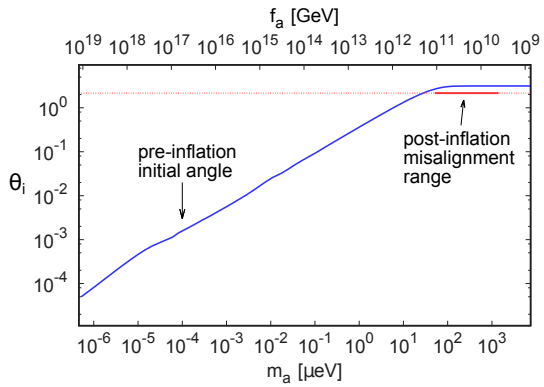

Figure 2.3: Axion dark matter production from the misalignment mechanism. The relation between the QCD axion mass m_a and the initial misalignment angle θ_i in the pre-inflationary scenario (blue) has to be fulfilled such that axions can account for the correct relic dark matter density in our universe. The figure is taken from [42]. In the post-inflationary scenario different misalignment angles appear in different regions of the observable universe. Therefore an averaged angle $\theta_i = 2.155$ is considered. The red solid line describes the range where the misalignement mechanism contributes significantly to the relic dark matter density. At the lowest bound $m_a = 26\,\text{meV}$ the misalignment mechanism produces 100% of the dark matter density. At the largest m_a of the solid red line the misalignment mechanism produces only 1% of the dark matter density. In this case the other 99% has to be produced for example by the decay of topological defects.

misalignment mechanism in the post inflationary scenario. However, for larger masses, m_a, less than 100% can be produced with the misalignment mechanism. At the upper bound of the red solid line, which is around $m_a = 1.5\,\text{meV}$, the misalignment mechanism produces only 1% of the dark matter abundance. Note that this does not mean that not enough axions can be produced. In the post-inflationary scenario the initial axion field is not uniform over the whole observable universe. Therefore QCD axions can also be produced by decays of topological defects such as strings or domain walls [47, 48]. In the high mass region the production of QCD axions form topological defects, such as strings and domain walls, is therefore important since the production form the misalignment mechanism is subdominant.

When we consider the QCD axion production from topological defects in the post-inflationary scenario we have to distinguish between two cases. If the domain wall number $N_{\text{DW}} = 1$ then the topological defects decay around the QCD phase transition. In this case the so called *domain wall problem*, where the topological defects over close the universe, does not occur. In this case a preferred axion mass around $26.2 \pm 3.4\,\mu\text{eV}$ is found [49, 50]. In the middle line in figure 2.4 we show in yellow the axion mass prediction for the $N_{\text{DW}} = 1$ case with an uncertainty range. For very small masses too much dark matter would be produced (overclosure) while for too large masses not enough dark matter is produced (subdominant). In the case that $N_{\text{DW}} > 1$ the PQ symmetry has to be broken explicitly in order to allow for the decay of the topological defects. In this case it can be shown that larger axion masses are favored. The authors of [51] point out that for $N_{\text{DW}} = 6$ the mass interval $0.56\,\text{meV} \leq m_a \leq 130\,\text{meV}$ is allowed. The respective QCD axion mass interval is shown in the bottom row of the summary figure 2.4. Very recent studies confirm this and find $m_a > 3.5\,\text{eV}$ [52] for $N_{\text{DW}} = 6$. Note that the simulation of the contribution of topological defects to the QCD axion dark matter density is computationally very expensive. Therefore the estimates for the QCD axion mass range where topological defects can account for the axion dark matter density have huge uncertainties. It is topic of todays research to improve these simulations.

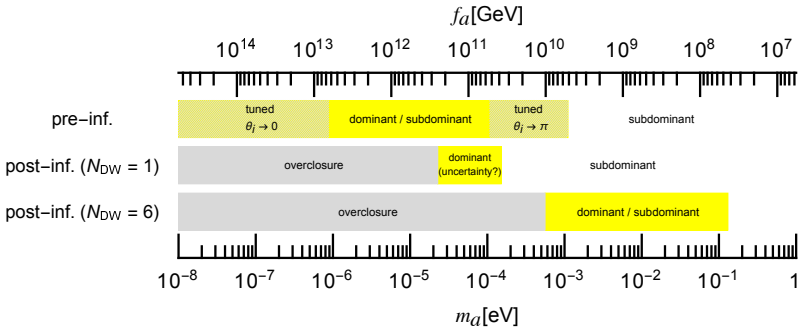

Figure 2.4: QCD axion mass range predictions in different scenarios. The yellow regions depict the preferred QCD axion mass region where the correct dark matter relic density can be produced. In the top row the PQ symmetry was broken before or during inflation (pre-inflationary scenario). The middle and bottom row show the scenario that the PQ symmetry was broken before or during inflation, restored afterwards and then broken again (post-inflationary scenario). In the post-inflationary scenario the case $N_{\mathrm{DW}} = 1$ and $N_{\mathrm{DW}} > 1$ have to be distinguished. In the case $N_{\mathrm{DW}} > 1$ much larger axion masses can match the dark matter density, since decays of topological defects contribute to the dark matter density. The figure is taken from Ref. [23].

Overall we can conclude that searching for QCD axions in the range $10^{-12}\,\mathrm{eV}$-$10^{-1}\,\mathrm{eV}$ is theoretically well motivated. The lower bound comes from the fact that $m_a \approx 10^{-12}\,\mathrm{eV}$ corresponds to an f_a which is on the order of the Planck scale. The upper bound comes from astrophysical constraints and the fact that it is hard to get the right dark matter relic density from topological defects for QCD axion masses that are larger than $0.1\,\mathrm{eV}$.

Finally let us also consider the more general case of ALPs, which are defined in the Lagrangian (2.26) with m_a and $g_{a\gamma}$ being independent. ALPs can also constitute the dark matter density in a large parameter. The following discussion is adapted form Refs. [53–55]. In the red regions in figure 2.5 ALPS can constitute the dark matter relic density due to the misalignment mechanism. Decays from topological defects are not discussed for ALPs here, but can in principle also contribute to the dark matter density. The red region which is labeled 'Standard ALP CDM' describes the standard case in which the present day ALP mass m_0 equals the mass of the ALP at time t_1 where the ALP field starts to oscillate: $3H(t_1) = m_a(t_1) =: m_1$, where H is the Hubble constant. The striped red regions above the standard ALP region in figure 2.5 belong to the case where $\frac{m_1}{m_0}\left(\frac{\Lambda}{T}\right) \ll 1$, where Λ is the scale at which an additional $SU(N)$ group condenses and T is the temperature of the additional $SU(N)$ sector. β follows from instanton calculations. In figure 2.5 the red stripes correspond to a variation of $\beta = 1, 3, 5, 7, 9$. The red region in figure 2.5, that is labeled $m_1 > 3H(T_{eq})$ is the most conservative bound which all ALP models have to fulfill. It comes from the requirement that at temperature T_{eq} where matter radiation equality is reached, the ALP mass has to be larger than the Hubble constant [53].

In the region in figure 2.5, that is labeled $\tau < 10^{17}\,\mathrm{s}$, the life time of the ALPS is shorter than the age of the universe. Therefore the ALPS in this parameter space cannot be a dark matter candidate. In the parameter region where $\tau > 10^{17}\,\mathrm{s}$ a fraction of the ALPs can still decay. These decays have consequences for the extragalactic background light (EBL). However, no clear signal hs been detected in the EBL, which leads to the exclusion of the region that is labeled EBL in figure 2.5. The regions, which are labeled 'Optical' and 'X-Rays', are bounds which arise when one analyzes X-rays and optical light that propagate in the universe. ALP dark matter – if it exists in the right mass range – would lead to spectral lines in the X-ray or optical spectra. Since no direct evidence is found the corresponding exclusions in figure 2.5 can be made. The exclusion region χ_{ion} corresponds to the case when the ALPs trigger a reionization in the early universe which

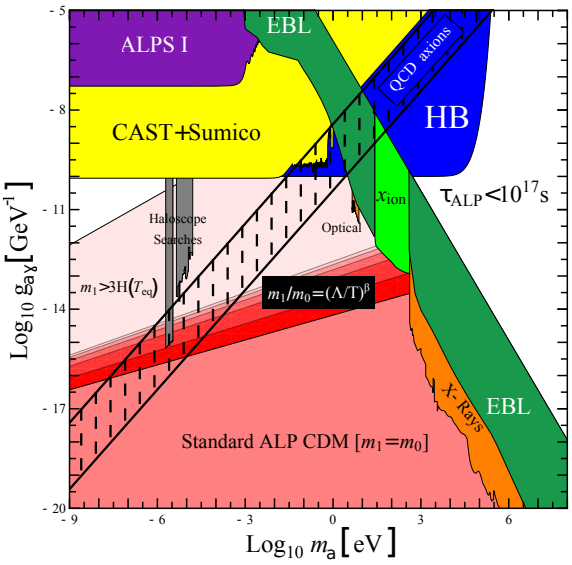

Figure 2.5: Axion parameter space in the m_a-$g_{a\gamma}$ region. The axion QCD band is represented by the hatched band. The preferred axion dark matter regions are marked in different shades of red. In the figure we take into account only the contributions from the misalignment mechanism. For a detailed discussion we refer to the text. The figure is taken from [53].

happens to early. The exclusion, which is labeled 'HB', comes from the observation of horizontal branch stars. The exclusion regions labeled 'CAST+Sumico' and 'ALPS I' come from two direct detection experiments. CAST searches for solar axions that arrive on Earth while ALPS I is a light shining through a wall experiment. We will study several extensions the descendant ALPS II in depth in chapter 3 and therefore postpone a more detailed discussion until then.

The local dark matter density is estimated as [56]:

$$\rho_{\mathrm{DM}} = \frac{300\,\mathrm{MeV}}{\mathrm{cm}^3}, \tag{2.27}$$

where the estimate comes with an uncertainty of a factor 2 or 3 [56]. From the dark matter density we can estimate the number density of the dark matter particles:

$$\mathcal{N}_{\mathrm{DM}} = 10^{13}\frac{1}{\mathrm{cm}^3}\left(\frac{30\,\mu\mathrm{eV}}{m_{\mathrm{DM}}}\right), \tag{2.28}$$

where in our case the mass of the dark matter particle is the axion mass $m_{\mathrm{DM}} = m_a$. The number of dark matter particles in a cube with the length of one de Broglie wavelength is:

$$N_{\mathrm{DM}} = \mathcal{N}_{\mathrm{DM}}\lambda_{dB}^3 = 7\times 10^{23}\left(\frac{30\,\mu\mathrm{eV}}{m_{\mathrm{DM}}}\right)^4\left(\frac{10^{-3}}{v_{\mathrm{DM}}}\right), \tag{2.29}$$

where the de Broglie wavelength for a non relativistic dark matter particle is given by:

$$\lambda_{\mathrm{dB}} = \frac{2\pi}{m_{\mathrm{DM}}v_{\mathrm{DM}}} = 41.3\,\mathrm{m}\left(\frac{30\,\mu\mathrm{eV}}{m_{\mathrm{DM}}}\right)\left(\frac{10^{-3}}{v_{\mathrm{DM}}}\right). \tag{2.30}$$

For dark matter particle masses $m_{\mathrm{DM}} > 27\,\mathrm{eV}$ we get $N_{\mathrm{DM}} < 1$. Therefore, in the case that $m_{\mathrm{DM}} = m_a < 27\,\mathrm{eV}$ we can describe the axion as a coherent state that oscillates in time:

$$a(t) = \hat{a}e^{i\omega t}. \tag{2.31}$$

The amplitude $\hat{a}$ can be inferred from measurements of the local dark matter density ρ_a:

$$\frac{m_a^2|\hat{a}|^2}{2} = \rho_a \stackrel{!}{=} \rho_{\mathrm{DM}} = \frac{300\,\mathrm{MeV}}{\mathrm{cm}^3}. \tag{2.32}$$

The axion field, that is described in equation (2.31), is in the zero velocity limit. The velocity of the axions in the Galaxy halos is $v_a = v_{DM} = 10^{-3}$ [57]. This can be described in the plane wave approximation as:

$$a(\boldsymbol{x}, t) = \hat{a} e^{i\omega t + i\boldsymbol{k}_{\mathrm{DM}}\boldsymbol{x}}. \tag{2.33}$$

where $\boldsymbol{k}_{\mathrm{DM}}$ depends on the direction with which the DM particles move with respect to the Earth.

Chapter 3

A generalized matrix formalism for axion-photon mixing

The axion-Maxwell equations that arise from the Lagrangian in equation (2.26) give rise to a rich phenomenology and many detection ideas for axions. In this section we first study the general one dimensional solutions of the axion-Maxwell equations in the presence of an external B-field in a single homogeneous medium. The solutions are given to all orders in the axion-photon coupling in a medium with finite permittivity, permeability and conductivity. We classify the solutions in weak and strong mixing regions.

Based on the solution in a single medium we develop a matrix formalism, which computes the solutions for the electromagnetic and axion fields in systems where different media are stacked together to a multi layer system. This goal is achieved by matching the solutions in the different media by applying interface conditions to the involved fields. In this way we obtain the solution for all electromagnetic and axion fields that leave the multi layer systems. The matrix formalism is valid for axions of arbitrary velocity. We show that in the zero or small velocity limit the matrix formalism reduces to the existing formalism in Ref. [58, 59].

Although the derived equations are very general and can be applied to astrophysical as well laboratory experiments we only apply them here to laboratory scenarios which involve ultra relativistic axions. We show that one can rederive the axion-photon conversion formula for ultra relativistic axions [60] that travel through a magnetized region. Furthermore we show how dielectric layers can improve the sensitivity of light shining through a wall experiments.

3.1 Solution of axion-Maxwell equations to all orders

In this section we solve the axion-Maxwell equations to all orders in the axion-photon coupling $g_{a\gamma}$ in the presence of a strong external B-field. We first compute the result in a medium which is characterized by constant permittivity ϵ, permeability μ, conductivity σ and external B-field $\boldsymbol{B}_e$. In the following sections we use the results obtained here to construct the solution of the axion-Maxwell equations in media with various ϵ, μ, σ and regions of different external B-fields. Our results in this section extend the results of Ref. [61], which does the computation in a perfect vacuum ($\epsilon = 1, \mu = 1, \sigma = 0$).

The macroscopic axion-Maxwell equations can be obtained from the Lagrangian in equa-

tion (2.26) [62] by a following transition to macroscopic field equations [58]:

$$\begin{aligned} \nabla \cdot \boldsymbol{D} &= \rho_f + \rho_a, && (3.1)\\ \nabla \times \boldsymbol{H} - \partial_t \boldsymbol{D} &= \boldsymbol{J}_f + \boldsymbol{J}_a, && (3.2)\\ \nabla \cdot \boldsymbol{B} &= 0, && (3.3)\\ \nabla \times \boldsymbol{E} + \partial_t \boldsymbol{B} &= 0, && (3.4)\\ (\partial_\mu \partial^\mu + m_a^2) a &= g \boldsymbol{E} \cdot \boldsymbol{B}, && (3.5) \end{aligned}$$

where a is the pseudo-scalar axion field, m_a its mass, $\boldsymbol{E}$ is the electric field, $\boldsymbol{B}$ the magnetic field, $\boldsymbol{D}$ the displacement field, $\boldsymbol{H}$ the magnetic field strength, ρ_f the free charge density and $\boldsymbol{J}_f$ the free current density which fulfill the continuity equation $\nabla \cdot \boldsymbol{J}_f + \dot{\rho}_f = 0$ as in usual electrodynamics. We furthermore have defined the axionic charge and current density, $\rho_a = -g_{a\gamma} \boldsymbol{B} \cdot \nabla a$ and $\boldsymbol{J}_a = g_{a\gamma}(\boldsymbol{B}\partial_t a - \boldsymbol{E} \times \nabla a)$, which fulfill the continuity equation $\nabla \cdot \boldsymbol{J}_a + \partial_t \rho_a = 0$. The axion photon coupling $g_{a\gamma}$ is also often expressed in terms of the dimensionless constant $C_{a\gamma}$, the axion decay constant f_a and the fine structure constant α as [43]:

$$g_{a\gamma} = -\frac{\alpha}{2\pi f_a} C_{a\gamma} = -1.16 \times 10^{-12}\,\mathrm{GeV}^{-1} \left(\frac{10^9 \mathrm{GeV}}{f_a} \right) C_{a\gamma}, \qquad (3.6)$$

where $C_{a\gamma}$ is a model dependent quantity of order unity [63].

In order to solve the specified axion-Maxwell equations we assume linear constitutive relations $\boldsymbol{D} = \epsilon \boldsymbol{E}$, $\boldsymbol{H} = \mu^{-1} \boldsymbol{B}$. We divide the B-field into an external background (e) and reaction (r) field $\boldsymbol{B} = \boldsymbol{B}^e + \boldsymbol{B}^r$. The background field fulfills separately Maxwell equations without axion source terms. The total current is $\boldsymbol{J}_f = \boldsymbol{J}_f^r + \boldsymbol{J}_f^e$, where $\boldsymbol{J}_f^e$ generates the external B-field and $\boldsymbol{J}_f^r = \sigma \boldsymbol{E}$ is the reaction current. Furthermore we set $\rho_f = 0$. The other fields are not divided into reaction and background fields.

The non-linear terms in the equations (3.1)-(3.5) can be linearized as the external B-field is required to be much larger than all other fields. We set $\rho_a \to -g_{a\gamma} \boldsymbol{B}^e \nabla a$, $\boldsymbol{E} \cdot \boldsymbol{B} \to \boldsymbol{E} \cdot \boldsymbol{B}^e$ and $\boldsymbol{J}_a \to g_{a\gamma} \boldsymbol{B}^e \partial_t a$. The linearization in $\boldsymbol{J}_a$ is only possible since $|\boldsymbol{E} \times \nabla a| < |\boldsymbol{B}^e \partial_t a|$. For zero velocity axions this is obviously fulfilled, since then $\nabla a = 0$. For non-zero velocity axions we define a characteristic velocity $v = \partial_t a / |\nabla a|$. Then the condition for the linearization is: $E < 3 \times 10^8 \frac{\mathrm{V}}{\mathrm{m}} \left(\frac{v}{3 \times 10^8\ \mathrm{m/s}} \right) \left(\frac{B^e}{1\,\mathrm{T}} \right)$, what is obviously fulfilled for ultra relativistic axions and existing E-field sources.

In the justification of the linearization we have only considered the absolute magnitude of the electromagnetic fields. However, if the external B-field is linearly polarized there is also a source term in the polarization, that is orthogonal to the B-field polarization and which is coming from the non-linear term $\boldsymbol{E} \times \nabla a$. However, the non-linear source term that is orthogonal to the external B-field is much smaller in magnitude than then source term of the external B-field. Therefore the non-linear source term can lead to a small polarization rotation which is neglected in the linearization that we make. We are not aware of any work that has investigated the effect of this non-linear source term which is probably due to the fact that an investigation would require to solve the nonlinear equations numerically.

In the following we reduce the problem to one dimension, e.g. all fields depend only on z and propagate only in z-direction. The electromagnetic fields are transverse and we set $E_z = 0 = B_z$. With all simplifications together we end up with the following coupled system of equations:

$$\begin{aligned} (-\partial_z^2 + \epsilon\mu\partial_t^2 + \mu\sigma\partial_t) E &= -\mu\varrho\partial_t^2 a, && (3.7)\\ (-\partial_z^2 + \partial_t^2 + m_a^2) a &= \varrho E, && (3.8) \end{aligned}$$

with $\varrho := g_{a\gamma} B^e$. The E-field that appears in (3.7) and (3.8) is the y-component, since we have assumed that the external B-field is polarized in the y-direction: $\boldsymbol{B}^e = \hat{\boldsymbol{e}}_y B^e$. The E_x-component

is not coupled to the axion in the linearized equations and fulfills equation (3.7) without an axion source term. We do not consider the x-component in the following and drop the y-index in the following notation.

3.1.1 Dispersion relation

To solve the coupled equations (3.7) and (3.8) we make the ansatz $X = \hat{X}e^{ikz-i\omega t}$ what is leading to the following equations of motions in momentum space:

$$(k^2 - \omega^2 n^2)\hat{E} = \mu\varrho\omega^2\hat{a}, \tag{3.9}$$

$$(k^2 - \omega^2 + m_a^2)\hat{a} = \varrho\hat{E}, \tag{3.10}$$

with $n^2 = \mu\epsilon(1 + \frac{i\sigma}{\omega\epsilon})$. Combining equation (3.9) with (3.10) we get a dispersion relation with the solutions:

$$k_\pm^2 = \frac{\omega^2}{2}\left[- \frac{m_a^2}{\omega^2} + n^2 + 1 \pm \left[\left(\frac{m_a^2}{\omega^2} + n^2 - 1\right)^2 + \tilde{x}^2\mu\right]^{\frac{1}{2}}\right], \tag{3.11}$$

where we have defined the dimensionless parameter:

$$\tilde{x} := \frac{2\varrho}{\omega}. \tag{3.12}$$

Equation (3.11) reduces to the result in [61] when we set $n = 1$[1]. However in the following discussion we leave n general and do not set it to one. The reason for this will become clear in section 3.4.

Due to energy conservation we have always $\frac{m_a^2}{\omega^2} \leq 1$ and therefore we find that $k_+^2 > 0$. k_-^2 can also become less than zero. However in the region

$$g_{a\gamma} \leq \frac{\omega}{B^e}\frac{n}{\sqrt{\mu}}\sqrt{1 - \frac{m_a^2}{\omega^2}} \tag{3.13}$$

k_-^2 is always positive. The equal sign in equation (3.13) refers to $k_-^2 = 0$. In the following we call the region in the m_a-$g_{a\gamma}$ plane the *oscillatory region* if the condition (3.13) is fulfilled. Outside of the oscillatory region the k_- mode is damped. A larger part of the parameter space gets damping if the strength of the external B-field is increased or if the frequency ω is decreased. Except from this section we will not consider the damping any more.

When we start with $(m_a, g_{a\gamma})$ that is inside the oscillatory region and go to larger m_a for a fixed $g_{a\gamma}$ the mode k_- approaches zero the closer we get to the boundary or the oscillatory region. Physically this means that $\lambda_- = \frac{2\pi}{k_-}$ gets larger. However, going to larger m_a does not change the k_+ mode abruptly. Starting at $(m_a, g_{a\gamma})$ inside the oscillatory region and going to larger $g_{a\gamma}$ along a line of fixed m_a we also observe that k_- approaches zero at the boundary of the oscillatory region. When we play the same game for k_+ the closer we get to the boundary of the oscillatory region the larger k_+ gets.

The dispersion relation can be Taylor expanded in $\tilde{x}$ if

$$\tilde{x}\sqrt{\mu} < \frac{m_a^2}{\omega^2} + n^2 - 1 \Leftrightarrow g_{a\gamma} < \frac{\omega}{B^e}\frac{1}{2\sqrt{\mu}}\Big(\frac{m_a^2}{\omega^2} + n^2 - 1\Big). \tag{3.14}$$

We call the region in the m_a-$g_{a\gamma}$ plane where (3.14) is fulfilled the *weak mixing region*. Note that if (3.14) is fulfilled then we also have $\tilde{x} < -\frac{m_a^2}{\omega^2} + n^2 + 1$, e.g. $\tilde{x}$ is smaller than the term in the dispersion relation, cf. equation (3.11), that is not under the square root. In the massless / ultra

[1] We have also changed the definition of the dimensionless parameter in comparison to [61].

relativistic limit the weak mixing region in equation (3.14) becomes smaller for large external B-fields, small ω and for very good vacuum ($n^2 - 1 \ll 1$) . Therefore extra care has to be taken in these cases. In the weak mixing region we can expand the dispersion relations in $\tilde{x}$:

$$k_+^2 = k_p^2 + \mathcal{O}(\tilde{x}^2) \tag{3.15}$$

$$k_-^2 = k_a^2 + \mathcal{O}(\tilde{x}^2), \tag{3.16}$$

with $k_p = n\omega$ and $k_a = \sqrt{\omega^2 - m_a^2}$. From our expansion we see that k_+ is the photon mode and k_- is the axion mode. Therefore the wave vectors, that describe the propagation, have a clear physical meaning in the weak mixing region. If $m_a \ll \omega$ and the medium has a refractive index close to one, then the axions and photons have almost the same k, e.g. the same wavelength.

The region in the parameter space where $\tilde{x}$ dominates over the term $\frac{m_a^2}{\omega^2} + n^2 - 1$ under the square root in the dispersion relation (3.11), but is smaller than $-\frac{m_a^2}{\omega^2} + n^2 + 1$, will be referred as the *strong mixing region* in the following. In the strong mixing region the axion photon coupling is in the range:

$$\frac{\omega}{B^e}\frac{1}{2\sqrt{\mu}}\Big(\frac{m_a^2}{\omega^2} + n^2 - 1\Big) < g_{a\gamma} < \frac{\omega}{B^e}\frac{1}{2\sqrt{\mu}}\Big(-\frac{m_a^2}{\omega^2} + n^2 + 1\Big). \tag{3.17}$$

In the strong mixing region we have two small parameters:

$$\zeta := \frac{\frac{m_a^2}{\omega^2} + n^2 - 1}{\tilde{x}\sqrt{\mu}}, \quad \chi := \frac{\sqrt{\mu}\tilde{x}}{-\frac{m_a^2}{\omega^2} + n^2 + 1}. \tag{3.18}$$

Expanding the dispersion relation in both small parameters yields:

$$k_\pm^2 = \frac{\omega^2}{2}\left(-\frac{m_a^2}{\omega^2} + n^2 + 1\right)\Big[1 \pm \chi + \mathcal{O}\left(\zeta^2, \chi^2\right)\Big]. \tag{3.19}$$

In the strong mixing we cannot identify $k_\pm$ with the free photon/axion propagation mode anymore. The upper bound of the strong mixing in equation (3.17) is always larger than the upper bound of the oscillatory region in equation (3.13). Therefore when we study the weak and strong mixing region we will automatically study the full oscillatory region.

In figure 3.1 we show the strong and weak mixing regions for $\Delta n = n - 1 = 10^{-6}$ and $\Delta n = 10^{-22}$. The region above the dashed lines is strongly mixed, while the region below the dashed lines is weakly mixed. The whole parameter space below the solid line is the oscillatory region. We show the results for $\omega = 1\,\mathrm{eV}$ and $B^e = 1\,\mathrm{T}$. If Δn is decreased the region between weak and strong mixing appears at smaller couplings. The case that $\Delta n = \mathcal{O}(1)$ is not shown, since in this case the dashed line appears at couplings around the solid line.

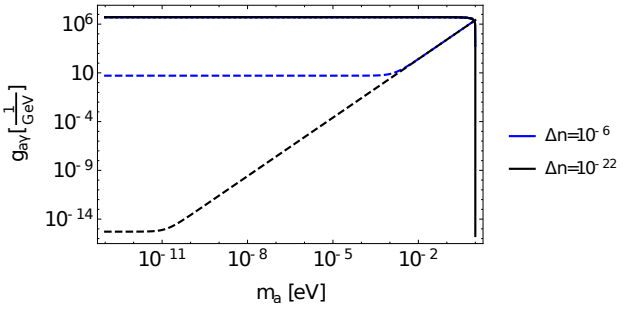

Figure 3.1: Weak and strong mixing regions in the case of $\Delta n = n - 1 \ll 1$. The dashed lines indicate $(g_{a\gamma})_w$ and therefore the region below the dashed lines is weakly mixed, while the region above is strongly mixed. The region below the solid line indicates the oscillatory region. The smaller Δn, the smaller are the couplings at which we find the transition between weak and strong mixing.

3.1.2 Physical scenarios

In the general discussion in the previous section it became clear that the approximations that we can make depend strongly on the refractive index n, the frequency ω, the axion mass m_a, the axion-photon coupling $g_{a\gamma}$ and the strength of the external B-field. In this chapter we focus mostly on scenarios that can be realized on Earth, however we also briefly mention astrophysical scenarios.

If we investigate photons that enter a magnetized region, the frequency ω is fixed by the photon energy. The axions that mix with the photons have the same frequency ω. For example the laser on the generation side in typical light shining through a wall experiments has $\omega = 1\,\mathrm{eV}$ [11] and therefore also the produced axions have this frequency. In this chapter we often refer to the $\omega = 1\,\mathrm{eV}$ case as a benchmark scenario. However, more energetic photons on Earth can be produced as for example with ultraviolet lasers or X-ray lasers like the XFEL with $\omega = 10^4\,\mathrm{eV}$ [64]. Gamma rays in the universe can have energies up to $\omega = 100$ TeV which was discussed in the scenario of axion-photon conversion in [65]. We have nothing to add to this discussion.

If axions enter a magnetized region and convert into photons, the photon frequency is set by the frequency of the incoming axions. For example the frequency of axions from the dark matter halo is determined up to small velocity corrections by the axion mass $\omega \approx m_a$.

In Earth based experiments a B-field of the order of a few Tesla can be realized. In this chapter our benchmark scenario B-field is $B^e = 1\,\mathrm{T}$. In an astrophysical context much stronger B-fields can be realized [66]. In our benchmark scenario we have:

$$\frac{\omega}{B^e} = 5.2 \times 10^6 \frac{1}{\mathrm{GeV}} \Big(\frac{\omega}{1\,\mathrm{eV}}\Big)\Big(\frac{1\,\mathrm{T}}{B^e}\Big). \tag{3.20}$$

In the previous section, cf. equation (3.13), we noted that axions with group velocity v_g are damped if $g_{a\gamma} > v_g \frac{\omega}{B^e}\frac{n}{\sqrt{\mu}}$. For axions of the galactic halo we have typically $v_g = v_a = 10^{-3}$, such that damping happens at reasonable axion-photon couplings only for very light axions.

The boundary between strong and weak mixing region, cf. dashed lines in figure 3.1,

$$(g_{a\gamma})_{sw} := \frac{\omega}{B^e}\frac{1}{2\sqrt{\mu}}\left(\frac{m_a^2}{\omega^2} + n^2 - 1\right) \tag{3.21}$$

appears to be at very large couplings in our benchmark scenario, cf. equation (3.20). In two cases $(g_{a\gamma})_{sw}$ can appear at very small axion-photon couplings. First in the case of low velocity axions from the galactic halo ($\omega \approx m_a$) the upper bound $\frac{\omega}{B^e}$ becomes lower for smaller axion masses. An axion mass $m_a = 10^{-17}\,\mathrm{eV}$ would lead to a boundary between weak and strong mixing that is around $(g_{a\gamma})_{sw} = 10^{-11}\frac{1}{\mathrm{GeV}}$. Second for ultra relativistic axions ($m \to 0$) the range of weak and strong mixing depends very sensitive on $n^2 - 1$. Solid bodies (for example dielectric materials) have $\mathcal{O}(n^2 - 1) = \mathcal{O}(n^2 + 1)$. In this case the strong mixing region is very small and almost the whole oscillatory region is weakly mixed. Nevertheless in the case that we investigate gases or non-perfect vacua $n^2 - 1$ can be very close to zero. In this case $(g_{a\gamma})_{sw}$ can be decreased by orders of magnitudes and become comparable to current limits on the axion-photon coupling [56]. For example $n^2 - 1 = 10^{-17}$ leads to $(g_{a\gamma})_{sw}(m = 0) = 10^{-11}\frac{1}{\mathrm{GeV}}$ what is close to the ALPS II sensitivity reach [11].

The most important effect which contributes to $n^2 - 1$ in Earth based experiments is due to residual gases. The exact value of $n^2_{\mathrm{gas}} - 1$ depends on the pressure. In Earth based experiments typically one distinguishes between ultra high vacuum (UHV) and extreme high vacuum (XHV). UHV corresponds to a pressure between $10^{-8} - 10^{-12}\,\mathrm{mbar}$. XHV corresonds to pressure regions below $10^{-12}\,\mathrm{mbar}$ [67–69]. According to [69] a XHV pressure is now technological possible for systems of any length and cross section. Since the refraction index of air at normal pressure and temperature is of the order of $n^2_{\mathrm{gas}} - 1 = 10^{-4}$ we get at normal temperature in UHV a refractive index between $n^2_{\mathrm{gas}} - 1 = 10^{-15} - 10^{-19}$. In XHV $n^2_{\mathrm{gas}} - 1$ can be even smaller. As an example let

us mention the ALPS II experiment which has a residual pressure of 10^{-6} mbar what corresponds to $\Delta n = 10^{-13}$.

Residual gas is not the only contribution to $n^2 - 1$ in a vacuum that is magnetized. At some point QED effects become important [60, 70]. The QED effects can be converted into a refractive index. In our one dimensional model, where the momenta are perpendicular to the external B-field, $n^2_{\text{QED}} - 1$ is of the order [60]:

$$n^2_{\text{QED}} - 1 = 10^{-24} \times \left(\frac{B^e}{1\,\text{T}}\right)^2. \tag{3.22}$$

In this chapter the overall vacuum refractive index is $n = n_{\text{QED}} + n_{\text{gas}}$. For a good vacuum the refractive index is close to one. As we will point out in this chapter, in some situations the exact quality of the vacuum matters. To describe this we define $\Delta n = n - 1$, which specifies the difference of the vacuum refractive index to the refractive index of a perfect vacuum[2]. The Farady effect will not play any role in our studies, since the external B-field is always perpendicular to the momenta.

3.1.3 Solutions in a homogeneous medium

The most general solution in a medium with constant ϵ, μ, σ and B_e is:

$$E(z) = \hat{E}^{++}e^{ik_+ z} + \hat{E}^{+-}e^{-ik_+ z} + \hat{E}^{-+}e^{ik_- z} + \hat{E}^{--}e^{-ik_- z}, \tag{3.23}$$

$$a(z) = \hat{a}^{++}e^{ik_+ z} + \hat{a}^{+-}e^{-ik_+ z} + \hat{a}^{-+}e^{ik_- z} + \hat{a}^{--}e^{-ik_- z}, \tag{3.24}$$

where we have omitted the time dependence which is for all terms $e^{-i\omega t}$. We refer to the fields $\hat{E}^{+\pm}$ and $\hat{a}^{+\pm}$ also as photon-like fields, since they propagate with k_+ which is to lowest order in $\tilde{x}$ in the weak mixing regime the typical photon dispersion. Similar we call the fields $\hat{E}^{-\pm}$ and $\hat{a}^{-\pm}$ axion-like, since k_- is in the weak mixing region to lowest order in $\tilde{x}$ given by the free axion wave number k_a.

After plugging the equations (3.23) and (3.24) into the equations of motion we find the relations:

$$\hat{E}^{-\pm} = \omega\mu\delta\hat{a}^{-\pm}, \tag{3.25}$$

$$\hat{a}^{+\pm} = \omega^{-1}\mu\delta\hat{E}^{+\pm}, \tag{3.26}$$

where we have defined in analogy to [61] the dimensionless parameter:

$$\delta = \frac{\tilde{x}}{\frac{m^2}{\omega^2} + n^2 - 1 + \left[\left(\frac{m^2}{\omega^2} + n^2 - 1\right)^2 + \mu\tilde{x}^2\right]^{\frac{1}{2}}}. \tag{3.27}$$

In the weakly mixed region we can expand δ in $\tilde{x}$:

$$\delta = \delta^L + \mathcal{O}(\tilde{x}^2), \text{ with } \delta^L = \frac{\tilde{x}/2}{\frac{m^2}{\omega^2} + n^2 - 1}. \tag{3.28}$$

In the following sections we always use the convention that we write an index L if the variables are only considered up to linear order in the weak mixing regime[3]. In the strong mixing regime we find:

$$\delta = \frac{1}{\sqrt{\mu}}(1 - \zeta) + \mathcal{O}\left(\zeta^2\right). \tag{3.29}$$

The axion-like E-field $\hat{E}^{-\pm}$ is also called the axion induced E-field and the photon-like axion field $\hat{a}^{+\pm}$ is called the photon induced axion field. In regions without external B-field we have $\delta = 0$

[2] A perfect vacuum cannot be achieved in reality and therefore we always have $\Delta n > 0$.

[3] Only for the k-vectors we use a different convention, i.e. k_a is the lowest order of k_- and k_p is the lowest order of k_+.

and therefore no axion induced E-fields or photon induced axion fields. Often we consider the situations that axions or photons are coming in from the negative z-direction into a magnetized region and then propagate towards positive z-values. In this case it is convenient to define the incoming axion induced E-field:

$$\hat{E}^a := \hat{E}^{-+} \tag{3.30}$$

and photon induced axion field:

$$\hat{a}^p := \hat{a}^{++}. \tag{3.31}$$

We use this convention in the following sections.

The original ansatz now reduces to:

$$E(z) = \hat{E}^{++}e^{ik_+z} + \hat{E}^{+-}e^{-ik_+z} + \omega\delta\mu\hat{a}^{-+}e^{ik_-z} + \omega\delta\mu\hat{a}^{--}e^{-ik_-z}, \tag{3.32}$$

$$a(z) = \omega^{-1}\delta\mu\hat{E}^{++}e^{ik_+z} + \omega^{-1}\delta\mu\hat{E}^{+-}e^{-ik_+z} + \hat{a}^{-+}e^{ik_-z} + \hat{a}^{--}e^{-ik_-z}. \tag{3.33}$$

In figure 3.2 we plot the δ parameter for $n-1 = 10^{-12}$ in the m_a-$g_{a\gamma}$ plane for our benchmark case ($B^e = 1\,\mathrm{T}$, $\omega = 1\,\mathrm{eV}$). The red line separates the weak and strong mixing regimes. In the strong mixing regime δ approaches 1 what is evident from equation (3.27). In the weak mixing region we find: $\delta \sim \tilde{x}$ and therefore δ is much smaller than in the strong mixing region. We show again only the case that $\Delta n \ll 1$, since in the case $\mathcal{O}(n-1) = 1$ the whole oscillatory region is weakly mixed (the red line would be at the top of the plots at very large couplings).

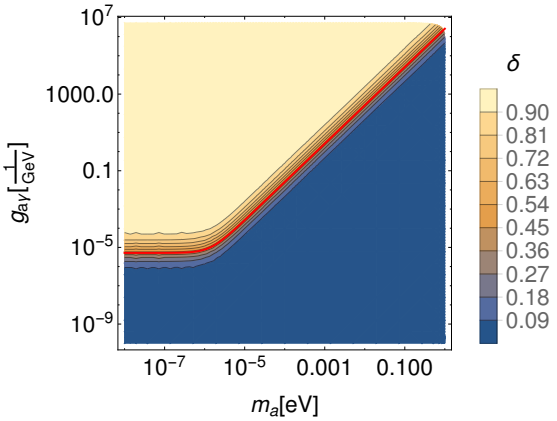

Figure 3.2: Mixing parameter δ in the m_a-$g_{a\gamma}$ plane for $\Delta n = n - 1 = 10^{-12}$. We use $\omega = 1.0\,\mathrm{eV}$, $B^e = 1\,\mathrm{T}$ and $\mu = 1$. We show only the oscillatory region. The red line separates the weak and strong mixing regions. In the weak mixing region we have: $\delta \sim \tilde{x} \ll 1$, while in the strong mixing region δ is close to one.

3.2 Single interface

In this section we consider two media with indices 0 and 1 that are separated at $z_0 = 0$. Medium 0 is characterized with $\epsilon_0, \mu_0, \sigma_0, B_0^e$ and medium 1 by $\epsilon_1, \mu_1, \sigma_1, B_1^e$.

The ansatz in medium $i = 0, 1$ is:

$$E_i = \hat{E}_i^{++}e^{ik_+^i z} + \hat{E}_i^{+-}e^{-ik_+^i z} + \omega\delta_i\mu_i\hat{a}_i^{-+}e^{ik_-^i z} + \omega\delta_i\mu_i\hat{a}_i^{--}e^{-ik_-^i z}, \tag{3.34}$$

$$a_i = \omega^{-1}\delta_i\mu_i\hat{E}_i^{++}e^{ik_+^i z} + \omega^{-1}\delta_i\mu_i\hat{E}_i^{+-}e^{-ik_+^i z} + \hat{a}_i^{-+}e^{ik_-^i z} + \hat{a}_i^{--}e^{-ik_-^i z}. \tag{3.35}$$

In total there are 8 parameters. In the case of incoming axions from medium 0, a_0^{++} is given and $E_0^{-+} = 0 = E_1^{+-} = 0 = a_1^{--}$. In the case of incoming photons E_0^{++} is given and $a_0^{-+} = 0 =$

$E_1^{+-} = 0 = a_1^{--}$. Note that we do not split the E-field into an external and background field and therefore it is the total E-field.

The solutions of the two media can be linked by the appropriate interface conditions. The interface conditions for the electromagnetic fields follow from the linearized axion-Maxwell equations. We define $\boldsymbol{D}_a := \boldsymbol{D} + g_{a\gamma}\boldsymbol{B}^e$ and $\boldsymbol{H}_a := \boldsymbol{H} - g_{a\gamma}\boldsymbol{E}a$. With the new fields we can write the axion-Maxwell equations in the form of the ordinary Maxwell equations. If follows that the corresponding interface conditions are:

$$\begin{aligned} \boldsymbol{n} \cdot (\boldsymbol{D}_{a,0} - \boldsymbol{D}_{a,1}) &= \rho_{f,S}, && (3.36)\\ \boldsymbol{n} \times (\boldsymbol{H}_{a,0} - \boldsymbol{H}_{a,1}) &= \boldsymbol{J}_{f,S}, && (3.37)\\ \boldsymbol{n} \times (\boldsymbol{E}_0 - \boldsymbol{E}_1) &= 0, && (3.38)\\ \boldsymbol{n} \cdot (\boldsymbol{B}_0 - \boldsymbol{B}_1) &= 0, && (3.39) \end{aligned}$$

where $\rho_{f,S}$ and $\boldsymbol{J}_{f,S}$ are free surface charge and current density. Both are assumed to be zero in the following. In our one dimensional considerations we have $\boldsymbol{n} = \hat{\boldsymbol{e}}_z$, while the electromagnetic fields are transversal. Therefore, the equations (3.36) and (3.39) are trivially fulfilled.

The interface condition for the axion field follows from the Klein-Gordon equation. We integrate the Klein-Gordon equation over an infinitesimal interval around the interface and apply the fundamental theorem of calculus. In the limit that the interval around the interface goes to zero we get that the normal derivative of the axion field has to be continuous, since all other terms vanish in this limit. Therefore, we get:

$$\partial_z a_0 = \partial_z a_1. \tag{3.40}$$

As an additional interface condition we require that the axion field itself is continuous:

$$a_0 = a_1. \tag{3.41}$$

Note that contrary to the other interface conditions this condition does not follow from the equations of motions in integral form.

With the equations (3.40) and (3.41) the equations (3.37) and (3.38) become for the one dimensional case that we consider:

$$E_0 = E_1, \tag{3.42}$$
$$H_0 = H_1. \tag{3.43}$$

After evaluation of all interface conditions we end up with the following matrix system:

$$\boldsymbol{t}_1 = \boldsymbol{S} \cdot \boldsymbol{t}_0, \quad \boldsymbol{S} = \boldsymbol{M}_1^{-1} \cdot \boldsymbol{M}_0, \tag{3.44}$$

with:

$$\boldsymbol{t}_i = \begin{pmatrix} \hat{E}_i^{++} \\ \hat{E}_i^{+-} \\ \hat{a}_i^{-+} \\ \hat{a}_i^{--} \end{pmatrix}, \quad \boldsymbol{M}_i = \begin{pmatrix} \mu_i^{-1} k_+^i & -\mu_i^{-1} k_+^i & \omega k_-^i \delta_i & -\omega k_-^i \delta_i \\ 1 & 1 & \mu_i \omega \delta_i & \mu_i \omega \delta_i \\ \omega^{-1} \mu_i \delta_i k_+^i & -\omega^{-1} \mu_i \delta_i k_+^i & k_-^i & -k_-^i \\ \omega^{-1} \mu_i \delta_i & \omega^{-1} \mu_i \delta_i & 1 & 1 \end{pmatrix}. \tag{3.45}$$

3.2.1 Incoming axions

In this section axion that are coming in from the negative z direction, $\hat{a}_0^{-+}$, are given and we set all other incoming fields to zero: $\hat{a}_1^{--} = 0 = \hat{E}_0^{++} = 0 = \hat{E}_1^{+-}$. The incoming axions come along with an axion induced E-field $\hat{E}^a = \omega\mu\delta\hat{a}^{-+}$.

Solving in this case the matrix equation for the four unknowns yields:

$$\begin{pmatrix} \hat{E}_0^{+-} \\ \hat{a}_0^{--} \\ \hat{E}_1^{++} \\ \hat{a}_1^{-+} \end{pmatrix} = \hat{a}_0^{-+} \begin{pmatrix} \frac{S_{24}S_{43}-S_{23}S_{44}}{S_{22}S_{44}-S_{24}S_{42}} \\ \frac{S_{23}S_{42}-S_{22}S_{43}}{S_{22}S_{44}-S_{24}S_{42}} \\ \frac{-S_{12}S_{23}S_{44}+S_{12}S_{24}S_{43}+S_{13}S_{22}S_{44}-S_{13}S_{24}S_{42}-S_{14}S_{22}S_{43}+S_{14}S_{23}S_{42}}{S_{22}S_{44}-S_{24}S_{42}} \\ \frac{-S_{22}S_{33}S_{44}+S_{22}S_{34}S_{43}+S_{23}S_{32}S_{44}-S_{23}S_{34}S_{42}-S_{24}S_{32}S_{43}+S_{24}S_{33}S_{42}}{S_{24}S_{42}-S_{22}S_{44}} \end{pmatrix}. \tag{3.46}$$

Note it was necessary to have four interface conditions (3.42)-(3.40) to solve for the four unknown parameters in equation (3.46).

3.2.1.1 B-field discontinuity

In the case that we have an external B-fields in medium 0 and 1 that are different in magnitude from each other and both media have the same $n_1 = n_2 = n$, $\mu_1 = \mu_2 = 1$ and $\sigma_0 = 0 = \sigma_1$ we obtain in the weak mixing regime for the emitted fields:

$$\begin{pmatrix} \hat{E}_0^{+-} \\ \hat{a}_0^{--} \\ \hat{E}_1^{++} \\ \hat{a}_1^{-+} \end{pmatrix} = \begin{pmatrix} (\hat{E}^a_{L,0} - \hat{E}^a_{L,1})\frac{k_a-k_p}{2k_p} \\ 0 \\ (\hat{E}^a_{L,0} - \hat{E}^a_{L,1})\frac{k_a+k_p}{2k_p} \\ \hat{a}_0^{-+} \end{pmatrix} + \mathcal{O}(\tilde{x}^2). \tag{3.47}$$

From equation (3.47) we see directly that the transmitted axions $\hat{a}_1^{-+}$ are not modified and there are no reflected axions $\hat{a}_0^{--}$ up to linear order in $\tilde{x}$. In the case that we have ultra relativistic axions $m_a \ll \omega$ and $n-1 \ll 1$ the photons, that are emitted in the negative z-direction $\hat{E}_0^{+-}$ are suppressed by a factor $k_p - k_a \approx (n-1)\omega + \frac{m_a^2}{2\omega}$. The limit $m_a \ll \omega$ and $n-1 \ll 1$ in equation (3.47) always has to be understood such that we are still in the weak mixing region. We cannot fully take the limit $m_a \to 0$ together with $n \to 1$, since this would only be valid if we at the same time let the axion-photon coupling go to zero (in order to stay in the weak mixing regime). The emitted axions in the direction of the incoming axions $\hat{E}_1^{++}$ are not suppressed and are proportional to the difference of the axion induced fields in both media.

In figure 3.3 we illustrate the situation in the form of waves. In the top left figure medium 0 is magnetized and medium 1 is not. Therefore we have an axion-induced E-field (blue) in medium 0. The incoming axions are ultra relativistic. To guarantee the continuity of the E-field a photon-like E-field (red) is radiated off the interface. The photon-like E-field that is radiated off in the direction opposed to the incoming ultra relativistic axions ($m_a \ll \omega$) is suppressed and therefore the photon-like E-field, that is emitted in the direction of the axions, has almost the same amplitude as the axion-induced field in the magnetized region. If the incoming axions are not ultra relativistic, the photon-like field, that is radiated off in the direction opposed to the direction of the incoming axions, is not suppressed anymore. This can be seen in figure 3.3 (top right). In the figure 3.3 (bottom) medium 0 is unmagnetized and medium 1 is magnetized. The incoming axions are ultra relativistic and $n - 1 \ll 1$. Again the the total E-field is continuous over the interface between unmagnetized and magnetized regions. The reflected photon-like field $\hat{E}_0^{+-}$ is very small and cannot be recognized from the figures. The wavelength of the blue and red curves in figure 3.3 (top left and bottom) is not exactly the same, since the red wave propagates with k_p and the blue with k_a. Nevertheless in the case of weak mixing with $m_a \ll \omega$ and $n - 1 \ll 1$ the difference between both cannot be recognized on the scale of a few wavelengths.

In the case that $\mathcal{O}(n-1) = 1$ and $m_a \ll \omega$ we do not get the strong enhancement of the photon E-field in the direction of the axions. There will also be a significant reflected component. This situation can be realized, if we have the B-field discontinuity for example inside a dielectric medium with $\mathcal{O}(n-1) = 1$.

Finally let us also mention that in the strong mixing regime we can use a similar illustration in terms of waves that we used in figure 3.3. However, the wavelength and amplitude then strongly

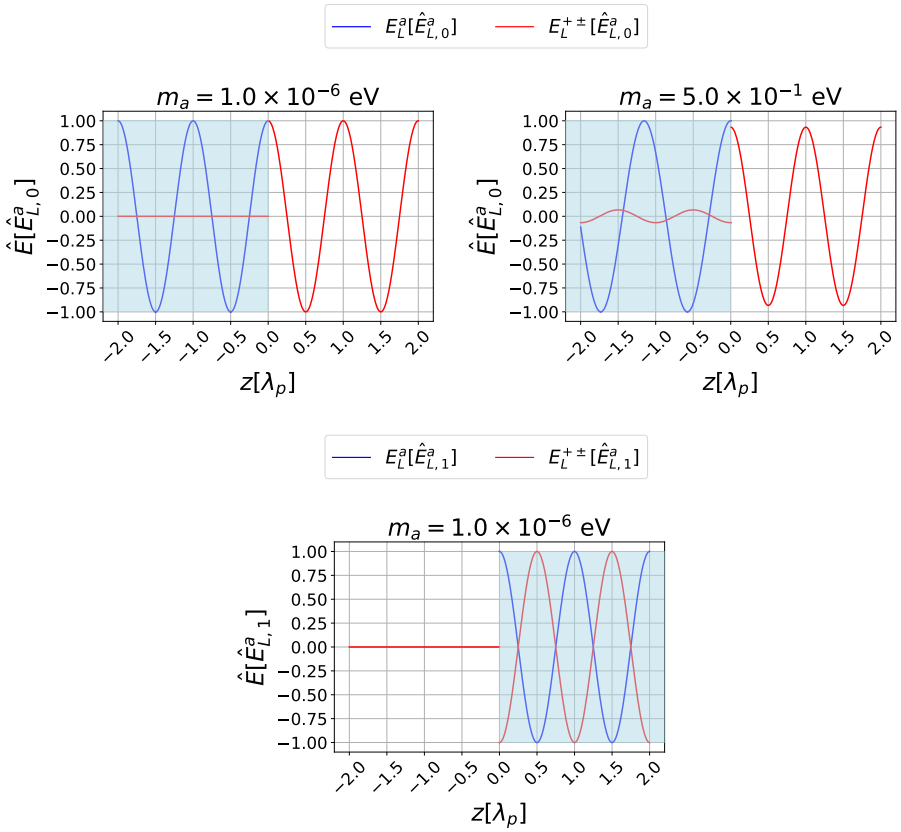

Figure 3.3: Axions are coming in from the left and hit an interface between a magnetized region (blue) and a non-magnetized region. Both regions have the same refractive index $n - 1 \ll 1$. The fields that we show are the fields that are linear (L) in $\tilde{x}$. All fields are normalized to the axion induced field $\hat{E}^a_{L,0}$ and the length scale on the z-axis is given in terms of the photon wavelength λ_p. The governing frequency is $\omega = 1\,\text{eV}$. Top left: ultra relativistic axions induce the axion-induced E-field $\hat{E}^a_{L,0}$ (blue) in the magnetized region $z < 0$. The emitted fields with a photon dispersion are drawn in red. The photon-like E-fields in the direction of the axions are strongly enhanced, since the axions are highly relativistic. Top right: If the axions are not ultra relativistic, the photon-like E-field, that propagates in negative z-direction, is not completely suppressed anymore. Bottom: The incoming axions are ultra relativistic but the magnetized region is now in $z > 0$. The photon-like E-fields are mainly emitted in the direction of the incoming ultra relativistic axions, i.e. in the positive z-direction.

depend on the coupling $g_{a\gamma}$. We will not write down the full result for the reflected and transmitted components here. We discuss them in the case of B-fields with finite length in section 3.4.

3.2.1.2 Permittivity discontinuity

In this section medium 0 has refractive index $n_0^2 = \epsilon_0$ and medium 1 $n_1^2 = \epsilon_1$. The external B-field is the same in both media and we set $\mu_0 = \mu_1 = 1, \sigma_0 = 0 = \sigma_1$. Since we now have two dielectric media the border between weak and strong mixing regime is determined by $\min(n_0^2 - 1, n_1^2 - 1)$. In the weak mixing regime we obtain the emitted fields:

$$\begin{pmatrix} \hat{E}_0^{+-} \\ \hat{a}_0^{--} \\ \hat{E}_1^{++} \\ \hat{a}_1^{-+} \end{pmatrix} = \begin{pmatrix} (\hat{E}_{L,0}^a - \hat{E}_{L,1}^a)\frac{\frac{k_a}{\omega} - n_1}{n_0 + n_1} \\ 0 \\ (\hat{E}_{L,0}^a - \hat{E}_{L,1}^a)\frac{\frac{k_a}{\omega} + n_0}{n_0 + n_1} \\ \hat{a}_0^{-+} \end{pmatrix} + \mathcal{O}(\tilde{x}^2). \tag{3.48}$$

Similar to the case of B-field discontinuities, to lowest order the reflected axions $\hat{a}_0^{--}$ are zero and the transmitted $\hat{a}_1^{-+}$ are not affected. For the emitted photon-like E-fields we discuss in the following two different scenarios: medium 0/1 is vacuum and medium 1/0 is a dielectric medium. In figure 3.4 (top left) medium 0 is a dielectric with $\mathcal{O}(n_0^2 - 1) = 1$ and medium 1 is vacuum $n_1^2 - 1 \ll 1$. In the ultra relativistic limit the axion induced field in vacuum is much larger than in the dielectric $\hat{E}_{L,1}^a \ll \hat{E}_{L,0}^a$. To fulfill the continuity at the interface a photon-like E-field, that is phase shifted by π with respect to the axion induced E-field, is emitted in the direction of the incoming axions (positive z-direction). The photon-like E-field that is emitted opposed to the direction of the incoming axions is suppressed by the factor $\frac{k_a}{\omega} - n_1 \ll 1$. The top right figure in 3.4 shows the case that the incoming axions are not ultra relativistic. Therefore the axion induced E-field in vacuum and in the dielectric are of the same order. Furthermore the suppression for the photon-like field that propagates opposed to the incoming axions $\hat{E}_0^{+-}$ is not suppressed anymore by the factor $\frac{k_a}{\omega} - n_1$. In figure 3.4 (bottom) we plot the case that medium 0 is vacuum and medium 1 is a dielectric. In this case the emitted photon-like E-fields $\hat{E}_0^{+-}$ and $\hat{E}_1^{++}$ are always of the same order, since the factor $\frac{k_a}{\omega} - n_1$ cannot become small.

It is straight forward to obtain the emitted unknown fields also in the case of permeability distcontinuities. We derive the respective equations in appendix A.1.

3.2.2 Incoming photons

In this section we consider photons that propagate in the positive z-direction ($\hat{E}_0^{++}$ is given) and hit at $z = 0$ a discontinuity. The other incoming fields are set to zero: $\hat{a}_1^{--} = 0 = \hat{a}_0^{-+} = 0 = \hat{E}_1^{+-}$. In analogy to the case of incoming axions we can define a photon induced axion field $\hat{a}^p = \omega^{-1}\delta\mu\hat{E}^{++}$.

Solving in this case the matrix equation for the four unknown fields yields:

$$\begin{pmatrix} \hat{E}_0^{+-} \\ \hat{a}_0^{--} \\ \hat{E}_1^{++} \\ \hat{a}_1^{-+} \end{pmatrix} = \hat{E}_0^{++} \begin{pmatrix} \frac{S_{24}S_{41} - S_{21}S_{44}}{S_{22}S_{44} - S_{24}S_{42}} \\ \frac{S_{22}S_{41} - S_{21}S_{42}}{S_{24}S_{42} - S_{22}S_{44}} \\ \frac{-S_{11}S_{22}S_{44} + S_{11}S_{24}S_{42} + S_{12}S_{21}S_{44} - S_{12}S_{24}S_{41} - S_{14}S_{21}S_{42} + S_{14}S_{22}S_{41}}{S_{24}S_{42} - S_{22}S_{44}} \\ \frac{-S_{21}S_{32}S_{44} + S_{21}S_{34}S_{42} + S_{22}S_{31}S_{44} - S_{22}S_{34}S_{41} - S_{24}S_{31}S_{42} + S_{24}S_{32}S_{41}}{S_{22}S_{44} - S_{24}S_{42}} \end{pmatrix}. \tag{3.49}$$

In the following we derive only the emitted fields for the case of B-field discontinuities. The two other cases of permittivity and permeability discontinuities can be found in appendix A.1.

The refractive index in both media is assumed to be the same ($n_0 = n = n_1$ and $\mu_0 = 1 = \mu_1$) but the external B-field jumps from medium 0 to medium 1. In the weak mixing regime we get

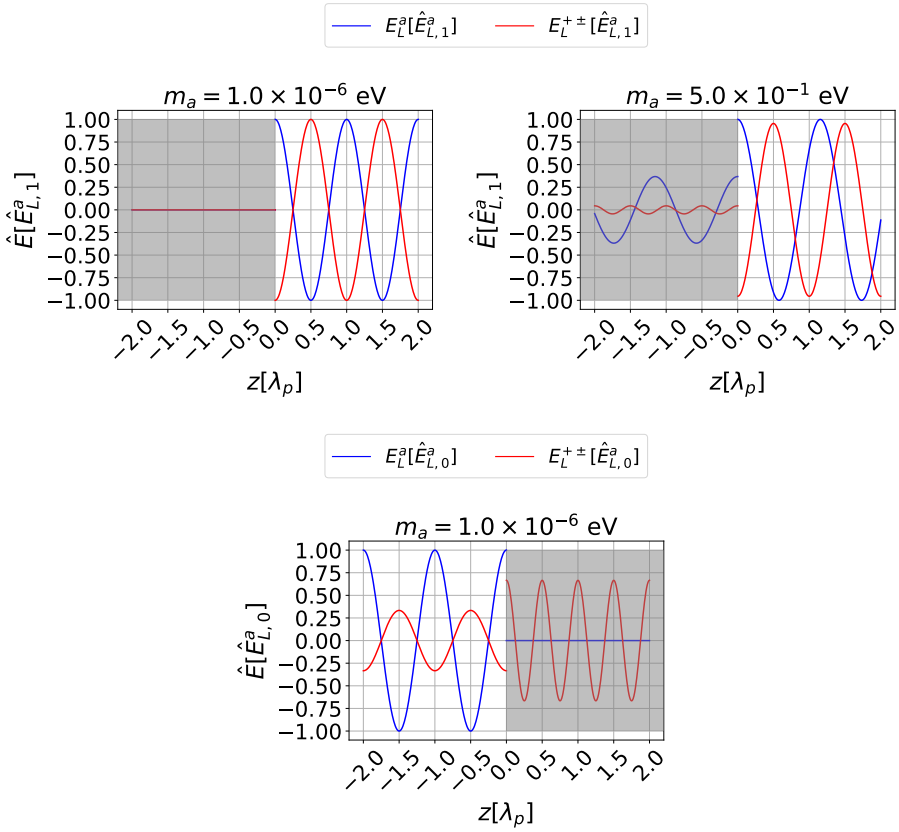

Figure 3.4: Axions that are coming in from the left hit an interface between two media of different refractive index. The external B-field in both media has the same magnitude B^e. The gray area represents a dielectric material with $n = 2$ and the white area is vacuum with $n - 1 \ll 1$. Top left: ultra relativistic axions with $\frac{m_a}{\omega} = 10^{-6}$ are coming in. The axion-induced E-field is drawn in blue and the photon-like E-fields (red) are mainly emitted in the direction of the incoming axions. One can clearly see that the sum of photon-like and axion induced fields are continuous over the interface between dielectric and vacuum region. Top right: same situation as in the top left figure, but now the incoming axions are not ultra relativistic $\frac{m_a}{\omega} = 0.5$. In this case the photon-like radiation in the direction opposed to the incoming axions is not suppressed. Bottom: medium 0 is vacuum and medium 1 a dielectric. Even in the case of ultra relativistic axions the photon-like radiation in the direction of the axions and in the direction opposed to them is of the same order.

the following fields:

$$\begin{pmatrix} \hat{E}_0^{+-} \\ \hat{a}_0^{--} \\ \hat{E}_1^{++} \\ \hat{a}_1^{-+} \end{pmatrix} = \begin{pmatrix} 0 \\ -(\hat{a}_{L,0}^p - \hat{a}_{L,1}^p)\frac{k_a - k_p}{2k_a} \\ \hat{E}_0^{++} \\ (\hat{a}_{L,0}^p - \hat{a}_{L,1}^p)\frac{k_a + k_p}{2k_a} \end{pmatrix} + \mathcal{O}(\tilde{x}^2), \tag{3.50}$$

with $k_p = n\omega$. The form of the equations in (3.50) is very similar to the case of the incoming axions (compare equation (3.47)), but now the photon induced axion fields plays the role of the axion induced photon fields. We can understand the formulas, in analogy to the incoming axion case, graphically with a continuous argument for the axion fields. Nevertheless we believe that this is clear and we do not explicitly show a figure in this case.

In equation (3.50) we observe that the axion fields that propagate in the negative z-direction $\hat{a}_0^{--}$ are suppresses in the limit $m_a \ll \omega$ and $n - 1 \ll 1$, what is similar to the case of incoming axions. Furthermore the incoming photons are not affected up to linear order by the B-field discontinuity. Note that in the expansion (3.50) there appears a factor $\frac{1}{k_a}$ that diverges for $m_a \to \omega$. Nevertheless this does not lead to problems, since if $g_{a\gamma} \neq 0$ the oscillatory region stops shortly before m_a can approach ω. We have discussed this in detail in section 3.1.

3.3 Matrix formalism

In this section we generalize our approach from a singe interface to N interfaces. The approach that we present in the following is valid up to all orders in the axion photon coupling $g_{a\gamma}$ and for arbitrary materials with ϵ, μ, σ and external B-fields. Furthermore our approach is valid for arbitrary axion velocities. A matrix approach up to linear orders in the axion photon coupling for zero or low velocity axions has been presented before in [58, 59]. A matrix approach for arbitrary axion velocities, but only for two B-field discontinuities and under the assumption of a perfect vacuum was written down in Ref. [61].

In our notation we have in total $N+1$ media. Medium $r-1$ and r are separated by an interface at z_r. Furthermore we define $z_0 = z_1$. Each medium r is characterized by $\epsilon_r, \mu_r, \sigma_r$ and B_r^e. The naming convention for all media is shown in figure 3.5.

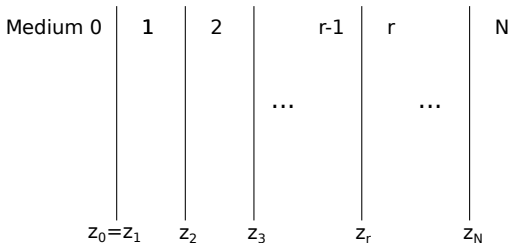

Figure 3.5: Multi layer system with different material layers. We have $N + 1$ layers which are separated at z_r. Each medium is characterized by $\epsilon_r, \mu_r, \sigma_r$ and B_r^e.

In analogy to the single interface we make an ansatz for the fields in medium r:

$$E_r(z) = \hat{E}_r^{++} e^{ik_+^r(z-z_r)} + \hat{E}_r^{+-} e^{-ik_+^r(z-z_r)} + \mu_r\omega\delta_r \hat{a}_r^{-+} e^{ik_-(z-z_r)} + \mu_r\omega\delta_r \hat{a}_r^{--} e^{-ik_-(z-z_r)} \tag{3.51}$$

$$a_r(z) = \frac{\hat{E}_r^{++}\mu_r\delta_r}{\omega} e^{ik_+^r(z-z_r)} + \frac{\hat{E}_r^{+-}\mu_r\delta_r}{\omega} e^{-ik_+^r(z-z_r)} + \hat{a}_r^{-+} e^{ik_-^r(z-z_r)} + \hat{a}_r^{--} e^{-ik_-^r(z-z_r)} \tag{3.52}$$

After applying the interface conditions at interface z_r we obtain the following matrix system:

$$\boldsymbol{M}_{r-1} \cdot \boldsymbol{P}_{r-1} \cdot \boldsymbol{t}_{r-1} = \boldsymbol{M}_r \cdot \boldsymbol{t}_r, \tag{3.53}$$

where we have defined:

$$\boldsymbol{M}_r = \begin{pmatrix} \frac{k_+^r}{\mu_r} & -\frac{k_+^r}{\mu_r} & \omega\delta_r k_-^r & -\omega\delta_r k_-^r \\ 1 & 1 & \mu_r\omega\delta_r & \mu_r\omega\delta_r \\ \frac{\mu_r\delta_r}{\omega}k_+^r & -\frac{\mu_r\delta_r}{\omega}k_+^r & k_-^r & -k_-^r \\ \frac{\mu_r\delta_r}{\omega} & \frac{\mu_r\delta_r}{\omega} & 1 & 1 \end{pmatrix} \quad \text{and} \quad \boldsymbol{t}_r = \begin{pmatrix} \hat{E}_r^{++} \\ \hat{E}_r^{+-} \\ \hat{a}_r^{-+} \\ \hat{a}_r^{--} \end{pmatrix} \tag{3.54}$$

and

$$\boldsymbol{P}_r = \mathrm{diag}\begin{pmatrix} e^{i\Delta_+^r} & e^{-i\Delta_+^r} & e^{i\Delta_-^r} & e^{-i\Delta_-^r}, \end{pmatrix} \tag{3.55}$$

with $\Delta_\pm^r = k_\pm^r(z_{r+1} - z_r)$.

In the case of a single interface we get:

$$\boldsymbol{t}_1 = \boldsymbol{S} \cdot \boldsymbol{t}_0 \text{ with } \boldsymbol{S} = \boldsymbol{M}_1^{-1} \cdot \boldsymbol{M}_0 \cdot \boldsymbol{P}_0. \tag{3.56}$$

For two interfaces we obtain:

$$\boldsymbol{t}_2 = \boldsymbol{S} \cdot \boldsymbol{t}_0, \text{ with } \boldsymbol{S} = \boldsymbol{M}_2^{-1} \cdot \boldsymbol{M}_1 \cdot \boldsymbol{P}_1 \cdot \boldsymbol{M}_1^{-1} \cdot \boldsymbol{M}_0 \cdot \boldsymbol{P}_0 \tag{3.57}$$

and for N interfaces we have:

$$\boldsymbol{t}_N = \boldsymbol{S} \cdot \boldsymbol{t}_0, \tag{3.58}$$

with

$$\boldsymbol{S} = \boldsymbol{M}_N^{-1} \cdot \boldsymbol{M}_{N-1} \cdot \boldsymbol{P}_{N-1} \cdot \boldsymbol{M}_{N-1}^{-1} \cdots \boldsymbol{M}_0 \cdot \boldsymbol{P}_0. \tag{3.59}$$

To describe the photon-like E-fields that are emitted in the direction of incoming axions ($\hat{a}_0^{-+}$) we define a boost factor as:

$$\beta = \left| \frac{\hat{E}_N^{++}}{\hat{E}^a} \right|, \tag{3.60}$$

where $\hat{E}^a = \max[\hat{E}_r^a]$ in the case of a multilayer system. This definition is in analogy to the matrix formalism for zero and small velocity axions [58, 59]. In the case of incoming photons ($\hat{E}_0^{++}$) we define a boost factor to describe the amount of emitted axions in the direction of the incoming photons:

$$\beta = \left| \frac{\hat{a}_N^{++}}{\hat{a}^p} \right|, \tag{3.61}$$

where $\hat{a}^p = \max[\hat{a}_r^p]$. Note that we have defined a boost factor for the case of incoming axions and photons with the same symbol. Which one we refer to will always be clear in the respective context.

If one is only interested in the weak mixing region up to linear order one can simplify the results because the reflected axions are zero up to linear order and the transmitted axions just get a phase shift. Therefore we get in the weak mixing region:

$$\begin{pmatrix} \hat{E}_N^{++} \\ \hat{E}_N^{+-} \end{pmatrix} = \begin{pmatrix} S_{11} & S_{12} \\ S_{21} & S_{22} \end{pmatrix} \begin{pmatrix} \hat{E}_0^{++} \\ \hat{E}_0^{+-} \end{pmatrix} + \hat{a}_0^{-+} \begin{pmatrix} S_{13} \\ S_{23} \end{pmatrix} + \mathcal{O}(\tilde{x}^2), \tag{3.62}$$

where the S matrix elements are understood to be perturbed up to linear order in $\tilde{x}$. In appendix A.2 we give an explicit expression for the relevant S matrix elements. Note that equation (3.62) is valid for incoming axions as well as for incoming photons.

3.4 B-fields of finite size

In this section we consider incoming axions and photons on a magnetized region of finite length ℓ. In the language of the introduced formalism we have three media $r = 0, 1, 2$ which are separated by $z_0 = z_1$ and z_2. Finally the results are combined to describe light shining trough a wall experiments.

3.4.1 Incoming axions

In this section axions coming in from medium 0 are given, $\hat{a}_0^{-+}$, while the other incoming fields are set to zero: $\hat{a}_2^{--} = 0 = \hat{E}_0^{++} = 0 = \hat{E}_2^{+-}$. The general solution in terms of the S-matrix was already written down in equation (3.46), when we replace on the left hand side $1 \leftrightarrow 2$ and use the S matrix for our specific case. Medium 1 is magnetized in the following, while media 0 and 2 are not magnetized ($\delta_0 = 0 = \delta_2,\ \delta_1 = \delta$). Furthermore we consider media with $\mu_r = 1, \sigma_r = 0$ as well as $n_r = n$. In the weak mixing regime we find the unknown field amplitudes:

$$\begin{pmatrix} \hat{E}_0^{+-} \\ \hat{a}_0^{--} \\ \hat{E}_2^{++} \\ \hat{a}_2^{-+} \end{pmatrix} = \hat{a}_0^{-+} \begin{pmatrix} -\frac{i\omega^2}{2n\tilde{q}_L} e^{\frac{i\ell\tilde{q}}{2}} \sin\left(\frac{\ell\tilde{q}}{2}\right)\tilde{x} \\ 0 \\ -\frac{i\omega^2}{2nq_L} e^{\frac{il\tilde{q}_L}{2}} \sin\left(\frac{\ell q}{2}\right)\tilde{x} \\ e^{ilk_-} \end{pmatrix} + \mathcal{O}(\tilde{x}^2) = \begin{pmatrix} -i\hat{E}^a_{L,1} e^{i\ell\frac{\tilde{q}}{2}} \left(1 - \frac{k_a}{k_p}\right) \sin\frac{\tilde{q}\ell}{2} \\ 0 \\ -i\hat{E}^a_{L,1} e^{i\ell\frac{\tilde{q}}{2}} \left(1 + \frac{k_a}{k_p}\right) \sin\frac{q\ell}{2} \\ \hat{a}_0^{-+} e^{ilk_-} \end{pmatrix} + \mathcal{O}(\tilde{x}^2), \tag{3.63}$$

where $\ell = z_2 - z_1$ is the length of the magnetized region and $E^a_{L,1}$ is the axion induced E-field (linear term) in medium 1. As we expect from the results from the single interface section the reflected axions are zero up to linear order and the transmitted axions get a phase shift. In equation (3.63) we have expanded all quantities in $\tilde{x}$ except the phases, for a reason that will become clear later on. For now one can always replace $q \to q_L$ in the phases in equation (3.63). If we expand q and $\tilde{q}$ we get:

$$q = k_+ - k_- = \underbrace{k_p - k_a}_{=:q_L} + \mathcal{O}(\tilde{x}^2), \quad \tilde{q} = k_+ + k_- = \underbrace{k_p + k_a}_{=:\tilde{q}_L} + \mathcal{O}(\tilde{x}^2). \tag{3.64}$$

In the ultra relativistic limit together with $n - 1 \ll 1$ we have $k_p \backsimeq k_a$ and therefore $q_L\ell/2$ can be very small for Earth based setups:

$$\frac{q_L\ell}{2} \overset{m_a<\omega}{\approx} \frac{m_a^2\ell}{4\omega} + \frac{\ell\omega(n-1)}{2}, \tag{3.65}$$

$$\frac{m_a^2\ell}{4\omega} = 1.25 \times 10^{-4} \left(\frac{m_a}{1\,\mu\text{eV}}\right)^2 \left(\frac{1\,\text{eV}}{\omega}\right)\left(\frac{\ell}{100\,\text{m}}\right), \tag{3.66}$$

$$\frac{\ell\omega(n-1)}{2} = 2.5 \times 10^{-4} \left(\frac{\ell}{100\,\text{m}}\right)\left(\frac{1\,\text{eV}}{\omega}\right)\left(\frac{n-1}{10^{-12}}\right). \tag{3.67}$$

We therefore notice that the argument of the sine in equation (3.63) can only become on the order of one for relatively large masses for fixed $n - 1$ and ℓ.

If $q\ell/2 \ll 1$ and $\lambda_a \backsimeq \lambda_p < 4\pi\ell$ it is easy to see that also in the case of two interfaces the amplitude of the photons $\hat{E}_0^{+-}$, that travel in the direction opposed to the incoming axions, is smaller than the amplitude of the photons $\hat{E}_2^{++}$, that propagate in the direction of the incoming axions. In the following we focus only on the photon field $\hat{E}_2^{++}$. We show two representations for $\hat{E}_2^{++}$ in equation (3.63). The first one does not contain the axion induced field, while the second one is rewritten such that the definition of the axion induced field appears. In the following we point out the advantages of both representations.

In the first representation in equation (3.63) we see explicitly that when $q_L \to 0$ we get a finite result for $\hat{E}_2^{++}$, since it cancels with the q in the sine function. Although the limit exists it is important to understand that it is not valid for all couplings. If we send $q_L \to 0$ this means that

we send $m_a \to 0$ and $n \to 1$. In the weak mixing region, where equation (3.63) is valid, this cannot be realized for a finite coupling $g_{a\gamma}$. Therefore the limit $m_a \to 0$ and $n \to 1$ has to be understood as $m \ll \omega$ and $n-1$ is very close to zero, such that the considered couplings are still weakly mixed. The case $q_L \to 0$ is called coherent production in the literature [71]. The incoming axions produce via mixing photons which are coherently added, since the axion and photons waves are always in phase.

The second representation in equation (3.63) uses the axion induced E-field and is suited for the physical interpretation in terms that are coming from the discontinuities at the interfaces. Since now we have two interfaces the photon-like waves, that are emitted from the two interfaces in the direction of the incoming axions, interfere in medium 2. The interference effect is represented by the sine term and becomes stronger the more relativistic the axions are and the more closer $n-1$ is to zero. We illustrate this for the ultra relativistic (left) and a semi relativistic case (right) in figure 3.6. The axions propagate in the positive z-direction and excite an axion induced E-field in medium 1 (light blue colored). The photon-like E-fields from $z_1 = 0$ are drawn in red and the photon-like E-fields form the interface at $z_2 = 2\lambda_p$ are drawn in dark red. The orange dashed line shows the sum of the two photon-like E-fields that propagate into the positive z-direction and interfere in medium 2. In the left figure 3.6 the incoming axions are ultra relativistic $\frac{m_a}{\omega} = 10^{-6}$ and therefore the photon-like E-fields that travel in the negative z-direction are suppressed. The two photon like E-fields, that are emitted from the interfaces in the positive z-direction, interfere destructively in medium 2 with each other (since we have ultra relativistic axions and $n-1$ is close to zero). In the right figure 3.6 the axions are not ultra relativistic anymore ($\frac{m_a}{\omega} = 0.7$) and therefore the photon-like E-fields in the negative z-direction are not suppressed anymore. Furthermore the axion and photon wavelengths are fundamentally different and therefore the interference after two wavelength is not destructive anymore, i.e. the amplitude of the orange dashed line is not suppressed. One could now think that the total emitted photon like E-field $\hat{E}_2^{++}$ in medium 2 is much larger in the non-relativistic case. However, this is not the case! The reason for this is that the amplitude $\hat{E}_{L,1}^{a}$ in the non-relativistic case is smaller than in the ultra-relativistic case. To distinguish in which of the both shown cases the largest total photon-like field $\hat{E}_{L,2}^{++}$ is emitted we have to look at the first representation in equation (3.63). Only there we see that the fields in the ultra relativistic limit are larger, since it contains a sinc function with the momentum transfer q in the argument (that becomes small in the ultra relativistic limit with $n-1$ close to one.). Nevertheless the emitted field $\hat{E}_{L,2}^{++}$ differs in both cases only by orders of magnitudes if the momentum transfer q_L is very large.

Our discussion of the two representations in equation (3.63) brings together two pictures. The first representation in equation (3.63) shows the well known $\frac{2}{q_L \ell} \sin(\frac{q_L \ell}{2})$ conversion term when axions mix with photons in external magnetic fields. Contrary to previous studies [60, 71, 72], which use an overlap integral formalism or a mixing approach, we have used a classical calculation and obtained the sine term through the application of interface conditions for the electromagnetic and axion fields. The second representation in equation (3.63) is in terms of the axion induced field which is usually used for axion haloscopes [58]. We have now shown that the two pictures are equivalent and that the results can be derived from the presented matrix formalism.

In the previous discussion we have calculated the emitted photons from a constant magnetized region of finite length ℓ. However, in the calculation the transition from the magnetized region to the non-magnetized region was discontinuous, since we have used the matrix formalism with one magnetized layer. A realistic B-field is continuous in a medium with the same refractive index. In the following we show that the matrix formalism with one magnetized layer gives to good approximation the emitted E-fields if the realistic external B-field can be approximated well with one magnetized slice.

To calculate the exact emitted E-fields in the case of an arbitrarily shaped external B-field

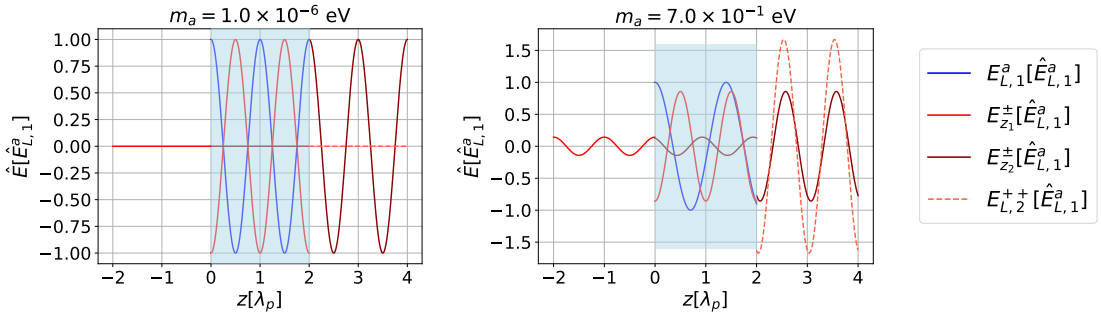

Figure 3.6: Axions with $\omega = 1\,\text{eV}$ are coming in from the left and propagate in positive z-direction. Region 1 in blue is magnetized and region 0 and 2 (left and right from the blue region) are not magnetized. The index of refraction is very close to one. The incoming axions induce the axion induced E-field which is plotted in blue. To fulfill the continuity requirements for the total E-field, photon-like fields are emitted from both B-field discontinuities. The photon-like E-fields, that are emitted from the discontinuity at $z_1 = 0$ and $z_2 = 2\lambda_p$, are called $\hat{E}^{\pm}_{z_1}$ and $\hat{E}^{\pm}_{z_2}$ and drawn in red and dark red. The red and dark red fields that propagate in positive z-direction interfere in medium 2. The sum of the them is $\hat{E}^{++}_{L,2}$ and is drawn in dashed orange. Left: ultra relativistic case ($\frac{m_a}{\omega} = 10^{-6}$). We see that the dashed orange field is phase suppressed. Right: non-relativistic case ($\frac{m_a}{\omega} = 0.7$). When comparing the left and right figures, note that the normalization $\hat{E}^a_{L,1}$ is much larger in the ultra relativistic case. This cancels the effect of the phase suppression and we find that in total the $\hat{E}^{++}_{L,2}$ field is larger in the ultra relativistic limit (left). This is however only evident from the first representation in equation (3.63) and not evident from the figures.

we assume that the medium under consideration has refractive index $n = \sqrt{\epsilon}$ everywhere. We compute the total E-field solution to linear order in $\tilde{x}$, i.e. we apply a perturbation approach to all fields that appear in equations (3.1)-(3.5): $X(\boldsymbol{x}, t) = X^{(0)}(\boldsymbol{x}, t) + \tilde{x}X^{(1)}(\boldsymbol{x}, t) + \cdots$, where $X = \boldsymbol{D}, \boldsymbol{E}, \boldsymbol{H}, \boldsymbol{B}, \rho_f, \boldsymbol{J}_f, a$. Here we have $\boldsymbol{E} = \epsilon \boldsymbol{D}, \boldsymbol{H} = \boldsymbol{B}, \rho_f = 0 = \boldsymbol{J}_f$. Furthermore we have only an external B-field: $\boldsymbol{B}^{(0)}(\boldsymbol{x}) = \hat{B}^{(0)}\hat{\boldsymbol{B}}^{(0)}(\boldsymbol{x}) \sim \hat{\boldsymbol{e}}_y$, where $\hat{B}^{(0)} = B^e$ is a constant and $\hat{\boldsymbol{B}}^{(0)}(\boldsymbol{x})$ is a function of the order one. We have no external E-field: $\boldsymbol{E}^{(0)} = 0$. Incoming axions are described by the zeroth order field $a^{(0)}$. The first order field solutions are then given by the retarded potentials[4] as:

$$\boldsymbol{E}^{(1)} = -\nabla\Phi^{(1)} - \partial_t \boldsymbol{A}^{(1)}, \tag{3.68}$$

$$\boldsymbol{B}^{(1)} = \nabla \times \boldsymbol{A}^{(1)} \tag{3.69}$$

with

$$\boldsymbol{A}^{(1)} = \frac{1}{4\pi}\int d^3x' \frac{1}{|\boldsymbol{x} - \boldsymbol{x}'|}\boldsymbol{J}^{(1)}_a(\boldsymbol{x}', t - \sqrt{\epsilon}|\boldsymbol{x} - \boldsymbol{x}'|), \quad \boldsymbol{J}^{(1)}_a(\boldsymbol{x}, t) = \frac{g_{a\gamma}}{\tilde{x}}\boldsymbol{B}^{(0)}(\boldsymbol{x})\partial_t a^{(0)}(\boldsymbol{x}, t). \tag{3.70}$$

In a one dimensional problem we have: $a^{(0)} = \tilde{a}^{(0)}e^{-i\omega t + ik_a z}$, $\hat{\boldsymbol{B}}^{(0)}(z)$ and $\Phi^{(1)} = 0$. In this case the physical E-field in the direction of the incoming axions is given by:

$$E^{(1)}_y \tilde{x} = \frac{i\omega^3 \tilde{x}}{4k_p}\tilde{a}^{(0)}e^{i(k_p z - \omega t)}\ell F, \text{ with } F = \frac{1}{\ell}\int dz' \hat{B}^{(0)}_y(z')e^{-iq_L z'}. \tag{3.71}$$

Let us now consider the situation the we have a magnetized region ℓ where the external B-field is constant and at the boundaries of the magnetized region the external B-field drops continuously

[4]Note that the retarded potentials are usually computed for a perfect vacuum medium, i.e. $\epsilon = 1 = \mu$. However, one can show that the calculation also goes through for the case of a homogeneous medium with $\epsilon > 1$ and constant everywhere if we add the $\sqrt{\epsilon}$ in the argument of the current density in equation (3.70) and use a slightly modified Lorenz Gauge.

to zero on a length scale ℓ_b. We assume $\ell \gg \ell_b$. In this case the external B-field can be well approximated with one magnetized layer of length ℓ. The integral over the constant magnetized region ℓ in equation (3.71) gives exactly the result that one obtains from the matrix formalism with one magnetized layer of length ℓ. In addition one gets also contributions from the integral in equation (3.71) over the boundary of length scale ℓ_b. However, these contribution give only relatively small contributions since $\ell \gg \ell_b$.

If the realistic external B-field cannot be approximated with a single layer in the matrix formalism one can use more layers to approximate the shape of the external B-field. For low velocity axions Axion-photon mixing in the presence of inhomogeneous B-fields has already been studied in one and two dimensions [73–75] and also explicitly in three dimensions [76] with different approaches. We have nothing more to add to this discussion.

Finally let us also discuss the emitted fields in the strong mixing regime. We split the refractive index $n = 1 + \Delta n$ and focus on the case $\Delta n \ll 1$, since only then the strong mixing region can come close to axion-photon couplings which are not already excluded by experiments, cf. figure 3.1. In the following only the massless limit $m_a \to 0$ is discussed, since as we will see, in this limit interesting effects can arise. We have in this case $n^2 + 1 \approx 2, \chi \approx \frac{\tilde{x}}{2}$ and $\zeta = \frac{2\Delta n}{\tilde{x}}$. Expanding the dispersion relation and δ in the small parameters ζ and χ, cf. equation (3.18), leads to:

$$\begin{aligned} k_\pm &= \omega + \mathcal{O}(\chi, \zeta^2), \\ \delta &= 1 - \zeta + \mathcal{O}(\zeta^2). \end{aligned} \tag{3.72}$$

For the emitted photon field in the direction of the incoming axions we get to lowest order in the strong mixing regime:

$$\hat{E}_2^{++} = \hat{a}_0^{-+} \frac{1}{\zeta} \left(-i\omega e^{i\frac{\tilde{q}\ell}{2}} \sin\frac{q\ell}{2} + \mathcal{O}(\chi, \zeta) \right), \tag{3.73}$$

$$= -\hat{a}_0^{-+} \frac{i\omega\tilde{x}}{2\Delta n} e^{i\frac{\tilde{q}\ell}{2}} \sin\left(\frac{q\ell}{2}\right), \tag{3.74}$$

where we have again done the expansion not in the phases and we left out the $\mathcal{O}$ in the last line, since from now on we look only at the leading order term. Very analogous expansions as we did in equation (3.74) can be done for the other fields $\hat{a}_0^{--}, \hat{E}_0^{+-}, \hat{a}_2^{-+}$. In all cases we find that the fields are proportional to $\frac{1}{\zeta}$.

Since we are in the zero mass limit we get in the strong mixing region $q = k_+ - k_- = \omega\chi + \mathcal{O}(\chi^2, \zeta^2)$ and $\tilde{q} = k_- + k_+ = 2\omega + \mathcal{O}(\chi, \zeta^2)$. The leading order result in the strong mixing region in equation (3.74) has the same structure as the leading order result in the weak mixing region if we take in equation (3.63) the massless limit, i.e. $\frac{\omega}{nq_L} \to \frac{1}{\Delta n}$. Therefore, in the massless limit the main difference between strong and weak mixing region comes from the argument of the sine function. While in the weak mixing region we have $q \to \Delta n\omega$, we have in the strong mixing region $q \to \omega\frac{\tilde{x}}{2}$. In conclusion the result in the weak mixing region cannot be enhanced for small Δn, since the Δn from the sine argument and the Δn in the denominator cancel. However, in the strong mixing region the Δn in the denominator is not canceled with the $q = \omega\tilde{x}/2$, which is in the argument of the sine function. Therefore in the strong mixing region the emitted field $\hat{E}_2^{++}$ can be enhanced for small Δn. If $\frac{q\ell}{2} \ll 1$ the ratio between the result in the strong and weak mixing is $\frac{\tilde{x}}{2\Delta n} \gg 1$. Therefore using the weak mixing result in a parameter space where one should actually use the strong mixing result, leads to an emitted E-field that is to small.

The Δn enhancement in equation (3.74) was not discovered in previous calculations which use a mixing approach [60, 71]. In appendix A.3 we therefore discuss if our result violates energy flux conservation. And indeed we find that the matrix formalism can give in parts of the strong mixing region large energy flux non-conserving results. Therefore the Δn enhancement, that we find in equation (3.74), is not physical in parts of the strong mixing region. We have explicitly checked

that the mixing formalism of Ref. [60, 71] conserves the energy flux under all circumstances. In the next section, where we consider incoming photons, we compare the strong mixing result from the matrix formalism, which is also Δn enhanced, to the result of [71]. We then also give an outlook what could solve the energy non-conservation in the strong mixing region and how the calculations could be improved.

In figure 3.7 (left) we show $\hat{E}_2^{++}$ in the whole m_a-$g_{a\gamma}$ plane. For relatively large masses we get a peaked structure in the weak mixing regime (below the red line). This structure comes from the sine term in equation (3.63). If we increase the length ℓ by a factor b the peak at the lowest mass will appear at a mass that is by a factor $\sqrt{b}$ lower. One can see that by expanding the argument of the sine term in equation (3.63). In figure 3.7 (right) we zoom in into the blue box in the left figure, that also contains a part of the strong mixing regime. Now we see that the peaks which are not fully resolved in the left figure are bended horizontally and do not go straight up vertically. This result cannot be seen from the weak mixing calculation, but from equation (3.74), where we did the expansion in the strong mixing regime for the massless case, which also applies to the case of small masses $m_a \ll \omega$. The argument of the sine term in the strong mixing region depends on $\chi = \frac{\tilde{x}}{2}$ and therefore we observe a horizontal bending in figure 3.7 (right). The minima can be found at:

$$g_{a\gamma} = 6.4 \times 10^{-2} \times j \times \frac{1}{\mathrm{GeV}} \Big(\frac{1\,\mathrm{T}}{B^e}\Big) \Big(\frac{100\,\mathrm{m}}{\ell}\Big),\ j \in \mathbb{N}. \tag{3.75}$$

Therefore making the external B-field longer/stronger will linearly shift the minima. This is in contrast to the vertical peaks in the weak mixing region: Scaling the length of the B-field had only a square root dependence and scaling the B-field strength had no influence on the peak positions.

Note, that when we make the external B-field much longer we can get the horizontal minima stripes also in the weak mixing regime. This can be seen from the result in the weak mixing region in equation (3.63) and is the reason why we have not expanded the phases equation (3.63). We have $\hat{E}_2^{++} \sim \sin((k_+ - k_-)\ell/2)$. For zero axion masses ($m_a = 0$) we get $k_+ - k_- = (n-1)\omega + \mathcal{O}(\tilde{x}^2)$. The zeroth order term is per definition of the weak mixing region always smaller than the higher order terms. But if the external B-field is long enough the higher order terms multiplied by the length ℓ can become order one in the weak mixing regime. The term $\omega(n-1)\ell$ is only a constant phase. In this case the sine oscillations of the horizontal lines appear in the weak mixing region and are sensitive to the coupling $g_{a\gamma}$. A detailed calculation yields that the length of the B-field has to be larger than:

$$\ell = 2.5 \times 10^6\ \mathrm{m}\ \left(\frac{\mathrm{eV}}{\omega}\right) \left(\frac{10^{-12}}{\Delta n}\right), \tag{3.76}$$

such that the horizontal minima stripes appear in the weak mixing region. We will not further consider this case here, but want to mention that this can happen in general. In the plots a magnetized length of $\ell = 100\,\mathrm{m}$, which is typical for light shining trough a wall experiments, is chosen. For this value the horizontal bending of the peaks happens at very large coupling which are already excluded by for example horizontal branch stars [77]. The effects that we observe here can be important in very strong or spatial long external B-fields in an astrophysical context.

3.4.2 Incoming photons

In this section we investigate photons coming in from the negative z direction $\hat{E}_0^{++}$ which hit a finite magnetized region of length ℓ. The other incoming fields are set to zero: $\hat{a}_2^- = 0 = \hat{a}_0^+ = 0 = \hat{E}_2^-$. The general solution is given as in equation (3.49), by replacing the index $1 \leftrightarrow 2$ in the vector on the left side of the equation and using the S matrix for our specific case. We consider the case that medium 1 is magnetized, while medium 0 and 2 are not magnetized ($\delta_0 = 0 = \delta_2,\ \delta_1 = \delta$). All three media have the same index of refraction. We set $\mu_r = 1, \sigma_r = 0, r = 0, 1, 2$ and $n_0 = n_1 = n_2 = n$.

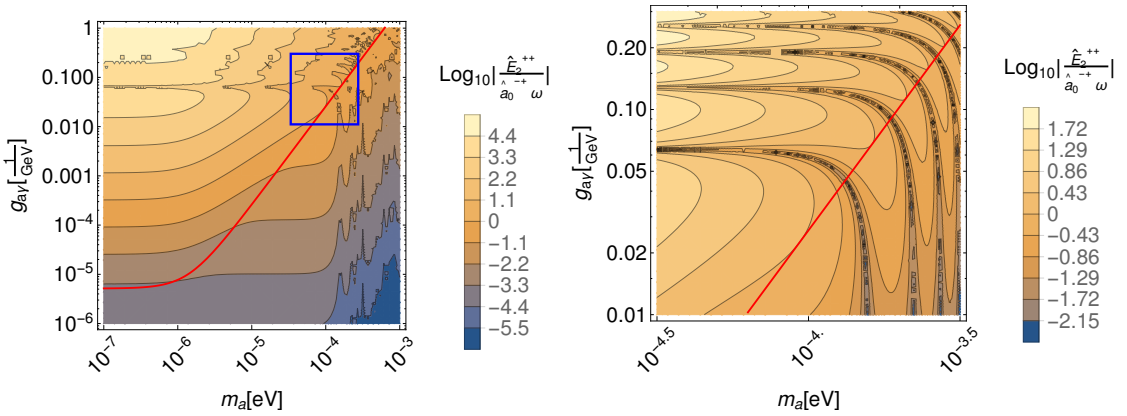

Figure 3.7: Incoming axions $\hat{a}_0^{-+}$ that propagate in the positive z-direction hit a magnetized region of length $\ell = 100\,\text{m}$ and with external B-field strength $B^e = 1\,\text{T}$. The magnitude of the photons that leave the magnetized region in the positive z-direction is called $\hat{E}_2^{++}$. We plot $\hat{E}_2^{++}$ in the m_a-$g_{a\gamma}$ plane. The incoming axions have $\omega = 1\,\text{eV}$ and all media have the same refractive index $n = 1 + 10^{-12}$. In the left figure we plot a large range in the m_a-$g_{a\gamma}$ plane. Below/above the red line we find the weak/strong mixing region. The vertical oscillations in the weak mixing regime arise when the argument of the sine term in equation (3.63) becomes order one. The blue box tags the zoomed plot range for the right figure. We see that the peaks in the high mass region, that arise in the weak mixing regime, bend and become horizontal in the strong mixing regime. This effect arises, since $\hat{E}_2^{++}$ in the strong mixing regime is proportional to $\sin(\frac{g_{a\gamma}B^e}{2}\ell)$, cf. equation (3.74).

In the weak mixing region the generated axions in the direction of the incoming photons are:

$$\hat{a}_2^{-+} = \hat{E}_0^{++}\frac{i\omega}{2k_a q_L}e^{\frac{i l\tilde{q}}{2}}\sin\left(\frac{\ell q}{2}\right)\tilde{x} + \mathcal{O}(\tilde{x}^2). \tag{3.77}$$

Equation (3.77) is very similar to the generated axions in the case of incoming photons, cf. equation (3.63). A discussion is therefore very similar to the case of incoming photons.

In the strong mixing region and zero mass limit we obtain up to leading order for the axions, that are generated in the direction of the incoming photons:

$$\hat{a}_2^{-+} = \hat{E}_0^{++}\frac{i\tilde{x}}{2\omega\Delta n}e^{\frac{i\ell\tilde{q}}{2}}\sin\left(\frac{\ell q}{2}\right), \tag{3.78}$$

where we have again done the expansion not in the phases.

As in the case of incoming axions we observe a non-conserving energy flux Δn enhancement for the generated axions, cf. equation (3.78). At this point we want to compare our calculation, that is based on the axion-Maxwell equations plus the interface conditions with existing mixing formalism calculations [72, 78] and in particular with [71] which uses the formalism of [60] to write down a solution for generated axions to all orders in the coupling $g_{a\gamma}$. Taking the massless limit of equation (32) in [71] yields:

$$\hat{a}_2^{-+} \sim \frac{\tilde{x}/2}{\sqrt{\Delta n^2 + \tilde{x}^2/4}}\sin\left(\frac{\ell}{2}\sqrt{\Delta n^2 + \tilde{x}^2/4}\right). \tag{3.79}$$

This result suggests that in the strong mixing region, where we have $\tilde{x} > n^2 - 1$, the prefactor goes to one. However, with the matrix formalism in the strong mixing region we find in equation (3.78) that the outgoing axions are enhanced by a factor of Δn, since we have $q \to \omega\frac{\tilde{x}}{2}$.

In appendix A.3 we have shown that the Δn enhancement can lead to order one energy flux non-conservation in parts of the strong mixing region. This points in the direction that the Δn enhancement is in parts of the strong mixing region non-physical. We expect that this result is

due to the interface condition for the continuity of the axion field, cf. equation (3.41), because it is the only interface condition which does not follow directly from the equations of motion. However, replacing the continuity condition for the axion field with an equation that enforces energy flux conservation at each interface would come with the difficulty that an energy flux conserving equation is always quadratic in the fields. This would lead to a system for the field amplitudes, that is much harder to solve, than the linear systems in the matrix formalism, cf. section 3.3. We explain this possibility of energy flux conserving interface conditions further in appendix A.3. A point that concerns the mixing formalism form Ref. [60] is that there no reflected fields appear. However, in a scattering problem we expect that reflected fields arise. Therefore another future study would be to use a manifestly energy flux conserving QFT calculation/ matrix formalism.

Except for a small part in the next section we do not discuss the discrepancy between the presented result with the Δn enhancement and the result in [71] further in this chapter. The reason for this is twofold. First, only a $\Delta n \leq 10^{-17}$ leads to a strong mixing region that affects current exclusion regions in the m_a-$g_{a\gamma}$ plane. As it was discussed in section 3.1, $\Delta n \leq 10^{-17}$ can be achieved, however currently running experiments would require an update to reach such values. Second, in the rest of this chapter only weak mixing is considered and we have shown that in this case the used interface conditions for the electromagnetic and axion fields can reproduce existing results and are therefore appropriate.

3.4.3 Light shining through a wall experiments

In this section we combine the results from the matrix formalism from the previous sections to obtain the sensitivity of LSW experiments [72]. In an LSW experiment laser photons $\hat{E}^{++}_{0,g}$ generate axions $\hat{a}^{-+}_{2,g}$ in a magnetized region. These generated axions then travel through a wall. Behind the wall the axions $\hat{a}^{-+}_{2,g} =: \hat{a}^{-+}_{0,r}$ regenerate in a second magnetized region into photons which we call $\hat{E}^{++}_{2,r}$.

The outgoing E-field behind the wall in the weak mixing regime can be obtained by multiplying the results from equation (3.63) and (3.77):

$$\hat{E}^{++}_{2,r} = \hat{E}^{++}_{0,g} \frac{\omega}{n k_a} \left(\frac{\omega}{2q_L}\right)^2 e^{i\tilde{q}\ell} \sin^2\left(\frac{\ell q}{2}\right) \tilde{x}^2 + \mathcal{O}(\tilde{x}^3), \tag{3.80}$$

where we have assumed that the length ℓ and strength B^e of the external B-field before and after the wall are the same.

The outgoing power from the regeneration region is:

$$P = \frac{1}{2} |\hat{E}^{++}_{0,g}|^2 \left|\frac{\hat{E}^{++}_{2,r}}{\hat{E}^{++}_{0,g}}\right|^2 A, \tag{3.81}$$

where A is the cross sectional area of the incoming laser beam in the generation region. The power of the laser, which is coming into the generation region, is called $P_{0,g}$. We obtain:

$$P = P_{0,g} \left|\frac{\hat{E}^{++}_{2,r}}{\hat{E}^{++}_{0,g}}\right|^2 \beta_c^2, \tag{3.82}$$

where we have introduced a power build up factor β_c that is reached by surrounding the magnetized regions by high quality cavities.

If the experiment is background dominated and no significant signal over background is found we can set 95% exclusion limit by requiring that the signal rate n_s is smaller than $2\sqrt{\frac{n_B}{\tau}}$ [78–80], where n_B is the background event rate and τ the measurement time. The 95% exclusion will then

be defined by:

$$\frac{P}{\omega} = 2\sqrt{\frac{n_B}{\tau}}. \tag{3.83}$$

Combining equation (3.82) and (3.83), we obtain for typical LSW experimental values

$$\left|\frac{\hat{E}^{++}_{2,r}}{\hat{E}^{++}_{0,g}}\right| = 2.4\times 10^{-18}\Big(\frac{\omega\hbar}{1\,\mathrm{eV}}\Big)^{\frac{1}{2}}\Big(\frac{n_b}{10^{-4}\frac{1}{\mathrm{s}}}\Big)^{\frac{1}{4}}\Big(\frac{100\,\mathrm{h}}{\tau}\Big)^{\frac{1}{4}}\Big(\frac{3\,\mathrm{W}}{P_{g,L}}\Big)^{\frac{1}{2}}\Big(\frac{10^{10}}{\beta_c^2}\Big)^{\frac{1}{2}}, \tag{3.84}$$

what makes the smallness of the generated E-field clear.

In the following we derive a sensitivity estimate for LSW experiments in the zero mass limit. Later we plot the sensitivity in the whole m_a-$g_{a\gamma}$ plane. We estimate the sensitivity in the weak mixing region. In the context of laboratory experiments on Earth we can always write in the weak mixing region $\frac{q\ell}{2} \approx \frac{q_L\ell}{2}$, since we have seen in equation (3.76) that higher order effects (horizontal bending of the minima peaks in the weak mixing regime) in $\tilde{x}^2$ can only be important for very long B-fields that cannot be realized in Earth based experiments. The sensitivity in the weak mixing region is now given by plugging equation (3.80) into equation (3.84).

If $\frac{q_L\ell}{2} = \frac{\omega\Delta n\ell}{2} \geq 1$ the sine term is of the order of one and the $q_L = \omega\Delta n$ does not cancel with the argument of the sine function in equation (3.80). Physically this can happen, when the vacuum is not very good, cf. equation (3.67). For example for our benchmark $\ell = 100\,\mathrm{m}$ this happens for $\Delta n > 10^{-8}$. We obtain (setting now $\sin\frac{q_L\ell}{2} \approx 1$) the following sensitivity:

$$(g_{a\gamma})_w = 2.6\times 10^{-9}\times(g_{a\gamma})_{sw}\times\Big(\frac{\omega}{1\,\mathrm{eV}}\Big)^{\frac{1}{4}}\Big(\frac{3\,\mathrm{W}}{P_{0,g}}\Big)^{\frac{1}{4}}\Big(\frac{n_B}{10^{-4}\frac{1}{\mathrm{s}}}\Big)^{\frac{1}{8}}\Big(\frac{100\,\mathrm{h}}{\tau}\Big)^{\frac{1}{8}}\Big(\frac{10^{10}}{\beta_c^2}\Big)^{\frac{1}{4}}, \tag{3.85}$$

where

$$(g_{a\gamma})_{sw} = \frac{\Delta n\omega}{B_e} = 5.2\frac{1}{\mathrm{GeV}}\Big(\frac{\Delta n}{10^{-6}}\Big)\Big(\frac{\omega}{1\,\mathrm{eV}}\Big)\Big(\frac{1\,\mathrm{T}}{B_e}\Big) \tag{3.86}$$

is the line between the strong and weak mixing regimes in the massless limit. In summary the sensitivity in the coupling constant decreases in the zero mass limit if Δn increases, i.e. if the vacuum is not very good. A similar statement was also made in [71] although the way how the result was obtained is different.

If $\frac{q_L\ell}{2} = \frac{\ell\omega\Delta n}{2} \ll 1$ we can expand the argument in the sine function. We obtain the already well known sensitivity estimate for LSW experiments [71, 78] in the weak mixing region. The sensitivity for small masses is:

$$(g_{a\gamma})_w = 7.5\times 10^{-11}\frac{1}{\mathrm{GeV}}\Big(\frac{1\,\mathrm{T}}{B_e}\Big)\Big(\frac{100\,\mathrm{m}}{\ell}\Big)\Big(\frac{n_B}{10^{-4}\frac{1}{\mathrm{s}}}\Big)^{\frac{1}{8}}\Big(\frac{100\,\mathrm{h}}{\tau}\Big)^{\frac{1}{8}}\Big(\frac{\omega}{1\,\mathrm{eV}}\Big)^{\frac{1}{4}}\Big(\frac{3\,\mathrm{W}}{P_{0,g}}\Big)^{\frac{1}{4}}\Big(\frac{10^{10}}{\beta_c^2}\Big)^{\frac{1}{4}}. \tag{3.87}$$

The sensitivity in equation (3.87) scales with length ℓ, external B-field strength and frequency ω. Making the external B-field longer also requires a better vacuum such that equation (3.87) applies. Increasing the external B-field strength increases the sensitivity linearly. However, increasing the photon energy of the laser increases the sensitivity only with $\omega^{1/4}$.

In figure 3.8 we show the sensitivity plot for an LSW configuration with $B^e = 1\,\mathrm{T}$, $\ell = 100\,\mathrm{m}$ on both sides of the wall and for two different vacuum refraction indices ($\Delta n = 10^{-6}, 10^{-12}$). The area above the dashed lines is the strong mixing regime, while the area below is weakly mixed. The solid lines are the sensitivity curves which are based on the full formulas which come out of the matrix formalism. In the following we want to validate that for small masses they agree with our derived formulas. In the case $\Delta n = 10^{-6}$ we found that we can use the weak mixing calculation in equation (3.85), since we have $\frac{q_L\ell}{2} \leq 1$. The LSW sensitivity is nine orders of magnitude below $(g_{a\gamma})_{sw}$ in the weak mixing region around $10^{-8}\frac{1}{\mathrm{GeV}}$. If we decrease Δn further to 10^{-12} we have $\frac{q\ell}{2} \ll 1$ and therefore equation (3.87) applies. In this case we get an even better LSW sensitivity.

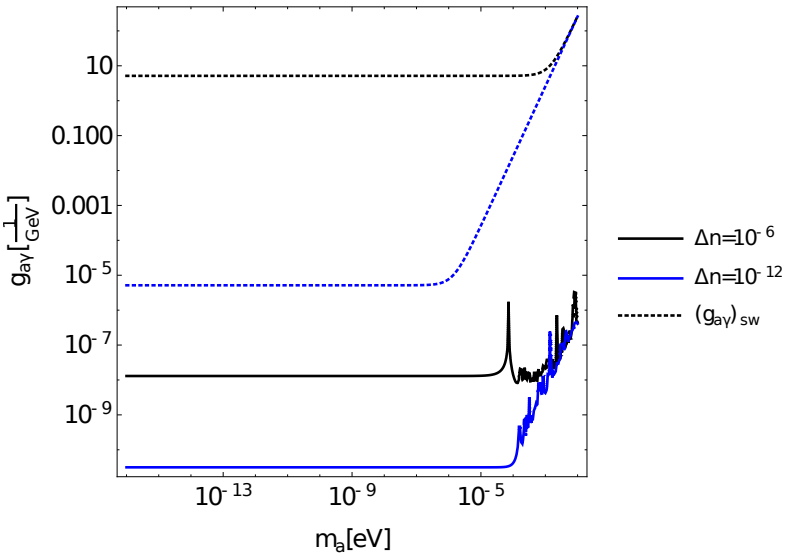

Figure 3.8: Light shining through the wall experiment sensitivity for different refractive indices $n-1=\Delta n=10^{-6},10^{-12}$. The length $\ell=100\,\mathrm{m}$ and strength $B_e=1\,\mathrm{T}$ of the external B-field on both sides of the wall are the same. The laser in the generation cavity has $\omega=1.0\,\mathrm{eV}$. The dashed lines indicate the boundary between weak and strong mixing regions $(g_{a\gamma})_{sw}$, while the solid lines are the sensitivity lines for the different refractive indices. For $\Delta n=10^{-6}$ and $\Delta n=10^{-12}$ we can use the weak mixing calculations, since both sensitivity lines are below the dashed lines. The oscillation peaks at larger masses arise always in the weak mixing region. We do not resolve them completely in this figure for better visibility of the plot.

Therefore we have explicitly shown that the sensitivity of LSW experiments scales with Δn in the weak mixing region.

The sensitivity reach in equation (3.87) does not depend anymore on Δn. Therefore one could think that making the vacuum much better does not yield any advantage. However, if Δn is decreased the boundary between strong and weak mixing is moving to lower couplings, cf. equation (3.86). Therefore at some point when making Δn small enough $(g_{a\gamma})_{sw}$ will be equal or even below $(g_{a\gamma})_w$. This would then mean that the weak mixing calculation is not valid anymore, since the weak mixing sensitivity estimate would then be in the strong mixing region. The situation $(g_{a\gamma})_{sw}<(g_{a\gamma})_w$ can be translated to:

$$1>1.4\times10^{-5}\ \left(\frac{10^{-12}}{\Delta n}\right)\left(\frac{100\,\mathrm{m}}{\ell}\right)\left(\frac{1\,\mathrm{eV}}{\omega}\right)^{\frac{3}{4}}\left(\frac{n_B}{10^{-4}\frac{1}{\mathrm{s}}}\right)^{\frac{1}{8}}\left(\frac{100\,\mathrm{h}}{\tau}\right)^{\frac{1}{8}}\left(\frac{3\,\mathrm{W}}{P_{g,L}}\right)^{\frac{1}{4}}\left(\frac{10^{10}}{\beta_c^2}\right)^{\frac{1}{4}}. \tag{3.88}$$

Therefore in typical LSW setups the described situation can happen for $\Delta n<10^{-17}$. In section 3.1.2 it was pointed out that $\Delta n<10^{-17}$ can be reached with current technology but existing LSW experiments do not reach such a high vacuum [11].

If $\Delta n<10^{-17}$ could be reached in LSW experiments the matrix formalism would predict a sensitivity enhancement which is due to the Δn enhancement that was described in the previous sections. Therefore if the vacuum is so good that equation (3.88) is not fulfilled the sensitivity would be:

$$(g_{a\gamma})_s = (g_{a\gamma})_w^{\frac{1}{2}}\left(\frac{\Delta n\omega}{B_e}\right)^{\frac{1}{2}} \tag{3.89}$$

$$= 6.23\times10^{-13}\frac{1}{\mathrm{GeV}}\left(\frac{(g_{a\gamma})_w}{7.5\times10^{-11}\frac{1}{\mathrm{GeV}}}\right)^{\frac{1}{2}}\left(\frac{\Delta n}{10^{-22}}\right)^{\frac{1}{2}}\left(\frac{\omega}{1\,\mathrm{eV}}\right)^{\frac{1}{2}}\left(\frac{1\,\mathrm{T}}{B_e}\right)^{\frac{1}{2}}, \tag{3.90}$$

where $(g_{a\gamma})_w$ has to be taken from equation (3.87) and is independent of Δn. The sensitivity in equation (3.90) would be two orders of magnitude better than previously thought. Note that one cannot make Δn much smaller due to QED effect, cf. section 3.1.2.

We do not show the sensitivity estimate for an ultra high vacuum configuration with $\Delta n < 10^{-17}$, cf. equation (3.90), in figure (3.8). This is because in appendix A.3, we have observed that in parts of the strong mixing region order one energy non-conservation effects can appear. Although in the case $\Delta n = 10^{-22}$ the energy violation would be small in the region where the LSW sensitivity is enhanced, further studies have to investigate this effect, before a definitive claim can be made.

3.5 Systems with dielectrics

While in the previous section we have investigated the emitted axions and photons from magnetized regions with the same refractive index, here we consider dielectric multilayer systems. In all layers the same homogeneous external B-field B^e is present. All following calculations are done in the weak mixing region, i.e. we consider only masses and refractive indices such that condition (3.14) is fulfilled. For low velocity dark matter axions multilayer calculations in the context of axion haloscopes already exist in Refs. [58, 59]. Therefore, we focus here on the ultra relativistic limit ($m_a \ll \omega$), which is not already worked out in the literature.

In section 3.5.1-3.5.3 we calculate the emitted photons from a single dielectric layer, two dielectric layers and 200 dielectric layers in the case of incoming relativistic axions. The results for the reverse process, i.e. the emitted axions in the case of incoming photons, is not discussed separately, since – as we have seen in the previous sections – they are very similar.

3.5.1 Single dielectric layer

We investigate a dielectric layer of thickness d with refractive index n, which is surrounded by vacuum with refractive index n_v.

In the case of massless axions $\hat{a}_0^{-+}$ that propagate in positive z-direction the emitted E-field in the direction of the incoming axions in the weak mixing regime is:

$$\hat{E}_2^{++} = -\hat{E}^a_{L,0}\frac{(n-1)^2 e^{i(\Delta_a+2\Delta_p)} - e^{i\Delta_a}(n+1)^2 + 4e^{i\Delta_p}n}{(-1+e^{2i\Delta_p})\,n^2 - 2\,(1+e^{2i\Delta_p})\,n + e^{2i\Delta_p} - 1} + \mathcal{O}(\tilde{x}^2), \tag{3.91}$$

with the phase depths $\Delta_p = n\omega d$ and $\Delta_a = \omega d$. We did not explicitly write down the equations for the other unknown fields, since in the following the discussion is focused on the generated photons in the forward direction. In figure 3.9 (left) we show $\hat{E}_2^{++}$ normalized to the axion induced E-field in vacuum, i.e. $\beta = \left|E_2^{++}/\hat{E}^a_{0,L}\right|$, for $n = 3$. We observe maxima lines for $\Delta_p - \Delta_a = (2j+1)\pi, j \in \mathbb{N}_0$ and minimum lines at $\Delta_p - \Delta_a = 2j\pi, j \in \mathbb{N}_0$.

If n is large we have $\Delta_p \gg \Delta_a$ and therefore maximums are at $\Delta_p \approx (2j+1)\pi, j \in \mathbb{N}_0$ and minima at $\Delta_p \approx 2j\pi, j \in \mathbb{N}_0$. Note that not every point in figure 3.9 (left) is allowed since in the massless limit Δ_p and $\Delta_a = \Delta_p/n$ are related. In figure 3.9 (right) we use this relation and show β only with respect to the phase depth Δ_p. For $n = 2$ we have $\Delta_p - \Delta_a = \omega d = \Delta_p/2$ and therefore we find the first maximum at $\Delta_p = 2\pi$. For larger n we observe a sharp peak around $\Delta_p = 2(j+1)\pi$ and minima around $\Delta_p = 2j\pi$. At the other points $\beta \to 1$ in the limit of large n.

In figure 3.10 we show the dielectric layer that is surrounded by vacuum and we illustrate in forms of waves the emitted E-fields from both interfaces. In this particular example we choose $n = 2$ and $d = \lambda_p^v$, where λ_p^v is the photon wavelength in vacuum. In this case we have $\Delta_p - \Delta_a = \pi$ and therefore we expect maximum emission. The axion induced E-field in figure 3.10 is shown in black and all other emitted fields are normalized to the magnitude of this field. The axions

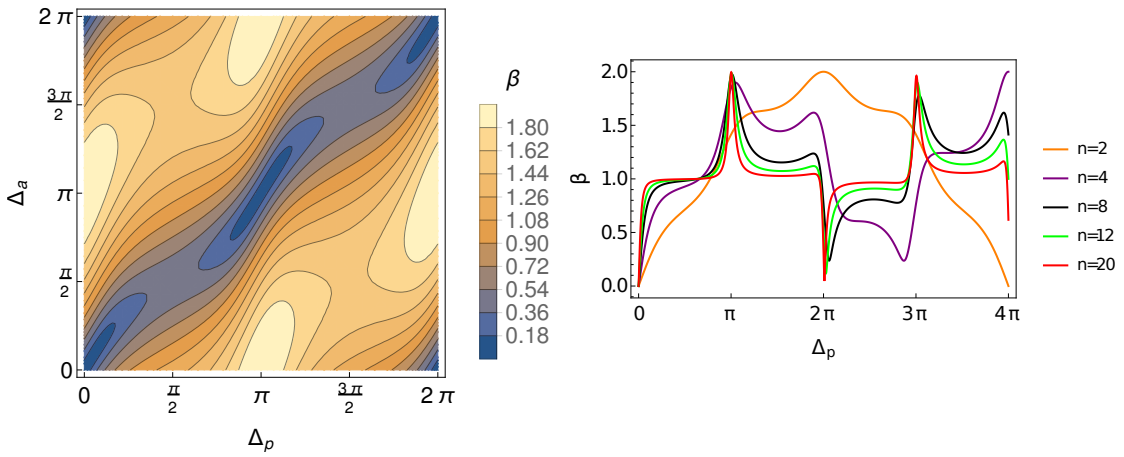

Figure 3.9: Massless axions hit a magnetized dielectric layer of thickness d and refractive index n. We show the emitted E-field normalized to the axion induced E-field in vacuum, i.e. the boost factor $\beta = \left|E_2^{++}/\hat{E}^a_{0,L}\right|$. From the left figure we see that the maximum lines occur at $\Delta_p - \Delta_a = (2j+1)\pi, j \in \mathbb{N}_0$ while the minima lines can be found at $\Delta_p - \Delta_a = 2j\pi, j \in \mathbb{N}_0$. In the left figure we use $n = 3$. Note that in the ultra relativistic limit $\Delta_a = \omega d$ and $\Delta_p = n\omega d = n\Delta_a$. This relation is used in the right figure to show the boost factor for different refractive indices with respect to Δ_p. In the large n limit sharp maximum peaks around $\Delta_p = (2j+1)\pi$ and minimum peaks around $\Delta_p \approx 2j\pi$ are observed.

propagate in positive z-direction and so does the axion induced E-field. This is indicated by the black arrow. The emitted photon-like E-fields from the left interface are shown in blue and red. Their propagation direction is signified with the arrows in the respective colors. The same is done for the photon-like E-fields that are emitted off the right interface. The incoming axions in figure 3.10 are ultra relativistic, what is immediately clear, since the axion induced and photon-like E-fields have very similar wavelength in the vacuum region. The red wave, that is emitted off the left interface and propagates into the positive z-direction, hits the right interface and gets transmitted into the right vacuum region (without a phase shift). Therefore the red and green wave interfere constructively in the vacuum that is right to the dielectric layer. Therefore in total we have maximum E-field emission of the dielectric layer in the described scenario. Note that a part of the red wave also gets reflected at the right interface. The reflected part of the red wave bounces back and fourth between the two interfaces. However, the part that leaves the disk to the right always interferes constructively with the green wave, since a wave gets a phase shift of π if it is reflected at a medium which has lower refractive index as the medium in which it is propagating. This kind of *recursive propagation* to construct the total emitted E-field gives a physical picture of what the matrix formalism does and helps to interpret its results.

Note that the above discussion was for massless axions. However, the results are also valid for ultra relativistic axions ($m_a \ll \omega$). This becomes directly evident from the physical picture that we have drawn in figure 3.10. Small nonzero axion masses change the axion-like wavelength and make it slightly larger $\lambda_a = \frac{2\pi}{\omega}\left(1 + \frac{m_a^2}{2\omega^2}\right)$. However, if the axions are ultra relativistic this change is not very severe. If the thickness of the dielectric layer is not larger than a few wavelength – what is the case in figure 3.10 – then it is obvious that the emitted E-field will not differ much from the massless case.

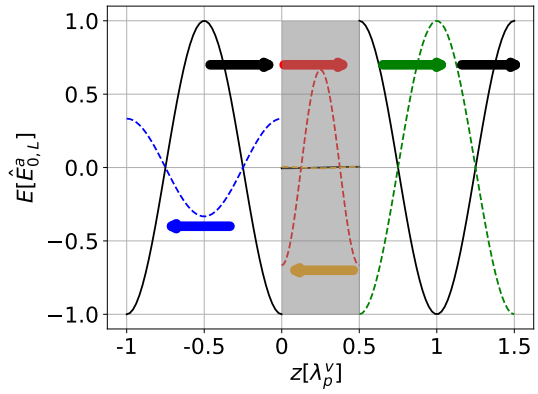

Figure 3.10: The incoming massless axions induce an axion induced E-field which is shown in black. All other photon-like E-fields are normalized to the magnitude of the axion induced field in vacuum that surrounds the dielectric layer (gray). An external B-field is present in all media. To fulfill the continuity requirement for the E-field at the interfaces photon-like E-fields are emitted in both directions. These fields are shown in red and blue at $z = 0$ and green and yellow at $z = \lambda_p^v/2$, where λ_p^v is the photon E-field wavelength in vacuum. The direction of propagation of the E-fields is depicted with the colored arrows. In the chosen example the dielectric layer has $\Delta_p = 2\pi$ and $\Delta_a = \pi$. Therefore $\Delta_p - \Delta_a = \pi$ and we have maximal emission form the layer. Physically this means that when the red wave is transmitted into the right vacuum region the red and green waves interfere constructively.

3.5.2 Two dielectric layers

For a single magnetized dielectric layer β is at most 2, since in this case the emission from the two surfaces interferes constructively in the direction of the incoming ultra relativistic axions. Here we consider now two dielectric layers and show that one can reach $\beta > 2$. Each layer has the same thickness d and refractive index n. The distance between both layers is ℓ_d and the vacuum that surrounds the layers is n_v. The reasoning in the following is based on the intuition that we have gained in the previous section for a single layer.

In the following we discuss two types of layer configurations. In the transparent case the emission is coherently added without the system itself being resonant. We can reach $\beta = 4$ in this case. In the resonant case the layers are configured such that $\beta > 4$ can be achieved in very resonant configurations.

3.5.2.1 Transparent case

In the *transparent case* we require that all layers are completely transparent to all electromagnetic radiation, i.e. $\Delta_p = \pi h, h \in \mathbb{N}_0$, and emit the maximum amplitude, i.e. $\Delta_p - \Delta_a = (2j+1)\pi, j \in \mathbb{N}_0$. Combining the two conditions each layer has to have a thickness of $d = \frac{\pi}{\omega}(h-2j-1)\pi$ and refractive index $n = \frac{h}{-2j-1+h}$. It is important to note that in reality the discrete condition for the refractive index might not be fulfilled exactly. However, one can always choose j and h such that one comes close to the real refractive index. In this case only small deviations from our idealized results are expected.

In figure 3.11 we consider as an example ultra relativistic axions that hit a two layer system. We chose $j = 0$ and $h = 2$ what gives $d = \frac{\pi}{\omega} \approx \frac{\lambda_p^v}{2}$, where λ_p^v is the photon-like wavelength in the vacuum around the layers. Furthermore we choose $n = 2$. The axion induced E-field is shown in black and the photon-like E-fields are colored. All fields are normalized to the axion induced E-field in vacuum and their direction of propagation is depicted with the respective arrows. In the

chosen example both layers emit the maximum photon-like E-field amplitude ($\beta = 2$) as it was demonstrated in the previous section.

The distance between the two layers in figure 3.11 (left) is $\ell_d = \lambda_p^v/2$. Since the axions are ultra relativistic the difference between the photon-like E-field and the axion-like E-field is not very visible in the figure. The red and green waves in figure 3.11 (left), that are emitted from first layer and propagate in the positive z-direction, interfere constructively in the vacuum between both layers. For better visibility the red wave from the interface at $z = 0$ is not drawn in the medium between both layers. The emission from the first layer then hits the layer on the right. The green wave from the first disk is transmitted [5] into the right layer, what is explicitly shown in the figure and depicted with the green arrow in the right layer. In the chosen situation this radiation then interferes destructively with the other green wave, that is emitted from $z = \frac{3}{2}\lambda_p^v$, into the right vacuum. To avoid this destructive interference the photon-like emission, that propagates in positive z-direction from the left layer, has to gain an additional phase shift of π (with respect to the axion induced field) when it hits the right layer. Physically this can be achieved if $\ell_d(k_p - k_a) = \pi$. In the ultra relativistic limit this means that the distance between both layers has to be:

$$\ell_d = \frac{\pi}{\Delta n_v \omega + \frac{m_a^2}{2\omega}}. \tag{3.92}$$

If equation (3.92) is fulfilled the emitted photon-like E-fields from both layers do not interfere destructively anymore but they are coherently added. In this case we can achieve $\beta > 2$ for a two layer system. We draw this situation in figure 3.11 (right). Again both layers emit the maximum photon-like E-field amplitude. However, if the distance between both layers is chosen as in equation (3.92), the photon-like radiation from the left layer (green) is in phase with the axion induced field (black) when it hits the right layer. In this case the photon-like radiation from the left disk interferes constructively with the photon-like radiation from the right disk when it travels into the positive z-direction.

Practically the condition (3.92) means that by choosing ℓ_d and Δn_v appropriate one can generate scenarios which give $\beta = 4$ at specific masses. For a mass $m_a^2 > 2\Delta n_v \omega^2$ we can generate large boost factors if we set $\ell_d = 2\pi\omega/m_a^2$. In figure 3.11 (left) we show this exemplary for $\ell_d = 1\,\mathrm{m}$ ($m_a \approx 1\,\mathrm{meV}$) and $\Delta n_v = 10^{-12}$. For all masses that fulfill $m_a^2 > 2\Delta n_v \omega^2$ we can therefore generate boost factor of $\beta = 4$ by choosing the distance ℓ_d properly. However, if our focus is on masses that fulfill $m_a^2 < 2\Delta n_v \omega^2$ then we can choose a distance $\ell_d = \frac{\pi}{\Delta n_v \omega}$ which leads to a boost factor of 4 in this mass range, cf. figure 3.11 (right).

Until now we have only looked at the case of emitted photons in the case of incoming ultra relativistic axions. However, similar results are also valid for the case of incoming photons and generated axions.

3.5.2.2 Resonant case

In the transparent case each individual layer emits the maximal amplitude while at the same time we require that the reflectivity (transmissivity) of the layers is zero (one) such that the emitted radiation is coherently added. If we want to optimize the system to be more resonant we have to give up the restriction of zero reflectivity. In particular we want maximum reflectivity what corresponds to $\Delta_p = \frac{2j+1}{2}\pi, j \in \mathbb{N}_0$ [58]. To maximize the reflectivity we require the refractive index n to be large. The reflectivity of one layer is $R = \frac{n^2-1}{n^2+1}$[58]. Note that in practice one might use dielectric mirrors as highly reflective media, however we model this situation with a

[5] The reflected part from this interface is again not shown for better visibility. This should not be confused with the total reflectivity of the disk which is zero in the transparent case. Here we just speak about the reflectivity at a single surface. The total reflectivity could be computed by recursively propagating the incoming radiation between both surfaces.

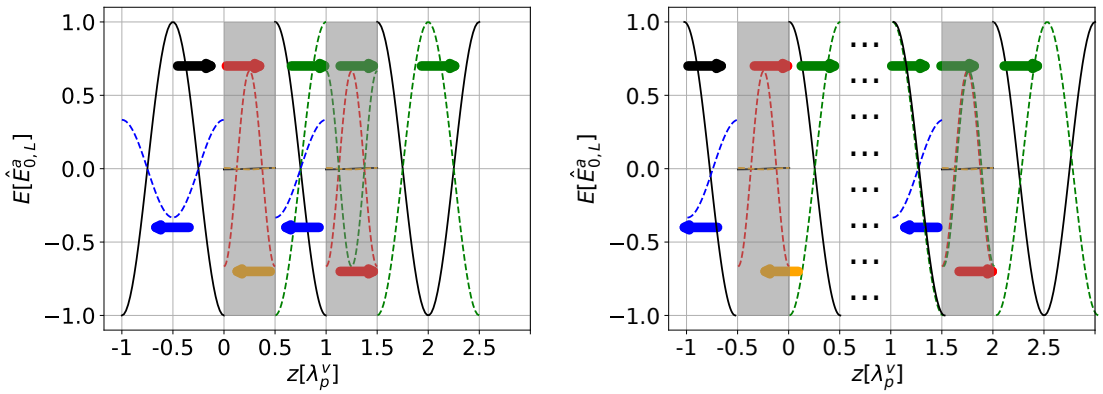

Figure 3.11: Two magnetized dielectric layers with thickness $d = \lambda_a/2$ and $n = 2$. Ultra relativistic axions are coming in from the left $\hat{a}_0^{-+}$ and induce the E-field in black. The photon-like emission that is emitted from each interface is colored and the direction of propagation is depicted with the arrows. In the shown example each layer itself emits the maximal emission, since the red and green wave interfere constructively. In the left figure the waves from the different layers interfere destructively. The green wave, that is emitted form $z = \lambda_a/2$ in the positive direction, enters the right layer and then interferes destructively with the green wave that is emitted form $z = 1.5\lambda_a$ in the positive z-direction. To obtain constructive interference between the waves form the two layers either the distance between both layers has to be increased or the refractive index between bot layers. In this case the photon-like and axion-like E-fields can gain an additional phase difference of π at the right layer. This situation is depicted in the right figure. The dots indicate that now the distance between both layers in increased to be exactly ℓ_d. The axion induced field (black) and the photon-like field from the left layer (green) at the right layer are now in phase giving constructive interference in the vacuum medium on the right.

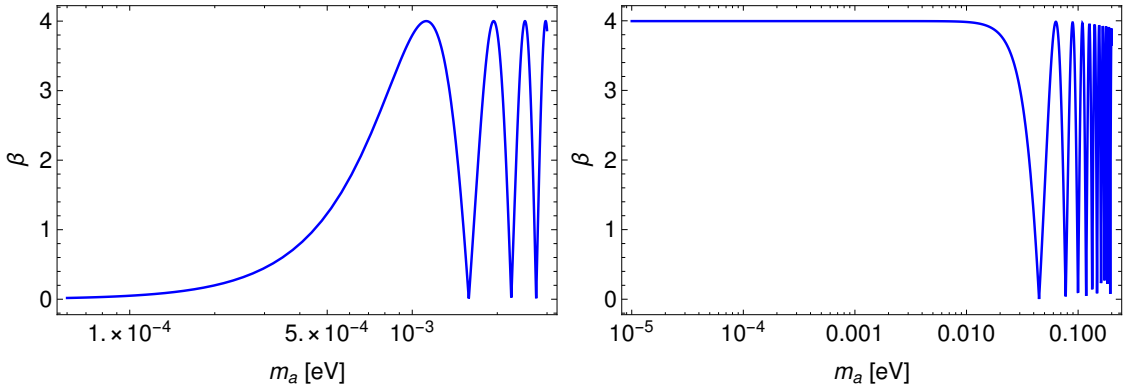

Figure 3.12: Boost factor for the generated E-field when ultra relativistic axions ($m \ll \omega = 1\,\text{eV}$) hit two dielectric layers. Both dielectric layers have refractive index $n = 2$ and thickness $d = \lambda_p^v/2$ and therefore emit a maximal $\beta = 2$. We show the two described scenarios from the text. Left: In the large mass scenario we choose the vacuum refractive index between the layers $n_v = 1 + 10^{-12}$. The distance between both layers is chosen to be $\ell_d = 1\,\text{m}$, what corresponds to $\beta = 4$ around $\omega = 1\,\text{meV}$. Right: The vacuum refractive index is now $n_v = 1 + 10^{-3}$ and the distance between the layers is chosen according to equation (3.92) in the small mass scenario: $\ell_d = \frac{\pi}{\Delta n_v \omega}$. As a result small masses have $\beta = 4$ in the right figure.

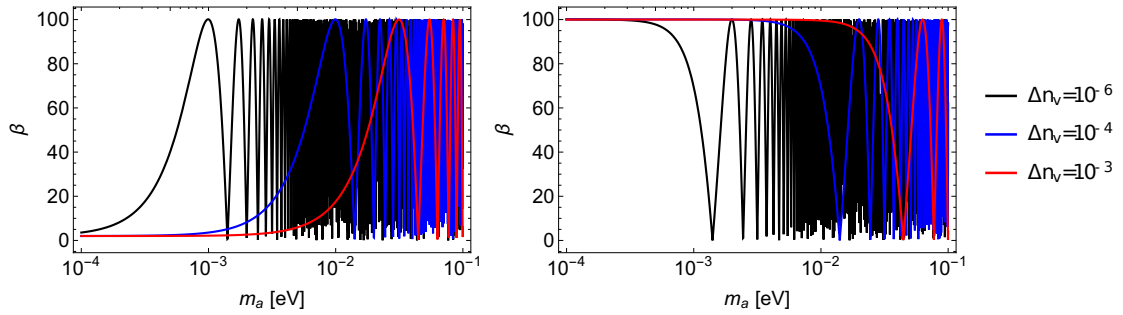

Figure 3.13: Boost factor for the generated E-field when ultra relativistic axions ($m \ll \omega = 1\,\text{eV}$) hit two dielectric layers. Both dielectric layers have refractive index $n = 100$ and are optimized to be maximal reflective. The vacuum refractive index is n_v in both figures is varied. The distance between the layers is chosen to be $\ell_d = \frac{2\pi}{\Delta n_v \omega}$ in left figure and $\ell_d = \frac{\pi}{\Delta n_v \omega}$ in the right figure.

single dielectric layer with large n and $\Delta_p = \frac{2j+1}{2}\pi$. The thickness of the layers is then given by $d = \frac{2j+1}{2\omega n}\pi$. In this case the amplitude of radiation from each layer is not maximal anymore, cf. figure 3.9 (left). Nevertheless the radiation form the layers can now bounce many times between the two layers giving rise to a resonance and large β.

In the following we discuss two particular resonant configurations. We find that setting the distance between both layers to $\ell_d = \frac{\pi}{\Delta n_v \omega}$ gives a large boost factor for small masses. Doubling the distance to $\ell_d = \frac{2\pi}{\Delta n_v \omega}$ gives a large boost factor at specific larger masses. In figure 3.13 we confirm this by computing the boost factor with the matrix formalism for the described configurations. In the left figure we show the case that $\ell_d = \frac{2\pi}{\Delta n_v \omega}$. The first maximum always appears for masses $\frac{m_a^2}{2\omega} > \omega \Delta n_v$. In the right figure we set $\ell_d = \frac{\pi}{\Delta n_v \omega}$. In this case we obtain large boost factors for small masses and for specific peaks at larger masses. Both cases are shown for different vacuum refractive indices. The first maximum and minimum of the β curves scales with $\sqrt{\Delta n_v}$. The maximum peaks of β grow linear with n and can therefore be increased even further for larger reflectivity.

3.5.3 200 layer setup

In this section we discuss the boost factor for a system with 200 dielectric layers. The results are calculated for incoming ultra relativistic axions but exact same configurations can be overtaken to boost the generation of axions in the case of incoming photons.

3.5.3.1 Transparent case

We consider the transparent case in which each layer emits the maximal E-field amplitude and the radiation from all layer is coherently added. It was shown that a boost factors of $\beta = 2$ for a two interface system (one dielectric layer) and $\beta = 4$ for a four layer system (two dielectric layers) can be obtained in the transparent case. Here we consider a 200 dielectric layer system in the transparent case for which we expect a maximum boost factor of $\beta = 400$. All dielectric layers have the same thickness d and refractive index n. The distance between the layers is ℓ_d and the vacuum between the layers has refractive index n_v.

To give an explicit example we choose a layer refractive index $n = 2$ and a thickness $d = \frac{\pi}{\omega} = 0.6\,\mu\text{m} \Rightarrow \Delta_p = 2\pi$. The governing frequency is again $\omega = 1\,\text{eV}$. Note that these are just example values and in reality n will probably be different from the chosen value her. However, then one can still achieve maximal emission from each layer ($\beta = 2$) by choosing the thickness as $d = \frac{(2j+1)\pi}{(n-1)\omega}$. In this case then Δ_p can also take values in which case reflection of the layers is not zero, since

zero reflection is only guaranteed for $\Delta_p = j\pi, j \in \mathbb{N}_0$.

In the following we consider again the large and small mass scenario from section 3.5.2.1. In the large masses scenario we consider masses and vacuum refractive indices such that $\Delta n_v < \frac{m^2}{2\omega^2}$. Therefore in equation (3.92) Δn can be neglected and the optimal distance of the layers is set by the mass where the boost factor should be maximal. As an example we consider axion masses $m_a = 1.12\,\text{meV}$ and $n_v - 1 = 10^{-12}$. According to equation (3.92) the distance of the layers is then $\ell_d = 1\,\text{m}$. In figure 3.14 (blue) we compute the boost factor for the described configuration with the matrix formalism. As expected we get a sharp peak around $m_a = 1.12\,\text{meV}$. The bandwidth of the peak is now much smaller than in the cases where we had less dielectric layers. We also investigate the effect of uncertainties.

The red green and black curve in figure 3.14 show the effect of dielectric layers with slightly varying thickness. The red curve was generated by adding to each layer thickness a random number of a normal distribution multiplied with $d/100$, where d is the thickness of the layer. Our results make clear the the layers have to be manufactured with high precision. The criterion of very precisely manufactured layers will be one of the most important criterion when a material for the layers is selected. For larger masses the precision of the dielectric layers has to be even better. We find that we need a precision of $\delta d = d/50$ $(d/60)$ for $m_a \approx 1\,\text{meV}$ $(m_a \approx 10\,\text{meV})$ in order to maintain at least 20% of the β that is reached in the $\delta d = 0$ case. The overall needed precision with which the layers have to be manufactured is therefore on the order of 10 nm. This will be challenging but not impossible.

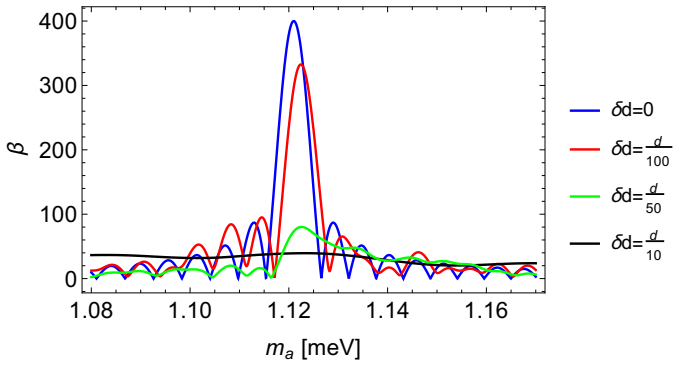

Figure 3.14: Incoming ultra relativistic axions ($\omega = 1\,\text{eV}$) generate a photon like E-field in a 200 dielectric layer system. The boost factor for the emitted electromagnetic field is shown over different axion masses. Each layer has $n = 2, d = \frac{2\pi}{n\omega}$ and therefore emits the maximal amount of radiation. The vacuum between the layers has a refractive index of $n_v = 1 + 10^{-12}$ and the layers have a thickness of $\ell_d = 1\,\text{m}$ (large mass scenario). The boost factor peaks at a specific mass. It is very important that the layers are produced with a high accuracy. The blue line corresponds to perfectly manufactured layers, while the other curves add a random uncertainty to each layer thickness. For example the red curve adds $\mathcal{N}\frac{d}{100}$ to each layer, where $\mathcal{N}$ is a random number from a normal distribution and $d = 0.6\,\mu\text{m}$.

To achieve large β for small masses we can set the distance of all layers to $\ell_d = \frac{\pi}{(n_v-1)\omega}$. We then obtain $\beta = 400$ for small masses. However, in section 3.5.4 we show that in the transparent case dielectric layers cannot lead to an improvement of magnetic conversion experiment. In the picture of Ref. [81] this is because for small masses axions and photons stay coherent over the whole length of the magnetized region if the vacuum is good enough. Therefore dielectric layers, which can correct a phase difference in the transparent case, would not lead to an improvement in the conversion rate. We show this in more detail in section 3.5.4 and do not discuss the possibility of large boost factors in the small mass scenario here any further.

3.5.3.2 Resonant case

In the two layer system we have discussed that highly reflective layers can lead to large boost factors. Here we consider 200 highly reflective layers which all have the same distance ℓ_d to each other.

We discuss a particular example with layer reflectivity of $R = \frac{n^2-1}{n^2+1} = 1 - 10^{-6}$, i.e. $n = 1000$ in the following. The distance of the layers is $\ell_d = \frac{2\pi}{\Delta n_v \omega}$ and they have a thickness of $d = \frac{3}{2}\frac{\pi}{\omega n}$, corresponding to maximal reflectivity. In figure 3.15 we show the boost factor over of the resonant system normalized to the boost factor of a transparent system $\tilde{\beta} = \beta/\beta_t$ with the same amount of layers. In our explicit example we have $\beta_t = 2 \times 200$. The resonance peak in figure 3.15 scales again with $\sqrt{\Delta n_v}$.

The needed precision of the shown resonances will again depend very sensitively on the thickness of the materials. However, the used large n materials are just taken to model for example dielectric mirrors which have a large reflectivity. In reality one has to take these details into account to estimate the precision with which the highly reflective materials have to be manufactured. Naively one expects that the precision with which the materials have to be manufactured has to be much smaller than the photon wavelength in these materials. More detailed studies are left for future work.

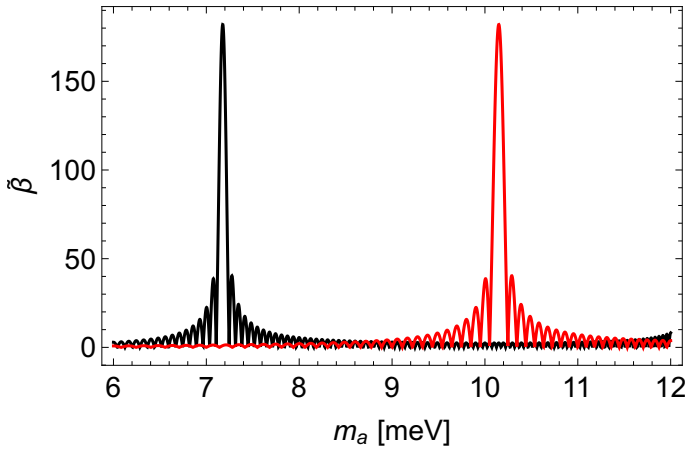

Figure 3.15: Boost factor of a 200 layer setup in a resonant configuration. The boost factor is normalized to the boost factor from a transparent setup with the same number of layers, i.e. $\tilde{\beta} = \beta/\beta_t$, with $\beta_t = 2 \times 200$. The reflectivity of each layer is $1 - R = 1 - \frac{n^2-1}{n^2+1} = 10^{-6}$. In black we show the case that $\Delta n_v = n_v - 1 = 10^{-4}$, while in red we show the case $\Delta n_v = 2 \times 10^{-4}$. The resonance frequency scales with $\sqrt{\Delta n_v}$. The distance between the layers is $\ell_d = \frac{2\pi}{\Delta n_v \omega}$.

3.5.4 Light shining through a wall experiments with dielectric layers

In this section we discuss how dielectric layers can be used to improve the sensitivity of LSW experiments. In figure 3.16 we show an exemplary sketch wich is called *LSW dielectric* setup in the following. Photons are converted into axions in the generation region (magnetized region before the wall) and these are then reconverted into photons in the regeneration region (beyond the wall). Each layer has a thickness d and refractive index n. The distance of each layer to the neighboring layer is ℓ_d. The total length ℓ of the magnetized regions on both sides of the wall is the same.

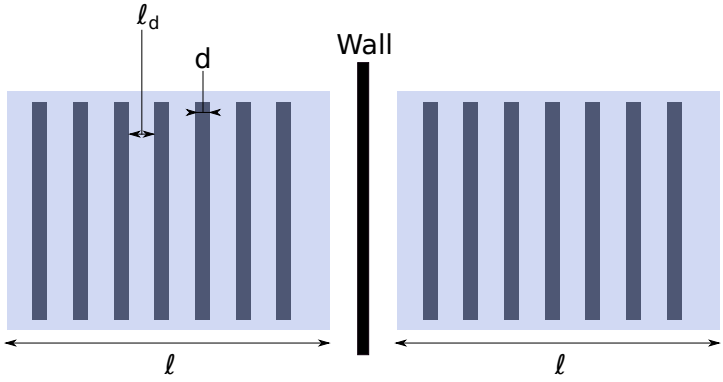

Figure 3.16: LSW dielectric setup. Dielectric disks (gray) are placed inside a magnetized region (blue). Before the wall (generation side) photons are converted into axions. The axions then pass the wall and are converted back into photons behind the wall (regeneration side). The dielectric layers have thickness d and refractive index n. The distance between the layers is ℓ_d and the vacuum around the disks has refractive index n_v.

We start to compare the sensitivity of the transparent case with the sensitivity of an *ordinary LSW* experiment, i.e. a magnetized region without dielectric layers. The sensitivity can be calculated by requiring background domination $n_s < 2\sqrt{\frac{n_b}{\tau}}$ [78–80], what is fulfilled for sufficiently long measurement times. n_s is the signal rate, n_b the background rate and τ the measurement time. The signal rate can be calculated from the signal power that leaves the regeneration cavity $n_s = P/\omega$ with $P = P_L\beta^4\delta^4$, where δ is evaluated in the vacuum region and P_L the power of the laser on the generation side.

To compare the sensitivity of the ordinary LSW setup with the LSW dielectric setup in the transparent case we express the sensitivity reach as:

$$g_{a\gamma} > (2\omega)^{\frac{1}{4}} \left(\frac{n_b}{\tau}\right)^{\frac{1}{8}} \left(\frac{1}{P_L}\right)^{\frac{1}{4}} \left(\frac{1}{B^e\ell}\right) \times \varsigma, \tag{3.93}$$

where ς is a factor that is different in the ordinary LSW scenario and in the LSW dielectric setup in the transparent case. In the ordinary LSW case we find:

$$\varsigma = \frac{2}{|F|\beta_c}, \tag{3.94}$$

where β_c is a power build up factor that arises when we place a cavity around the magnetized regions before and after the wall. We have furthermore defined the form factor $F = \frac{2}{q_L\ell}\sin\left(\frac{q_L\ell}{2}\right)$ which leads to a sensitivity loss in the large mass region for ordinary LSW experiments.

For the LSW dielectric setup in the transparent case we use that around the axion mass of interest we have $\delta = \frac{\tilde{x}/2}{m_a^2/\omega^2+2\Delta n_v} = \frac{\ell_d g_{a\gamma} B^e}{2\pi}$. Therefore we find:

$$\varsigma = \frac{\pi}{\beta_c}, \tag{3.95}$$

where we have used that $\beta\ell_d = 2N_{\text{layer}}\ell_d = 2\ell$, where N_{layer} is the total number of dielectric layers. Furthermore we have also assumed that a cavity encloses both magnetized regions in the LSW dielectric setup, i.e. a power build up factor β_c also appears in equation (3.95). This works, since the dielectric layers in the transparent case do not destroy the resonance of the cavity, since they are completely transparent.

By comparing equation (3.94) and (3.95) we see that dielectric layers in the transparent mode cannot increase the LSW sensitivity for small axion masses, since in this case $F \to 1$. Physically one can understand this in the picture that was described in Ref. [71, 81] and section 3.4.1. For sufficiently low masses and Δn_v the axion and photon do not run out of phase over the length of the magnetized region and therefore axions and photons are coherently produced over the length of the magnetized region. The coherent production cannot be increased by dielectric layers, since the two waves are already in phase.

However, in the large mass range where $\frac{1}{F} \sim \frac{q_L \ell}{2} \sim \frac{m_a^2 \ell}{4\omega} + \frac{\ell \omega \Delta n_v}{2}$ the normal LSW sensitivity decreases. In this case dielectric layers can bring the axions and photons back into phase. This was first pointed out in Ref. [81] and results in the constant sensitivity also for relatively large axion masses, cf. equation (3.93) and (3.95). In Ref. [81] the maximal number of studied layers is 20, while in the previous section many more layers have been studied. We have also investigated the needed precision of the dielectric layers in the previous section. For a 200 layer system the precision of the disks has to be better $\tan \delta d = \frac{d}{50}$ in order to maintain more than 20% compared to the power output of a perfect system. We also find with our matrix formalism that the required precision increases with the number of layers. The thickness of the layers in the transparent case (optimized for relatively large axion masses) is

$$d = \frac{\pi}{\omega}(h - 2j - 1) = 0.6\,\mu\text{m}\left(\frac{1\,\text{eV}}{\omega}\right)\left(\frac{h-2j-1}{1}\right) \tag{3.96}$$

where h and j are integers such that $d > 0$.

In figure 3.17 we compare the sensitivity of the ordinary LSW setup with LSW dielectric setup in the transparent case. We use typical values for the ALPS II experiment, i.e. $\ell = 100\,\text{m}, B^e = 1\,\text{T}, P_L = 3\,\text{W}, \omega = 1\,\text{eV}$. The two setups are labeled ALPS II and ALPS dielectric in figure 3.17. We have incorporated a sensitivity loss 80% for the ALPS dielectric sensitivity in order to account for imprecise dielectric layers. The 80% are motivated by the $\delta d = d/50$ configuration, cf. figure 3.14.

Note that it is practically not possible to scan the whole ALPS dielectric mass range in figure 3.17. If a sufficiently good vacuum is present the mass range where large maximal boost factors can be achieved is set by the distance of the layers. Therefore to scan different mass ranges different numbers of layers have to be inserted into the magnetized regions. In detail one finds that in order to be sensitive to masses around m_a one needs

$$N_{\text{layer}} = 8 \times 10^3 \left(\frac{\ell}{100\,\text{m}}\right)\left(\frac{m_a}{10^{-2}\,\text{eV}}\right)^2\left(\frac{1\,\text{eV}}{\omega}\right) \tag{3.97}$$

layers. Therefore the sensitivity estimate has to be seen as the sensitivity that could be reached for specific masses if the appropriate number of dielectric layers would be inserted. This can be useful to reach hints from astrophysics or other experiments which would not be reachable without dielectric layers.

The chosen mass range for ALPS dielectric reaches from the mass, where $\ell_d = \ell$, i.e. one dielectric layer has to be inserted, to $m_a = 0.1\,\text{eV}$, where 8×10^5 layers would be needed. We do not show a higher sensitivity for larger masses, since there even more layers with an higher precision would be necessary.

In contrast to Ref. [81] we show the sensitivity estimate for the ALPS II. In the high mass region the sensitivity is close to the QCD band in yellow.

Finally let us also discuss the LSW dielectric sensitivity if the layers are configured in a resonant configuration. For the factor f in the sensitivity estimate, cf. equation (3.93) we obtain:

$$\text{large mass region: } \varsigma = \frac{2\pi}{\tilde{\beta}}, \qquad \text{small mass region: } \varsigma = \frac{\pi}{\tilde{\beta}} \tag{3.98}$$

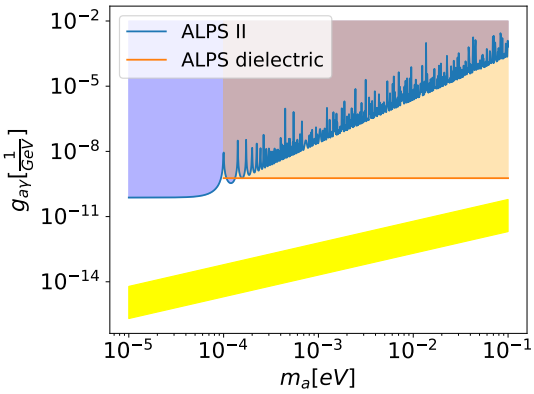

Figure 3.17: Sensitivity for ALPS II and ALPS dielectric in the transparent case. In ALPS dielectric the magnetized regions before and after the wall contain dielectric layers. For each mass m_a a different number of dielectric layers has to be inserted. Therefore practically ALPS dielectric would be only capable to search for axions with a specific mass. This is because scanning over the full mass range, that is indicated in the figure, is practically impossible, since then the number of layers has to be changed constantly what is not practically inconvenient when a lot of layers are involved. The number of dielectric layers increases with increasing mass. However, if another experiment finds an axion signal in the mass range $10^{-3} - 10^{-1}$ eV inserting the exact number of layers, such that ALPS dielectic is sensitive at the exact axion mass, the sensitivity that is indicated in the figure can be achieved for a small mass range. ALPS dielectric has only an advantace over ALPS II in the large mass region, since in the small mass region ALPS II has already a maximal coherent conversion. The QCD band in yellow corresponds to the values $\frac{E}{N} = 3 - 0.1$.

where we have used that $\delta = \frac{g_{a\gamma} B^e \ell_d}{2}$ what is always true for the first maximum that appears in the case, when only relatively large masses have large β, cf. figure 3.15 or figure 3.13 (left) and for all small frequencies in the case that small masses have a large β, cf. figure 3.13 (right).

The result in equation (3.98) demonstrates the difference between using a cavity around the magnetized region, cf. equation (3.95) and (3.95) and arranging the dielectric layers directly in a resonant manner. In both cases highly resonant systems have to be build. If the magnetized regions are surrounded by a cavity the power build up factor of the cavity β_c should be large. If the dielectric system in the magnetized region is used it should have a large boost factor $\tilde{\beta}$. While the possibility of a cavity that surrounds the magnetized region was already mentioned in [82, 83] the possibility of building a resonant system inside the magnetized region in the context of LSW experiments is new. To compete with the idea of a cavity that surrounds the magnetized region, boost factors $\tilde{\beta}$ which are on the order of β_c or higher have to be reached. The ALPS II experiment has $\beta_c \approx 70$ for the generation side and $\beta_c \approx 200$ for the regeneration side [11]. Further studies have to investigate if the described resonant configuration practically increase the sensitivity of LSW experiments. Its realizability strongly depends on the precision with which the layers can be manufactured. If it is technologically possible to to beat for example the rather low β_c of ALPS II for the generation side, higher sensitivities in figure 3.17 can be reached.

An advantage of a very resonant LSW dielectric setup would be that one has access to specific masses as has been demonstrated in figure 3.15. Different axion masses can be reached by changing the vacuum refractive index and the distance of the dielectric layers, which enables one to confirm or exclude possible future detection claims / hints. In an ordinary LSW experiment this would not be possible, since one is always sensitive to a huge axion mass range.

3.6 Summary

Axions and photons can mix with each other in magnetized media. As a consequence axions, which propagate in a magnetized medium, can produce photons and vice versa. In this chapter we solved the axion-Maxwell equations to all orders in the axion-photon coupling in a medium with arbitrary permittivity, permeability, and conductivity. The discussed solutions of the axion-Maxwell equations are classified into weak and strong mixing regions.

Taking the solutions in a single medium as a basis we introduced a matrix formalism to describe the axion-photon mixing in media which are made out of different materials and external B-field configurations. The matrix formalism matches the solutions of the axion-Maxwell equations in the different materials by applying appropriate interface conditions for the involved fields. Contrary to previous studies in the Refs. [58, 59] the presented matrix formalism is valid for arbitrary, not just for small, velocities.

To validate the matrix formalism in the weak mixing region we have reproduced well known conversion formulas for photons and axions that propagate in magnetized media. Regions of not already excluded axion-photon couplings can only be strongly mixed in situations of an extremely high vacuum. Although it is challenging to achieve these high vacua experimentally we have shown that the matrix formalism predicts an enhanced axion-photon conversion in the strong mixing region. However, these results have to be confirmed by further studies, since in parts of the strong mixing region energy flux non-conservation scenarios can occur. In all other studies of the chapter we focused therefore only on the weak mixing region.

In the second part of this chapter we studied how dielectric layers can influence the axion-photon conversion in the case of ultra relativistic axions. We interpreted the results in form of waves that are emitted from the interfaces in order to fulfill the interface conditions. The matrix formalism was then applied to LSW experiments with dielectric layers in the magnetized regions. We identified two different layer configurations. The layers can be arranged in a transparent or in a resonant configuration.

In the *transparent* case all layers are transparent to electromagnetic radiation, such that the emitted radiation from all layers is coherently added. The sensitivity of LSW experiments in the transparent case cannot be increased for low masses. However, for relatively large masses the dielectric layers can increase the sensitivity compared to ordinary LSW experiments. While this was already pointed out in Ref. [81] here we rederived this statement with the matrix formalism. Additionally we demonstrated that the matrix formalism can be used to compute the precision with which the layers have to be manufactured. Furthermore we considered many more layers in comparison to Ref. [81]. The mass range where LSW experiment with dielectric layers is sensitive to can be tuned by the distance of the layers. This feature is in contrast to ordinary LSW experiments which are always sensitive to large axion mass interval and loose sensitivity for relatively large axion masses. Therefore, the dielectric layers can be used to confirm or exclude specific relatively large axion masses which cannot be probed with ordinary LSW experiments. To be more precise we focused on the ALPS II experiment with dielectric layers in the (re)generation regions. We called this setup ALPS dielectric. The ALPS dielectric sensitivity was shown in figure 3.17. Dielectric layers give an advantageous sensitivity for axion masses that are larger than $10^{-4}\,\mathrm{eV}$. To probe different axion masses with the ALPS dielectric setup a different number of dielectric layers is necessary. The layer surfaces have to be manufactured with high precision on the order of 10 nm, which is technologically challenging but not impossible. A sensitivity loss due to imprecisely manufactured layers was already incorporated in the ALPS dielectric sensitivity estimate.

The dielectric layers can also be configured as a *resonant* system, giving rise to a large power amplification. The axion mass region where a large power amplification can be achieved can be set with the distances of the layers and the refractive index of the gas between the layers. We found

that these resonant layer configurations could in principle be used as an alternative to the existing cavities, which surround the (re)generation regions, in ordinary LSW experiments. Nevertheless, in both cases very resonant systems have to be build with high precision. Therefore our findings can be seen as a possible alternative to the existing power boost from cavities that surround the (re)generation regions in ordinary LSW experiments. Future studies have to investigate from a technological point of view if the dielectric layers can achieve a larger power boosts than the cavities.

Chapter 4

Three dimensional effects in open axion haloscopes

In recent years many ideas, how to directly detect dark matter axions on Earth, have been proposed. For an overview see the review in Ref. [84]. This chapter focuses on two possibilities to detect axion dark matter via the axion-photon coupling, namely with *dish antennas* and *dielectric haloscopes*. Dish antennas and dielectric haloscopes belong to the class of open *open axion haloscopes*, which are – in contrast to axion cavity experiments – open systems. A dish antenna is a magnetized perfect electric conductor (PEC) in a dark matter axion background. It was first worked out in Ref. [85] that in the axion background electromagnetic radiation is emitted from the dish antenna. A dish antenna can reach high sensitivities in the axion-photon coupling for very large dish antenna surfaces or large external B-field strengths. The generalization of a dish antenna to a system of many magnetized material interfaces, which all emit electromagnetic radiation in an axion dark matter background, is called dielectric haloscope and was proposed as an open system in Ref. [58, 86]. A dielectric haloscope is made of a single PEC and additional dielectric disks. Since electromagnetic radiation is emitted from all magnetized interfaces/surfaces, effectively large conversion surfaces can be achieved, what gives rise to a high sensitivity reach. Dielectric haloscopes can be tuned to be sensitive to specific axion masses intervals by varying the distances of the dielectric disks.

The one-dimensional description of a dish antenna and dielectric haloscopes is reviewed in section 4.1. In the following we then focus on three dimensional effects which can arise in open axion haloscopes. In section 4.3 two methods which are useful to carry out three dimensional calculation in axion electrodynamics are introduced. These techniques are then applied to a free space permeated by an external B-field (section 4.4), a dish antenna (section 4.5), a single dielectric disk (section 4.6), a minimal dielectric haloscope (section 4.7) and more realistic dielectric haloscopes with many dielectric disks (section 4.8). The studied dish antenna cases in section 4.5 are motivated by the planned BRASS experiment [87] and the studied dielectric haloscope cases in section 4.8 are motivated by the planned MADMAX [58, 86] experiment. The two open axion haloscopes, that are investigated in this chapter, operate between the axion masses of $10\,\mu$eV and 10 meV [58, 87]. This corresponds to a frequency range of 2.4 GHz-2.4 THz. As a benchmark scenario an axion mass of 40 µeV which corresponds to a frequency of 10 GHz is used.

Note that in this chapter we refer to material layers as disks, where in the previous chapter we just talked about layers. This change in terminology is due to the fact that here the considered material disks are relatively thick. The corresponding wavelength interval in this chapter ranges from 12.5 cm to 125 µm and therefore the considered disks will have thicknesses of this order. However, conceptually there is no difference between the terminology of layers and disks.

Copyright information for this chapter: The following sections 4.2-4.7 are based on the publications [1, 3] and the proceeding [4]. This chapter therefore describes the main contributions to [1, 3, 4] by the author of this thesis. Non-original results, in particular those that have been obtained by others, are properly cited in the following. Note that in the PhD thesis [88] large parts of the text, which was written in close collaboration together by myself and Stefan Knirck, in the publication [1] are overtaken. The results in Ref. [1] that are produced by myself and also appear in [88] have a reference to my thesis. In the sections 4.2,4.3,4.4 and 4.5 of this chapter there are small text overlaps to the publication [1]. However, this overlapping text was contributed by myself to the publication [1] and does not appear in [88].

4.1 Review on one dimensional axion electrodynamics for dish antennas and dielectric haloscopes

In this section the working principle of dish antennas and dielectric haloscopes are reviewed within a *one dimensional model*. A homogeneous, constant and linear polarized external B-field B^e is assumed to be present in all media in this chapter. Furthermore only dielectric materials ($\mu = 1$) with refractive index n are considered. Axion haloscopes attempt to detect axions from the dark matter halo which have typically a velocity that is small compared to the speed of light. Therefore in this short review a zero axion velocity is assumed. For a discussion of small axion dark matter velocities in a one dimensional model we refer to Ref. [59]. The axion zero velocity limit implies $m_a = \omega$. In the previous chapter 3 it was shown that axions and photons in this limit are weakly mixed if the coupling is smaller than:

$$g_{a\gamma} < \frac{m_a}{2B^e} = 2.6 \times 10^{-6} \frac{1}{\text{GeV}} \left(\frac{m_a}{10^{-12}\,\text{eV}}\right) \left(\frac{10\,\text{T}}{B^e}\right), \tag{4.1}$$

where $n = 1$ was used, what is well justified to describe a medium with refractive index close to one in the zero velocity limit, cf. equation (3.14). For media with $n > 1$ the limit in equation (4.1) gets order one corrections, cf. equation (3.14).

The limit in equation (4.1) is always fulfilled in the case of axion haloscopes because they search for axions in the mass range 10^{-12} eV-1 eV and the current existing constraints for $g_{a\gamma}$ are at much smaller couplings [56]. Therefore throughout this chapter it is always assumed that axions and photons are weakly mixed. Since all calculations are done in the weak mixing regime all results are given up to first order in $\tilde{x}$ without writing an extra $\mathcal{O}(\tilde{x}^2)$.

One can now use the matrix formalism from the previous chapter 3 in the weak mixing regime together with the zero velocity limit to calculate the power output of dish antennas and dielectric haloscopes in a one dimensional model. However, this is not necessary, since these calculations have already been done in Ref. [58] which starts directly with a matrix formalism in the weak mixing regime in the zero velocity limit.[1] Therefore in the rest of this section the results from Ref. [58] are reviewed but the notation of the previous chapter is kept.

To linear order in the axion photon coupling two modes exist:

$$k_p = n\omega, \tag{4.2}$$

$$k_a = 0. \tag{4.3}$$

The k_p mode is the photon mode and the k_a mode the long wavelength axion mode. Since the zero velocity limit is considered the dark matter axions are described by $\hat{a}e^{-im_a t}$ in the weak mixing

[1] It was shown in appendix A.2 that the matrix formalism of the previous chapter 3 reduces in the weak mixing and zero velocity limit to the matrix formalism of Ref. [58]. Therefore reviewing the results of Ref. [58] here is in agreement with the matrix formalism of the previous chapter.

regime. In the language of the previous chapter this means that all $\hat{a}_i^{-+}$ are equal up to $\mathcal{O}(\tilde{x}^2)$ and a phase. This was explicitly shown in the previous chapter. The common magnitude here is named $\hat{a}$ and can be inferred from the dark matter density. All reflected axions $\hat{a}_i^{--}$ are zero up to $\mathcal{O}(\tilde{x}^2)$ terms.

The discussed settings in the following are a homogeneous medium with an external B-field, a single magnetized dielectric interface, a magnetized dish antenna/dielectric disk and a dielectric haloscope. The goal of this section is to clarify the fundamental physical principles behind the mentioned cases. In sections 4.2-4.8 the discussion is generalized to three dimensions.

4.1.1 Homogeneous medium

We consider a homogeneous medium with constant refractive index n. Furthermore, a constant and homogeneous external B-field that is polarized in y-direction is present.

The dark matter axions induce an E-field that is polarized parallel to the external B-field, which is called axion induced E-field in the following:

$$\hat{E}_a = \frac{g_{a\gamma} B^e}{n^2} \hat{a}. \tag{4.4}$$

The definition of the axion induced field coincides with the definition from the previous chapter in equation (3.30) when the zero velocity limit is taken. However, in this chapter the index a is a subscript rather than a superscript.

However, this has no influence on the results in the following. The axion induced E-field propagates with the same wave vector as the axions. Therefore in the zero velocity limit the axion induced E-field does not propagate at all.

The axion induced E-field has an infinite wavelength in the zero velocity limit. If finite velocities are considered the axion de Broglie wavelength is [58]:

$$\lambda_a = \frac{2\pi}{k_-} = 12.4\,\mathrm{m} \left(\frac{100\,\mu\mathrm{eV}}{m_a}\right) \left(\frac{10^{-3}}{v_a}\right), \tag{4.5}$$

where v_a is the axion velocity. The result again given in the weak mixing regime up to leading order. Equation (4.5) clarifies that the axion velocity effects can be neglected if masses are considered that lead to a de Broglie wavelength which is much larger than the experimental setup.

In the zero velocity limit the axion induced E-field oscillates in a medium with a frequency, that is determined by the axion mass. If a dielectric disk or a perfect electric conductor is brought into the axion induced E-field, additional radiation with a photon dispersion is generated. This is discussed explicitly in the following section.

4.1.2 Single interface

Consider now the interface between two media, referred to as 0 and 1 in the following. Medium 0 has refractive index n_0 and medium 1 has n_1. The external B-field B^e has the same field strength in both media. Since the axion induced field $\hat{E}_a$ is discontinuous if $n_1 \neq n_0$ additional propagating electromagnetic fields are needed in order to make the total transverse electric field is continuous over the interface. The propagating fields are also called *photon-like*, since they propagate with a photon dispersion. From equation (3.47) one can read off the amplitudes of the E-fields that propagate in medium 0 and 1 with a photon dispersion relation:

$$\begin{aligned} \hat{E}_0^{+-} &= \frac{n_1}{n_0+n_1}(\hat{E}_{a,1} - \hat{E}_{a,0}), \\ \hat{E}_1^{++} &= \frac{n_0}{n_0+n_1}(\hat{E}_{a,0} - \hat{E}_{a,1}), \end{aligned} \tag{4.6}$$

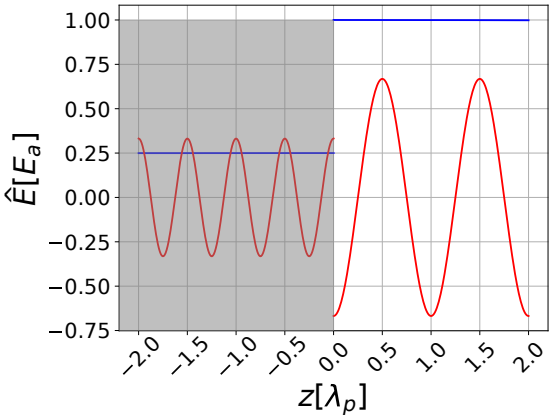

Figure 4.1: Electric fields over a surface between a dielectric (gray medium) which has $n_0 = 2$ and vacuum ($n_1 = 1$). The blue field is the axion induced field which has a huge wavelength. The red fields have a photon dispersion and propagate away from the interface between dielectric and vacuum. Adding all fields at the interface illustrates that the total transversal electric field is continuous over the interface. The length scale on the x-axis is shown in units of the photon-wavelength λ_p in vacuum.

which is in agreement with the results in Ref. [58]. We illustrate the involved electromagnetic fields in figure 4.1 for the situation that $n_0 = 2$ and $n_1 = 1$. The axion induced E-fields are shown in blue. The E-fields which propagate away from the interface with a photon dispersion are shown in red.

In the limit $n_0 \to \infty$ and medium 1 is vacuum ($n_1 = 1$) the emitted fields, that have a photon dispersion, are:

$$\hat{E}_0^{+-} = 0, \tag{4.7}$$
$$\hat{E}_1^{++} = -\hat{E}_{a,1} = -gB^e\hat{a} =: -E_a, \tag{4.8}$$

where the axion induced field in vacuum is defined as:

$$E_a = g_{a\gamma}B^e\hat{a}. \tag{4.9}$$

The limit $n_0 \to \infty$ physically means that medium 0 becomes a perfect electric conductor (PEC)[2]. A magnetized PEC in a dark matter axion background is also called *dish antenna*.

The emitted power from a dish antenna in the presence of dark matter axions is [58]:

$$P = 2.2 \times 10^{-27}\ \text{W} \left(\frac{B^e}{10\,\text{T}}\right)^2 C_{a\gamma}^2 \left(\frac{A}{1\ \text{m}^2}\right), \tag{4.10}$$

where an external B-field of 10 T and a dish antenna surface $A = 1\ \text{m}^2$ is used. Using the Dicke radiometer equation [89] the following signal over noise rate is obtained [58]:

$$\frac{S}{N} = \frac{P}{T_{\text{sys}}}\sqrt{\frac{\Delta t}{\Delta\nu_a}} = 1.0 \times 10^{-4} \left(\frac{A}{1\ \text{m}^2}\right) \left(\frac{100\,\mu\text{eV}}{m_a}\right)^{\frac{1}{2}} \left(\frac{\Delta t}{\text{week}}\right)^{\frac{1}{2}} \left(\frac{8\,\text{K}}{T_{\text{sys}}}\right) \left(\frac{B^e}{10\,\text{T}}\right)^2 C_{a\gamma}^2, \tag{4.11}$$

where Δt is the measurement time, $\Delta\nu_a = 10^{-6}m_a$ the axion linewidth, T_{sys} the system temperature and A the surface of the dish antenna.

For a discovery one typically needs $S/N > 1$. Therefore it becomes clear at this point that in order to directly detect QCD dark matter axions a single dish antenna with $A = 1\ \text{m}^2$ and

[2]More precisely a PEC would correspond to the limit $\sigma_0 \to \infty$. However, in our case, the limits $n_0 \to \infty$ and $\sigma_0 \to \infty$ lead to the same result.

$B^e = 10\,\mathrm{T}$ is not sufficient [90]. A power boost by at least four orders of magnitude is needed in order to reach interesting regions in the QCD axion band. In section 4.1.4 it is worked out how this can be achieved with radiation from multiple interfaces.

4.1.3 Dielectric disk

In this section two interfaces are considered. Medium 0 and 2 are vacuum and medium 1 is a dielectric with refractive index n. To describe the electromagnetic fields that propagate away from the disk a *boost amplitude* is introduced [58]. The E-fields that propagate with a photon dispersion are measured in units of the axion induced E-field in vacuum:

$$\mathcal{B} = \frac{\hat{E}_2^{++}}{E_a}. \tag{4.12}$$

In the axion zero velocity limit the boost amplitude to both sides of the disk is equal in magnitude and therefore defined in equation (4.12) only the boost amplitude for the fields that propagate in the positive z direction is defined. The *boost factor* is defined as:

$$\beta = |\mathcal{B}|, \tag{4.13}$$

and

$$\beta^2 \tag{4.14}$$

is called the *power boost factor* in the following.

For a single dielectric disk it is found [58]:

$$\mathcal{B} = \frac{(n^2-1)\sin(\Delta/2)}{n^2\sin(\Delta/2) + in\cos(\Delta/2)}, \tag{4.15}$$

with $\Delta := \Delta_p = n\omega d$, where d is the thickness of the dielectric disk. It will turn out to be physically enlightening to also consider the reflection and transmission coefficients of a dielectric disk [58]:

$$T = \frac{2in}{2in\cos(\Delta) + (n^2+1)\sin(\Delta)}, \tag{4.16}$$

$$R = \frac{(n^2-1)\sin(\Delta)}{2in\cos(\Delta) + (n^2+1)\sin(\Delta)}. \tag{4.17}$$

The boost factor (dashed line) together with the reflection (dotted line) and transmission (solid line) coefficients are shown in figure 4.2. At maximal boost factor $\Delta = \pi$ the reflection coefficient is zero while the transmission coefficient is maximal. Physically this behavior can be understood in the picture that each surface emits radiation in the presence of an axion induced E-field, cf. figure 4.1. The coherent superposition of the emitted waves from two interfaces leads to the boost factor curve that is shown in figure 4.2.

In the case that $\Delta = \pi, 2\pi, \cdots$ it is referred to the *transparent case*. The case $\Delta = \frac{1}{2}\pi, \frac{3}{2}\pi, \cdots$ is called *reflective case*. For reasons that will become obvious in section 4.1.4 the reflective case is also called *resonant case* and the transparent case *coherent case*.

4.1.4 Dielectric haloscope

A dielectric haloscope is in general a multilayer system in an axion dark matter background. The interfaces are magnetized due to an externally applied B-field B^e. In contrast to conventional resonant axion cavity searches, dielectric halosopes can also be tuned to be more broadband [90]. To describe the power output of the emitted electromagnetic radiation the generalization of the boost amplitude, that appeared already for a single dielectric disk, is defined in the following [58].

Figure 4.2: Transmission coefficient $|T|$ (solid line), reflection coefficient $|R|$ (dotted line) and boost factor β (dashed) for a single dielectric disk. Three different refractive indices $n = 2, 3, 4$ are shown with respect to the photon phase depth $\Delta = n\omega d$, where d is the thickness of the dielectric disk. The figure is taken from Ref. [58].

In the dielectric haloscopes that are considered here medium 0 will always be a PEC such that it only makes sense to consider the boost amplitude to the right of the multilayer system:

$$\mathcal{B} = \frac{\hat{E}_m^{++}}{E_a}. \tag{4.18}$$

The boost factor is defined in analogy to the previous section as $\beta = |\mathcal{B}|$.

A *minimal dielectric haloscope* consists of a dielectric disk and a PEC. In figure 4.3 (left) the minimal haloscope setup is shown. The distance between disk and PEC is called d_v while the thickness of the disk is d_ϵ. An exemplary electric field from the one dimensional model is also drawn.

A dielectric disk and dish antenna alone cannot give a power boost factor that is larger than one. However, combined to a minimal dielectric haloscope, boost factors, that are larger than one [58], can be reached. In figure 4.3 (right) the boost factor β from the one dimensional model is shown for different phase depths $\delta_\epsilon = n\omega d_\epsilon$ and $\delta_v = \omega d_v$, where $n = 3$ is the refractive index of the dielectric disk. In the shown parameter space configurations exist with a boost factor much larger than one. The white dashed line tags the points with the largest β for a given δ_ϵ. We have furthermore marked the points with the largest boost amplitude as "resonant" in the plot. At these positions the reflectivity of the dielectric disk is maximal [58]. Therefore the emitted fields are reflected back and forth between the PEC and the disk many times giving rise to a very resonant system with a large boost factor. The point that is marked as "transparent" corresponds to maximal transmissivity of the dieletric disk. In this case the emitted waves of the disks are added coherently also giving rise to a boost amplitude that is larger than one. Therefore one could also call the point that is marked as "transparent" coherent. However we stick to the convention that was used in Ref. [58] and call the case of coherent superposition "transparent" in the following discussion. The resonant peak of the power boost amplitude β^2 of the minimal dielectric haloscope scales as n^2, while the width scales as $1/n^2$ [58].

In section 4.1.2 it was pointed out that a power boost factor at the order of $\beta^2 = 10^4$ is needed to reach axion models in the QCD band. It is therefore intriguing to consider even more

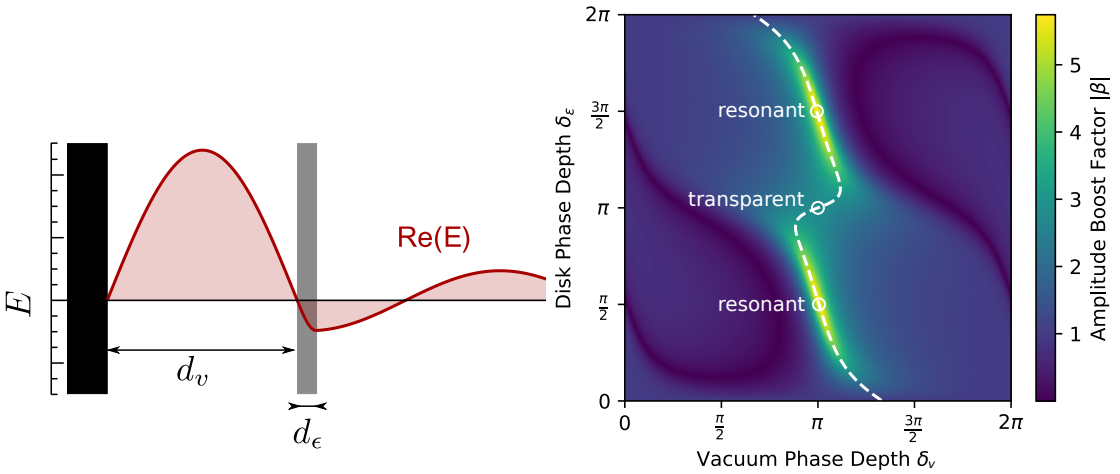

Figure 4.3: Left: The minimal dielectric haloscope consisting of a PEC (black) and a dielectric disk (gray). The figure is taken from [58]. d_v is the distance between PEC and disk and d_ϵ is the thickness of the dielectric disk. The electric field from the one dimensional model is also shown exemplary. Right: Boost factor β from the one dimensional model in the δ_ϵ-δ_v plane. The figure is taken from Ref. [58]. $\delta_\epsilon = n\omega d_\epsilon$ is the phase depth of the dielectric disk, while $\delta_v = \omega d_v$ the phase depth of the vacuum gap between disk and PEC. The refractive index was chosen to be $n = 3$. The white dashed line depicts for each δ_ϵ the optimal δ_v that maximizes the boost amplitude. The white dashed line was maximized in Ref. [88] while the figures are adapted from Ref. [58].

dielectric disks on top of the minimal dielectric haloscope and to investigate further boost factor enhancements.

In analogy to the minimal dielectric haloscope a haloscope with more than one dielectric disk can operate in a more transparent or resonant mode. This is possible since a dielectric haloscope with N dielectric disks has in principle many unknown parameters, since the disks thicknesses and disk distances can all be different. In a transparent setup the vacuum gap between the disks is $\delta_v = \pi$ and all disks have the same phase depth $\delta_\epsilon = \pi$. In a resonant setup the phase depths are $\delta_\epsilon = \frac{\pi}{2}$ and $\delta_v = \pi$. Increasing the refractive index of the disks is advantageous, since in this case the emitted amplitude from each interface increases, cf. equation (4.6). The authors of Ref. [58] identify two candidate materials with low dielectric losses and large permittivity: Sapphire with $n = 3$ and $LaAlO_3$ with $n = 5$.

Realistic haloscopes operate between the transparent and resonant mode. One reason for that is that a very resonant operation would not be possible from a practical point of view, since the disk thicknesses would have to be adjusted during scanning. This is practically not possible, since only a few sets of disks with fixed thickness will be available. More than one set of disks is definitively required, since at specific frequencies a single disk has zero β, cf. figure 4.2. In the following from here it is assumed that all disks in the dielectric haloscope have the same disk thickness.

It was shown first in Ref. [58] that the distances between the disks can be used to optimize the boost factor with respect to its bandwidth, maximal value and central frequency. This is possible for a large range of frequencies even with fixed disk thicknesses. This is because there is still enough freedom by adjusting the distances of the disks in order to shape the boost factor as desired. In figure 4.4 a setup with 20 dielectric disks is shown. Each disk has a thickness of 1 mm and $n = 5$. While most of the disk distances are around $\lambda_p/2$, it is possible to fine tune the system such that one configuration has a maximal $\beta \approx 140$ and a bandwidth of 50 MHz, while another configuration has a much larger bandwidth of 200 MHz but a smaller maximal β.

The power boost factor β^2 is a periodic function of frequency. It was shown rigorously in

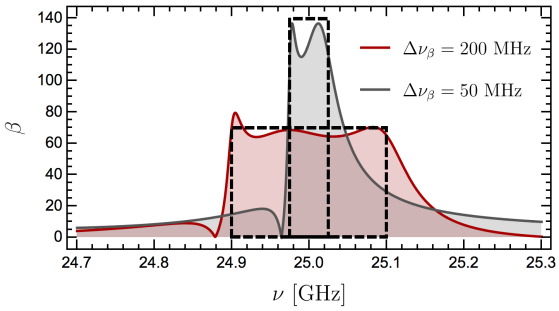

Figure 4.4: Boost factor curves for two different disk configurations. In both configurations 20 dielectric disks with a thickness of 1 mm and $n = 5$ are used. It is explicitly shown here that different configurations with different bandwidths and maximal values for β can be obtained by changing the distance between the 20 disks. The figure is taken from Ref. [58].

Ref. [58] that the area below β^2 is constant over one frequency period. This finding is called *area law*. In practice the disks in a dielectric halosopes are configured such that a large power boost is achieved over one frequency interval $\Delta\nu$, that is smaller than one period of the boost factor. This means that most of the area below β^2 is included in this smaller interval, $\Delta\nu$. Then the area law implies that changing $\Delta\nu$ to a larger or smaller value (by changing the disk distances) conserves the area below the main power boost factor peak, i.e. $\beta^2\Delta\nu$ is constant for the different configurations. The area law is sketched in figure 4.4. The $\Delta\nu = 200\,\text{MHz}$ configuration $\beta = 70$, i.e. $\beta^2\Delta\nu = 98 \times 10^4\,\text{Hz}$, is reached. However, the more resonant configuration with $\Delta\nu = 50\,\text{MHz}$ reaches $\beta = 140$, and therefore the same $\beta^2\Delta\nu = 98 \times 10^4\,\text{Hz}$ is obtained.

In an axion search experiment scanning large frequency intervals is required. The area law together with the Dicke radiometer equation [89] implies that it is advantageous to scan with frequency intervals that are as small as possible. However in reality this statement does not hold anymore because very narrow bandwidths might easily be distorted by mispositioning of the many disks in the haloscope. However as it was outlined before more broadband boost factors, which are more stable against disk mispositionings, can also be achieved.

Another finding from the area law is that the area under the power boost factor curve scales linearly with the number of dielectric disks [58]. This gives the possibility to estimate the number of disks that are needed to achieve the sensitivity necessary for the QCD axion according to the theoretical models. In Ref. [58] a full scale experiment with 80 disks is suggested which also serves as a benchmark case in this chapter. However cases with a smaller amount of disks (20), which are motivated by the planed MADMAX prototype booster,are also investigated.

Finally, it should be mentioned that dielectric haloscopes are limited to lower axion masses already from one dimensional considerations. The length of the booster becomes larger the smaller the axion masses, that shall be probed, since the distance of the disks is around $\lambda_p/2$. Therefore to probe very small axion masses external longer external B-fields are needed. For example in an 80 disk setup an external B-field of $\frac{\lambda_p}{2} \times 80 = 1.2\,\text{m}$ is needed to probe axions with a mass of 40 µeV. Therefore probing axion masses of 4 µeV would require an external B-field of 12 m, what is very challenging to achieve. A high mass limitation is given by the requirement that the disk diameter should be larger than the axion de Broglie wavelength. For $m_a = 400\,\mu\text{eV}$ a de Broglie wavelength of 3 m is obtained. The authors of Ref. [58] suggest a mass range between 40 µeV and 400 µeV from dielectric haloscopes based on one dimensional calculations.

In the following sections we show how one can compute three dimensional effects in open axion haloscopes (dish antennas and dielectric haloscopes). We will show that not only the length of the external B-field is a limiting factor for dielectric halosopes, but also diffraction effects which become large for small axion masses.

4.2 Axion-Maxwell equations

The three dimensional macroscopic axion-Maxwell equations [62] are already written down in chapter 3, cf. equations (3.1)-(3.5). They are a coupled system of partial differential equations (PDEs) which can be solved by existing numerical algorithms. However, it is computationally very expensive to solve this highly coupled system of PDEs. In this chapter we are interested in low velocity axions from the dark matter halo. In this case the axions and photons are weakly mixed. To obtain uncoupled equations, we extend the perturbation approach [91] to all fields, i.e. we expand all fields in $\tilde{x}$, which is the fundamental expansion parameter in the weak mixing regime:

$$X(\boldsymbol{x},t) = \sum_{i=0}^{\infty} \tilde{x}^i X^{(i)}(\boldsymbol{x},t), \tag{4.19}$$

with $X^{(i)} = \boldsymbol{E}^{(i)}, \boldsymbol{D}^{(i)}, \boldsymbol{B}^{(i)}, \boldsymbol{H}^{(i)}, \boldsymbol{J}_f^{(i)}, \rho_f^{(i)}$, and $a^{(i)}$. The equations corresponding to zeroth order in $\tilde{x}$ are the well known classical Maxwell equations plus a free Klein-Gordon equation for the axion field. The free current density and charge density appearing in the zeroth order case can be chosen such that one generates the desired zeroth order $\boldsymbol{E}^{(0)}$ and $\boldsymbol{B}^{(0)}$ fields.

Since $\tilde{x}$ is a small parameter it is sufficient to consider only the first order axion-Maxwell equations in $\tilde{x}$:

$$\nabla \cdot \boldsymbol{D}^{(1)} = \rho_f^{(1)} + \rho_a^{(1)}, \tag{4.20}$$

$$\nabla \times \boldsymbol{H}^{(1)} - \partial_t \boldsymbol{D}^{(1)} = \boldsymbol{J}_f^{(1)} + \boldsymbol{J}_a^{(1)}, \tag{4.21}$$

$$\nabla \cdot \boldsymbol{B}^{(1)} = 0, \tag{4.22}$$

$$\nabla \times \boldsymbol{E}^{(1)} + \partial_t \boldsymbol{B}^{(1)} = 0, \tag{4.23}$$

$$(\Box + m_a^2) a^{(1)} = \frac{g}{\tilde{x}} \boldsymbol{E}^{(0)} \cdot \boldsymbol{B}^{(0)}, \tag{4.24}$$

with

$$\rho_a^{(1)} = -\frac{g_{a\gamma}}{\tilde{x}} \boldsymbol{B}^{(0)} \cdot \nabla a^{(0)}, \tag{4.25}$$

$$\boldsymbol{J}_a^{(1)} = \frac{g_{a\gamma}}{\tilde{x}} (\boldsymbol{B}^{(0)} \partial_t a^{(0)} - \boldsymbol{E}^{(0)} \times \nabla a^{(0)}). \tag{4.26}$$

The perturbative approach leads to a decoupling of the first order Klein-Gordon equation from the other first order equations. It also guarantees that the free charge continuity equation $\nabla \cdot \boldsymbol{J}_f^{(1)} + \partial_t \rho_f^{(1)} = 0$ and axion continuity equation $\nabla \cdot \boldsymbol{J}_a^{(1)} + \partial_t \rho_a^{(1)} = 0$ hold. Of course this statement is correct for all orders. Physically this means that the zeroth order fields induce first order fields, e.g. by inducing first order charge and current densities. The first order charge and current density source the first order E and B-fields, which then induce second order fields and so on. Furthermore it becomes clear that axions are sourced only at first order if $\boldsymbol{E}^{(0)} \cdot \boldsymbol{B}^{(0)} \neq 0$. The back reaction of photons to sourced axions will always be at higher order, and will thus be negligible.

We consider perfect conductors as inner boundaries of the simulation domain. Objects with finite conductivity σ can be included by setting $\boldsymbol{J}_f^{(1)} = \sigma \boldsymbol{E}^{(1)}$ inside. In this chapter we further assume that linear constitutive relations are fulfilled $\boldsymbol{D} = \epsilon \boldsymbol{E}$, $\boldsymbol{H} = \mu^{-1} \boldsymbol{B}$, where ϵ is the relative electric permittivity and μ the relative magnetic permeability. If the linear constitutive relations are inserted into the equations (4.20)–(4.24) and we combine[3] equation (4.21) with equation (4.23) we obtain a wave equation for $\boldsymbol{E}^{(1)}$:

$$\nabla \times (\mu^{-1} \nabla \times \boldsymbol{E}^{(1)}) + \partial_t^2 \epsilon \boldsymbol{E}^{(1)} + \sigma \partial_t \boldsymbol{E}^{(1)} + \partial_t \boldsymbol{J}_a^{(1)} = 0. \tag{4.27}$$

[3] Equations (4.20) and (4.22) can be treated as initial conditions to be valid at $t = t_0$ if the two continuity equations hold separately. In the case of harmonic time dependence equations (4.20) and (4.22) are trivially fulfilled.

This wave equation is a PDE for $\boldsymbol{E}^{(1)}$ which can be solved with standard numerical methods.

As dark matter must be highly non-relativistic, the axion de Broglie wavelength is much larger than the size of the setups that are considered in the following sections. Therefore, the axion field $a^{(0)}$ can be treated as spatially constant over the size of the experiment. It was pointed out already in the previous section that for small velocities one can model the background axion field as the real part of $a^{(0)}(\boldsymbol{x}, t) = a^{(0)}(t) = \hat{a}e^{-i\omega t}$, with $\omega = m_a$ and a constant $\hat{a}$. Throughout this chapter we always assume that the axion velocity and therefore the gradient of the axion field is negligible. Only in section 4.5 we describe what happens when we also take velocity effects into account. To simulate an axion haloscope a strong and static external B-field $\boldsymbol{B}^{(0)}(\boldsymbol{x})$ and no external E-field[4] $\boldsymbol{E}^{(0)} = 0$ is assumed. The axion induced E-field in three dimensions is defined as:

$$\boldsymbol{E}_a(\boldsymbol{x}) := -g_{a\gamma}\hat{a}\boldsymbol{B}^{(0)}(\boldsymbol{x}), \tag{4.28}$$

equation (4.27) reduces in this case to

$$\nabla \times (\mu^{-1}\nabla \times \boldsymbol{E}) - \omega^2 n^2 \boldsymbol{E} = -m_a^2 \boldsymbol{E}_a, \tag{4.29}$$

with $\omega = m_a$ (from the zeroth order Klein-Gordon equation), the complex refractive index $n^2 = \epsilon\mu(1 + \frac{i\sigma}{\omega\epsilon})$ and the physical first order E-field $\boldsymbol{E} = \tilde{x}\boldsymbol{E}^{(1)}$. Furthermore, $\boldsymbol{E}$ has harmonic time dependence, because of our time harmonic choice of $a^{(0)}$ and the assumption that time and spatial coordinates in $\boldsymbol{E}$ are separable.

The definition of the axion induced field in equation (4.29) is the three dimensional generalization of the axion induced field. In this work we define the external magnetic field as $\boldsymbol{B}^{(0)} = \hat{B}^{(0)}\hat{\boldsymbol{B}}^{(0)}(\boldsymbol{x})$, where $\hat{B}^{(0)}$ is the constant magnitude and $\hat{\boldsymbol{B}}^{(0)}(\boldsymbol{x})$ contains the spatial dependency and is of order one. We use the symbol E_a both for the constant field $E_a = g_{a\gamma}\hat{a}\hat{B}^{(0)}$ as well as for the magnitude $|\boldsymbol{E}_a(\boldsymbol{x})| = E_a = g_{a\gamma}\hat{a}B^{(0)}(\boldsymbol{x})$, since from the context it will be clear what case we mean[5]. In the language of the one dimensional model from section 4.1 $\hat{B}^{(0)}$ is the external B-field that was called B^e.

In this chapter we further assume only pure dielectric materials ($\mu = 1$) without losses ($\sigma = 0$, $n^2 = \epsilon$) or perfect electrical conductors (PEC) as described above.

We would like to stress, that the formalism applied here can also be applied to hidden photons [85], where we would have to expand the the dark E and B-fields instead of the pseudo-scalar axion field. The source term in equation (4.29) would then include the dark E and B-fields. As for the axion field, they can be treated as spatially constant for non-relativistic CDM velocities and sufficiently small masses.

In the following section methods to solve the axion-Maxwell equations in three dimensions for open axion haloscopes are presented. We pursue two different methods – specialized finite element methods and recursive propagation approaches.

4.3 Solution strategies for three dimensional axion-Maxwell equations

In this section two methods to solve the axion-Maxwell equations in three dimensions (3D) are presented. Comparing the two methods enables us to validate them against each other. Moreover, we will cross check them against other well-understood analytical approaches specialized for a free space situation in section 4.4 and for a dish antenna in section 4.5. Both methods, that

[4] More generally $\boldsymbol{E}^{(0)}$ only appears in (4.29) if one assumes that the axions have a velocity.

[5] Note, that the three dimensional definition of the axion induced field in equation (4.28) contains a minus sign. The reason for that will become clear in section 4.4. The definition of E_a does not include a minus sign what is in agreement with the definition of the one dimensional calculation, cf. equation (4.9) with $B^e = \hat{B}^{(0)}$.

are described in the following, are tailored to solve the axion-Maxwell equations for open axion haloscopes in an efficient way.

4.3.1 Specialized finite element method

Equation (4.29) can be solved for realistic three dimensional geometries numerically by the finite element method (FEM). The FEM is a general method for solving partial differential equations (PED) [92]. In the following the finite domain, where the solution with the FEM is computed, is called solution domain or simulation domain. The FEM discretizes the solution domain into a finite mesh. An example mesh can be seen in figure 4.5. The solution of the PDE is then approximated on the discretized grid points. In the following the most important details about a FEM solution are summarized. For a more detailed review see for example Ref. [93].

Since the FEM solves the PDE on a finite solution domain, suitable boundary conditions have to be chosen. In this thesis scattering problems are considered, which would in principle propagate infinitely into free space. Therefore boundary conditions which approximate an infinite large simulation domain have to be chosen. One possibility to simulate an infinite space is to use so called impedance boundary conditions [93]. Another possibility is to use the more sophisticated *perfectly matched layers* (PMLs) [93–95], which absorb to a good approximation radiation that impinges on the boundaries of the solution domain. In this thesis only PML are used since it was found that they absorb the impinging radiation best [96]. All FEM solutions are computed with COMSOL Multiphysics ® [95] wave-optics module. A more detailed description of the implementation in COMSOL given in appendix B.2, where it is described amongst others how to incorporate the axion source term, cf. section B.2.1.

Discretising the solution domain leads to a linear matrix system that has to be solved. The solutions of the linear system then give to a good approximation the solution of the PDE in the discretized solution domain. However, depending on the size of the solution domain the resulting linear matrix system can be very large. Therefore different solvers for the matrix system exist. They can be classified as *direct* and *iterative solvers*. Direct solvers solve the matrix system directly [93] while iterative solvers approximate the solution iteratively. Typically direct solvers are faster than iterative solvers, however they require more Random-Access Memory (RAM) than iterative solvers. In the case of very large simulation domains iterative solvers may have more problems to converge to a stable solution. However, direct solvers are often hard to use for very large simulation domains, since the required RAM can easily exceed many Gigabites. A three dimensional simulation domain is considered to be "large" if its size in each dimension is larger than a few wavelengths. Typically good results are obtained if 5-10 discretization points per wavelength are used. In this thesis only direct solvers are used. When the simulation domain becomes too large, in order to use a direct solver, symmetries are used to reduce the degrees of freedom. This makes it possible to still use a direct solver for relatively large simulation domains and obtain a full three dimensional solution. More concrete, radial symmetries are used to reduce three dimensional problems to two dimensions. This is well justified, since many real experimental setups are to a good approximation radial symmetric.

In the following it is explicitly shown how a three dimensional problem with a radial symmetric geometry can be reduced to a two dimensional problem. An additional complication is that the external B-field, which enters the current density in equation (4.29), is linearly polarized and therefore breaks the radial symmetry. However, it is shown in the following that the problem can still be reduced to two dimensions by decomposing the linear source term in two different circular modes. The used approach is called "2D3D approach" in this chapter.

The linear polarized source of equation (4.29) is decomposed[6] as follows:

$$\boldsymbol{E}_a(r,z) = \boldsymbol{E}_a^+(r,\phi,z) + \boldsymbol{E}_a^-(r,\phi,z), \tag{4.30}$$

where we have assumed that the $\boldsymbol{E}_a = -E_a(r,z)\hat{\boldsymbol{e}}_y$ depends only on r and z and that the external B-field points in y-direction $\boldsymbol{B}^{(0)} \sim \hat{\boldsymbol{e}}_y$. $r = \sqrt{x^2+y^2}$ is the radial coordinate. With $m = \pm 1$ we can write:

$$\boldsymbol{E}_a^m = \tilde{\boldsymbol{E}}_a^m e^{im\phi} = \frac{E_a(r,z)}{2}(-\hat{\boldsymbol{e}}_\phi + im\hat{\boldsymbol{e}}_r)e^{im\phi}. \tag{4.31}$$

Since we are only interested in a constant external B-field over the dielectric haloscope or the dish antenna, it is not important for us that the external magnetic field can only depend on r and z. This ansatz splits the problem into the solution of two independent differential equations, each for one source term $m = \pm 1$, respectively:

$$\nabla \times (\nabla \times \boldsymbol{E}^m) - k_0^2 \epsilon \boldsymbol{E}^m = -k_0^2 \boldsymbol{E}_a^m, \tag{4.32}$$

where $k_0 = \omega$. For the corresponding E-field solution we make the ansatz $\boldsymbol{E}^m = \tilde{\boldsymbol{E}}^m(r,\phi,z)e^{im\phi}$ with

$$\tilde{\boldsymbol{E}}^m = \tilde{E}_r^m(r,z)\hat{\boldsymbol{e}}_r + \tilde{E}_\phi^m(r,z)\hat{\boldsymbol{e}}_\phi + \tilde{E}_z^m(r,z)\hat{\boldsymbol{e}}_z, \tag{4.33}$$

and $e^{im\phi}$ factors out in equation (4.32). Since the ϕ dependence is known, we solve the equation for $\phi = 0$ in the r,z plane. We use COMSOL to compute the unknown functions $\tilde{E}_r^m(r,z), \tilde{E}_\phi^m(r,z)$ and $\tilde{E}_z^m(r,z)$ on the discretized mesh. The total solution is obtained as a superposition:

$$\boldsymbol{E} = \tilde{\boldsymbol{E}}^+ e^{i\phi} + \tilde{\boldsymbol{E}}^- e^{-i\phi}. \tag{4.34}$$

Therefore, we get the complete 3D solution for a geometry that is radial symmetric by solving two ($m = \pm 1$) two dimensional (2D) problems. Using the decomposition of the source term as in equation (4.30) is also done for in simulations of radial symmetric antennas [97]. We can interpret the strategy as if one decomposes the fields into left and right circular polarized components [98]. For the first time we apply this strategy to axion-electrodynamics. The H-field follows as $\boldsymbol{H} = \frac{\nabla \times \boldsymbol{E}}{i\omega\mu}$. The time averaged pointing vector is $\bar{\boldsymbol{S}} = -\frac{1}{2}\mathrm{Re}\boldsymbol{E} \times \boldsymbol{H}^*$. The power in z-direction that passes through a circular surface which sits at z gives:

$$P_z = -\mathrm{Re}\frac{i\pi}{\omega\mu}\sum_{m=\pm 1}\int_0^{R_p} dr\tilde{E}_\phi^m\left(r\partial_z\tilde{E}_\phi^{m*} + im\tilde{E}_z^{m*}\right) + r\tilde{E}_r^m\left(\partial_z\tilde{E}_r^{m*} - \partial_r\tilde{E}_z^{m*}\right), \tag{4.35}$$

where R_p is the radius of the circular surface.

For an external B-field that is linearly polarized in y-direction we find the following relations in the 2D3D approach:

$$\tilde{E}_r^- = -\tilde{E}_r^+, \tag{4.36}$$

$$\tilde{E}_\phi^- = \tilde{E}_\phi^+, \tag{4.37}$$

$$\tilde{E}_z^- = -\tilde{E}_z^+. \tag{4.38}$$

It is shown in appendix B.2.2 that the relations above hold. Note, that the equations (4.36)- (4.38) are only valid, since the external B-field was chosen to be polarized in the y-direction. If we would chose the polarization to be in the x-direction we would have $\tilde{E}_r^- = \tilde{E}_r^+, \tilde{E}_\phi^- = -\tilde{E}_\phi^+$ and $\tilde{E}_z^- = \tilde{E}_z^+$ instead.

In the following the relations (4.36)- (4.38) are always used unless stated otherwise and the approach is named "2D3D". However, to for validation purposes we sometimes do not use the

[6] For more complicated source terms one can also chose a more general decomposition $\sum_{m\in\mathbb{Z}} \tilde{\boldsymbol{E}}_a^m e^{im\phi}$. The steps which we are doing will go through in exact analogy, but one has to do M 2D simulations in the end, where M is the number of $\tilde{\boldsymbol{E}}_a^m$'s which are nonzero.

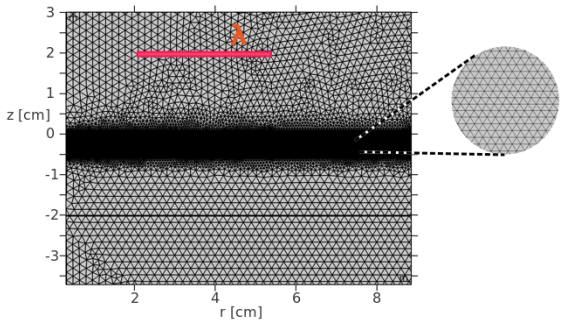

Figure 4.5: Example mesh for a radial symmetric minimal dielectric haloscope. The dielectric disk is 0.5 cm thick and between $z = 0$ and $z = -0.5$ cm. The PEC is at $z = -2$ cm. Inside the disk the mesh is finer, since the photon wavelength is smaller. The mesh is shown here for a typical 2D3D simulation in the rz-plane.

relations (4.36)- (4.38). This case is then referred to as "2D3D(2)" and the case where the relations (4.36)- (4.38) are used is referred to as "2D3D(1)". The (2) means that two 2D solutions for the modes $m = \pm$ are computed and the relations (4.36)- (4.38) are not used. The (1) means that the relations (4.36)- (4.38) are used and we just have to do one 2D calculation. A calculation which is purely three dimensional and does not use the 2D3D approach is called "standard" three dimensional calculation in the following. A comparison of the 2D3D approach against a standard three dimensional simulation can be found in appendixB.2.2.

In the following sections of this chapter we show that the 2D3D approach makes it possible to solve problems which involve geometries that would be very challenging to solve with a standard three dimensional FEM study. For example in section 4.8 we compute the emitted E-fields for a dielectric haloscope with 80 disks and disk radii with $R = 0.5$ m at 1.4 cm wavelength. This correspond approximately to three dimensional domain of $40\lambda_p \times 40\lambda_p \times 40\lambda_p$ only for the booster not taking into account the free space around it. It immediately becomes clear that a computation with a standard three dimensional FEM calculation would be very challenging and the 2D3D approach is inevitable.

4.3.2 Recursive propagation approaches

In section 4.1 the emission of electromagnetic waves at material discontinuities in the presence of an external B-field and galactic axions was reviewed. We find non-propagating solutions and solutions that propagate with a photon dispersion $k^2 := k_p^2 = n^2\omega^2$ (photon-like). Only the propagating modes are resonantly enhanced and are detected later. Following from here we will skip the subscript 'p' in this chapter, since we mostly assume the zero velocity limit where $k_a = 0$.

The model in section 4.1 is one dimensional and real setups will also have three dimensional effects. Here we use the physical picture that was developed in the one dimensional model to generalize to three dimensions. For this we use the amplitudes of the photon-like emission that propagates away from the material discontinuities. The amplitudes are given in equation (4.6).

Consider now a three dimensional multilayer system as in figure 4.6. In figure 4.6 (left) a multilayer system as in the one dimensional case is shown. Each layer can have a different refractive index n_i. However, contrary to the one dimensional model the diameter of the radiating surfaces is not infinite anymore. This becomes clear form figure 4.6 (right) where a circular surface is shown as an example. It should be noted that the circular surface is just an example and arbitrary surfaces can be used. An example of a rectangular surface is discussed in section 4.5.

The idea of the recursive propagation approach is that each finite surface of the multilayer system is discretized as shown in figure 4.6 (right). Each discretization point at each interface is

initialized with the photon-like electromagnetic fields, cf. equation (4.6), that are then propagated away from the interface. The key idea is now to use three dimensional propagation equations which we will discuss later in this section. For now we just assume that these three dimensional propagation equations exist. However, we want to point out already at this stage that the discretization is due to the fact that the three dimensional propagation equations include integrals over the interface surfaces, which can be computed numerically on a grid that is shown in figure 4.6.

In figure 4.6 (left) the propagation through the multilayer system is shown for the photon-like radiation that is coming from the interface at z_2. In the first step (red) the electromagnetic fields from interface z_2 are propagated to the interfaces z_1 and z_3. At both interfaces reflection and transmission coefficients are applied. At an interface between medium i and j the reflection and transmission coefficients are

$$R_{ij} = \frac{n_i - n_j}{n_i + n_j}, \quad T_{ij} = \frac{2n_i}{n_i + n_j}, \tag{4.39}$$

where the radiation is coming from medium i. The reflection and transmission coefficients are from one dimensional plane wave calculation. They can be applied to a three dimensional model if the wave vector of the incoming radiation is approximately perpendicular to the next interface. On can see this explicitly by expanding the Fresnel equations [99] around an incident angel $\frac{\pi}{2}$.

After applying the reflection and transmission coefficients at the interfaces z_1 and z_3 the electromagnetic fields from z_3 are propagated to z_2 and z_4 (blue). The fields from z_1 are propagated to the outside and to z_2 (blue). Reflection and transmission coefficients at z_2 and z_4 are applied again. In the next step (green) the fields are propagated again from z_2 and z_4 to the neighboring interfaces and reflection and transmission coefficients are applied. The procedure is repeated until a good convergence of the fields, that come out of the multilayer system, is found. Convergence is guaranteed, because the multiplication by the reflection and transmission coefficients makes the fields smaller and smaller.

Similar steps, as described for the radiation that is coming from interface z_2 in figure 4.6, have to be done for all other interfaces to arrive at the final result, i.e. the total E-field output of the multilayer system.

Until now it was assumed that the photon-like electromagnetic fields can be propagated through a homogeneous medium in three dimensions. In the following it is described how this can be done by giving explicit propagation equations for electromagnetic fields. The propagation equations can be obtained with classical electrodynamics because we are only interested in the propagation of photon-like electromagnetic radiation.

The simples propagation equation can be obtained by neglecting near field effects, i.e. $\nabla \cdot \boldsymbol{E} = 0$. In this case the electric field fulfills a classical wave equation:

$$-\nabla^2 \boldsymbol{E} - \omega^2 n^2 \boldsymbol{E} = 0. \tag{4.40}$$

Solutions to equation (4.40) are called scalar, since all three components of the electric field decouple. This is a direct consequence of $\nabla \cdot \boldsymbol{E} = 0$.

Solutions of the wave equation (4.40) can describe the diffraction of electromagnetic waves. One particular solution, that is also suited to do far field expansions of the emitted E-fields, was developed by Kirchhoff and Rayleigh [99]. If the E-field components E_i in the xy-plane (S) at $z_s = 0$ is given, then the fields in whole space are [99]:

$$E_i(\boldsymbol{x}) = \frac{k}{2\pi i} \int_S dA' \frac{e^{ikD}}{D} \left(1 + \frac{i}{kD}\right) \frac{\boldsymbol{n}' \cdot \boldsymbol{D}}{D} E_i(x', y'), \tag{4.41}$$

with $\boldsymbol{D} = \boldsymbol{x} - \boldsymbol{x}'$, $\boldsymbol{n}'$ is the normal vector on the surface S at point $\boldsymbol{x}'$ pointing into the diffraction region. For large observer distances near the z-axis we can expand D in $(x - x')/z$ and $(y - y')/z$ in equation (4.41) [100]. With equation (4.41) the E-fields that are specified at $z_s = 0$ can be

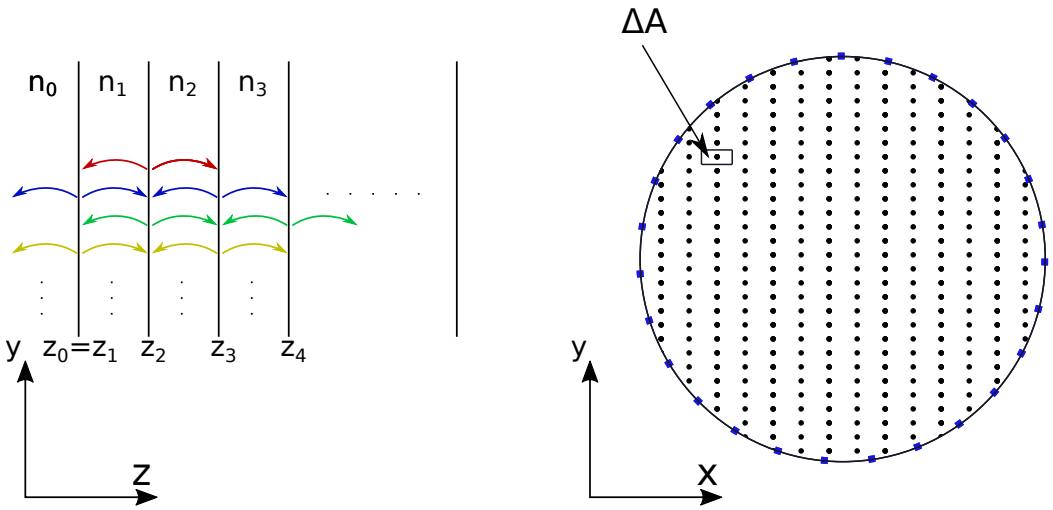

Figure 4.6: Illustration of the recursive propagation approach for a three dimensional multilayer system. In the left figure we show a multilayer system. If all interfaces are magnetized and axion dark matter background exists, all interfaces emit photon-like E-fields. The radiation coming from z_2 is shown exemplary. By applying appropriate reflection and transmission coefficients, the recursive propagation approach uses three dimensional integral equations to propagate the photon-like E-fields through the multilayer system. In the right figure we show a radial symmetric interface. In a dielectric haloscope this could be for example the surface of a dielectric disk. All discretized points are initialized by the photon-like E-fields at each interface accoriding to equation (4.6). A discretization of the interfaces between the different layers with refractive index n_i is needed to evaluate the three dimensional propagation equations.

propagated to other points in space with $z > 0$. If S is not located at $z_s \neq 0$ then the propagated fields can be obtained after a translation from equation (4.41). A similar argument is also valid for all following propagation equations and therefore the surface S can without loss of generality be assumed to be at $z_s = 0$.

In the far field we obtain for the propagated field just a single Fourier transformation of the field on the surface S

$$E_i(\boldsymbol{x}) = \frac{k}{2\pi i}\frac{1}{z}e^{ikz}e^{i\frac{kr^2}{2z}}\int_S dA' e^{-i\frac{k}{z}(xx'+yy')}E_i(x',y'), \tag{4.42}$$

where we have assumed that $\frac{k(x'^2+y'^2)}{2z} < 1$. Equation (4.42) is used for the dish antenna case in order to describe axion velocity effects in section 4.5.

At this point is becomes clear why we have discretized the surface in figure 4.6 in small area elements. The propagation integral in equation (4.42) that has to be performed numerically is performed over the grid with finite area elements ΔA which are shown around the grid points in figure 4.6.

The propagation equation (4.42) is a scalar diffraction theory, because the different E-field components do not couple to each other. Another important scalar theory can be directly derived from equation (4.40) as Fourier decomposition:

$$E_i(\boldsymbol{x}) = \int_{\mathbb{R}^3}\frac{dk^3}{(2\pi)^3}\hat{E}_i(\boldsymbol{k})e^{i\boldsymbol{k}\cdot\boldsymbol{x}}, \tag{4.43}$$

We assume again that the E-field components E_i are specified at an interface at $z_s = 0$. In this case the propagated field is [99, 100]:

$$E_i(\boldsymbol{x}) = \int_{\mathbb{R}^2}\frac{dk_x dk_y}{(2\pi)^2}\mathcal{F}(E_i)(k_x,k_y)e^{izk_z(k_x,k_y)}e^{ik_x x}e^{ik_y y}, \tag{4.44}$$

where $\mathcal{F}$ is the two dimensional Fourier transformation and the propagation in equation (4.44) is to positive z-values. To propagate to negative z-values one has to introduce a minus sign in the exponent. $k_z(k_x, k_y)$ can be expressed as:

$$k_z(k_x, k_y) = \sqrt{(\omega n)^2 - k_x^2 - k_y^2}. \tag{4.45}$$

For a radial symmetric system equation (4.44) reduces to:

$$E'(r, z) = \int_0^\infty dk_r \; k_r \int_0^R dr' \; r' E_0(r') J_0(r' k_r) e^{\pm i\sqrt{\omega^2 - k_r^2} z} J_0(r k_r), \tag{4.46}$$

where $E_0(r)$ is the E-field on the surface at $z_s = 0$. The derivation of equation (4.46) can be found in appendix B.1 together with a further simplification if $E_0 = \text{const}$. Note that in equation (4.46) one momentum space integral and one radial real space integral has to be performed. Therefore in this case it is enough to discretize the radial component of the surface in figure 4.6.

An essential point, which becomes important later on, can already be seen from equation (4.45). The transverse wave number becomes smaller in three dimensions. In one dimension we just have $k_x = 0 = k_y$ and therefore $k_z = n\omega$, i.e. a photon dispersion relation.

If the propagation formula in equation (4.44) is used to calculate the emitted field of a multilayer system with the recursive propagation approach it will be referred to as the *recursive Fourier propagation approach* (RFP). The Fourier propagation equation (4.44) is used in section 4.5 for dish antennas and in section 4.6 for a dielectric disk.

A vectorial propagation equation for the electromagnetic fields, that takes into account near field effects, is the *Kirchhoff diffraction formula* [99]:

$$\boldsymbol{E}_k(\boldsymbol{x}) = \int_S dA' \Big[i\omega(\boldsymbol{n}' \times \boldsymbol{B}) G + (\boldsymbol{n}' \times \boldsymbol{E}) \times \nabla' G + (\boldsymbol{n}' \cdot \boldsymbol{E}) \nabla' G \Big], \tag{4.47}$$

where $\boldsymbol{n}'$ and S are defined as in equation (4.41). The E and B-fields which appear in equation (4.47) depend on the primed variables.

Let us discuss the E_i's for the case of circular PEC, which is magnetized with a homogeneous external B-field. The photon-like E-field can be assumed as constant from each part of the PEC. Therefore the E_i are only nonzero and constant over the PEC: $r = \sqrt{x^2 + y^2} < R$, i.e. $\boldsymbol{E} = E_a \hat{\boldsymbol{e}}_y$ and $\boldsymbol{B} = -E_a \hat{\boldsymbol{e}}_x$. The E_i's are zero for $r = \sqrt{x^2 + y^2} > R$. We discuss the Kirchhoff diffraction theory in section 4.5 for a dish antenna together with more sophisticated propagation equations.

Scalar diffraction theories are good approximations of a full vectorial treatment if the diameter of the radiating object is much larger than the wavelength [99]. For the BRASS dish antenna [87] or the MADMAX haloscope [101, 102] this condition is satisfied. Throughout this chapter we make comparisons between scalar/vector propagation diffraction approaches and FEM solutions, that were introduced in the previous section. As we will see, in all cases that are of interest for us, their results agree very well with each other.

The recursive propagation approach that was presented here can effectively be used in order to study effects such as B-field inhomogeneities, axion velocity effects and other experimental uncertainties in multilayer systems. For example B-field inhomogeneities can be studied by initializing the field values on the discretized surface as a function of the external B-field. Velocity effects can be studied by giving the initial E-fields on the surfaces a different phase. In this thesis we only study axion velocity effects in section 4.5.2 for a dish antenna. The other mentioned effects are studied with the RFP approach by our collaborator [1, 88]. Furthermore in the propagation approach, whose foundations are introduced in this thesis, is evaluated for the simplest geometries, i.e. a dish antenna and a dielectric disk. Systems with more interfaces were studied by our collaborator [88] with the RFP approach.

Finally we want to mention that the introduced recursive propagation approaches always give an approximate solution to the emitted photon E-field in axion electrodynamics. This is because for example radiation from the rims of the finite size disks are not taken into account. Only the FEM solutions computes the full solution to the vectorized Helmholtz equation (4.29). However, we show in the following sections that the recursive propagation approaches can give a satisfactory approximation of the FEM solution in the case of the investigated open axion haloscope setups.

4.4 Free space solution with an external B-field

In this section the E-field solution from the axion-Maxwell equations in the presence of an external B-field in vacuum ($\mu = 1,\ \epsilon = 1,\ \rho_f = 0$, and $\boldsymbol{J}_f = 0$) is discussed. The involved axions are assumed to have zero velocity and are described by a homogeneous oscillatory field $a^{(0)} = \hat{a}e^{-im_a t}$.

The theory of retarded potentials canbe used to obtain a full analytic solution for the axion-Maxwell equations in free space since the zeroth order axion charge and current terms as in equations (4.25) and (4.26) are known through the external fields. Doing the math we obtain the electric field:

$$\boldsymbol{E}(\boldsymbol{x}) \quad = \quad E_a \left[\omega^2 \int d^3x' \hat{\boldsymbol{B}}^{(0)}(\boldsymbol{x}') G - \int d^3x' \ \ \nabla' G \ \nabla' \cdot \hat{\boldsymbol{B}}^{(0)}(\boldsymbol{x}') \right], \tag{4.48}$$

with $E_a = g_{a\gamma}\hat{B}^{(0)}\hat{a}$ the axion induced field. Further, $\boldsymbol{B}^{(0)} = \hat{B}^{(0)}\hat{\boldsymbol{B}}^{(0)}(\boldsymbol{x})$, where $\hat{B}^{(0)}$ is the constant magnitude of the external B-field and $\hat{\boldsymbol{B}}^{(0)}(\boldsymbol{x})$ contains the spatial dependency and is of order one. G is the Green's function of the scalar wave equation $G(\boldsymbol{x}, \boldsymbol{x}') = \frac{e^{i\omega|\boldsymbol{x}-\boldsymbol{x}'|}}{4\pi|\boldsymbol{x}-\boldsymbol{x}'|}$. Note that in the FEM simulations we have to put an external B-field by hand which can be non-physical, i.e. $\nabla \cdot \hat{\boldsymbol{B}}^{(0)} \neq 0$. Such a non-physical B-field with small gradients is not problematic as we will see later. However, it leads to the second term in the analytical solution in equation (4.48). It comes from an artificial charge density $\partial_t \rho^{(1)}_{\text{art}} = -\nabla \cdot \boldsymbol{J}^{(1)}_a$ which guarantees that the continuity equation is also fulfilled. If this term is not included the retarded potential solution is not equivalent to the FEM solution of the vectorized Helmholtz equation (4.29). Equation (4.48) is similar to the equation that was written down in Ref. [103]. However, they did not include the second term in equation (4.48).

Because the external B-field varies only on length scales that are much larger than the photon-wavelength we can write the total E-field as the axion-induced field and a small E-field which can be seen as a radiative correction:

$$\boldsymbol{E}(\boldsymbol{x}) = \boldsymbol{E}_a + \boldsymbol{E}_{\text{rad}}. \tag{4.49}$$

If the external B-field gradients are small on scales of the wavelength, then the radiative corrections are small and the total axion-induced E-field follows the shape of the external B-field $\boldsymbol{B}^{(0)}$ [75]. In the following we demonstrate this for an explicit example.

We choose an external B-field of the form:

$$\hat{\boldsymbol{B}}^{(0)}(\boldsymbol{x}) = \hat{\boldsymbol{e}}_y \sin^2\left(\frac{\pi x}{L_x}\right) \sin^2\left(\frac{\pi y}{L_y}\right) \sin^2\left(\frac{\pi z}{L_z}\right). \tag{4.50}$$

The domain, where the E-field solutions are computed has the size $[0, L_x] \times [0, L_y] \times [0, L_z]$. The chosen external B-field is not physical, i.e. $\nabla \cdot \hat{\boldsymbol{B}}^{(0)} \neq 0$ and falls off towards the boundaries of the solution domain such that no additional radiation is generated at the boundaries of the domain.

In figure 4.7 the computed E-field for the free space situation is shown for $L_x = L_y = 9\lambda$, $L_z = 20\,\text{cm} \approx 6.7\lambda$ with $\lambda = 3\,\text{cm}$. In the chosen case the external B-field drops to zero on scales that are much larger than the photon wavelength $L_x, L_y, L_z \gg \lambda$. It is therefore expected that the solution for the E-field has the shape of the external B-field. This fact becomes directly evident

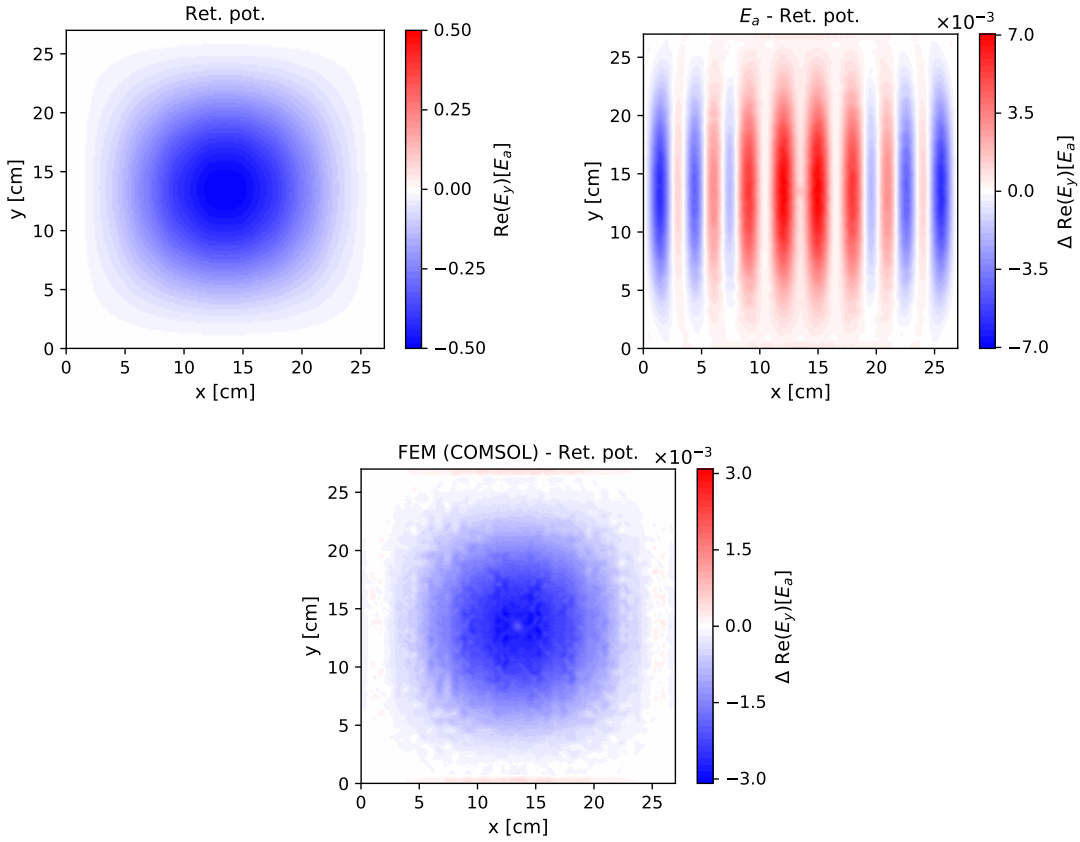

Figure 4.7: Electric field solution of axion electrodynamics in the presence of an external B-field and an axion dark matter background. The external B-field is polarized in y-direction and drops to zero towards the boundaries. The axion mass is $m_a = 40\,\mu\text{eV}$ what corresponds to a photon wavelength of $\lambda = 3\,\text{cm}$. Top left: E-field solution that was obtained with the retarded potential, cf. equation (4.48). Top: right: Difference of the retarded potential solution and the axion induced E-field. The difference is small, since the external B-field changes on scales that are much larger than the photon wavelength. Bottom: Difference of the FEM simulation and the retarded potential solution. Both results agree up to numerical noise.

from equation (4.29) since $\nabla \times \nabla \sim \frac{1}{L^2} \ll \frac{1}{\lambda^2}$, where L is of the order of L_x, L_y, L_z. Therefore to first approximation the double curl in equation (4.29) can be dropped and the solution is given by the axion induced field.

In figure 4.7 (top left) the solution from the retarded potential is shown, while in figure 4.7 (top right) the difference to the axion induced field can be seen. The two figures confirm our previous statement, that in the chosen case the solution is roughly given by the axion induced field $\boldsymbol{E}_a$. The radiative corrections are small, but can in principle be computed with equation (4.48). In figure 4.7 (bottom) the difference of the retarded potential solution and the standard three dimensional FEM solution is shown. The difference is again small and gives a good validation of the FEM, since in our case a full analytical solution is known. In figure 4.7 (bottom) we also confirm that the FEM has enough accuracy to resolve the radiative corrections. The difference between both approaches is just numerical noise. Another important conclusion that can be drawn from 4.7 (bottom) is that the chosen PML at the boundaries absorb the incoming radiation and do not reflect it.

Finally, we want to point out that until now we looked only at the case of a slowly varying external B-field. Our developed methods are also fully capable of computing the emitted fields when the external B-field changes on scales that are smaller than the photon wavelength. In this

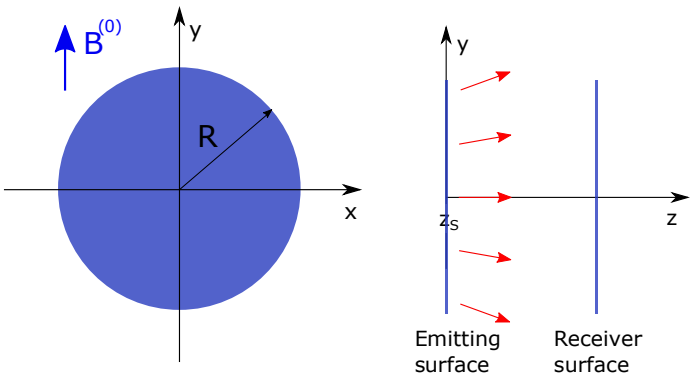

Figure 4.8: Left: Circular perfect electric conductor (PEC) in an external B-field that is polarized in the y-direction. The PEC has radius R and lies in the xy-plane. In the context of axion detection the setup is called dish antenna. The axion induced field $\boldsymbol{E}_a$ induces electromagnetic radiation that propagates away from the dish antenna. This is shown in the right figure. The emitting dish antenna is positioned at $z_s = 0$. An imaginary receiver surface is also shown. The fraction of emitted power that goes through the receiver surface quantifies the diffraction loss of the emitted radiation.

case order one radiative corrections can be found.

4.5 Dish antenna

In this section a finite size dish antenna in an axion dark matter background is studied. A dish antenna [85] is a perfect electric conductor (PEC) that is magnetized. A sketch of a circular dish antenna is shown in figure 4.8 (left). The blue region represents the PEC, while everything around the PEC is vacuum. In this section always a circular dish antenna is studied unless otherwise stated. An external B-field, that is polarized parallel to the PEC surface, is applied. It was pointed out already in the free space section 4.4, that the external B-field induces a static electromagnetic field $\boldsymbol{E}_a$ that oscillates in time, but has negligible small propagating modes if the external B-field is slowly varying. Due to the interface conditions for the electromagnetic fields, the tangential electric field has to vanish at the PEC. Therefore E-fields with a photon dispersion relation (photon-like E-fields) are emitted off the PEC surface. This is depicted by the red arrows in figure 4.8 (right). In total the photon-like E-field and the axion induced field sum up to zero at the PEC interface. In the following the focus lies on the emitted field with the photon dispersion relation, since these fields can propagate away from the dish antenna and are target of detection. Therefore the E-field that is described in the following describes only the photon-like E-field and not the total E-field solution of the wave equation (4.29) which includes also the axion induced field.

4.5.1 Diffraction

Since the dish antenna has a finite size, the emitted electromagnetic radiation experiences diffraction. Diffraction effects can be studied with the Fourier propagation, cf. equation (4.44) if the diameter of the disk is larger than the wavelength [99]. Under the assumption that the external B-field is homogeneous over the whole PEC the magnitude of the emitted photon-like E-field on each point of the PEC is the same. A short calculation (see appendix B.1) starting from equation (4.44) leads to the propagated photon-like E-field in positive z-direction:

$$\frac{E_y(\tilde{r},\tilde{z})}{E_a} = \int_0^\infty d\tilde{k}_r e^{i\sqrt{\tilde{\omega}^2 n^2 - \tilde{k}_r^2}\tilde{z}} J_0(\tilde{r}\tilde{k}_r) J_1(\tilde{k}_r), \tag{4.51}$$

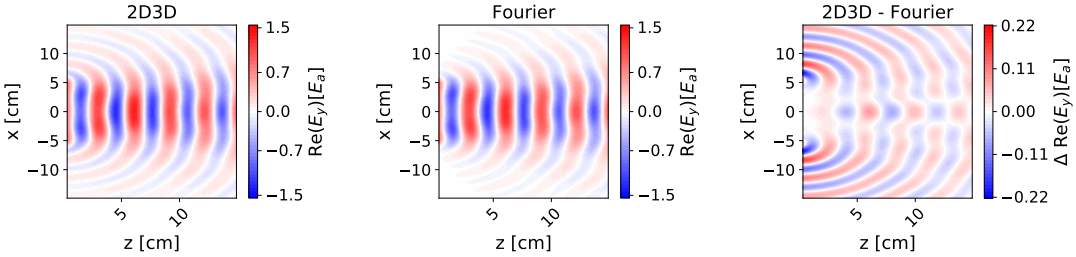

Figure 4.9: Radiation form a dish antenna in an axion dark matter background. The radius of the dish antenna is $R = 6\,\text{cm} = 2\lambda$ and the zx-slices are shown at $y = -2.5\,\text{cm}$. The basis frequency is 10 GHz what corresponds to an axion mass of $m_a = 40\,\mu\text{eV}$ and photon wavelength of $\lambda = 3\,\text{cm}$. In the left plot the result from the 2D3D approach is shown, while in the center plot the Fourier propagation result, cf. equation (4.51), can be seen. The right figure show the difference between the left and center plot. The largest differences are found at the rims of the dish antenna and are due to near field and boundary charges.

with $r = \sqrt{x^2 + y^2}$ the radial coordinate and the normalized variables $\tilde{k}_r = k_r R$, $\tilde{r} = \frac{r}{R}$, $\tilde{z} = \frac{z}{R}$ and $\tilde{\omega} = \omega R$. Here R is the radius of the dish antenna. Note that only the E_y component is nonzero and $E_x = 0 = E_z$ when the Fourier propagation approach is used. The reason for this is that the Fourier approach is a scalar diffraction theory and if only E_y is nonzero at the PEC, then only E_y is nonzero in the whole space. Later in this section the E_x and E_z-components are also investigated.

In figure 4.9 the Fourier propagation for a dish antenna is compared to the FEM solution[7]. Since the dish antenna is radial symmetric the FEM solution uses the 2D3D method. The radius of the dish antenna is $R = 2\lambda = 6\,\text{cm}$ and therefore diffraction effects are quite pronounced. In the right figure the difference between the left and center figure is shown. In the forward z-direction both approaches agree best with each other. The largest differences are observed at the rims of the dish antenna. It will become clear later that the fields at the rims, which are not described by the Fourier approach, are due to near field and boundary effects that are not included in the Fourier propagation. However, it should be noted that even without near field and boundary effects the Fourier approach and the FEM calculation agree within the forward region. Realistic dish antennas and axion haloscopes such as BRASS or MADMAX will have a diameter that is much larger with respect to the wavelength. In this case the near field and boundary effects will play an even smaller role, because in the infinite radius limit the emitted waves are just plane waves.

In figure 4.10 the Diffraction effect from a circular dish antenna is discussed for different axion masses (left) and different dish antenna radii (right). The parameter $\bar{U}$ is the fraction of power that is emitted from the dish antenna and goes through the imaginary surface at a distance z away from the emitting dish antenna, cf. figure 4.8 (right). The obvious statement from figure 4.10 is that due to diffraction less power goes through the imaginary surface if it is further away from the emitting dish antenna. From the left figure it becomes clear that the smaller the axion mass (larger the wavelength), the more pronounced is the power loss due to diffraction. Therefore dish antennas and also dielectric haloscopes are limited in sensitivity by going to low axion masses. The usage of dish antennas and dielectric haloscopes becomes critical if the photon wavelength comes close to the diameter of the involved PEC/dielectric disks. For the BRASS dish antenna, which has a diameter of 10 m this happens at an axion mass of 0.12 µeV and for the MADMAX haloscope, whose disks will have a diameter of 1 m it happens at an axion mass of 1.2 µeV. In figure 4.10 (right) we show the diffraction loss for different disk radii. Increasing the disk radius for a fixed

[7] To make them comparable we have subtracted the axion induced field from the FEM solution.

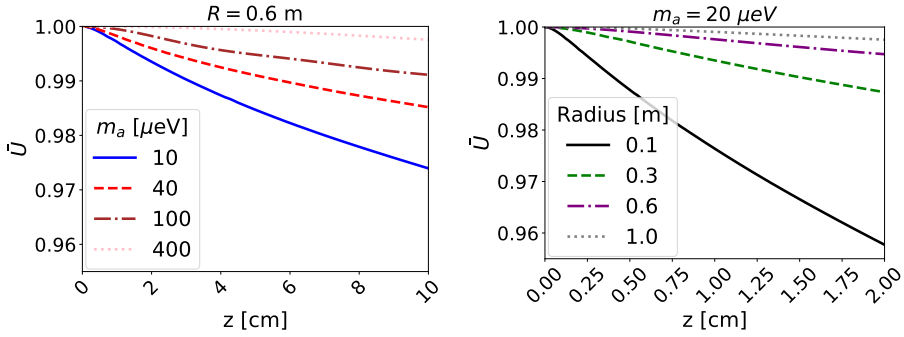

Figure 4.10: Diffraction losses for an imaginary surface that has a distance z from the emitting dish antenna, cf. figure 4.9. The parameter $\bar{U}$ is the fraction of received and emitted power, cf. figure 4.8 (right). In the left figure $\bar{U}$ is shown for a fixed radius of $R = 0.6\,\mathrm{m}$ for different axion masses. In the right figure an axion mass of $m_a = 20\,\mu\mathrm{eV}$ is fixed and $\bar{U}$ is shown for different radii.

frequency minimizes the diffraction loss. Again, this can be understood in the infinite radius limit in which diffraction effects have to vanish and plane waves are emitted. The results in figure 4.10 show directly the diffraction loss for a dish antenna and also give a first idea for the diffraction loss in a dielectric haloscope, where many emitting interfaces are involved. In a dielectric haloscope like MADMAX the distance between the emitting interfaces is around $\lambda/2$ what is in the cm regime as depicted in figure 4.10.

The overall message from figure 4.10 is that diffraction losses tend to vanish in the infinite frequency or infinite radius limit. This statement will be important for the rest of this chapter also when more radiating interfaces are involved.

The calculations above illustrates the effects of diffraction a few cm away from the PEC. In dish antenna experiments the receiver might be placed much further away from the PEC. A scalar diffraction theory which is suited to do far field expansions of the emitted E-fields was developed by Kirchhoff and Rayleigh [99]. Here we use the far field formula that was given in equation (4.42). In particular, for a circular PEC in a homogeneous external magnetic field as depicted in figure 4.8 this leads the well known Airy disk formula [100, 104]:

$$\frac{E_y(\boldsymbol{x})}{E_a} = -ikR^2 \frac{e^{ikz}}{z} e^{\frac{ik}{2z}r^2} \frac{J_1(R\,m_a\,\tan\theta)}{R\,m_a\,\tan\theta}, \tag{4.52}$$

where we use spherical coordinates and θ is the polar angle. The opening angle[8] of the diffraction pattern is found at [100]

$$\tan\theta \approx 1.22\,\frac{\lambda}{2R}. \tag{4.53}$$

Equation (4.53) confirms the message of figure 4.10. Diffraction effect increase for small disk radii and low axion masses/large photon wavelengths.

4.5.2 Axion velocity effects

In this section we demonstrate how CDM axion velocity effects can be included by using the Fourier propagation method from section 4.3.2. While we describe the foundations for a Dish antenna, the method was generalized for a multidisk system with the RFP approach by our collaborator [88]. In this section the discussed dish antennas are flat, i.e. they are located in the xy-plane. In Ref. [105, 106] velocity effects for spherical dish antennas are discussed.

[8] When we require all observer coordinates to be large, i.e. $D = |\boldsymbol{x}| - \frac{\boldsymbol{x}\cdot\boldsymbol{x}'}{|\boldsymbol{x}|} + \mathcal{O}(1/|\boldsymbol{x}|^2)$ [99], we obtain $\sin\theta = 1.22\lambda/(2R)$.

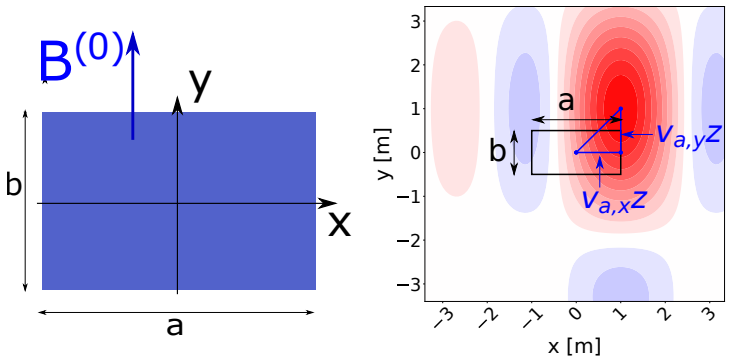

Figure 4.11: Left: Rectangular dish antenna in the xy-plane at $z_S = 0$. The external B-field is homogeneous over the entire dish antenna and points in y-direction. The rectangular dish antenna has a size of $a = 2\,\text{m}$ and $b = 1\,\text{m}$. Right: Diffraction pattern of at distance of $z = 10\,\text{m}$ away from the emitting rectangular dish antenna. The axion velocity was set to a large value of $v_{a,x/y} = 0.1$ to illustrate the influence of the finite axion velocity better. The maximum of the diffraction pattern is now shifted from $x = 0$ and $y = 0$ to $x = v_{a,x}z$ and $y = v_{a,y}z$. A wavelength of $\lambda = 30\,\text{cm}$ is used.

We describe the axion field in this case as $a^{(0)} = \hat{a}e^{-i\omega t + i\boldsymbol{k}_a \cdot \boldsymbol{x}}$, where $\boldsymbol{k}_a$ is the axion field wave vector which is only non-zero since we now allow a finite axion velocity. The considered dish antenna is centered around the coordinate center in the xy-plane and has dimensions (a, b) as sketched in figure 4.11 (left). A rectangular geometry is used in various dish antenna experiments [87, 107, 108].

A homogeneous external B-field pointing in y-direction magnetized the rectangular dish antenna. To compute the far field of the emitted E-field from the dish antenna we use the scalar diffraction theory by Kirchhoff and Rayleigh, which was introduced in the previous section in equation (4.42). The emitted field on the surface S, which now represents the rectangular dish antenna in the xy-plane, is given by $E_a e^{i\boldsymbol{k}^S \cdot \boldsymbol{x}}$, where $\boldsymbol{k}^S$ is the wave vector of the emitted E-field. Due to momentum conservation we have $k^S_{x,y} = k_{a,x/y} = v_{a,x/y}\omega$, where $\boldsymbol{v}_a$ is the axion group velocity, and $k^S_z \approx \omega = k$ [59]. The angles $\tan\alpha \equiv \frac{k^S_x}{k} \approx v_{a,x}, \tan\beta \equiv \frac{k^S_y}{k} \approx v_{a,y} \lesssim 10^{-3}$ correspond to the parallel velocities $v_{a,x}, v_{a,y}$ of the axion to the surface. Below we see that they define the angle of the emitted radiation in the far field. With the scalar diffraction theory we describe only the emitted E-field component parallel to the external B-field, which is the leading E-field component. The other E-field components are proportional to the axion velocity [59], which is small. After inserting everything into equation (4.42) we get for the emitted photon-like E-field in the far field approximation:

$$\frac{E_i(\boldsymbol{x})}{E_a} = \frac{e^{ikz}}{i\lambda z} e^{i\frac{kr^2}{2z}} ab\,\text{sinc}\left[\frac{ka}{2}\left(v_{a,x} - \frac{x}{z}\right)\right]\text{sinc}\left[\frac{kb}{2}\left(v_{a,y} - \frac{y}{z}\right)\right], \tag{4.54}$$

with $\text{sinc}(x) \equiv \frac{\sin(x)}{x}$. It is evident that the velocity effect leads to a shift of the diffraction maximum to $(v_{a,x}z, v_{a,y}z)$ after distance z. To illustrate this we plot the fields of a rectangular PEC with dimensions $2\,\text{m} \times 1\,\text{m}$ at distance $z = 10\,\text{m}$ for a relatively high axion velocity $v_{a,x/y} = 0.1$ in figure 4.11 (right).

The width of the diffraction pattern can also be determined from equation (4.54). In x and y-direction it is given by $\Delta x = z\frac{\lambda}{a}$ and $\Delta y = z\frac{\lambda}{b}$. The ratio between width and shift of the diffraction peak in the x-direction is

$$\frac{\Delta x}{v_{a,x}z} = \frac{\lambda}{a v_{a,x}} = 10 \times \left(\frac{\lambda}{10\,\text{cm}}\right)\left(\frac{10\,\text{m}}{a}\right)\left(\frac{10^{-3}}{v_{a,x}}\right). \tag{4.55}$$

A similar expression is obtained for the fraction of shift and width in the y-direction. For a discovery phase it is advantageous if the width of the diffraction maximum is larger than the shift. From equation (4.55) we see that this is the case for $\lambda > 1\,\mathrm{cm}$ ($(m_a < 120\,\mu\mathrm{eV})$. If axions are found its velocity effects become visible if the fraction of width and shift is smaller than one. This happens for $\lambda < 1\,\mathrm{cm}$ ($m_a > 120\,\mu\mathrm{eV}$. Of course this statement depend on the size of the dish antenna. We have taken the planned size of the BRASS dish antenna for our estimates. A similar result on the possibility of directional detection is also pointed out in Ref. [109]. However, their calculation is different and they do the calculation for a spherical dish antenna, while here a rectangular dish antenna is investigated.

In a resonant configuration the emitted fields in a dielectric haloscopes propagate many times back and forth between the dielectric interfaces. In turn the shiftmaximum of the diffraction pattern becomes larger with increasing propagation distance z. Therefore this can also be a loss mechanism. The case of velocity effects for a dielectic haloscope are discussed more in Ref. [88].

4.5.3 Near Fields

In section 4.5.1 it was shown that diffraction effects for the emitted radiation of a dish antenna can be described well by the Fourier propagation equation, cf. equation (4.44) and (4.51). The agreement between the FEM solution and the Fourier approach was below 10% in the forward direction. However, additional radiation, especially at the rims of the disk, was observed. This radiation could not be explained by the Fourier approach. In addition the Fourier approach can only describe the y-component of the emitted electromagnetic E-field, if the external B-field is only polarized in the y-direction. In the three dimensional FEM solution we observe that also the other photon-like E-field components are non-zero away from the emitting dish antenna. To understand this we have to take into account the vector nature of the emitted electromagnetic field together with boundary effects at the emitting dish antenna. Both effects are beyond a simple scalar diffraction theory that was discussed in section 4.5.1.

A vectorial propagation approach was already mentioned in section 4.3. The *Kirchhoff diffraction theory* is given in equation (4.47) and does not assume $\nabla(\nabla \cdot \boldsymbol{E}) = 0$, i.e. does not neglect near field effects. Assuming over the dish antenna a constant external B-field, which is polarized in y-direction, we can chose the initializing electromagnetic fields on the xy-plane to be only non-zero for $r = \sqrt{x^2 + y^2} < R$, i.e. on the circular dish antenna surface S. In particular the initializing electromagnetic fields on the dish antenna surface are the constant E-field $\boldsymbol{E} = E_a \hat{\boldsymbol{e}}_y$ and B-field $\boldsymbol{B} = -E_a \hat{\boldsymbol{e}}_x$. From equation (4.47) it becomes clear that with our assumptions we also get an additional non-zero z-component when using the Kirchhoff diffraction theory. However, the x-component of the E-fields is still zero. This is in contrast to the FEM solution.

We have to take care of the boundary charges at the rims of the PEC in order to describe the x-component of the E-field in the right manner. The Kirchhoff formula does not take these into account and therefore cannot describe the E_x component. Physically the boundary charges arise due to the axion induced field $\boldsymbol{E}_a$ which moves the free electrons of the PEC up and down. Since the PEC is of finite size, the electrons hit the boundary and accumulate there. In turn charge and current densities arise at the boundaries.

Mathematically the boundary charges at the rims of the circular dish antenna are described as a line charge density $\sigma_L \sim \sin\phi$ and a line current density $\boldsymbol{K}_L \sim \cos\phi \hat{\boldsymbol{e}}_\phi$, where ϕ is the azimuth angle of cylinder coordinates. Both σ_L and $\boldsymbol{K}_L$ contribute additional radiation to the E-field that is emitted from the dish antenna. The resulting terms that have to be added are:

$$\boldsymbol{E}_b(\boldsymbol{x}) = R \int_0^{2\pi} d\phi' \sigma_L (\nabla G)_L + i\omega R \int_0^{2\pi} d\phi' \boldsymbol{K}_L G_L, \tag{4.56}$$

where the subscript L at G and ∇G means that we evaluate the corresponding term at $\boldsymbol{x}' =$

$R\cos\phi'\hat{\boldsymbol{e}}_x + R\sin\phi'\hat{\boldsymbol{e}}_y$. The terms in equation (4.56) are referred to as *boundary terms* in the following. The total emitted E-field is then given as the sum of the Kirchhoff and boundary terms: $\boldsymbol{E} = \boldsymbol{E}_k + \boldsymbol{E}_b$, where $\boldsymbol{E}_k$ is from equation (4.47).

The charge density term in (4.56) also naturally arises when one takes into account that the E and B-fields in the Kirchhoff formula are actually not allowed to be discontinuous in the xy-plane (surface S). In the case of discontinuous fields one gets a correction term which is exactly the charge density term in (4.56). The Kirchhoff terms in combination with the charge density term in (4.56) are known also as the Stratton-Chu formula [110].

In figure 4.12 the FEM solution is compared to the analytical expressions, that is the fields from the boundary charges/ currents plus the Kirchhoff terms. The exact magnitude of the line charge and current density are not known in general and therefore they were scaled. However, such a scaling is not harmful, since we want to identify the underlying physical processes that lead to the shown E-fields. After the scaling all three components in figure 4.12 of the E-fields agree. This gives us confidence that we have understood the physics behind the FEM solution.

The different disks in dielectric haloscope have typically distances around $\lambda/2$ [58]. In this regime near field and boundary effects can be important as we have seen in this section. In section 4.7 and 4.8 this point is explicitly discussed by comparing the RFP results, which neglect near fields and boundary charges, to the full 3D FEM result.

4.6 Dielectric disk

In this section we investigate finite size effects of a dielectric disk inside an external B-field and a homogeneous cold dark matter (CDM) axion background. The B-field is polarized parallel to the dielectric disk surface in y-direction, is homogeneous over the dielectric disk and falls off to zero outside of the disk on a scale that is much larger than the photon wavelength. Throughout the whole section the dielectric disk has a radius of $R = 2\lambda = 6\,\text{cm}$ and a permittivity of $\epsilon = 9$. The chosen radius is smaller than the radius of the dielectric disks for the MADMAX haloscope (the MADMAX prototype has $R = 15\,\text{cm}$ and the final MADMAX experiment has $R \approx 1\,\text{m}$). The smaller disk radius is chosen here, because then three dimensional effects are more pronounced and can therefore be visualized much better.

In figure 4.13 the E-field, that is propagating away from the dielectric disk with a photon dispersion (photon-like radiation), is shown. The disk has a thickness of $d_\epsilon = 5\,\text{mm}$ what corresponds to a phase depth of $\delta_\epsilon = n\omega d = \pi$, i.e. maximal emission from the dielectric disk. The left figure represents the result that is obtained with the FEM using the 2D3D approach. This calculation includes all possible effects, since it is the full three dimensional solution of the vectorized Helmholtz equation, cf. equation (4.29). Note, that the FEM gives the total E-field solution. In figure 4.13 the axion induced field is subtracted such that only the propagating E-field is shown. The propagating E-field mode is compared to the result of the recursive Fourier propagation (RFP) approach in figure 4.13 (center). We use equation (4.46) in the implementation of the RFP and propagate the photon-like radiation 25 times between both disk surfaces. In figure 4.13 (right) we show the difference between the RFP approach and the 2D3D FEM solution. Similar to the case of the dish antenna the Fourier approach and the three dimensional FEM solution agree very well within the forward region of the dielectric disk. However, differences are observed at the rims of the disk. This is due to the fact that if the external B-field becomes parallel to the surface at the rims, additional charges accumulate at the rims and as a consequence radiation is emitted from these surfaces. This additional radiation is not included in the RFP approach and leads to the observed differences. In the following sections it becomes clear that this is no problem in the cases that we are interested in. For systems with more than one dielectric disk we are interested in the

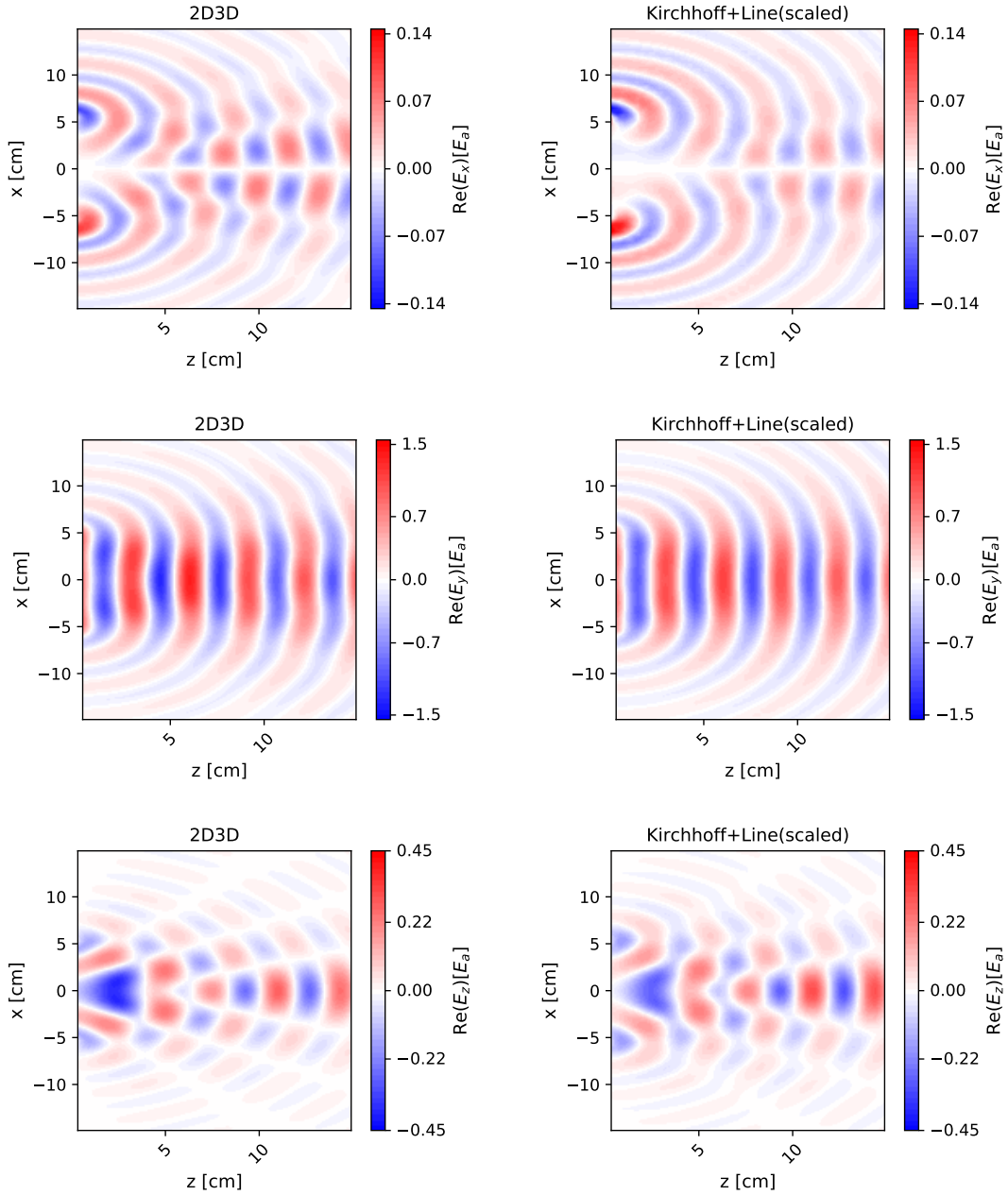

Figure 4.12: E-field emitted from a circular dish antenna with radius $R = 6\,\text{cm} = 2\lambda$. From top to bottom we shown all E-field components. In the right column the results from the Kirchhoff equation together with the boundary E-fields that arise due to boundary charges and currents, are shown. In the left column the solution from the 2D3D approach can be seen. The 2D3D approach is based on the FEM and represents a complete 3D solution. In the 2D3D model the axion induced field was subtracted in order to make the two results comparable (the propagation approaches describe only the photon-like E-fields). The E-field components from both approaches agree well with each other, what confirms that we understand the underlying phyiscs of the FEM solution.

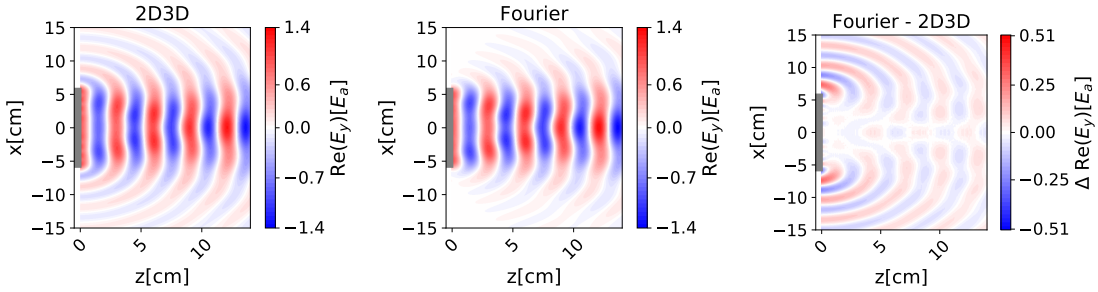

Figure 4.13: Photon-like E-field emission from a magnetized dielectric disk of thickness $d = 0.5\,\text{cm}$, radius $R = 6\,\text{cm} = 2\lambda$ and refractive index $n = 3$. The configuration corresponds to a phase depth of π and therefore to maximal emission. The external B-field is polarized in y-direction and homogeneous over the whole disk. The slice is shown at $y = 1.5\,\text{cm}$. Three dimensional calculations from the 2D3D (left) and RFP (center) approach are compared. In the right figure we show the difference between both approaches. They agree better in the forward region than on the rims of the disk. This is due to the fact that the emission from the rims is not included in the RFP.

resonant enhancement of the electromagnetic fields that propagate transversely away from many dielectric disc. The waves which propagate away from the rims are not resonantly enhanced and are all on the order of one, while the transversely propagating fields are resonantly enhanced and therefore much larger. Furthermore here we show an example of a rather small disk radius to test the two approaches in the most extreme case. In realistic haloscopes the disk radius compared to the wavelength is much larger and therefore the radiation from the rims influences the overall result less.

The 2D3D FEM result in figure 4.13 was obtained with one mode, i.e. using the relations (4.36)-(4.38). A direct comparison to the case when the relations (4.36)-(4.38) are not used can be found in appendix B.2.2. We show explicitly that both approaches agree up to a level of 10^{-12}, cf. figure B.3. We also compare in the appendix B.2.2 the 2D3D method with a standard three dimensional simulation and we find again an agreement up to numerical noise, cf. figure B.2.

In figure 4.14 the radius $R = 2\lambda = 6\,\text{cm}$ and the frequency $f = 10\,\text{GHz}$ of the circular dielectric disk are fixed. The power boost factor β^2 is shown with respect to the dielectric disk thickness. We compare the one dimensional model (blue) to two three dimensional calculations: the 2D3D approach (orange) and a standard three dimensional FEM solution (green crosses). The three dimensional calculations agree with the one dimensional model up to small 10% deviations which are cause by the finite size of the disk. The standard three dimensional calculation was done only for 5 disk thicknesses, since the computation takes much longer than the 2D3D approach, which also gives the full 3D solution for the radial symmetric setup. For the computed points the standard 3D FEM solution agrees perfectly with the 2D3D solution.

The diffraction losses in figure 4.14 are not very sophisticated, since a dielectric disk is not a very resonant system by itself. In the following section, where a minimal dielectric haloscope is considered, we encounter for the first time larger differences between the three dimensional calculation and the one dimensional model.

4.7 Minimal dielectric haloscope

A minimal dielectric haloscope consists of one PEC and a dielectric disk, cf. figure 4.3 (left). In the one dimensional model section 4.1.4 it was pointed out that – contrary to a dish antenna and a dielectric disk – a minimal dielectric haloscope can produce power boost factors that are larger than one. Here we discuss the effects of three dimensional effects on the power boost factor and

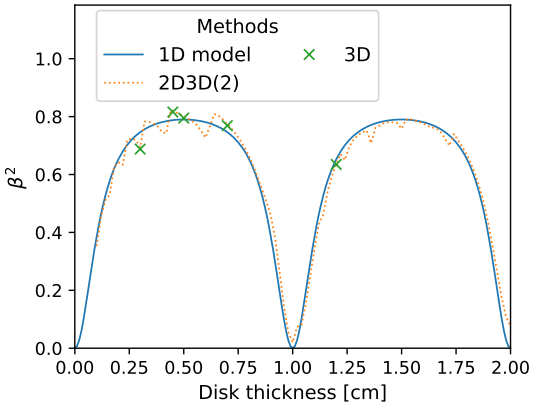

Figure 4.14: Power boost factor of a dielectric disk with respect to its thickness. The disk radius is $R = 6\,\text{cm}$ and its refractive index is $n = 3$, what is motivated by the material sapphire. The governing frequency is $f = 10\,\text{GHz}$. The one dimensional model (blue) is compared to the three dimensional 2D3D approach (orange) and a standard 3D FEM solution (green crosses). The 2D3D calculation uses explicitly two modes, however in the appendix B.2.2 we show that this can also be reduced by using the relations (4.36)-(4.38). The three dimensional calculations agree perfectly with each other and have small 10% deviations to the one dimensional model that arise due to finite size effects of the dielectric disk.

how they can lead to a reduction.

In figure 4.15 the power boost factor β^2 is shown with respect to the phase depth of the dielectric disk δ_ϵ. For each δ_ϵ the optimal δ_v is chosen, cf. white dashed line in figure 4.3 (right). The optimization of the white line was done in Ref. [88]. In each figure in 4.3 the different three dimensional calculations are compared to the one dimensional model (blue). We label the plots in the left columns with $\delta_v = \pi$, since the white dashed line in figure 4.3 (right) is around that value. The two plots in the right column are labeled by $\delta_v \approx 3\pi$ what means that we have added an additional factor of 2π to the δ_v that was determined by the white dashed line in figure 4.3 (right). Physically this means that the distance between disk and mirror is increased by a wavelength λ. In the top row of figure 4.15 the $n = 2$ case is shown and in the bottom row the comparison is done for the $n = 3$ case.

Before we compare the one dimensional model to the three dimensional results in figure 4.15 it should be noted that all three dimensional calculation techniques agree very well with each other. This gives a perfect validation of our methods that are presented in section 4.3. The 2D3D method with two modes and the external current formalism ("2D3D(2) EC") and the 2D3D method with uses the background field method together with the relations (4.36)-(4.38) ("2D3D(1) BF") agree in all cases perfectly. Both approaches give the full three dimensional solution of the vectorized Helmholtz equation (4.29). Finally the 2D3D method results also agree with the recursive Fourier propagation (RFP) approach which neglects near fields. This is an important result, since the disk and the PEC have only a distance of $\lambda/2$ and $\frac{3}{2}\lambda$ respectively. At these short distances it is not trivial that near field effects do not play a role. The recursive Fourier propagation results in figure 4.15 are from our collaborator [88].

Next the three dimensional results in figure 4.3 are compared to the one dimensional model. In all cases the largest reduction in the power boost factor β^2 is found in the most resonant case $\delta_\epsilon = \frac{\pi}{2}, \frac{3}{2}\pi, \cdots$. In the most resonant case the emitted fields from the three surfaces are reflected very often between PEC and dielectric disk. In this case diffraction effects are much more pronounced than in the case when the system is less resonant. Comparing now the two figures in

the top row in figure 4.15 it becomes immediately clear that the $\delta_v \approx 3\pi$ case has more diffraction losses as the $\delta_v \approx \pi$ case. The minimal dielectric haloscope is an open system and if the distance between disk and mirror is increased by λ more power is lost due to diffraction effects. If we compare the top plots ($n = 2$) with the bottom plots ($n = 3$) we see that the $n = 3$ case produces more pronounced resonances. This is because the dielectric disk has for $n = 3$ a larger reflectivity as for the $n = 2$ case, cf. figure 4.2 and therefore the radiation between PEC and disk is propagated more often. As a consequence the diffraction loss is also larger for the $n = 3$ case than in the $n = 2$ case.

In figure 4.16 the E_y-component of three dimensional E-field solution of the vectorized Helmholtz equation (4.29) is shown. The left column shows the E-field in the xy-plane at $z = 14\,\text{cm}$ away from the dielectric disk. In the right column we show the E-field in the yz-plane at $x = 0$ together with the PEC (black) and the dielectric disk (gray). From top to bottom different phase depths $\delta_\epsilon = \frac{1}{2}\pi, \frac{3}{4}\pi, \pi$ are shown where the corresponding δ_v was chosen in order to maximize the boost factor.

The case $\delta_\epsilon = \frac{\pi}{2}$ in figure 4.16 corresponds to the most resonant case. In the xy-plane a concentrated and approximately radial symmetric structure can be observed. The fields in the yz-plane are maximal between the disk and the PEC as expected from a one dimensional model. Going to less resonant configurations (from top to bottom in figure 4.16) we observe that the field amplitude decreases. Furthermore more substructure is observed, i.e. the beam shape in the xy-plane is not necessarily concentrated anymore in the center. The concentrated beam shape in the xy-plane in the resonant case ($\delta_\epsilon = \frac{\pi}{2}$) and the more substructure in the less resonant case ($\delta_\epsilon = \pi$) can be understood with a decomposition into eigenmodes of a radial symmetric dielectric waveguide [88]. It has been pointed out that the lowest mode, which has a similar form as the beam shape that is shown in figure 4.16 (top left), has the lowest transverse momentum [88]. In a very resonant case, where the fields are reflected back and forth between disk and mirror very often, the beam shape of the lowest mode (that is centered at the center of the disk) dominates, since it has the lowest transverse momentum. In the less resonant case ($\delta_\epsilon = \pi$) the dielectric disk is transparent and therefore the radiation that is emitted from the different surfaces is coherently added without the system itself being resonant. In this case the higher modes, which propagate with a different phase velocity due to higher transverse momentum, also appear in the beam shape and therefore more substructure is visible in figure 4.16 (bottom left).

In figure 4.17 we also show the other E-field components in the xy-plane. The E_x component shows a quadrupole structure and the E_z component a dipole structure. This is similarly to the fields that we observed for one circular PEC, cf. figure 4.12. We therefore understand that the fields in the E_x and E_z-components are induced by boundary charges and near fields. Most importantly we notice that the E_x and E_z-components are much smaller than the E_y-component. This is due to the fact that the axion induced field points in the direction of the external B-field, which is polarized in the y-direction. As a consequence only the E_y-component is resonantly enhanced. The fields that are polarized in the E_x and E_z-components are not resonantly enhanced and therefore much smaller. Another way to understand the smallness of the E_x component is via the boundary charges. In section 4.5.3 we pointed out that boundary charges induce E_x. Here we observe that the E_y-field drops off to the boundary of the PEC and dielectric disk. Therefore boundary charges can only be induced by the axion induced field, which is of the order one in the plots, but not by the enhanced photon-like E_y-field. Therefore the E_x-component is smaller than the E_y-component.

It is important to stress that only with the 2D3D method it was possible to run a FEM parameter sweep in figure 4.15 in a reasonable time and to get also the E_x and E_y components as shown in figure 4.17. The recursive Fourier propagation approach can only compute the E_y-component since it is based on a scalar diffraction theory. Therefore, the necessity of having two independent approaches, which calculate the outgoing power and the fields, becomes clear.

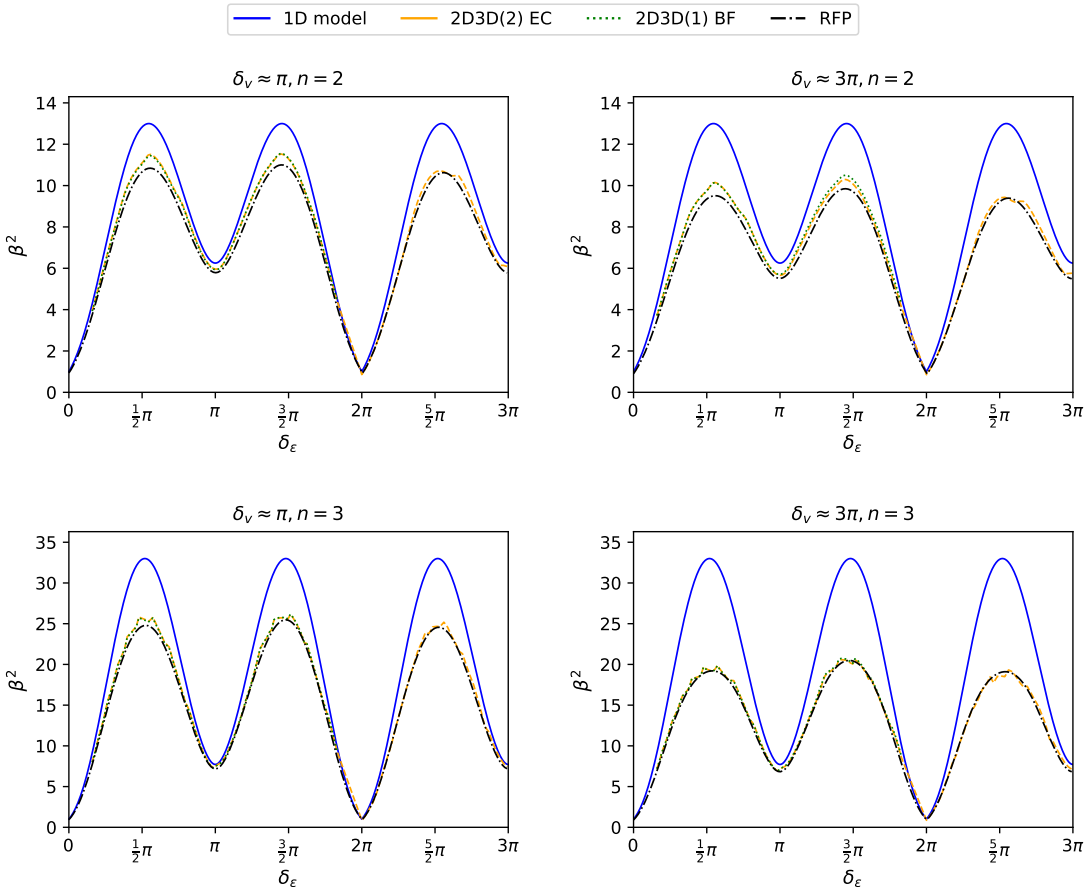

Figure 4.15: Power boost factor for a minimal dielectric haloscope with respect to the phase depth of the dielectric disk $\delta\epsilon = n\omega d_\epsilon$. The phase depth between disk and PEC was optimized for each point in order to obtain the largest β^2. The frequency is fixed to $f = 10\,\text{GHz}$ the phase depth is varied with the disk thickness. We show four different cases. In the top row the refractive index of the disk is $n = 2$, while the bottom row shows the $n = 3$ case. In the left column $\delta_v \approx \pi$, what corresponds to the white line in figure4.3 (right). The right column adds an extra distance of λ between disk and mirror resulting in $\delta_v \approx 3\pi$. We compare the one dimensional model [58] (blue) to three dimensional calculations. The "2D3D(2) EC" curve uses the 2D3D approach and the external current density while the "2D3D (1) BF" uses the background field method in COMSOL and the relations (4.36)-(4.38). It is not surprising that the 2D3D approaches agree, however we have included the two results for a further validation. We also show the RFP results from Ref. [88]. All three dimensional results agree up to small fluctuations. This gives us confidence that the approaches that we have introduced in section 4.3 can reliably calculate the power boost factor of dielectric haloscopes.

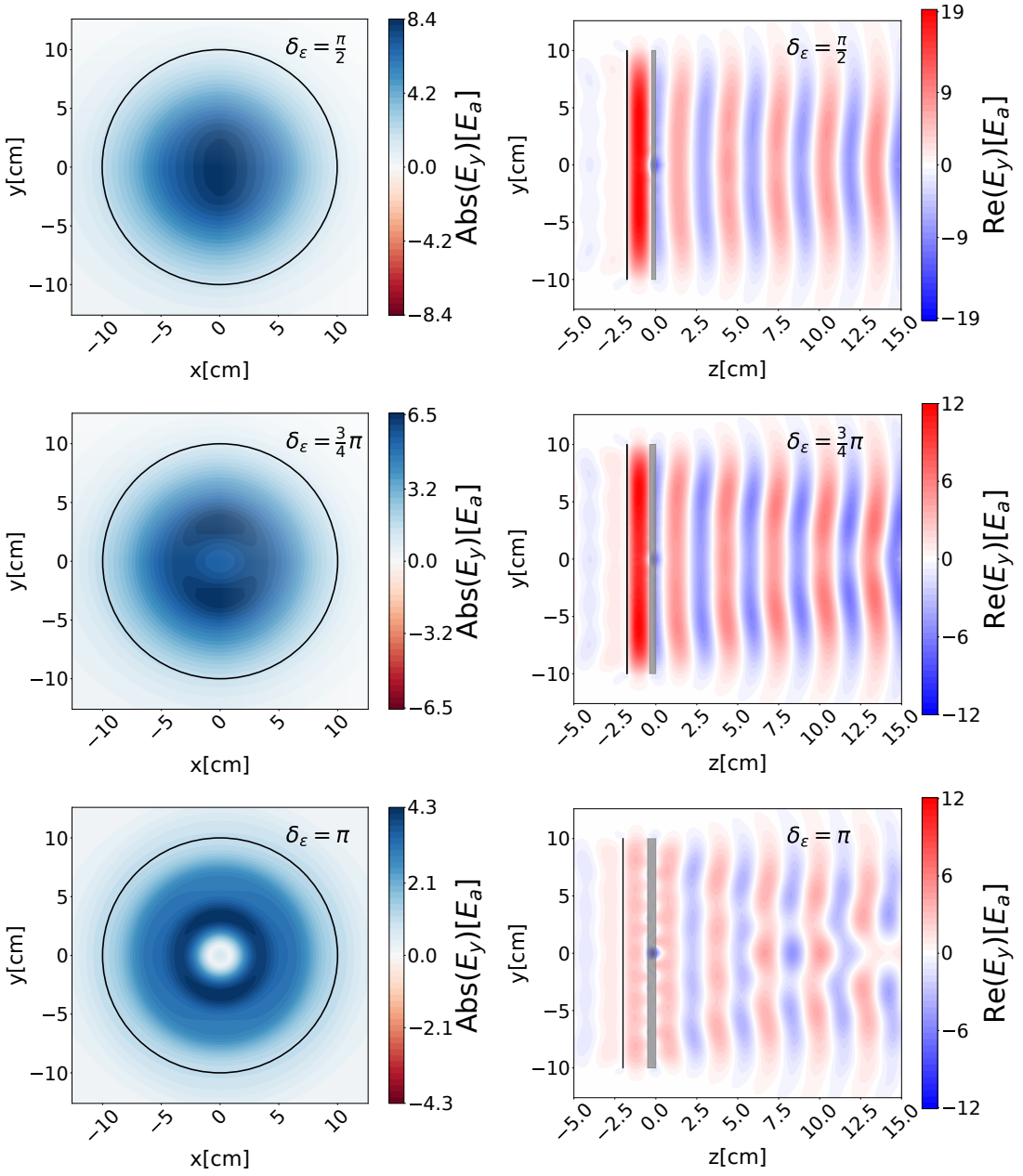

Figure 4.16: Beam shapes of the E_y field coming from a minimal dielectric haloscope. Left: Beam shapes in the xy-plane at $z = 14\,\text{cm}$ away from the booster. Right: Beam shapes in the zy-plane at $x = 0$. The disk radii are $R = 10\,\text{cm}$ and the frequency is $10\,\text{GHz}$ what corresponds to an axion mass of $m_a = 40\,\mu\text{eV}$. From top to bottom we show different disk phase depths which belong to a more resonant case (top) and to a less resonant (also called more transparent) case (bottom). The results are obtained with the 2D3D method.

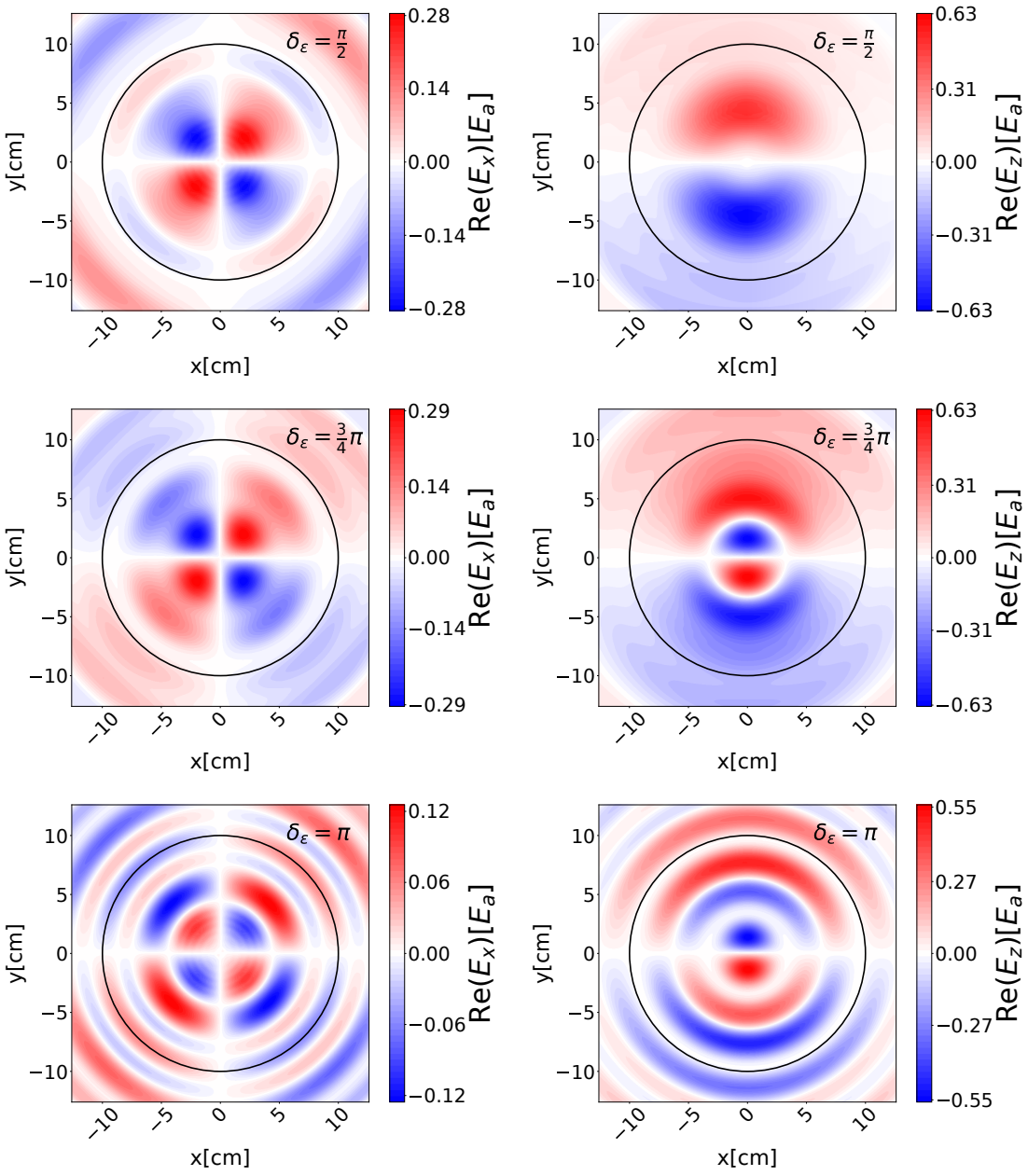

Figure 4.17: Beam shapes of the E_x (left) and E_z (right) components that are emitted from a minimal dielectric haloscope. The beam shapes are shown in the xy-plane at $z = 14\,\text{cm}$ away from the booster. The disk radii are $R = 10\,\text{cm}$ and the frequency is $10\,\text{GHz}$ what corresponds to an axion mass of $m_a = 40\,\mu\text{eV}$. From top to bottom we show different disk phase depths which belong to a more resonant case (top) and to a less resonant (also called more transparent) case (bottom). The results are obtained with the 2D3D method. The E_x component shows a characteristic quadrupole structure, while the E_z components shows a dipole structure.

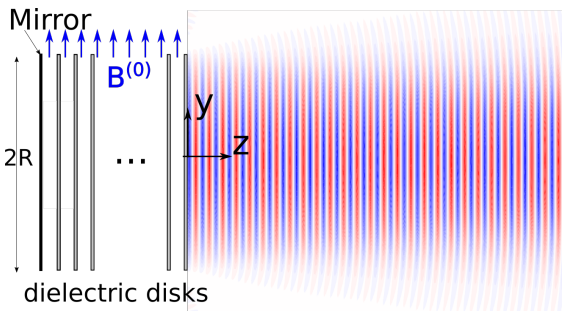

Figure 4.18: Sketch of the MADMAX booster. The mirror (PEC) is shown in black and the dielectric disks in gray. Both are radial symmetric and have radius R. In the MADMAX prototype booster (full scale MAMDAX experiment) we have 20 (80) dielectric disks with radius $R = 15\,\text{cm}$ ($R = 50\,\text{cm}$). An external B-field is applied in the y-direction $\boldsymbol{B}^{(0)} = B_e \hat{\boldsymbol{e}}_y$. The y-component of the emitted electric field is shown outside of the booster. Of course inside the booster the electric field is also non-zero, but for better visibility the electric field is only shown outside of the booster. The dielectric disks are made of lanthanum aluminate ($\epsilon = 24$).

4.8 MADMAX dielectric haloscope

In the previous sections of this chapter we have established two independent methods to calculate the emitted electromagnetic fields for open axion haloscopes in three dimensions. The methods were applied and validated against each other for simple systems such a dish antenna, a dielectric disk and a minimal dielectric haloscope.

In this section the focus lies on systems that have one perfect electric conductor (PEC) and more than one dielectric disk. In particular we focus on the MAMDAX prototype (20 dielectric disks with 30 cm diameter) and on the full scale MADMAX setup (80 dielectric disks with diameter of 1 m). Different effects on the power boost factor such as diffraction, near fields, and distortions in the disks are discussed. Within the next sections disk positions for the disks in the MADMAX haloscope are required to test different resonant configurations with different bandwidths. These disk positions were optimized by using the one dimensional model by our collaborator [88]. The thickness of the disks are 1 mm unless stated otherwise.

4.8.1 Diffraction

In this section diffraction and near field effects for the MADMAX prototype and the full scale MADMAX setups are discussed. The disks and the PEC are radial symmetric, while the external B-field is polarized in the y-direction. Furthermore the external B-field is homogeneous over the whole booster and falls off to zero outside of the booster on scales that are much larger than the photon wavelength. In figure 4.18 a sketch of the booster geometry in the zy-plane is shown. The dielectric disks are shown in gray and the PEC is shown in black. Exemplary we also show the outgoing electric field, that is polarized parallel to the external B-field with a blue and red color scale. The fields inside the booster are not shown in this simple sketch. The dielectric disks are made out of lanthanum aluminate ($\epsilon = 24$).

4.8.1.1 Prototype booster

The MADMAX prototype booster consists of 20 dielectric disks which all have a radius of $R = 15\,\text{cm}$. It addresses the frequencies between 18 GHz to 24 GHz.

In figure 4.19 (upper panels) the power boost factor β^2 is shown. The one dimensional model (blue) is compared to the three dimensional 2D3D model. For further validation the result from

the RFP approach from Ref. [88] is also shown. Both three dimensional models agree again within an accuracy of a few percent. This confirms what we have found already in section 4.7: near field effects and boundary charges do not influence the emitted power a lot, since the result from the RFP, which is based on a scalar diffraction theory, agrees well with the 2D3D method, which computes the full 3D solution of the vectorized Helmholtz equation. Here the optimization of the disk positions was done such that in both cases (left and right figures) a bandwidth of 50 MHz is achieved. In figure 4.19 (left) disk positions are chosen such that the boost amplitude is maximal around 18.6 GHz while in figure 4.19 (right) the disk positions are optimal for a power boost around 23.7 GHz.

The three dimensional power boost factor of the 2D3D curves in figure 4.19 is computed from the power that is emitted in z-direction, i.e. it is calculated with equation (4.35). The β^2 from the RFP curve was computed by integrating the time averaged pointing vector, which is approximately proportional to $|E_y|^2$, over the xy-plane sufficiently far away from the booster. Therefore both curves "2D3D" and "RFP" represent the power boost in z-direction. In the following we compute and compare always this quantity unless not otherwise stated. One example is the green curve in figure 4.19, where also a coupling to a Gaussian antenna is considered. The coupling to the Gaussian antenna reduces the power boost factor, since only the Gaussian contribution of the emitted field can be received by the antenna. A general E-field, that is described by the complex vector $\boldsymbol{E}$, has the following coupling efficiency to a Gaussian antenna:

$$C = \frac{\int dA \boldsymbol{E}_G \cdot \boldsymbol{E}^*}{\sqrt{\int dA \boldsymbol{E}_G \cdot \boldsymbol{E}_G^* \int dA \boldsymbol{E} \cdot \boldsymbol{E}^*}}, \tag{4.57}$$

where the $*$ stands for complex conjugation and the integration is done over a xy-plane a few wavelengths away from the booster. The field $\boldsymbol{E}_G$ has the form of a Gaussian beam and is defined as in Ref. [100]:

$$\boldsymbol{E}_G(r,z) = \hat{\boldsymbol{e}}_y \frac{w_0}{w} \exp\left[-\frac{r^2}{w^2} - ik(z-z_0) - i\frac{\pi r^2}{\lambda R} + i\phi_0\right], \tag{4.58}$$

$$w(z) = w_0 \sqrt{1 + \left(\frac{z-z_0}{z_R}\right)^2}, \tag{4.59}$$

$$R(z) = (z-z_0)\left[1 + \left(\frac{z_R}{z-z_0}\right)^2\right], \tag{4.60}$$

$$\phi_0 = \arctan\left[\frac{(z-z_0)}{z_R}\right], \tag{4.61}$$

where $z_R = \frac{\pi w_0^2}{\lambda}$ is the Rayleigh length, w_0 is the beam waist and z_0 the waist position. The coordinate system is chosen such that $z = 0$ corresponds to the outermost dielectric disk, cf. figure 4.18.

The power coupling between the electric field, that is emitted by the booster, and the Gaussian antenna is $|C|^2$. By maximizing $|C|^2$ for each frequency the optimal Gaussian antenna parameters w_0 and z_0 can be determined. They are shown in the lower panels in figure 4.19 together with the maximal $|C|^2$. For the optimization we use the beam shapes from the 2D3D approach. In both cases the optimal coupling can be achieved with $w_0 \approx 11\,\text{cm}$ and $z_0 = 0$ over a wide frequency interval where the boost factor is large. This is advantageous for the design of the antenna system, because it means that the same Gaussian antenna for scanning frequencies around 18 GHz and 23 GHz can be used. More simulations for a 50 MHz bandwidth confirm that for the full frequency interval of the prototype booster also optimal $w_0 = 11\,\text{cm}$ and $z_0 = 0$ is found. Later we will see that this does not only hold for a 50 MHz bandwidth, but also for larger and smaller bandwidths. When we study larger disk radii in the full MADMAX setup in section 4.8.1.2 the optimal w_0 changes and a rule of thumb for the optimal w_0 is given.

The curve that is labeled "2D3D approach (+antenna)" in the upper panel of figure 4.19 is the power boost factor β^2 from the "2D3D approach" curve multiplied by the respective $|C|^2$ for a fixed $w_0 = 11\,\text{cm}$ and $z_0 = 0$ and represents the actual power boost factor under the assumption that the antenna, that receives the fields which leave the booster, is of Gaussian type. Figures of the type 4.19 will appear more often in the following. Therefore for the description of all panels we always refer to the text in this section.

Next, the upper panels of figure 4.19 are discussed more. In both cases the three dimensional models yield a smaller β^2 which is also shifts with respect to the one dimensional model. The shift of the power boost factor appears because in three dimensions the transverse momentum is due to diffraction effects non-zero. In a one dimensional model the photon dispersion is $k_z = n\omega$. However, in three dimensions we get, cf. equation (4.45), $k_z = \sqrt{(n\omega)^2 - k_t^2}$, where $k_t = \sqrt{k_x^2 + k_y^2}$ is the transverse momentum. The disk positions are optimized in a one dimensional model and therefore to fulfill the resonance condition in three dimensions a slightly larger frequency is needed. This is the origin of the frequency shift that is observed in the upper panels of figure 4.19. In the next section we will see that the larger we make the disk radius, the smaller is the frequency shift. This is a very intuitive result, since in the infinite radius limit we expect to get the plane wave solution which has no frequency shift. In general we will see that in the large radius and frequency limit the three dimensional results converge towards the one dimensional result. This very intuitive statement is based on the findings in figure 4.10. We observed there that diffraction effects vanish in the limit of large radius and frequency, cf. figure 4.10. While we have outlined here how the frequency shift of the boost factor depends on the radius and the frequency, the shift can also be calculated explicitly with dielectric waveguide modes. Our collaborator finds [88]:

$$\Delta f = 13\,\text{MHz}\left(\frac{k_t}{16\text{m}^{-1}}\right)^2\left(\frac{22\,\text{GHz}}{f}\right), \tag{4.62}$$

where the transverse momentum k_t depends on the corresponding mode and scales inversely with the radius of the disks $\sim \frac{1}{R}$. The lowest Gaussian-like mode for $R = 15\,\text{cm}$ is $k_t = 16\text{m}^{-1}$ [88].

In figure 4.20 we show the beam shapes for the frequencies, which are marked by green vertical lines in figure 4.19 (right). The beam shapes are shown at $z = 15\,\text{cm}$ away from the booster and the projection of the disk radius is depicted with the black circle. The E_y-component (middle column) is always much larger than the other components E_x and E_z. This is due to the fact that the external B-field and the axion induced field are polarized in the y-direction and therefore only the E_y-component gets resonantly enhanced. The field patterns in the E_x/E_z component (left/right column) has the typical quadrupol/dipole structure that was also observed for a dish antenna and the minimal dielectric haloscope. We therefore conclude that their origin is due to the superposition of the fields from the boundary charges and near fields which are emitted from all involved dielectric disks and the PEC. However, the E_x and E_z components are much smaller than the E_y component, since they are not resonantly enhanced.

Next, we focus on the E_y component (middle column) in figure 4.20. The E_y component is centered in the middle of the black circle and drops off to the rims of the disks. Furthermore the beam shape is well approximated by a Gaussian beam shape (Gaussian-like) for the two lower frequencies 23.72 GHz and 23.75 GHz, while at the larger frequency 23.78 GHz small deviations from a radial symmetric Gaussian-like beam shape can be observed. Physically this behavior can be understood in the picture of dielectric waveguide modes, which are approximately eigenmodes of the whole booster system [88]. As pointed out by Ref. [88] the lowest mode, which can be well approximated with a Gaussian beam, has the smallest transverse momentum. We call this mode Gaussian-like mode in the following. Therefore the lowest mode appears at the lower frequencies in figure 4.19. This picture is confirmed by the fact that the two lowest frequencies, which are marked in figure 4.19, have almost a perfect coupling to the Gaussian antenna. Furthermore this can be

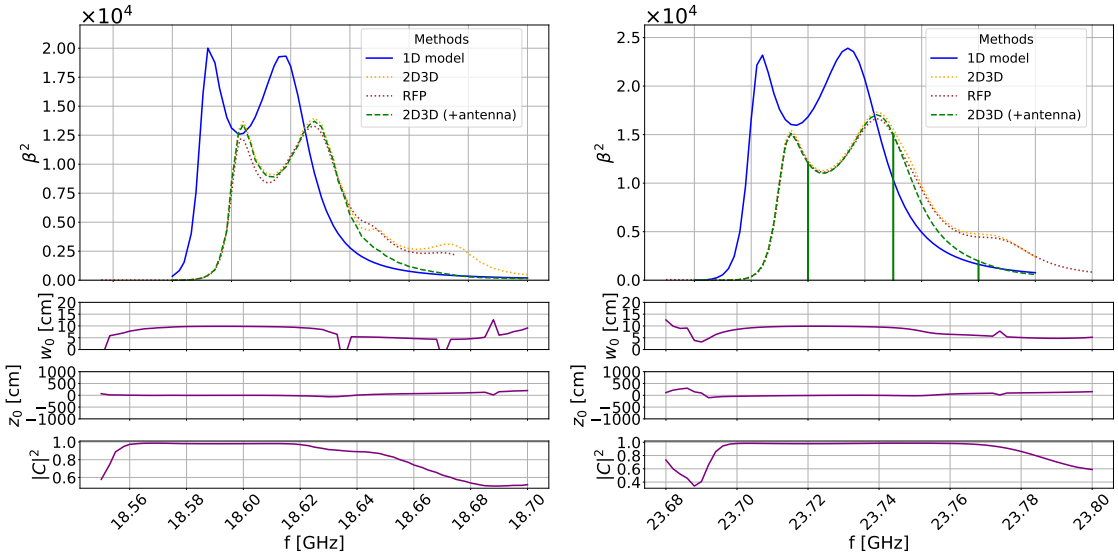

Figure 4.19: We show the power boost factor over frequency. Two disk configurations (left and right) for the prototype booster are shown. In the left figure the disk distances are configured such that a power boost factor with 50 MHz bandwidth is achieved around 18.6 GHz. In the right figure a boost factor which also has a bandwidth of 50 MHz around 23.7 GHz is shown. In the upper panel we compare the one dimensional model (blue) with two three dimensional models (orange and brown). The two three dimensional models show a satisfactory agreement, where the RFP result is from Ref. [88]. Three dimensional effects reduce the power boost factor and shift it to larger frequencies with respect to the one dimensional boost factor. In the lower panels the optimal coupling parameters to a Gaussian antenna are shown. For both cases the optimal beam waist is around $w_0 = 11\,\text{cm}$ while the optimal waist position is around $z_0 = 0$. The power coupling $|C|^2$ is close to one for a large range of frequencies. The green curve in the upper panel takes into account this power coupling to a Gaussian antenna with fixed $w_0 = 11\,\text{cm}$ and $z_0 = 0$. However, due to the fact that the power coupling is close to one for a large frequency interval, the green curve does not differ much from the orange curve in the main boost factor peak.

confirmed by looking at the figure 4.20 (center top and middle). The largest marked frequency 23.78 GHz does not have a good coupling to a Gaussian beam. The reason for this is that at larger frequencies also higher modes, which typically do not have the Gaussian shape anymore, appear. This is because the higher modes have larger transverse momentum and are therefore shifted to larger resonance frequencies. This statement can be confirmed directly from figure 4.20 (bottom center). Due to the higher modes the beam has more substructure on top of the Gaussian-like shape. More details regarding a diescription with dielectric waveguide modes can be found in Ref. [88].

In figure 4.21 we study a boost factor configuration around 22 GHz for different bandwidths. A bandwidth of 250 MHz is shown in figure 4.21 (left) and a configuration with a bandwidth of 20 MHz is shown in figure 4.21 (right). The blue, orange, brown and green curve in the upper panel are the power boost factor results from the one dimensional model, three dimensional 2D3D, RFP and the 2D3D calculation, which takes into account the coupling efficiency to a Gaussian antenna, respectively. The three lower patches describe the optimal beam waist, waist position and power coupling.

The shift of the three dimensional boost factor in figure 4.21 is approximately the same as the shift in the 50 MHz case, cf. figure 4.19. This is due to the fact that the frequencies in figure 4.21 and 4.19 are very similar and the radius of the disks are the same. Later we will see that the shift

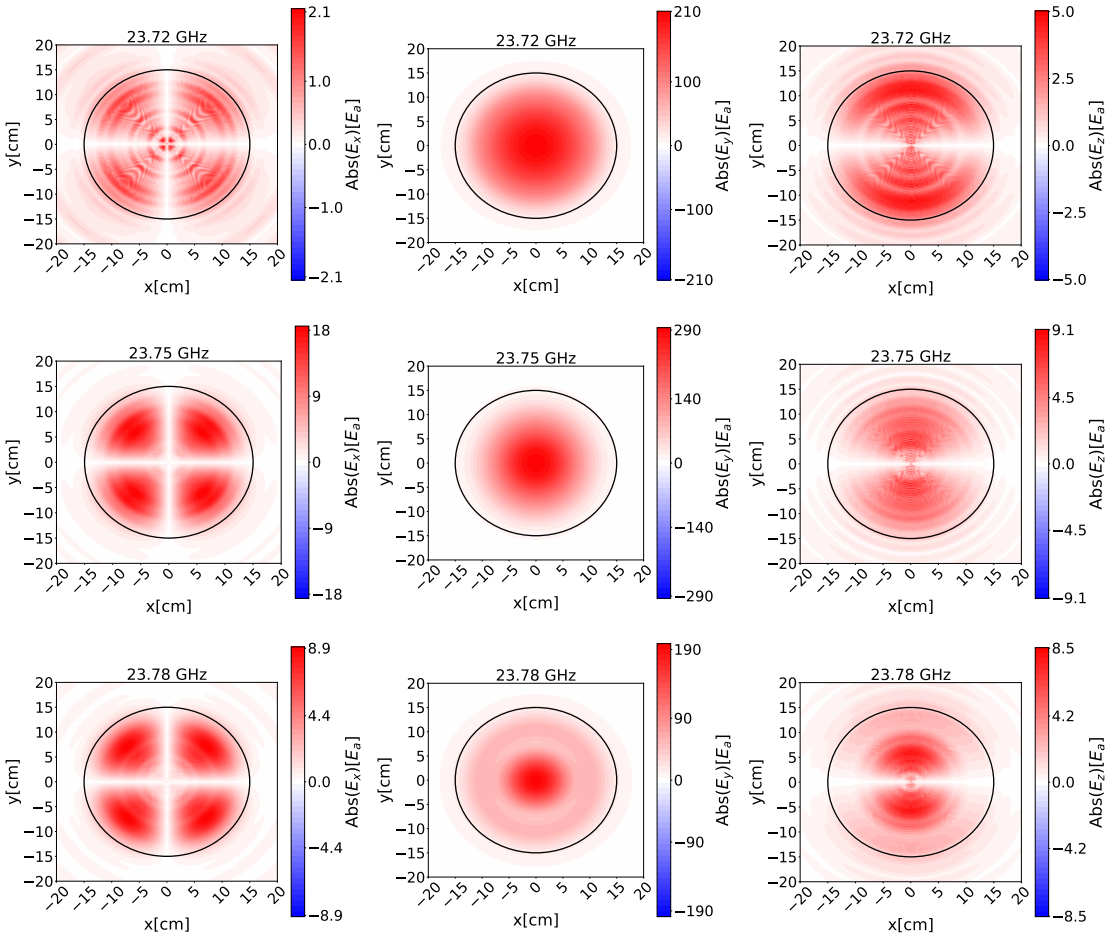

Figure 4.20: Beam shapes for the prototype booster 15 cm away from the outermost disk of the booster. The rings represent the radius of the disks of the booster. We show the beam shapes for the marked frequencies in figure 4.19 (right) from top to bottom. The fields are computed with the 2D3D method and therefore it is possible to compute all E-field components: E_x (left), E_y (middle), E_z (right). The E_x/E_z components have the characteristic quadrupole/dipole structure that was also obtained in the case of a dish antenna and minimal dielectric haloscope. The E_y component is approximately Gaussian for the two lowest frequencies and receives only for the largest shown frequency non Gaussian substructure.

will decrease for larger frequencies and larger disk radii.

The 20 MHz bandwidth case, shown in figure 4.21 (right), is similar to the cases that is shown in figure 4.19 in the sense that the main boost factor peak contains only Gaussian contributions. Higher non Gaussian-like modes appear only at very large frequencies, i.e. $f > 22.06\,\text{GHz}$, in figure 4.21 (right). This is directly evident from the coupling $|C|^2$ in the lowest panel, which is very close to one, but only decreases for $f > 22.06\,\text{GHz}$. The optimal Gaussian antenna parameters are similar to the case of the 50 MHz bandwidth case: $w_0 \approx 11\,\text{cm}$ and $z_0 = 0$.

In the case of the 250 GHz bandwidth, cf. figure 4.21 (left) also the main boost factor peak is reduced significantly when coupling it to a Gaussian antenna. This can again be understood in the picture of higher modes with higher transverse momenta [88]. The higher modes still get shifted to larger resonant frequencies, however due to the larger bandwidth these resonant frequencies still lie within the main boost factor peak and not outside as it is the case in figure 4.21 (right). The previous statement is confirmed by looking at the beam shapes. In figure 4.22 the E_y-component is shown in the xy-plane 15 cm away from the booster. We show the beam shapes for the three different frequencies, that are marked with green vertical lines, in figure 4.21 (left). For increasing frequency (left to right in figure 4.22) more and more substructure appears. This observation is in agreement with the observation from figure 4.21 (left), that for higher frequencies in the boost factor more and more non Gaussian contributions arise. The non Gaussian-like beam shapes arise at larger frequencies due to larger transverse momentum and introduce more substructure in the beam shape.

Finally in figure 4.23 we show a disk configuration, where all disk spacings and thicknesses are half of the values that were used in figure 4.21 (right). As a consequence we obtain in the one dimensional model a boost factor (blue) that has double bandwidth and is resonant at the double frequency. Note that this example is academic, since the current antenna and disk of the prototype booster are designed to target the frequency range between 18 GHz and 24 GHz. However, by studying this case we are able to confirm the physical intuition that we have gained in the previous examples. The shift of the three dimensional boost factor is now smaller. This is as expected, since in the limit $f \to \infty$ we expect the three dimensional result to be closer to the one dimensional result, because in the infinite frequency limit diffraction effects vanish. Furthermore the yellow dotted and green dashed line now also disagree in the main peak of figure 4.23. This means that the higher non Gaussian-like modes also appear in the main peak, while in the lower frequency case, cf. figure 4.21 (right), the higher non Gaussian-like modes appear at much larger frequencies and away from the green Gaussian-like mode peak. This behavior at larger frequencies is due to a constant transverse momentum. If the transverse momentum k_t in stays constant, but we go to larger frequencies, then the shift of the higher non Gaussian-like modes is also smaller since $k_z = \sqrt{(n\omega)^2 - k_t^2}$ gets closer to $n\omega$. Furthermore here we look at an example where the bandwidth is doubled with respect to figure 4.21 (right). One can see that the shift of the non Gaussian-like modes in the 44 GHz case is approximately 25 MHz, cf. figure 4.23, while the shift of the non Gaussian-like modes in the 22 GHz case, cf. figure 4.21, is much larger. The disk thicknesses (distances of the disks) in the 44 GHz case, cf. figure 4.23, was obtained by halving the disk thicknesses (distances of the disks) of the 22 GHz case. This is a valid strategy to obtain the optimized disk distances for a higher frequency case and leads to the optimal disk distance configuration for the 44 GHz case if the 22 GHz case was optimized properly. At the same time thinner disk – compared to the 22 GHz case – are used in order to keep the phase depths and therefore material losses minimal.

In the following we address the question how the coupling to the antenna influences the area law that was rigorously proven in Ref. [58] for the one dimensional model. We assume a fixed Gaussian antenna with with $w_0 = 11\,\text{cm}$ and $z_0 = 0$ in the following and focus on frequencies around 22 GHz. In figure 4.24 the area under the boost factor curve from the one and three dimensional calculations

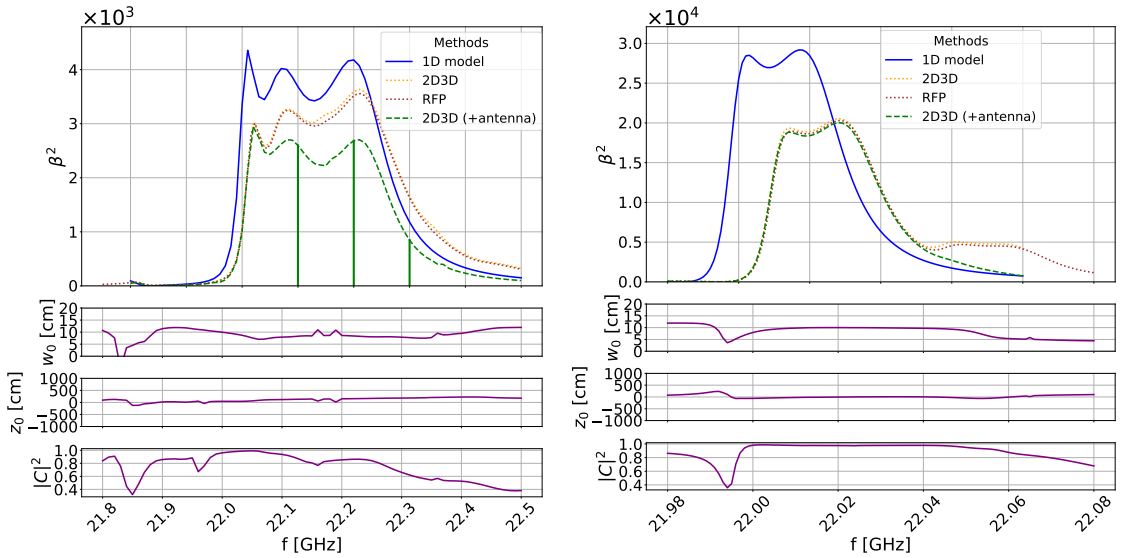

Figure 4.21: We show the power boost factor β^2 over frequency. Two disk configurations (left and right) for the prototype booster are shown. In the left figure the disk distances are configured such that a power boost factor with 250 MHz bandwidth is achieved at 22 GHz. In the right figure a power boost factor which has a bandwidth of 20 MHz at 22 GHz is shown. In the upper panel we compare the one dimensional model (blue) with two three dimensional models (orange and brown), where the RFP result is from Ref. [88]. The two three dimensional models which represent the total power in z-direction (2D3D and RFP) show a satisfactory agreement. Three dimensional effects reduce the power boost factor and shift it to larger frequencies with respect to the one dimensional boost factor. In the lower panels the optimal coupling parameters to a Gaussian antenna are shown. For both cases the optimal beam waist is around $w_0 = 11\,\text{cm}$ while the optimal waist position is around $z_0 = 0$. In the 20 MHz bandwidth case (right) the power coupling $|C|^2$ is close to one in the main peak. However, for the 250 MHz bandwidth case (left) the power coupling $|C|^2$ is also reduced inside the main peak. The green curve in the upper panel takes into account this power coupling to an antenna with fixed $w_0 = 11\,\text{cm}$ and $z_0 = 0$.

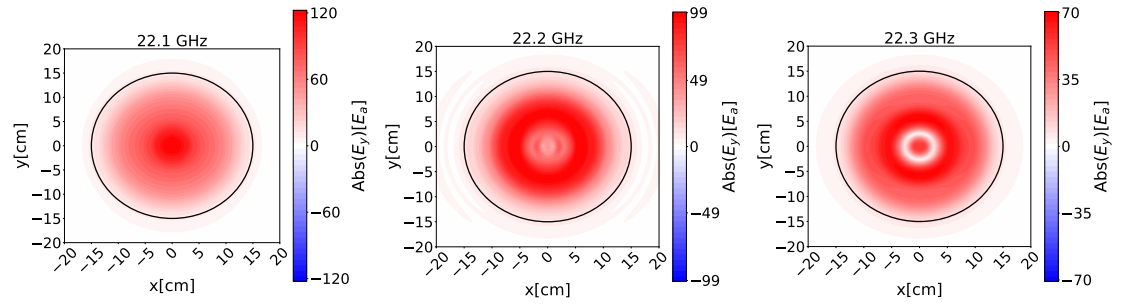

Figure 4.22: Beam shapes for the prototype booster at $z = 15\,\text{cm}$ away from the outermost disk of the booster. The rings represent the radius of the disks of the booster. We show the E_y beam shapes for the marked frequencies in figure 4.21 (left), i.e. for a 250 MHz configuration. We use the 2D3D method to compute the beam shapes. The E_y component is approximately Gaussian for the lowest shown frequency and receives for the larger frequencies non Gaussian substructure.

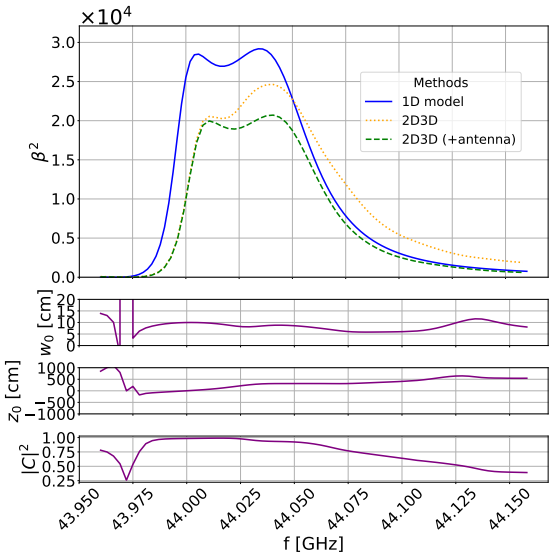

Figure 4.23: We show the power boost factor over frequency and study a disk configuration for the prototype booster (20 disks with $R = 15\,\text{cm}$) such that the power boost factor is at 44 GHz with a bandwidth of 40 MHz. Contrary to the previously studied cases the disks have now a thickness of 0.5 mm. In the upper panel we compare the one dimensional model (blue) with 2D3D three dimensional model (orange). Three dimensional effects reduce the power boost factor and shift it to larger frequencies. In the lower panels the optimal coupling parameters to a Gaussian antenna are shown. The optimal beam waist is around $w_0 = 11\,\text{cm}$ while the optimal waist position is around $z_0 = 0$. This is similar to the lower frequency case, cf. figures 4.19 and 4.21. The green curve in the upper panel takes into account the power coupling to an antenna with fixed $w_0 = 11\,\text{cm}$ and $z_0 = 0$. Due to the higher frequency the shift of the non Gaussian-like modes is not as severe as for example in figure 4.21 (right) and therefore the non Gaussian-like modes appear in the main peak of the boost factor. This is evident, since in the main peak the green curve is reduced with respect to the orange curve.

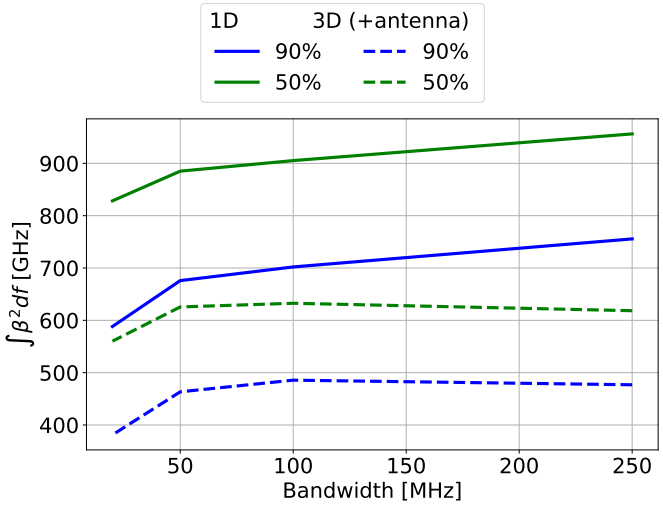

Figure 4.24: Comparison of the area law with the three dimensional (dashed) and one dimensional (solid) models. We show the area law for two thresholds. A threshold of 50% means for example that only the frequency interval where the boost is larger than 50% of it's maximal value is considered in the area law integral. The one dimensional model has a slight tendency to have less area for small bandwidths. This tendency is handed on to the three dimensional model case. The one dimensional model also favors large bandwidths. However, they are not favored in the three dimensional model due to the coupling to the Gaussian antenna with $w_0 = 11\,\text{cm}$ and $z_0 = 0$. The area under the boost factor curve in the three dimensional model is approximately constant for bandwidths larger than 50 MHz.

is compared to each other. We show two different thresholds values. A threshold value of 50% means that all frequencies which are larger than 50% of the maximum β^2 value are taken into account for the area integral. In figure 4.24 we plot the area under the boost factor against the different bandwidth. For both threshold values the one dimensional model gives a smallest area under the boost factor curve for small bandwidths. In theory the one dimensional area law should give just a horizontal line in the plot. However, the area for small bandwidths is reduced due to the fact that we take into account only the frequency interval where the boost factor is above a certain threshold. The area law was rigorously proven for the periodic frequency interval of the power boost factor. The behavior, that less area is under the boost factor for small bandwidths, is also visible in the three dimensional calculation. However, this effect is just inherited from the one dimensional model and is not of three dimensional nature.

The one dimensional area law shows a slight tendency to prefer large bandwidths. However, for larger bandwidths this effect is flattened out due to three dimensional effects. Physically this means that there is always the same area under the boost factor curves after we cut away the non Gaussian contribution due to the coupling to the antenna. In the 250 MHz bandwidth case in figure 4.21 (left) the situation looks bad, since a lot of the power is lost in the main peak after coupling to the Gaussian antenna. However, also in the 50 MHz case in figure 4.19 power is lost. This is just not so evident, since the higher non Gaussian-like modes are shifted to outside of the main boost factor peak.

4.8.1.2 Full scale MADMAX setup

In this section the number of dielectric disks is increased to 80 and the radius of the disks is now $R = 0.5\,\text{m}$. With the arguments from the previous sections we expect that due to the larger radius

the three dimensional result comes more close to the one dimensional model. This expectation is confirmed in figure 4.25 (upper panel) where the three dimensional and one dimensional results are compared to each other. The disk distances in figure 4.25 are configured such that a boost factor over a bandwidth of 50 MHz is obtained. In comparison to the MADMAX prototype case, where the disk radius is $R = 15\,\mathrm{cm}$, the total three dimensional power boost factors (orange and brown dotted line) are now much closer to the one dimensional model prediction (blue solid line). The brown dotted line which shows the RFP result [88] agrees almost perfectly with the orange dotted line from the 2D3D approach and therefore gives a satisfactory validation of both three dimensional methods. The agreement of both approaches for this highly non-trivial system shows that near fields effects can be neglected, when the disks do not have any distortions such as caused by tiling, cf. section 4.8.2. This is due to the fact that since the RFP approach is based on a scalar diffraction theory and agrees here with the full three dimensional solution (2D3D). Note, that this statement is not obvious, since the disks have typically a distance around $\lambda/2$, where near field effects can play a role.

In the three lower panels in figure 4.25 we show again the optimal fit to a Gaussian beam. The optimal beam waist is around $w_0 = 0.3\,\mathrm{m}$ and the waist position is $z_0 = 20\,\mathrm{m}$ away from the booster. In the lowest panel the power coupling $|C|^2$ is shown. We show it for the case that w_0 and z_0 are free parameters and can take independent values (solid line), $z_0 = 0$ is fixed and w_0 is a free parameter (dashed line) and $z_0 = 0$ and $w_0 = 0.3\,\mathrm{m}$ are both fixed (dotted line). The green dashed line in the top panel is obtained by multiplying the yellow dotted line by the dashed line in the lowest panel. It represents the power boost factor that can be received by a Gaussian antenna with fixed $w_0 = 0.3\,\mathrm{m}$ and $z_0 = 0$. We see explicitly that now also higher non Gaussian-like modes appear in the main boost factor peak. This is because for larger disk radii we have less transverse momentum and therefore the higher non Gaussian-like modes are not shifted far outside of the main boost factor peak as it was for example the case in figure 4.19.

From the results in this section and the previous section a rule of thumb for the optimal beam waist can be deduced:

$$w_0 \approx \frac{2}{3} R. \tag{4.63}$$

We do not show the beam shapes corresponding to the marked frequency lines in figure 4.25, since a discussion would be very similar to the prototype booster case. In the region where a significant boost is achieved the E_x and E_z-components are small compared to the E_y-component. The E_y-component has for the lowest marked frequency in figure 4.25 almost a Gaussian beam shape. For the larger marked frequencies also non Gaussian structures appear due to higher modes with larger transverse momentum. For a more detailed discussion of this we refer to the previous section, where the same effect was discussed in much greater detail.

4.8.2 Tiling

The dielectric disks of the booster have to have large permittivity and low dielectric losses. A promising candidate is lanthanum aluminate ($LaAlO_3$), which has a permittivity $\epsilon = 24$ and low loss $\tan\delta = 10^{-6}$ [102]. The effect of the dielectric loss was studied in a one dimensional model in Ref. [88, 111] and is neglected in the following. Lanthanum aluminate has to be grown as a crystal and therefore the produced pieces are limited in size [112]. The $LaAlO_3$ crystal size is $3''$. From these crystals hexagons will be cut and glued together to a full disk. The gap between the glued hexagons is 0.2 mm. In figure 4.26 a disk from the prototype booster is shown. The different hexagons are tiled together with glue (blue) which has $\epsilon = 5$ and a dielectric loss of $\tan\delta = 10^{-3}$ [1]. The dielectric loss of the glue is neglected in the following, since the effective area of the glue is much smaller than the surface area of the lanthanum aluminate material.

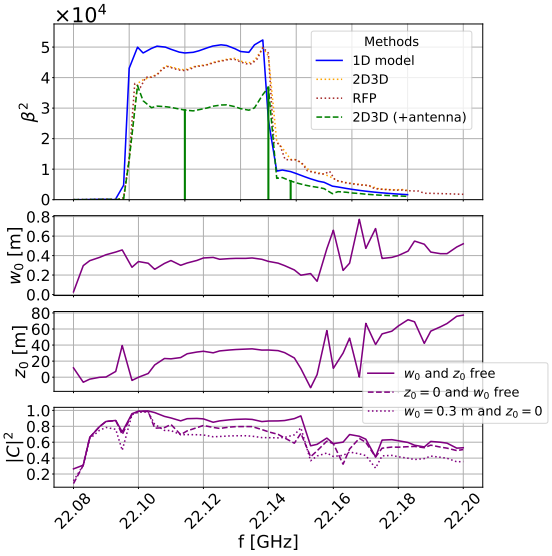

Figure 4.25: We show the power boost factor β^2 over frequency for a the full scale MADMAX setup with 80 disks. Each disk has a radius of 50 cm. The disk distances are configured to give a power boost around 22 GHz with bandwidth of 50 MHz. In the upper panel we compare the one dimensional model (blue) with two three dimensional models (orange and brown), where the RFP result is from Ref. [88]. Three dimensional effects reduce the power boost factor and shift it to larger frequencies. However, the shift is not so severe as in the case of the prototype booster, where the disk radius was smaller. In the lower panels the optimal coupling parameters to a Gaussian antenna are shown. We obtain an optimal $w_0 = 30\,\text{cm}$ while the optimal waist position is around $z_0 = 30\,\text{m}$. The power coupling in the lowest panel is shown for three cases: w_0 and z_0 free parameters (solid line), $z_0 = 0$ fixed and w_0 free parameter and $w_0 = 30\,\text{cm}, z_0 = 0$ fixed. The green curve in the upper panel takes into account this power coupling to an antenna with fixed $w_0 = 30\,\text{cm}$ and $z_0 = 0$. We have chosen $z_0 = 0$ instead of $z_0 = 30\,\text{m}$, since the difference between both cases is marginal small.

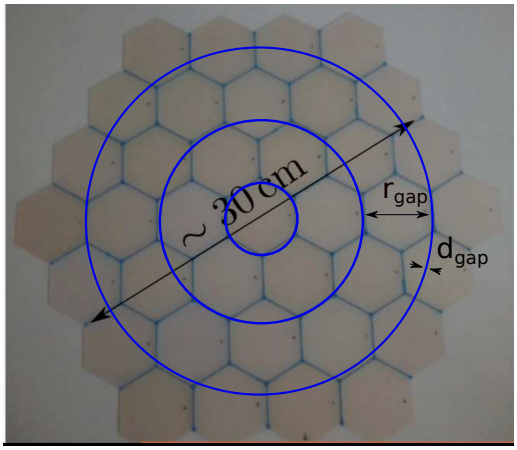

Figure 4.26: Tiled dielectric disk of the MADMAX prototype booster. The hexagons have to be tiled together with glue (blue). In this section the hexagonal structure is approximated by the radial symmetric tiles. The emitted E-fields and the power from the booster with the radial symmetric tiles can be effectively computed with the 2D3D method that was introduced in section 4.3. The figure was adapted from [112].

Since we can effectively calculate the outgoing power for a radial symmetric geometry (2D3D approach), the hexagonal structure is approximated by the radial symmetric structure which lies on top in figure 4.26. The parameters r_{gap} describes distance between two radial symmetric tiles and d_{gap} is set to the gap size between two hexagons: $d_{\text{gap}} = 0.2\,\text{mm}$. The "radial symmetric tiling" that is discussed in this section can be seen as a first step towards a more realistic estimation of tiling on the outgoing power and beam shape of dielectric haloscopes. Due to the fact that the radial symmetric tiles approximate the hexagons to a good degree, we think that the presented results cover the most important physical effect that will also arise in the more complicated case of hexagonal tiles.

Since the 2D3D method is used throughout this section to compute the power boost factor and the corresponding beam shapes, we do not label the results in the plots with "2D3D". Furthermore we do not compare the results in this section to the RFP approach, since as we show in the following, a scalar diffraction theory is not suited anymore to calculate the emitted E-fields in the case of tiling because not only the E-field component parallel to the external B-field is enhanced.

4.8.2.1 Prototype booster

In figure 4.27 two tiling configurations for the prototype booster are considered. In both cases the disk positions are optimized with the one dimensional model such that a 20 MHz bandwidth is achieved. We chose this relatively small bandwidth, since it corresponds to a relatively pronounced resonance in which effects from small tiling disturbances are expected to be maximal. In figure 4.27 (left) all disks have $r_{\text{gap}} = 4\,\text{cm}$ and all tiles are aligned from disk to disk. In figure 4.27 (right) the distance of the radial symmetric tiles vary randomly from disk to disk and are therefore not aligned. The upper panels of figure 4.27 shows in blue the power boost factor β^2 from the untiled one dimensional model and in orange the untiled three dimensional calculation with the 2D3D approach. The red curve includes tiling while still showing all emitted power in z-direction. The green curve includes additionally the effect of the coupling to a Gaussian antenna in the tiled disk case. The lower panels in figure 4.27 describe the optimal parameters for the coupling to a Gaussian antenna. They do not differ much from the untiled case, cf. figure 4.21 (right), and

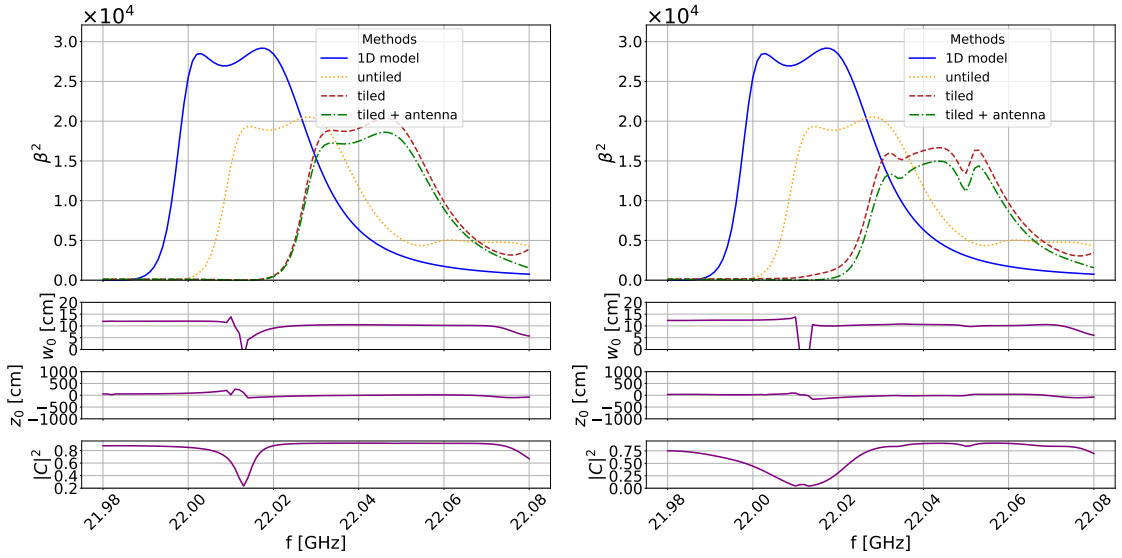

Figure 4.27: Power boost factor β^2 from a booster configuration that was optimized for a 20 MHz bandwidth. The booster has 20 disks with radius $R = 15\,\text{cm}$ and the disks have $\epsilon = 24$. Each disk has three radial symmetric tiles with $d_{\text{gap}} = 0.2\,\text{mm}$ and $\epsilon_{\text{gap}} = 5$. Left: All tiles are perfectly aligned from disk to disk with $r_{\text{gap}} = 4\,\text{cm}$. Right: The tiles are not aligned from disk to disk, but randomly positioned. The optimal antenna parameters, that are used to compute β^2 under consideration of a Gaussian antenna, are similar to the untiled case, i.e. $w_0 = 11\,\text{cm}, z_0 = 0$.

therefore they are not discussed separately here.

We start to discuss the upper panel fo figure 4.27 (left). The tiled result is shifted to larger frequencies with respect to the untiled case. Tiling introduces small disturbances in the material, which contribute more transversal momentum. Therefore the main resonance shifts again to larger frequencies. However, from the coupling to the Gaussian beam we see that only a small part of the main boost factor peak gets non Gaussian-like modes, since the green and red line are sill in good agreement. We do not show explicitly the beam shapes in this case, since from the previous discussion it is clear that the beam shape in the main peak is Gaussian-like.

In figure 4.27 (right) randomness is introduced by varying the distance between the different tiles from disk to disk according to a standard deviation of 8 mm. This scenario is motivated, since in a real experimental setup the hexagonal tiles also might not be perfectly aligned. The results from figure 4.27 (right) suggest that the non aligned tiles reduce the power boost factor further. However, the effect is not large and still a significant amount of power, compared to the untiled case, can be received by the Gaussian antenna.

The prototype booster setup that is studied here is planed to operate between frequencies of 18 GHz and 24 GHz. Since this frequency interval is not very large we expect the tiling results in the whole interval to be similar to the ones that are obtained in figure 4.27. The exact value of the shift depends on $d_{\text{gap}}, r_{\text{gap}}, \epsilon_{\text{gap}}$. For the realistic values that we have studied the frequency shift compared to the untiled case is around 20 MHz for a bandwidth of 20 MHz. Based on the mode picture we expect that for larger or smaller bandwidths the frequency shift will not change significantly since the transversal momentum is not changed when different bandwidths are considered.

We conclude that radial symmetric tiling of the dielectric disks in the MADMAX 20 disk prototype will not destroy the power boost factor, but shift it due to additional transversal momentum. In the next section the case of the full scale MADMAX setup is investigated with radial symmetric tiling. In this case the frequency interval is much larger and also the tiling effect is also discussed for larger and smaller frequencies.

4.8.2.2 Full scale MADMAX

In this section tiling effects are investigated for the full scale MADMAX setup with 80 discs. The disks have a radius of $R = 50\,\text{cm}$ and are radially symmetric tiled with the parameters $r_{\text{gap}} = 6\,\text{cm}$ and $d_{\text{gap}} = 0.2\,\text{mm}$. r_{gap} is now slightly larger as in the case of the prototype, however the chosen value is now close to the largest possible value which is available with current crystal growing techniques. Due to the larger total disk radius more radial symmetric glue strips are needed. In the prototype we have three radial symmetric glue strips, cf. figure 4.26, while for the full scale MADMAX now eight of them are necessary.

In figure 4.28 the tiling effect is shown for two different frequency ranges. Figure 4.28 (left) shows a configuration with disks of the thickness 1 mm which produces a boost factor around 22 GHz with 50 MHz bandwidth. The configuration at higher frequencies (right) was obtained by halving the disk thicknesses and the distances of the dielectric disks of the low frequency configuration, cf. figure 4.28 (left). The higher frequency configuration produces a boost factor around 44 GHz with a bandwidth of 100 MHz. The tiling parameters are the same in both figures in 4.28.

We start with the discussion of the lower frequency case, i.e. figure 4.28 (left). The untiled result (orange) and the tiled result (red) which represent the total power boost in z-direction, cf. equation (4.35), are shifted against each other. This feature was already discovered in the previous section where tiling effects in the prototype booster are discussed. However, in the prototype case the boost factor peak mainly contained Gaussian beam shapes, cf. in figure 4.27 where the green and red curve does not differ significantly. In the case that is discussed in figure 4.28 (left) the green curve is significantly below the red curve, which is due to large non Gaussian contributions. This becomes explicitly clear from the lowest panel in the figure, where the coupling to a Gaussian beam is computed. The optimal coupling, that can be reached, does not become much larger than 0.6 and can be much smaller. For a fixed antenna we estimate the optimal parameters to be $w_0 = 0.5\,\text{m}$ and $z_0 = 0$. Note, that the optimal beam waist is now larger than in the untiled case where we found $w_0 = 0.3\,\text{m}$ over a large frequency interval for the power boost factor. This feature is not harmful for a receiver, since it means that the beam widens less in the far field, what reduces the effective size of the antenna or a focusing mirror.

Before we reveal the reason for the boost factor reduction that is due to tiling, let us first also discuss figure 4.28 (right) where we show the situation at larger frequencies. Naively one would expect that the tiling leads to an even larger reduction if the frequency (wavelength) is increased (decreased), since then the smaller wavelength is more sensitive to the small tiled structures. However, from figure 4.28 we can see that this is not the case. The difference between the red an blue curve is not so severe as in the 22 GHz case (left). Furthermore the green curve is closer to the red curve what implies that the main peak contains now a larger amount of Gaussian contributions as in the lower frequency case. In the following we resolve this behavior by looking at the beam shapes and computing the contributions to the power from the basis vectors $\hat{\boldsymbol{e}}_r$ and $\hat{\boldsymbol{e}}_\phi$ in the 2D3D approach. We refer to the contribution of the $\hat{\boldsymbol{e}}_r$ ($\hat{\boldsymbol{e}}_\phi$) basis vector as the contribution from the $\hat{\boldsymbol{e}}_r$ ($\hat{\boldsymbol{e}}_\phi$) mode.

First, to understand the non Gaussian contributions that reduce the power boost factor in figure 4.28 we recall that in the 2D3D approach the E-field is decomposed into $\hat{\boldsymbol{e}}_r, \hat{\boldsymbol{e}}_\phi$ and $\hat{\boldsymbol{e}}_z$ basis vectors. In the case of radial symmetric tiles the $\hat{\boldsymbol{e}}_r$ basis vector is always perpendicular and the $\hat{\boldsymbol{e}}_\phi$ vector always parallel to the glue stripes. Since now we have much more tiles as in the prototype case it makes sense that the tiles have a larger effect on the transverse momentum of the two modes $\hat{\boldsymbol{e}}_r$ and $\hat{\boldsymbol{e}}_\phi$.[9] To prove this statement we decompose the emitted power into a part that comes form

[9] We do not include $\hat{\boldsymbol{e}}_z$ since its contribution is expected to be small compared to the discussed modes since the main propagation happens in z-direction.

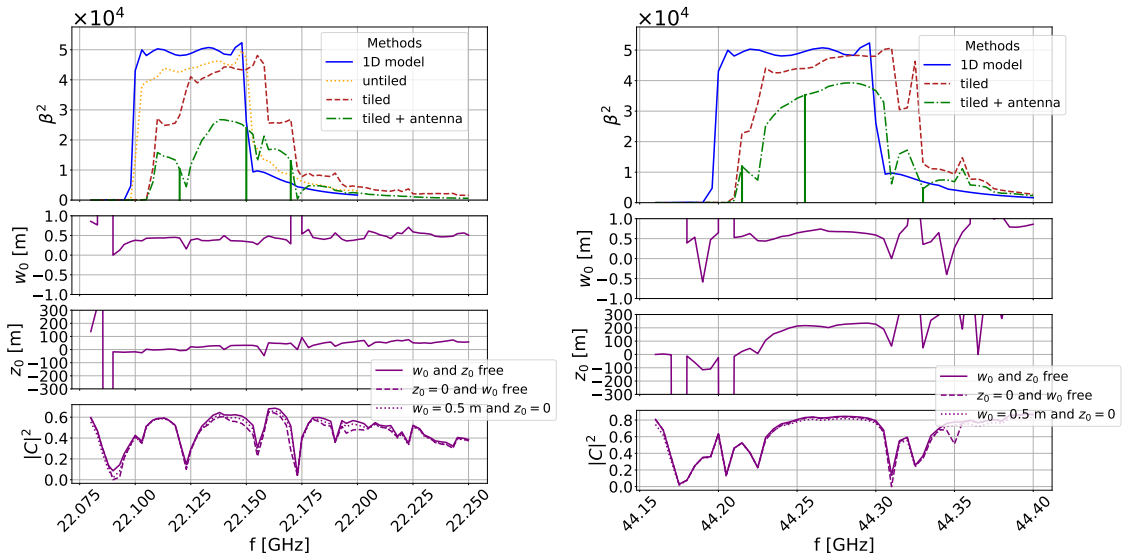

Figure 4.28: Radial symmetric tiling effect on the MADMAX haloscope which has 80 discs with radius $R = 0.5\,\mathrm{m}$. The eight radial symmetric tiles are aligned from disk to disk and have the parameters $d_{\mathrm{gap}} = 0.2\,\mathrm{mm}, r_{\mathrm{gap}} = 6\,\mathrm{cm}, \epsilon_{\mathrm{gap}} = 5$. The upper panels show the one dimensional power boost factor (blue). The three dimensional calculations are shown in orange (untiled), red (tiled) and green (tiled + antenna coupling). In the lower panels the optimization to Gaussian beam is shown with the optimal waist w_0, waist position z_0 and power coupling $|C|^2$.

the $\hat{\boldsymbol{e}}_r$ mode and another part from the $\hat{\boldsymbol{e}}_\phi$ mode:

$$P_z = -\mathrm{Re}\frac{i\pi}{\omega\mu}\sum_{m=\pm1}\int_0^{R_p} dr\, \underbrace{\tilde{E}_\phi^m\left(r\partial_z\tilde{E}_\phi^{m*} + im\tilde{E}_z^{m*}\right)}_{\hat{\boldsymbol{e}}_\phi\text{-contribution}} + \underbrace{r\tilde{E}_r^m\left(\partial_z\tilde{E}_r^{m*} - \partial_r\tilde{E}_z^{m*}\right)}_{\hat{\boldsymbol{e}}_r\text{-contribution}}. \tag{4.64}$$

In figure 4.29 we show the power boost factor for the one dimensional model (blue) the total power from the three dimensional 2D3D calculation (orange or red) and the different contributions from the $\hat{\boldsymbol{e}}_r$ and $\hat{\boldsymbol{e}}_\phi$ modes in black (dashed) and gray (dotted dashed). The top left plot shows the untiled situation at 22 GHz. In this case the $\hat{\boldsymbol{e}}_r$ and $\hat{\boldsymbol{e}}_\phi$ contributions are equally large and are not shifted against each other. However, in the corresponding case with tiling (top right) the contributions from $\hat{\boldsymbol{e}}_r$ and $\hat{\boldsymbol{e}}_\phi$ are shifted against each other. Both $\hat{\boldsymbol{e}}_r$ and $\hat{\boldsymbol{e}}_\phi$ receive additional momentum. However, $\hat{\boldsymbol{e}}_r$ receives more additional transverse momentum than $\hat{\boldsymbol{e}}_\phi$. Therefore the $\hat{\boldsymbol{e}}_r$ mode is shifted to larger frequencies in comparison to the $\hat{\boldsymbol{e}}_\phi$ mode.

In this picture we can now also understand the large non Gaussian contributions that came up when we studied the coupling to a Gaussian antenna in figure 4.28 (left). In the 2D3D approach the total E-field is given by (cf. equation (4.34)):

$$\boldsymbol{E} = \boldsymbol{E}^+ e^{i\phi} + \boldsymbol{E}^- e^{-i\phi}. \tag{4.65}$$

The $\hat{\boldsymbol{e}}_r$ and $\hat{\boldsymbol{e}}_\phi$ and $\hat{\boldsymbol{e}}_z$ contributions to $\boldsymbol{E}$ are:

$$\begin{aligned}
\boldsymbol{E}_r &\sim \tilde{E}_r^+(r,z)\sin\phi\begin{pmatrix}\cos\phi\\ \sin\phi\\ 0\end{pmatrix},\\
\boldsymbol{E}_\phi &\sim \tilde{E}_\phi^+(r,z)\cos\phi\begin{pmatrix}-\sin\phi\\ \cos\phi\\ 0\end{pmatrix},\\
\boldsymbol{E}_z &\sim \tilde{E}_z^+(r,z)\sin\phi\hat{\boldsymbol{e}}_z,
\end{aligned} \tag{4.66}$$

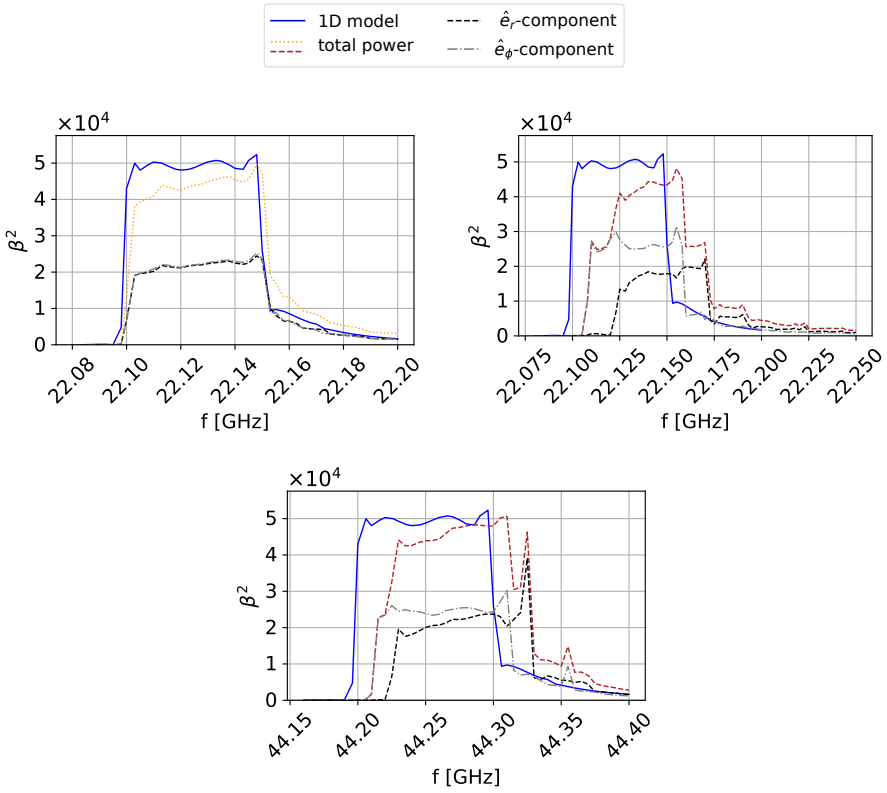

Figure 4.29: Decomposition of the power boost factor into the contribution from the different modes $\hat{\boldsymbol{e}}_r$ and $\hat{\boldsymbol{e}}_\phi$. The one dimensional model is shown in blue, while the total three dimensional power boost in z-direction from the 2D3D model is shown in orange. The two modes $\hat{\boldsymbol{e}}_\phi$ and $\hat{\boldsymbol{e}}_r$ are shown in black and gray respectively. All results are for an 80 disk configuration where all disk have a radius of $R = 0.5\,\mathrm{m}$. The top left figure depicts the untiled booster, while the top right figure shows the tiled booster case. In the bottom figure a tiled booster, which is tuned to be resonant at higher frequencies, is shown. In both tiled situations the $\hat{\boldsymbol{e}}_r$ mode receives additional transversal momentum and shifts to larger frequencies with respect to the $\hat{\boldsymbol{e}}_\phi$ mode. This leads in the end to a non Gaussian beam shape.

where we have used the relations (4.36)-(4.38).

Together with the shift of the $\hat{\boldsymbol{e}}_r$ contribution, cf. figure 4.29 (top right), and the contribution to the fields in equation (4.66) we expect to see in the E_y component for lower frequencies in the boost factor only the $\hat{\boldsymbol{e}}_\phi$ mode and therefore only a $\cos^2\phi$ structure. For larger frequencies we however expect more dominantly the $\hat{\boldsymbol{e}}_r$ mode and a beam shape that follows a $\sin^2\phi$ dependence. This expectation – and therefore also our interpretation in terms of $\hat{\boldsymbol{e}}_r$ and $\hat{\boldsymbol{e}}_\phi$ modes – is confirmed by looking at the beam shapes in figure 4.30 (center column), where we show the E_y-component for the frequencies that are marked with green vertical lines in figure 4.28 (left). The green line at the lowest frequency belongs to the part of the boost factor where the $\hat{\boldsymbol{e}}_\phi$ mode dominates. We expect to see a $\cos^2\phi$ beam shape, what is confirmed in figure 4.30 (top center). The middle frequency that is marked in figure 4.28 (left) should contain according to figure 4.29 (top right) both modes. This is confirmed by the beam shape in figure 4.30 (middle center). Finally the largest marked frequency in figure 4.28 (left) contains according to figure 4.29 (top right) only the $\hat{\boldsymbol{e}}_r$ mode. This is again confirmed by figure 4.30 (bottom center) which shows a $\sin^2\phi$ beam shape, cf. equations (4.66).

It is important to note that due to the shift of the $\hat{\boldsymbol{e}}_r$ mode the E_x-component is not necessarily

small compared to the E_y-component. We show the E_x-component in the left column of figure 4.30. The E_x component has the characteristic quadrupole structure which follows our expectations. In the equations (4.66) we showed that both the $\hat{\boldsymbol{e}}_r$ and the $\hat{\boldsymbol{e}}_\phi$ mode follow a $\sin\phi\cos\phi$ beam shape, what is exactly the quadrupole structure that we can see in the left column of figure 4.30. The E_x component therefore always keeps the characteristic quadrupole structure no matter if the $\hat{\boldsymbol{e}}_\phi$ or $\hat{\boldsymbol{e}}_r$ mode dominates. This is in contrast to the E_y component where we have seen that, dependent on which mode dominates, we can have either a vertical or horizontal dipole structure.

Finally, the E_z-component in figure 4.30 (right column) also follows the expected $\sin\phi$ beam shape that was found in equation (4.66). However, it is much smaller than the other two components.

Our results show that for more complicated setups, which include a lot of radial symmetric tiles, a scalar diffraction approach, as used in the recursive Fourier propagation approach, is not applicable. This is due to the fact that the scalar approach describes the E-field components independently and would miss for example the large E_x-component if only E_y-components on the surfaces are initialized.

To summarize we have now understood why the power boost factor in figure 4.28 shows the reduction when the coupling to a Gaussian antenna is considered. In the main peak the two modes $\hat{\boldsymbol{e}}_r$ and $\hat{\boldsymbol{e}}_\phi$ overlap. Effectively this gives a similar situation compared to the untiled case and therefore Gaussian beam shapes are present. When the contributions from the two modes do not overlap, the coupling to the antenna reduces significantly, since then the E_y beam shape follows a $\cos^2\phi$ or $\sin^2\phi$ beam shape.

At higher frequencies figure 4.29 (bottom) shows that the shift between the two modes $\hat{\boldsymbol{e}}_r$ and $\hat{\boldsymbol{e}}_\phi$ is slightly smaller as in the 22 GHz case (top right). In the 22 GHz case the shift is ≈ 16 MHz while in the 44 GHz case the shift between the $\hat{\boldsymbol{e}}_r$ and $\hat{\boldsymbol{e}}_\phi$ modes is 12 MHz. In our examples the 44 GHz case has a bandwidth of ≈ 100 MHz while the bandwidth in the 22 GHz case is ≈ 50 MHz. Therefore the relation of bandwidth to shift is much larger in the 44 GHz case, cf. figure 4.29 (bottom). In conclusion the absolute frequency range where the $\hat{\boldsymbol{e}}_r$ and $\hat{\boldsymbol{e}}_\phi$ modes overlap is larger than in the 44 GHz case. One can see this explicitly in the upper panel of figure 4.28 (right). Due to the larger overlapping frequency range of the $\hat{\boldsymbol{e}}_r$ and $\hat{\boldsymbol{e}}_\phi$ modes the main peak of the boost factor (green), where Gaussian beam shapes occur, is now larger than in the 22 GHz case. Making the boost factor width much smaller as in the examples, which we have discussed in figure 4.29 (top right), would lead to a situation where the two modes $\hat{\boldsymbol{e}}_r$ and $\hat{\boldsymbol{e}}_\phi$ do not overlap at all.

In figure 4.31 we show the E_y beam shapes corresponding to the frequencies that are marked with green vertical lines in figure 4.28 (right). Compared to the 22 GHz beam shapes in figure 4.30 we observe now on top of the characteristic $\sin^2\phi$ and $\cos^2\phi$ beam shapes a ring like structure. We interpret these structures as a manifestation of the radial symmetric tiles, since the number of the rings corresponds to the number of the tiles. For the larger frequency / smaller wavelength that is considered here the diffraction from the tiles itself is small. Therefore, the aligned tiles can be seen as resonant subsystems of the booster and in the beam shape we see for each tile the emitted E-field as a ringlike structure.

Finally let us also compare the 80 disk case, which was discussed in this section to the 20 disk case, which was discussed in section 4.8.2.1. In the 20 disk case only three radial symmetric tiles were present, while in the 80 disk case eight tiles correspond to one disk. Furthermore the radius in the 20 disk case is 15 cm, while in the 80 disk case the radius is 50 cm. In the 20 disk case the shift between the 1D model, cf. figure 4.27 (left) and the tiled result was around 30 MHz, while in the 80 disk case it is around 10 MHz. This observation is due to the fact that in the 80 disk case the radius is larger and therefore the shift is less severe. However, in the 80 disk case the tiling effects are much stronger. Therefore the shift between the $\hat{\boldsymbol{e}}_r$ and $\hat{\boldsymbol{e}}_\phi$ mode is much more severe as in the 20 disk case.

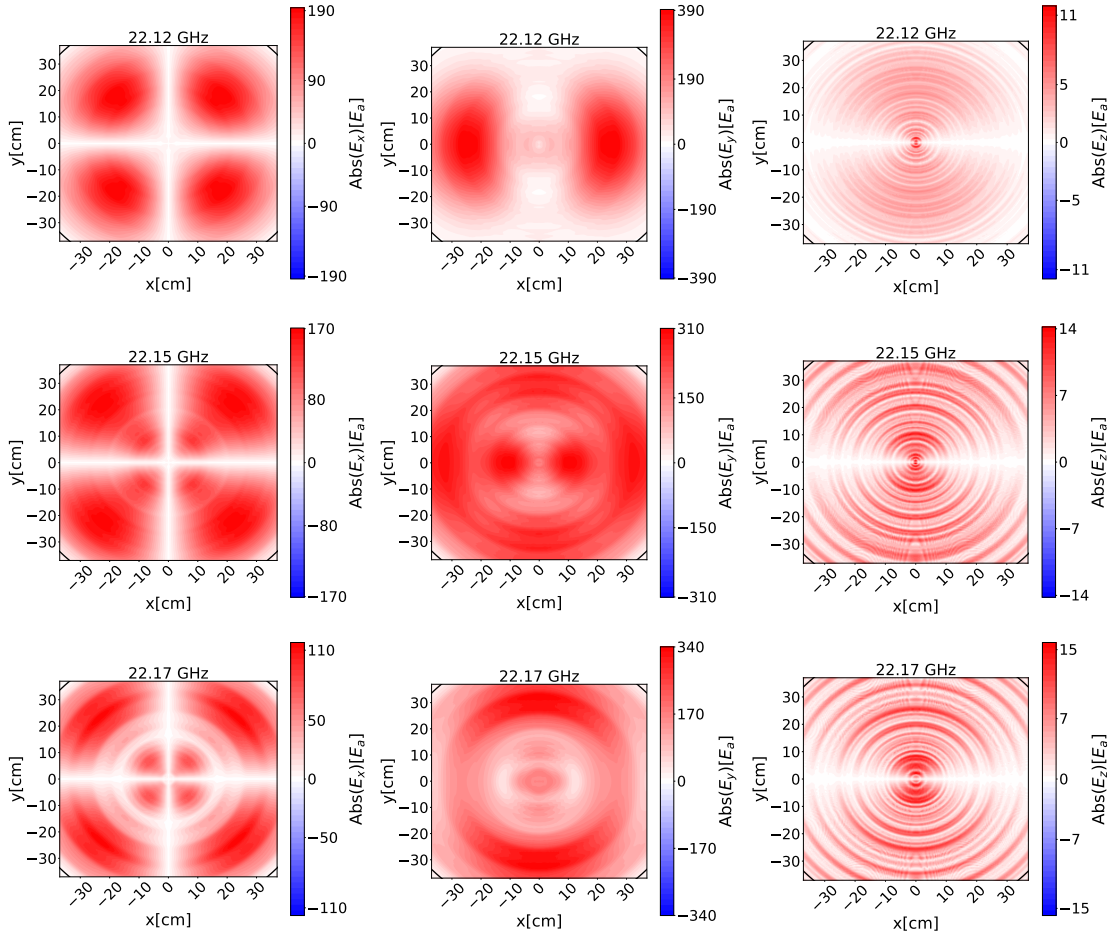

Figure 4.30: Beam shapes for the full scale MADMAX setup at $z = 15\,\text{cm}$ away from the outermost disk of the booster. We show the beam shapes for the marked frequencies in figure 4.28 (left) from top to bottom. The fields are computed with the 2D3D method and therefore it is possible to compute all E-field components: E_x (left), E_y (middle), E_z (right). The distances of the dielectric disks are optimized to give a boost factor with 50 MHz bandwidth around 22 GHz.

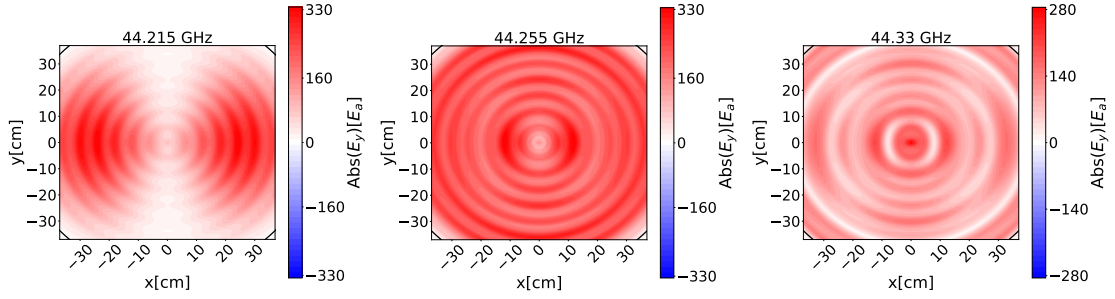

Figure 4.31: Beam shapes for the full scale MADMAX setup at $z = 8\,\text{cm}$ away from the outermost disk of the booster. We show the beam shapes for the marked frequencies in figure 4.28 (right). The fields are computed with the 2D3D method and the distances of the dielectric disks are optimized to give a boost with 100 MHz bandwidth around 44 GHz.

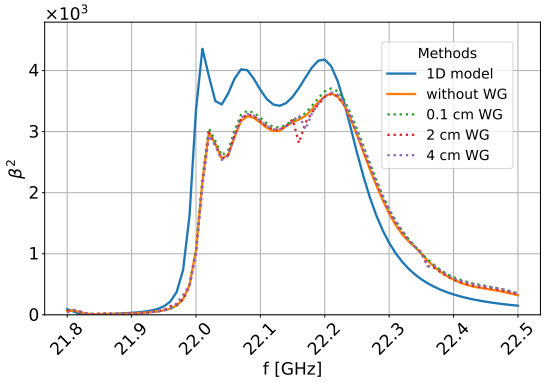

Figure 4.32: Power boost factor for the prototype booster with waveguide (WG) surrounding. The one dimensional model (blue), which includes no waveguide, is compared to several three dimensional calculations that are done with the 2D3D approach. The orange solid curve represents the power boost factor without surrounding waveguide. The dotted lines represent the situation where a cylindrical waveguide surrounds the booster. The distance of the waveguide to the outer rims of the dielectric disk is varied. The green, red and purple cases show the case of a waveguide which has a distance of 0.1 cm, 2 cm and 4 cm to the outer rims of the dielectric disks, respectively. No significant reduction compared to the case without waveguide is observed.

4.8.3 Waveguide surroundings

In a realistic dielectric haloscope the disks are not completely in free space but placed inside a cryogenic tube within the magnet bore. However, there is still a gap between the cryogenic tube and the disk rims. Here we investigate if the cryogenic tube has any influence on the emitted photon signal.

The cryogenic tube is modeled as a perfectly conducting circular waveguide. The circular waveguide has a radius that is larger than the disk radius. All considerations in this sections are for the prototype booster with 20 dielectric disks and radius $R = 15\,\text{cm}$. We vary the distance between waveguide and the outer rims of the dielectric disks. In figure 4.32 we show the 250 MHz bandwidth case for the prototype booster. For all shown distances (dotted lines) between circular waveguide and outer rims no significant reduction of the boost factor is observed.

The reason why the boost factor is not significantly influenced by an outer waveguide is very clear from the previous section 4.8.1 where diffraction effects are discussed. It was found that due to the three dimensional effects, the main field components fall off towards the rims of the disks. Therefore they cannot excite a significant resonance inside the waveguide. Resonances inside the waveguide can only be induced by the axion-like E-field, which is of the order one and may be the cause of the dip that we observe in figure 4.32 around 22.15 GHz.

In figure 4.32 we show the effects of the waveguide for the prototype booster. However, the effects for the full scale MADMAX experiment are expected to be much smaller, since the disks of the full scale MADMAX experiment have a much larger radius.

4.9 Summary

Open axion haloscopes search for axions from the dark matter halo and are – contrary to axion cavity searches – open systems. To the class of open axion haloscopes belong among others dish antennas and dielectric haloscopes. In an axion dark matter background magnetized material discontinuities lead to the emission of electromagnetic radiation with a photon dispersion. The simplest setup that is using this principle for axion dark matter detection is a dish antenna, which

is a magnetized perfect electric conductor. Dielectric haloscopes contain magnetized dielectric disks and therefore host more magnetized interfaces than a dish antenna. In dielectric haloscopes the feeble radiation from the interfaces can be resonantly enhanced in order to discover axion dark matter. The amount of amplification in dielectric haloscopes is expressed in terms of power boost factor β^2.

In this chapter two independent methods in order to calculate the electromagnetic fields in open axion haloscopes in three dimensions were introduced. First, the "recursive propagation approach" (RFP) uses integral formulas to propagate the electromagnetic fields between the involved interfaces back and forth. One possible propagation approach relies on the Fourier diffraction theory. The recursive Fourier propagation approach is applied to the examples of a dish antenna and a dielectric disk. More complex cases with the recursive Fourier propagation approach are studied in Ref. [88]. Propagation approaches, which take into account the vectorial nature of the electromagnetic fields, have also been studied for the case of a dish antenna. The second approach is based on the finite element method and can be applied to radial symmetric geometries even though the external B-field, that magnetizes the interfaces, is linearly polarized. The method is called "2D3D approach", since the calculation is effectively done in two dimensions and yields the full three dimensional result. We applied the 2D3D approach to simple benchmark cases such as a dish antenna and a dielectric disk but also to more complicated cases such as dielectric haloscopes with many dielectric disks. The 2D3D approach and the RFP were successfully validated against each other and therefore pave the way towards a realistic modeling of open axion haloscopes. They are inevitable in order to calculate the electromagnetic fields for more complicated setups such the MAMDAX dielectric haloscope, where standard three dimensional finite element solutions are computationally challenging due to a large domain size.

In this chapter we have computed the explicit field configuration that is emitted by a dish antenna including near field and boundary charge effects. Furthermore we have studied axion velocity effects on the radiation pattern of the dish antenna. The diffraction pattern is shifted when a finite axion dark matter velocity is considered. In case of a detection this shift can be used to deduce the direction of the cold axion dark matter wind.

Dielectric haloscopes with 20 and 80 dielectric disks are also studied. The setups are motivated by the MADMAX prototype and the full scale MADMAX setup respectively. We studied diffraction, near field, surrounding and disk tiling effects with the three dimensional 2D3D method. Most importantly, none of the studied three dimensional effects reduced the emitted signal by orders of magnitude. We can therefore conclude that from the point of view of the studied three dimensional effects the MADMAX haloscope is feasible.

In detail we found that diffraction effects shift the power boost factor resonance frequencies in dielectric haloscopes with respect to the one dimensional calculation. The shift to larger frequencies is less severe for larger disk radii and larger frequencies. The coupling to a Gaussian beam can lead to a power boost factor reduction (with respect to a one dimensional model) by 30%-40%. Although diffraction effects vanish in the infinite radius or frequency limit, the power reduction due to a Gaussian antenna coupling happens always in the specified range and does not reduce with increasing disk radius or frequency. Near field effects are negligible if the disks are assumed to be perfect. Surrounding waveguides do not influence the emitted signal, since the E-fields inside the dielectric haloscope fall off towards the rims of the disks. In reality the dielectric disks are not perfect but are tiled together from many lanthanum aluminate pieces. We found that disk tiling has the largest effect on the power boost factor, since it can introduce non Gaussian beam shapes which reduce the power coupling to a Gaussian antenna. This can lead to a power boost factor reduction of 40% to 50% in the most extreme cases, that were studied in this thesis.

Note that the disk distances of the dielectric haloscope have been optimized for a large power boost factor in a certain frequency interval. The optimization was done with a one dimensional

model. The stated reductions due to 3D effects is with respect to the one dimensional model. A potential future study could investigate if the reduction from the 3D effects could be minimized by readjusting the dielectric disks distances which were originally optimized with the one dimensional model.

Chapter 5

Axion quasiparticles and the quest for dark matter

The previous chapters of this thesis focused on axions in particle physics. However, axions can also be established as quasiparticles in condensed matter systems. To be very clear, these quasiparticles are not the same axions that we have discussed in the previous part of this thesis. Axions in condensed matter systems are quasiparticles and the particle physics axions are real particles.

Contrary to particle physics axions, axion quasiparticles (AQs) were proposed only very recently in topological magnetic insulators (TMI) [17]. AQs can also exist in Weyl semimetals, where they have already been detected [113]. The suggested model in [113] for the AQ has the famous $\boldsymbol{E} \cdot \boldsymbol{B}$ coupling, but other terms of the Klein Gordon equations make the AQs in Weyl semimetals different from the particle physics axions. We therefore consider only AQs in TMI in this chapter. Contrary to AQs in Weyl semimetals the AQs in TMIs have not been detected so far. The reason why AQs are also called axions is because they couple to electromagnetism exactly as the particle physics axions do.

Studying AQs in condensed matter systems is very appealing, since axions in particle physics elude detection until today. However, the idea of AQs in TMIs is very new and it has also not been demonstrated experimentally that one can really establish them in TMIs. On the road to a direct detection of AQs in TMIs one needs a detailed calculation of the expected signals. In section 5.2 we present such a calculation for a THz transmission experiment. We discuss explicitly the interface conditions for the electromagnetic and AQ fields. Furthermore we include magnon and photon losses.

In section 5.3 we assume that TMI materials with AQs can be established. We then show that – through resonant mixing – these materials can be used to search for dark matter axions (DAs) in the meV range. Contrary to previous calculations the presented signal calculation takes into account appropriate interface conditions for all fields. The influence of magnon and photon losses is discussed in order to specify benchmark TMIs that are suited for DA direct detection.

5.1 Realization of axion quasiparticles in topological magnetic insulators

In this section we give a brief review on TMIs and how dynamical AQs can be realized in them. The original idea of AQs in TMIs was first proposed in Ref. [17]. In this section we summarize the main results and give some additional informations. In the following sections we focus on how dynamical AQs in a TMIs can be detected (section 5.2) and how they can be used to search for

DAs (section 5.3).

In addition to the Lagrangian of classical electrodynamics it is possible to include an additional term [17]:

$$\frac{\Theta}{2\pi}\frac{\alpha}{2\pi}\boldsymbol{E}\cdot\boldsymbol{B}, \tag{5.1}$$

which is in agreement with all symmetries of the SM. α is the fine structure constant. If Θ is a constant the term in equation (5.1) can be written as a total derivative and therefore does not enter in the equations of motions. However, the Θ term in equation (5.1) can play a role if materials with constant nonzero Θ exists. Then Θ jumps discontinuously from zero to a non-zero value if the material with constant and nonzero Θ is for example surrounded by vacuum, which has $\Theta = 0$. It can be shown [17, 20] that the physical observables do not change if Θ is shifted by multiples of 2π. A consequence of this is that if time reversal symmetry is conserved only $\Theta = 0$ and $\Theta = \pi$ are allowed. Normal insulators are classified by $\Theta = 0$, while materials with $\Theta = \pi$ are called time reversal topological insulators [114, 115].

The authors of [17] discuss that in an antiferromagnetic phase the time reversal symmetry can be broken. As a consequence Θ is not fixed to 0 or π anymore. In the antiferromagnetic phase magnetic fluctuations can arise. The magnetic fluctuations can be described by *longitudinal spin waves*. The quanta of the spin wave are called magnons [116]. The magnetic fluctuations introduce a dynamical part to the Θ term: $\Theta \to \Theta + \delta\Theta(\boldsymbol{x}, t)$ [17] , where $\delta\Theta(\boldsymbol{x}, t)$ is the dynamical axion field in a TMI. The dynamical axion couples to photons which results in the axion polariton [17]. Due to the fact that a TMI is also an antiferromagnet they are also called axionic topological antiferromagnet [19]. In this thesis the term TMI is mostly used.

The authors in [117] discuss a concrete realization of a TMI which they call axionic antiferromagnet insulator. They show explicitly that the dynamical axion field arises due to a chiral anomaly, when Dirac quasiparticles in the antiferromagnet are coupled to the electromagnetic fields. The dynamical axion field is therefore also a quasiparticle.

Transversal spin waves in antiferromagnets have been studied already a long time ago. In figure 5.1 a semiclassical picture of a transversal spin wave in a one dimensional spin chain [118] is shown. The spins precess around an external magnetic field or around a magnetic anisotropy field of the material. In the ground state all spins precess at the same frequency and magnitude [118]. However, there can be higher spin waves modes. An example of a normal mode (spins on both sublattices precess in the same direction) is shown in figure 5.1. The precession of the spins can be resonantly enhanced by applying an external radio frequency (rf) B-field. This situation is then called antiferromagnetic resonance. The axion quasiparticles are associated to longitudinal spin wave modes. These correspond to fluctuations in the z-component of the spins that are shown in figure 5.1. The authors of Ref [17] realized that the longitudinal spin wave $\delta\Theta$ couples to $\boldsymbol{E}\cdot\boldsymbol{B}$.

The mass of the AQ is determined to a good approximation by the antiferromagnetic resonance frequency [19]:

$$m_\Theta = \gamma\sqrt{2H_E H_A + H_A^2} + \gamma H^e, \tag{5.2}$$

where $\gamma = g\mu_B$ is the gyromagnetic ratio, μ_B the Bohr magneton, $g \approx 1$ the Landé factor, H^e is an externally applied magnetic field and H_A is a material specific anisotropy field that guarantees that the spins in figure 5.1 are aligned and do not constantly change their z-direction [118]. The exchange field H_E describes the exchange interaction of two neighboring spins. If the material is doped, a doping factor x in front of the square root [19] in equation (5.2) has to be introduced. The mass m_Θ can differ for different materials due to different doping, H_A and H_E values. Furthermore it is important that the AQ mass can be tuned by an external field H^e. Note that in [19] a further factor related to the nearest neighbor hopping appears in the expression for the AQ mass. Here this factor is set directly to one which is a good approximation and is also done later on in [19].

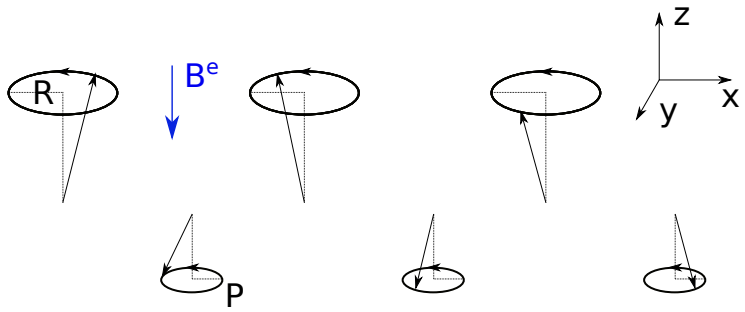

Figure 5.1: Semi classical picture of a normal spin wave mode in an antiferromagnetic spin chain. The magnetic field points in the negative z-direction. The spins in the upper row precess around the magnetic field with a positive S_z spin-component, while the spins in the lower row precess around a magnetic field with a negative S_z spin-component. The radii R and P shown in the figure are different for the spins in the upper and lower row, while also the precession frequencies can be different [118]. The figure is adapted from [118].

Dynamical AQs have not been detected in TMIs yet. However, several materials have been proposed that can host AQs. In [17, 19] Bi_2Se_3 doped with Fe impurities was suggested. In this chapter we follow this proposal. However, it has to be kept in mind that there are more material candidates that might host dynamical AQs.

The B-field dependence of the AQ mass in the chosen benchmark material is given by [19]:

$$m_\Theta = \left(0.12\left(\frac{B^e}{2\,\mathrm{T}}\right) + 0.6\right)\ \mathrm{meV}, \tag{5.3}$$

where $\gamma H_E = 1\,\mathrm{meV}$, [119], $\gamma H_A = 16\,\mathrm{meV}$ [120] and doping $x = 0.035$ [121] was used. The AQ 'decay constant' scales as [19]:

$$f_Q^2(B^e) = (190\ \mathrm{eV})^2\ \frac{m_\Theta(B^e = 2\,\mathrm{T})}{m_\Theta(B^e)}. \tag{5.4}$$

Form f_Q^2 the quantity:

$$b^2 = \frac{\alpha^2 (B^e)^2}{4\pi^3 \epsilon f_Q^2} = 0.34\ \mathrm{meV}^2 \left(\frac{B^e}{2\,\mathrm{T}}\right)^2 \left(\frac{100}{\epsilon}\right)\left(0.12\left(\frac{B^e}{2\,\mathrm{T}}\right) + 0.6\right) \tag{5.5}$$

can be derived.[1] In section 5.2 the importance of the parameter b for the polariton dispersion relation is pointed out. In [17] slightly different values for an external B-field of 2 T are found: $m_\Theta = 2\,\mathrm{meV}$, $b = 0.5\,\mathrm{meV}$ at $B^e = 2\,\mathrm{T}$. However, it is important to point out that both Refs. [17, 19] are not doing anything wrong in the AQ mass estimation. The results can be seen as a rough mass estimate and therefore differences can appear. As it is shown later, more important than the exact AQ mass value, is the dependence on the external B-field. In the end the mass of the AQ will depend mainly on material details such as the exact amount of doping. In the next section it is pointed out how all parameters of a TMI can be determined by comparing future measurements to the presented calculations. In this thesis the relations in the equations (5.3)-(5.5) are going to be used in all results. From equation (5.3) it becomes clear that typical AQ masses correspond to THz frequencies.

[1] The authors of [19] use a different convention for 1 T. In their convention $1\,\mathrm{T} = 194 \times \sqrt{4\pi}\ \mathrm{eV}^2$. We use the convention $1\,\mathrm{T} = 194\ \mathrm{eV}^2$

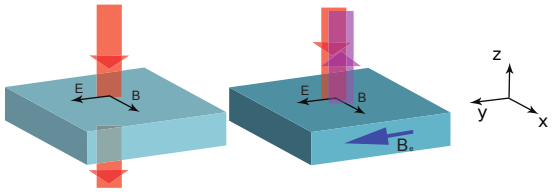

Figure 5.2: Attenuated total reflection method on a sample of TMI. The figure is taken from [17]. THz electromagnetic radiation (red) hits a layer of TMI. If no external B-field B^e is applied there is no mixing between AQs and photons (left). The material behaves effectively as a normal dielectric with a Θ surface term. When an external B-field $\boldsymbol{B}^e = B^e \hat{\boldsymbol{e}}_y$ is applied (right) there is a strong $\boldsymbol{E} \cdot \boldsymbol{B}^e$ mixing what can lead to total reflection of the THz radiation [17].

5.2 Detecting axion quasiparticles in topological magnetic insulators

AQs in TMIs can be detected with THz transmission spectroscopy. The THz sources are required since the mass of the AQ was predicted to be in the THz (meV) regime [17, 19]. In figure 5.2 a setup of the idea from [17] is shown. If no static external B-field (left) is applied, there is no strong $\boldsymbol{E} \cdot \boldsymbol{B}$ coupling and therefore the electromagnetic fields do not couple to the AQ. In this case the transmission spectrum for the incoming THz radiation (red) is not affected by the AQs. It is the spectrum of an ordinary topological insulator (TI), i.e. a dielectric material with a Θ term. If a strong and external B-field is present (right figure in 5.2) the AQs and photons couple, what can lead to total reflection of the incoming THz radiation. This was first shown in [17]. The goal of the following two sections is to work out a one dimensional signal calculation, which was not provided in Ref. [17]. The signal calculation includes reflection and transmission coefficients for arbitrary laser frequencies and TMI sample thicknesses. We also include material loss terms and appropriate interface conditions for all fields. The calculation is also compared to the case when no dynamical AQ is present and therefore important for future THz transmission experiments (which are also called attenuated total reflection (ATR) experiments) in order to discriminate between the case of a dynamical AQ and the case of no AQ.

5.2.1 Axion electrodynamics and Boundary conditions

In this section the axion-Maxwell equations for a TMI are reviewed. A one dimensional model and the correct interface conditions for all involved fields are discussed. Based on the one dimensional model the reflection and transmission coefficients for THz electromagnetic radiation that hits a TMI are computed.

5.2.1.1 General formulation

The macroscopic axion-Maxwell equations for a three dimensional TMI [17] are:

$$\begin{aligned}
\nabla \cdot \boldsymbol{D} &= \rho_f - \kappa \nabla(\delta\Theta + \Theta) \cdot \boldsymbol{B}, && (5.6)\\
\nabla \times \boldsymbol{H} - \partial_t \boldsymbol{D} &= \boldsymbol{J}_f + \kappa(\boldsymbol{B}\partial_t(\delta\Theta + \Theta) - \boldsymbol{E} \times \nabla(\delta\Theta + \Theta)), && (5.7)\\
\nabla \cdot \boldsymbol{B} &= 0, && (5.8)\\
\nabla \times \boldsymbol{E} + \partial_t \boldsymbol{B} &= 0, && (5.9)\\
\partial_t^2 \delta\Theta - \sum_{x,y,z} v_i^2 \partial_i^2 \delta\Theta + m_\Theta^2 \delta\Theta &= \Lambda \boldsymbol{E} \cdot \boldsymbol{B}, && (5.10)
\end{aligned}$$

where $\delta\Theta$ is the axion field, $\Theta \in [0, \pi]$ a constant, $\kappa = \frac{\alpha}{\pi}$, $\Lambda = \frac{\alpha}{4\pi^2 f_Q^2}$, $f_Q^2 = 2g^2 J$ the AQ decay constant, J the stiffness of the spin wave [17], v_i is the spin wave velocity in x, y and z direction, m_Θ the spin wave mass and the electromagnetic fields $\boldsymbol{E}$, $\boldsymbol{B}$, $\boldsymbol{D}$, $\boldsymbol{H}$ are defined as in section 3.1. ρ_f is the free charge density and $\boldsymbol{J}_f$ the free current density which fulfill the continuity equation $\nabla \cdot \boldsymbol{J}_f + \dot{\rho}_f = 0$ as in usual electrodynamics. Note, it is important to also write down the Θ term in the equations above. The Θ term is constant in the TMI, but zero in vacuum. Therefore the application of the nabla operator gives a delta function, i.e. a boundary charge term, at the boundaries of the TMI.

In analogy to the axion-Maxwell equations in particle physics the equations (5.6) and (5.7) can be rewritten such that the terms, that come with the dynamical AQ field $\delta\Theta$, can be interpreted as additional polarization and magnetization term:

$$\begin{aligned} \nabla \cdot \boldsymbol{D}_\Theta &= \rho_f, && (5.11)\\ \nabla \times \boldsymbol{H}_\Theta - \partial_t \boldsymbol{D}_\Theta &= \boldsymbol{J}_f, && (5.12)\\ \nabla \cdot \boldsymbol{B} &= 0, && (5.13)\\ \nabla \times \boldsymbol{E} + \partial_t \boldsymbol{B} &= 0, && (5.14) \end{aligned}$$

with

$$\begin{aligned} \boldsymbol{D}_\Theta &= \boldsymbol{D} + \kappa(\Theta + \delta\Theta)\boldsymbol{B}, && (5.15)\\ \boldsymbol{H}_\Theta &= \boldsymbol{H} - \kappa(\Theta + \delta\Theta)\boldsymbol{E}. && (5.16) \end{aligned}$$

To derive interface conditions for the electromagnetic fields we consider two domains which are labeled 1 and 2 in the following. Both domains have different ϵ, μ, Θ. Here we assume this general case, however we want to point out explicitly that the case of one medium being vacuum and the other one a TMI is included in this consideration. In analogy to the derivation of the interface conditions for the axion-Maxwell equations in particle physics we transform the equations (5.11) -(5.14) to their integral representation and apply the divergence/ Stokes' theorem to an infinitesimal volume/surface element. In the limit that the infinitesimal volume/surface elements shrink to zero this leads to the following interface conditions for the electromagnetic fields:

$$\begin{aligned} \boldsymbol{n} \times (\boldsymbol{E}_2 - \boldsymbol{E}_1) &= 0, && (5.17)\\ \boldsymbol{n} \cdot (\boldsymbol{D}_{\Theta,2} - \boldsymbol{D}_{\Theta,1}) &= \sigma_S, && (5.18)\\ \boldsymbol{n} \cdot (\boldsymbol{B}_2 - \boldsymbol{B}_1) &= 0, && (5.19)\\ \boldsymbol{n} \times (\boldsymbol{H}_{\Theta,2} - \boldsymbol{H}_{\Theta,1}) &= \boldsymbol{J}_S, && (5.20) \end{aligned}$$

where σ_S and $\boldsymbol{J}_S$ are free surface charge and current densities, which are assumed to be zero in the following. $\boldsymbol{n}$ is a unit vector pointing from domain 1 to domain 2. It is important to stress that equations (5.17)-(5.20) are interface conditions and not boundary conditions. As we have described above, interface conditions follow form the differential equations in their integral form. On the other side boundary conditions can be applied at the boundary of a domain in which a partial differential equation is solved. Boundary conditions do not follow from the integral representation of the differential equation. This is also the reason why the interface conditions are specified only for the electromagnetic fields and not for the dynamical axion field $\delta\Theta$. Consider for example the situations where a TMI is surrounded by a non-topological material ($\Theta = 0$). In this case only interface conditions are needed for the electromagnetic fields since they exist in the TMI and also in the neighboring non-topological material. In turn the dynamical AQ only exists in the TMI. Therefore no interface conditions, but only boundary conditions for the AQ are needed in this case. A more detailed discussion of this topic is given in section 5.2.2, where the reflection and transmission coefficients are calculated explicitly for a layer of TMI that is surrounded by vacuum.

5.2.1.2 One dimensional model

To develop a one dimensional model we consider the case that all fields depend only on the z-coordinate and time t. Furthermore all fields are taken to be transverse fields, i.e. $B_z = H_z = D_z = E_z = 0$. Taking into account all assumptions the equations (5.6)-(5.10) reduce on a domain with constant Θ to:

$$\partial_z \begin{pmatrix} -H_y \\ H_x \end{pmatrix} - \partial_t \begin{pmatrix} D_x \\ D_y \end{pmatrix} - \boldsymbol{J}_f = \kappa \left[\begin{pmatrix} B_x \\ B_y \end{pmatrix} \partial_t \delta\Theta + \begin{pmatrix} -E_y \\ E_x \end{pmatrix} \partial_z \delta\Theta \right], \tag{5.21}$$

$$\partial_z \begin{pmatrix} -E_y \\ E_x \end{pmatrix} + \partial_t \begin{pmatrix} B_x \\ B_y \end{pmatrix} = 0, \tag{5.22}$$

$$\partial_t^2 \delta\Theta - v_z^2 \partial_z^2 \delta\Theta + m_\Theta^2 \delta\Theta = \Lambda(E_x B_x + E_y B_y), \tag{5.23}$$

where it is assumed that no free charge density is involved $\rho_f = 0$.[2] The interface conditions (5.18) and (5.19) are trivially fulfilled in the one dimensional model, since the z-components of all electromagnetic fields vanish and $\boldsymbol{n} = \hat{\boldsymbol{e}}_z$.

5.2.1.3 Linearization

The sources in equation (5.21) and (5.23) are non-linear and therefore an analytical treatment in general does not seem to be possible. However, we are interested in the situation that a strong and static external B-field $\boldsymbol{B}^e = B^e \hat{\boldsymbol{e}}_y$ is present. Thus we describe in the following under what assumptions the equations can be linearized in the strong external B-field. The total B-field is divided into a reaction field and an external field $\boldsymbol{B} \to \boldsymbol{B}^e + \boldsymbol{B}$. In addition the free current $\boldsymbol{J}_f$ is split into a part which is the source of $\boldsymbol{B}^e$ and a reaction part: $\boldsymbol{J}_f \to \boldsymbol{J}_{f0} + \boldsymbol{J}_f$. $\boldsymbol{B}^e$ fulfills $\nabla \times \boldsymbol{H}_e = \boldsymbol{J}_{f0}$ and $\boldsymbol{J}_{f0}$ the continuity equation $\nabla \cdot \boldsymbol{J}_{f0} = 0$. With these assumptions the resulting equations are:

$$\partial_z \begin{pmatrix} -H_y \\ H_x \end{pmatrix} - \partial_t \begin{pmatrix} D_x, \\ D_y \end{pmatrix} - \sigma \begin{pmatrix} E_x \\ E_y \end{pmatrix} = \kappa \left[\begin{pmatrix} B_x \\ B^e \end{pmatrix} \partial_t \delta\Theta + \begin{pmatrix} -E_y \\ E_x \end{pmatrix} \partial_z \delta\Theta \right], \tag{5.24}$$

$$\partial_z \begin{pmatrix} -E_y \\ E_x \end{pmatrix} + \partial_t \begin{pmatrix} B_x \\ B_y \end{pmatrix} = 0, \tag{5.25}$$

$$\partial_t^2 \delta\Theta - v_z^2 \partial_z^2 \delta\Theta + m^2 \delta\Theta = \Lambda(E_x B_x + E_y B^e), \tag{5.26}$$

where the reaction current $\boldsymbol{J}_f$ was now replaced with the loss term $\sigma \boldsymbol{E}$ (Ohm's law). Furthermore it was used in equation (5.24) and (5.26) that the external field B^e is much larger than the reaction B-field that is parallel to the external B-field. The B-field was split up into an external and reaction part. However, we do not split up the E-field into an external and reaction part, i.e. the E-field in the equations includes external and reaction fields. An external E-field could be for example a laser field that impinges on the TMI. In the following we distinguish the two cases that an external laser field is parallel or orthogonal to the external B-field.

If the external B-field $\boldsymbol{B}^e = B^e \hat{\boldsymbol{e}}_y$ is parallel to the strong laser field, that is included in the E_y-component, it is obvious that $B^e \partial_t \delta\Theta \gg \partial_z \delta\Theta E_x$ since

$$B^e \frac{\partial_t \delta\Theta}{\partial_z \delta\Theta} = 3 \times 10^4 \frac{\mathrm{V}}{\mathrm{m}} \left(\frac{B^e}{1\,\mathrm{T}} \right) \tag{5.27}$$

and E_x is a small reaction field. In equation (5.27) a typical velocity $v_s = \frac{\partial_t \delta\Theta}{\partial_z \delta\Theta}$ that is of the order of the spin wave velocity $v_s = 10^{-4}$ [122] was used. The non-linear term in the second component

[2] This does not mean that $\boldsymbol{J}_f$ is also zero. ρ_f and $\boldsymbol{J}_f$ are connected via a continuity equation. If $\rho_f = 0$, $\boldsymbol{J}_f$ has to fulfill $\nabla \cdot \boldsymbol{J}_f = 0$.

on the right hand side (rhs). in equation (5.24) can therefore be neglected. The term $B_x\partial_t\delta\Theta$ in the first component of the source term of equation (5.24) includes only reaction fields and is therefore much smaller than the term $E_y\partial_z\delta\Theta$ which also includes the external laser field in E_y. However, also the term $E_y\partial_z\delta\Theta$ is nonlinear and has to be dropped for an analytical treatment. This can be justified with two arguments: (1) from equation (5.25) it is clear that $\partial_t B_y = -\partial_z E_x$ and therefore due to $H_y \sim B_y$ the source of the first component in equation (5.24) sources the x-component of the reaction E-field and not the y-component. In a reflection and transmission experiment as shown in figure 5.2 the main focus will be on the y-component, since the external B-field is polarized in y-direction and the dynamical axion field mixes only primarily with the E_y-component. This statement will become very clear in section 5.2.2 where the reflection and transmission coefficients are computed explicitly. (2) It can be argued that in the coupled system, cf. equations (5.24)- (5.25) only the magnitude of the source vectors matters. Taking this as the condition under which the linearization can be done leads to the statement that the THz laser amplitude has to be smaller than the value that is given in equation (5.27). Actually realistic E-field amplitudes of THz lasers are always smaller than the value that is specified in equation (5.27). Typical THz sources have a power around $P = 10^{-5}$ W what leads to $E_y = 27\frac{\mathrm{V}}{\mathrm{m}}$ for a beam surface area of 10 mm^2. Only for very small external B-fields the THz laser amplitude is not smaller than the limit that is given in equation (5.27). The nonlinear term E_xB_x in equation (5.26) can also be neglected, since it is much smaller than the term E_yB^e which includes two external fields.

In the case that the external B-field $\boldsymbol{B}^e = B^e\hat{\boldsymbol{e}}_y$ is orthogonal to an external laser the source of the Klein-Gordon equation (5.26) is zero to lowest order in κ. This is due to the fact that in this case the external laser has a E_x and B_y-component and the external B-field has only a y-component. As a consequence the product $\boldsymbol{E}\cdot(\boldsymbol{B}+\boldsymbol{B}^e)$ vanishes. A non zero E_y and B_x component can only be induced via polarization rotation at the interfaces due to a non zero Θ term. However, this mixing is suppressed by κ as one can see from the interface condition (5.20). The phenomenon of polarization rotation due to a nonzero Θ is discussed more in section 5.2.2. The linearization of the source term in (5.26) is justified if the external laser amplitude is smaller than $3\times10^8\frac{\mathrm{V}}{\mathrm{m}}$ $\left(\frac{B^e}{1\,\mathrm{T}}\right)$, where it was assumed that B_x and E_y are of the same order since they are both small reaction fields that can both only be induced by polarization rotation. The second component of equation (5.24) can be linearized if the laser amplitude is below the limit in (5.27). The first component of equation (5.24) can be linearized, i.e. the source terms are neglected, since both include small reaction fields that are only generated via polarization rotation.

In summary, in both cases (external laser E-field parallel and orthogonal to the external B-field) the equations can be linearized:

$$\partial_z^2E_x - n^2\partial_t^2E_x - \mu\sigma\partial_tE_x = 0, \tag{5.28}$$

$$\partial_z^2E_y - n^2\partial_t^2E_y - \mu\sigma\partial_tE_y = \kappa\mu B^e\partial_t^2\delta\Theta, \tag{5.29}$$

$$\partial_t^2\delta\Theta - v_z^2\partial_z^2\delta\Theta + m_\Theta^2\delta\Theta = \Lambda E_yB^e, \tag{5.30}$$

where linear constitutive equations $\boldsymbol{D} = \epsilon\boldsymbol{E}, \boldsymbol{H} = \mu^{-1}\boldsymbol{B}$ are assumed. Furthermore the refractive index $n^2 = \epsilon\mu$ is defined. The material properties $\mu, \epsilon, \sigma, \Theta$ are constants in the equations of motions. Only later the solutions in regions of different $\epsilon, \mu, \sigma, \Theta$ are linked via interface conditions.

The corresponding interface conditions are given in equation (5.17) and (5.20) with $\boldsymbol{n} = \hat{\boldsymbol{e}}_z$. Equation (5.17) remains unchanged after linearization, while the definition of $\boldsymbol{H}_\Theta$ in equation (5.20) changes due to the linearization to $\boldsymbol{H}_\Theta = \boldsymbol{H} + \kappa\Theta\boldsymbol{E}$.

5.2.1.4 Losses

In the linearized equations of motions (5.28)-(5.30) losses appear in the context of a finite conductivity σ. However, magnon losses and losses that mix between magnons and photons are not

included in the model until now. The following equations are the generalizations of the equations (5.28)-(5.30) and now also include all mentioned losses:

$$\boldsymbol{K}\partial_t^2\boldsymbol{X} - \boldsymbol{\Gamma}\partial_t\boldsymbol{X} + \boldsymbol{M}\boldsymbol{X} = 0, \tag{5.31}$$

with

$$\boldsymbol{X} = \begin{pmatrix} E_x \\ E_y \\ \delta\Theta \end{pmatrix}, \quad \boldsymbol{K} = \begin{pmatrix} 1 & 0 & 0 \\ 0 & 1 & \frac{\kappa B^e}{\epsilon} \\ 0 & 0 & 1 \end{pmatrix}, \quad \boldsymbol{\Gamma} = \begin{pmatrix} \Gamma_\rho & 0 & 0 \\ 0 & \Gamma_\rho & \Gamma_{\times,1} \\ 0 & \Gamma_{\times,2} & \Gamma_m \end{pmatrix}, \tag{5.32}$$

$$\boldsymbol{M} = \begin{pmatrix} \frac{k^2}{n^2} & 0 & 0 \\ 0 & \frac{k^2}{n^2} & 0 \\ 0 & -\Lambda B^e & v_z^2k^2 + m_\Theta^2 \end{pmatrix}, \tag{5.33}$$

where $\Gamma_\rho = \frac{\sigma}{\epsilon}$ was defined as the photon loss. Γ_m is the equivalent loss for magnons and $\Gamma_{\times,1/2}$ are mixed losses that can arise when photons and magnons interact. Note, that not all Γ's have the same mass dimension: $[\Gamma_\rho] = 1 = [\Gamma_m]$ and $[\Gamma_{\times,1}] = 3$, $[\Gamma_{\times,2}] = -1$. The approach also gives the possibility to define different refractive indices n and photon losses Γ_ρ for the E_x and E_y components. However, this is only important when polarization rotation effects are considered. In the following polarization rotation effect are computed, however the main effect comes from the Θ-term and not from different refractive indices in x and y-direction. Therefore our assumption that $n_x = n = n_y$ is justified here.

The interface conditions remain the same in the presence of losses, because it is assumed that all losses are bulk losses.

5.2.2 Transmission and reflection coefficients

Li et al. [17] proposed a transmission measurement (cf. figure 5.2) in order to measure the band gap in a TMI polariton spectrum, opened by the presence of the AQ (cf. figure 5.3). In the following, the transmission and reflection coefficients are computed. It is demonstrated how such an experiment can be used to determine all the parameters of interest, including the relevant terms of the loss matrix $\boldsymbol{\Gamma}$.

5.2.2.1 Solution of linearized equations

In the following the equations in a domain, where μ, ϵ and Θ are constants, are solved in general. Domains of different materials will be realized by applying interface conditions in the end. The **lossless case ($\boldsymbol{\Gamma} = 0$)** is discussed first. The dispersion relation for the E_x component (cf. equation (5.28)) is the usual photon dispersion relation:

$$k^2 = n^2\omega^2 =: k_p^2. \tag{5.34}$$

The E_y component mixes with the AQ and for $v_z = 0$ a typical polariton dispersion [18] relation is obtained:

$$\omega_\pm^2 = \frac{1}{2}\Big[\omega_{LO}^2 + \frac{k^2}{n^2}\Big] \pm \frac{1}{2}\Big[\big(\omega_{LO}^2 - \frac{k^2}{n^2}\big)^2 + 4b^2\frac{k^2}{n^2}\Big]^{1/2}, \tag{5.35}$$

where we have defined

$$b^2 := \frac{\kappa\Lambda(B^e)^2}{\epsilon}, \tag{5.36}$$

$$\omega_{LO}^2 := b^2 + m_\Theta^2. \tag{5.37}$$

In figure 5.3 (left) $\omega_\pm$ is shown as a function of the wave number k. The horizontal dashed black lines indicate the gap between m_Θ and ω_{LO} where total reflection is expected. In the plot typical

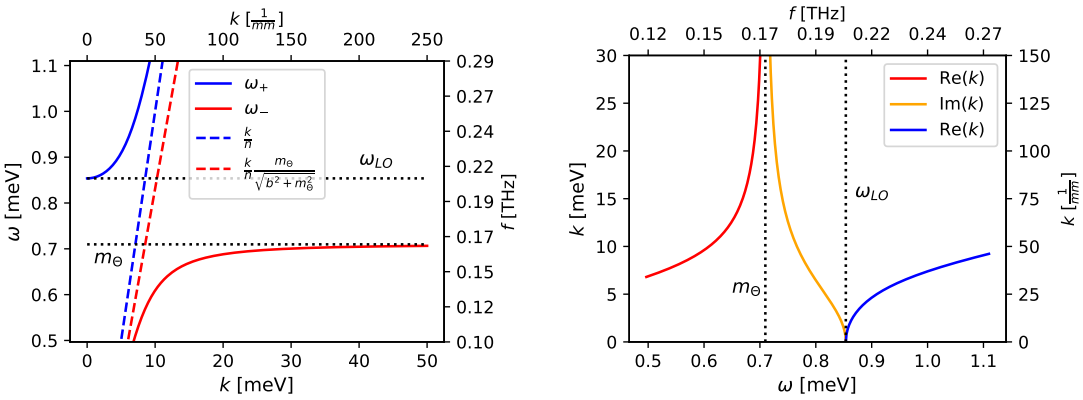

Figure 5.3: Polarition dispersion for the mixing between AQs and photons. The dispersion relation is shown for a spin wave velocity $v_z = 0$. Typical material values for a TMI with an external B-field of $B^e = 2\,\mathrm{T}$ are used: $m_\Theta = 0.72\,\mathrm{meV}, b = 0.5\,\mathrm{meV}$, cf. equation (5.3)-(5.5). Further parameters for the TMI are $n = 10$ and $\mu = 1$ [17]. The left figure shows the $\omega_\pm$ mode which has a bandgap between m_Θ and ω_{LO} (dotted vertical lines). In the right figure the inverse is illustrated. k has only an imaginary part inside the bandgap and no propagating modes exist.

values for a TMI with an external B^e of 2 T are chosen, cf. equation (5.3)-(5.5). The resulting frequencies for m_Θ and ω_{LO} are in the THz regime which explains why THz sources are needed to probe the gap in the dispersion relation. ω_+ converges for large k to a photon dispersion (dashed blue line). ω_- has an almost photon-like dispersion $\omega_- = \frac{k}{n}\frac{m_\Theta}{\sqrt{b^2+m_\Theta^2}}$ (red dashed line) for small k.

Inverting equation (5.35) yields two modes now, namely:

$$k^2 = n^2\omega^2\left[\frac{b^2}{m_\Theta^2 - \omega^2} + 1\right] =: k_\Theta^2. \tag{5.38}$$

From equation (5.38) one can read off directly that in the decoupling limit ($b \to 0$) an ordinary photon dispersion relation is obtained. For ω^2 we got two solutions while the solution for k^2 can be described by a single function. Inside the gap k^2 is negative, i.e. k has an imaginary part and no propagating mode is present. In the following section it is explicitly shown that this leads to total reflection and zero transmission.

The most general solutions that can be written down in a medium are:

$$E_x(z) = \hat{E}_x^+ e^{ik_p z} + \hat{E}_x^- e^{-ik_p z}, \tag{5.39}$$
$$E_y(z) = \hat{E}_y^+ e^{ik_\Theta z} + \hat{E}_y^- e^{-ik_\Theta z}, \tag{5.40}$$
$$\delta\Theta(z) = \delta\hat{\Theta}^+ e^{ik_\Theta z} + \delta\hat{\Theta}^- e^{-ik_\Theta z}, \tag{5.41}$$

where the time dependence $e^{-i\omega t}$ is omitted. After plugging in the solutions into the equations of motions the following relations are obtained:

$$\delta\hat{\Theta}^\pm = \Theta_E \hat{E}_y^\pm, \quad \Theta_E = \frac{\Lambda B^e}{m_\Theta^2 - \omega^2}, \tag{5.42}$$

or equivalently

$$\hat{E}_y^\pm = E_\Theta \delta\hat{\Theta}^\pm, \quad E_\Theta = -\frac{\mu\omega^2\kappa B^e}{k_p^2 - k_\Theta^2}. \tag{5.43}$$

In the following the relations in equation (5.42) are used to reduce the number of unknowns in the ansatz (5.41):

$$\delta\Theta(z) = \Theta_E \hat{E}_y^+ e^{ik_\Theta z} + \Theta_E \hat{E}_y^- e^{-ik_\Theta z}. \tag{5.44}$$

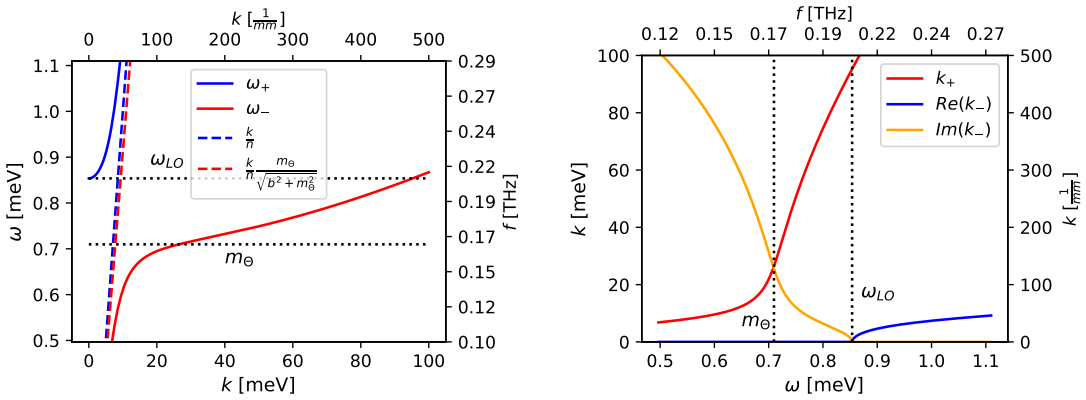

Figure 5.4: Dispersion relation for non vanishing spin wave velocity $v_z \neq 0$. The spin wave velocity in the plot is $v_z = 5 \times 10^{-3}$ and a little bit larger than assumed in the text in order to make the band crossing more visible visible. Typical material values for a TMI with an external B-field of $B^e = 2\,\mathrm{T}$ are used: $m_\Theta = 0.72\,\mathrm{meV}, b = 0.5\,\mathrm{meV}$, cf. equations (5.3)-(5.5). Further parameters for the TMI are $n = 10$ and $\mu = 1$ [17].

The remaining constants $\hat{E}_y^{\pm}$ can be determined by using the interface conditions. This is explicitly shown in section 5.2.2.2. The AQ field $\delta\Theta$ is completely determined, cf. equation (5.44), and no boundary conditions for $\delta\Theta$ have to be applied when for example a layer of TMI surrounded by vacuum is considered. It will become clear in the following that this is a consequence of the $v_z = 0$ limit.

Note, that the relations (5.43) could have also been used to reduce the constants in equation (5.40). However, one can see after a short calculation that in the end the same end result is obtained, no matter if the relation in equation (5.42) or (5.43) are used to reduce the constants.

A finite spin wave velocity $v_z \neq 0$ leads a slightly modified dispersion relation:

$$\omega_\pm^2 = \frac{1}{2}\Big[\omega_{LO}^2 + k^2(v_z^2 + \frac{1}{n^2})\Big] \pm \frac{1}{2}\Big[\big(\omega_{LO}^2 + k^2(v_z^2 - \frac{1}{n^2})\big)^2 + 4b^2\frac{k^2}{n^2}\Big]^{1/2}. \tag{5.45}$$

Equation (5.45) is not a typical polariton dispersion anymore, since the sign of v_z under the square root is positive and not negative. The dispersion relation $\omega_\pm$ is shown in figure 5.4 (left). The nonzero v_z leads to a gap-crossing of the ω_- mode. However, due to the smallness of the spin wave velocity with respect to the speed of light the gap crossing happens at large wave numbers k. Inverting equation (5.45) yields now two modes

$$k_\pm^2 = \frac{1}{2v_z^2}(\omega^2 - m_\Theta^2 + n^2\omega^2 v_z^2) \pm \frac{1}{2v_z^2}\Big(\big(m_\Theta^2 + \omega^2(n^2v_z^2 - 1)\big)^2 + 4\omega^2 n^2 b^2 v_z^2\Big)^{1/2}. \tag{5.46}$$

In the $v_z = 0$ case only one mode for k^2 was obtained, cf. equation (5.38). The functional dependence of equation (5.46) is shown in figure 5.4 (right). The imaginary part of the k_- mode, which was in the $v_z = 0$ part only present inside the gap, keeps also rising outside of the gap for frequencies $\omega < m_\Theta$. The k_+ mode crosses the gap such that for $\omega > \omega_{LO}$ two propagating modes exist. The wavelength of the $+$ mode is always much shorter than the wavelength of the $-$ mode.

The most general solution in the case of non vanishing spin wave velocity is:

$$E_x(z) = \hat{E}_x^+ e^{ik_p z} + \hat{E}_x^- e^{-ik_p z}, \tag{5.47}$$

$$E_y(z) = \hat{E}_y^{++} e^{ik_+ z} + \hat{E}_y^{+-} e^{-ik_+ z} + \hat{E}_y^{-+} e^{ik_- z} + \hat{E}_y^{--} e^{-ik_- z}, \tag{5.48}$$

$$\delta\Theta(z) = \delta\hat{\Theta}^{++} e^{ik_+ z} + \delta\hat{\Theta}^{+-} e^{-ik_+ z} + \delta\hat{\Theta}^{-+} e^{ik_- z} + \delta\hat{\Theta}^{--} e^{-ik_- z}. \tag{5.49}$$

In complete analogy to the case of $v_z = 0$ relations between the unknowns in the ansatz (5.47)-(5.49) can be derived. However, now also boundary conditions for the dynamical axion field would have

to be specified in order to determine all constants. The explicit calculation is not done here, since the difference to the $v_z = 0$ case is expected to be minimal due to the smallness of the spin wave velocity. In the following a qualitative argument is made why the small non zero spin wave velocity will lead only to a minor difference with respect to a calculation with a zero spin wave velocity. Consider an incoming wave which is described by $A_0 e^{ik_p z}$ and which impinges onto a material where two modes are present. The first mode k_s has a wavelength that is much shorter than k_p and the second mode k_l has a much longer wavelength than k_p, i.e. $|k_s| \gg |k_p| \gg |k_l|$. This situation is similar to the situation around ω_{LO} in figure 5.4. Neglecting reflections, the fraction of the amplitudes of the two modes in medium 1 are $\left|\frac{A_1^l}{A_1^s}\right| = \left|\frac{k_a - k_p}{k_p - k_l}\right| \approx \left|\frac{k_s}{k_p}\right| \gg 1$. Therefore the amplitude of long wavelength mode A_1^l is much larger than the amplitude of the short wavelength mode A_1^s. Around ω_{LO} in figure 5.4 (right) the short wavelength mode is k_+ which crosses the gap only due to a finite spin wave velocity. Based on the previous arguments the contribution of this mode can therefore be neglected even though it is in principle present. In the following the spin wave velocity is therefore always set to zero.

If **material losses ($\mathbf{\Gamma} \neq 0$)** are included, the dispersion relations (5.34) and (5.38) are modified. The dispersion relation of the E_x component is:

$$k^2 = n^2\omega^2(1 + i\frac{\Gamma_\rho}{\omega}) =: k_p^2 \tag{5.50}$$

and the dispersion relation for the mixed system of E_y and $\delta\Theta$ is:

$$k^2 = n^2\omega^2\left(1 + \frac{b^2}{-i\Gamma_m\omega + m_\Theta^2 - \omega^2} + i\frac{\Gamma_\rho}{\omega}\right) + n^2\omega\left(\frac{iB^e\left(\frac{\Gamma_{\times,2}\kappa\omega^2}{\epsilon} + \Lambda\Gamma_{\times,1}\right) - \omega\Gamma_{\times,1}\Gamma_{\times,2}}{-i\Gamma_m\omega + m_\Theta^2 - \omega^2}\right) =: k_\Theta^2. \tag{5.51}$$

The dispersion relation in equation (5.51) was written such that the first part does only include the diagonal losses Γ_m and Γ_ρ. The second part includes also mixed losses. In the following mixed losses are neglected, since it is expected that they are much smaller than Γ_ρ and Γ_m. Rewriting the dispersion relation (5.51) without mixed losses gives:

$$k^2 = n^2\omega^2\left(1 + \frac{(m_\Theta^2 - \omega^2)\omega b^2}{\Gamma_m^2\omega^2 + (m_\Theta^2 - \omega^2)^2} + i\frac{\Gamma_m\omega b^2}{\Gamma_m^2\omega^2 + (m_\Theta^2 - \omega^2)^2} + i\frac{\Gamma_\rho}{\omega}\right) =: k_\Theta^2. \tag{5.52}$$

Equation (5.52) makes clear that Γ_ρ always contributes the same loss to the dispersion relation if ω does not vary too much. The case that $\Gamma_m = 0$ but $\Gamma_\rho \neq 0$ is shown in figure 5.5 (left). As one can see the resonance is not affected much, however an almost constant imaginary part is present everywhere due to Γ_ρ. Magnon losses Γ_m are dominant around m_Θ. This can be seen from the third term in equation (5.52) which represents a Lorenzian curve that peaks around $\omega = m_\Theta$ and has a full width at half maximum (FWHM) of Γ_m. In figure 5.5 (center and right) photon losses Γ_ρ are neglected and magnon losses are varied. The larger the magnon loss Γ_m, the larger is the FWHM of the imaginary part that is introduced in the dispersion relation. Therefore the larger Γ_m, the more frequencies which are further away from the gap experience magnon losses, i.e. are damped. Furthermore for large magnon losses the resonant structure becomes less pronounced as can be seen from figure 5.5 (center and right). It becomes therefore immediately clear that large losses will make it harder to confirm that the spectrum is gapped and a dynamical AQ exists. This qualitative statement is worked out more quantitatively in section 5.2.2 where the reflection and transmission coefficients are calculated.

The form of the most general solution in equation (5.39)-(5.41) is in the case of losses still valid.

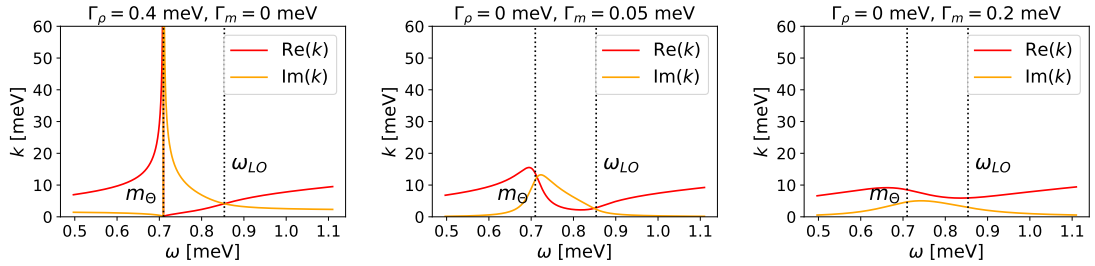

Figure 5.5: Dispersion relation of the axion-polariton for magnon Γ_m and photon Γ_ρ losses. Mixed losses are neglected. In the left figure magnon losses are neglected. Photon losses Γ_ρ introduce an lmost constant imaginary part to the dispersion relation if the chosen frequency interval is not too large. In the center and right figure photon losses are neglected. In the center figure $\Gamma_m = 0.05\,\text{meV}$ and in the right figure $\Gamma_m = 0.2\,\text{meV}$. The larger the magnon loss, the larger is the FWHM of the imaginary part in the dispersion relation. Typical material values for a TMI with an external B-field of $B^e = 2\,\text{T}$ are used: $m_\Theta = 0.72\,\text{meV}, b = 0.5\,\text{meV}$, cf. equations (5.3)-(5.5). Further parameters for the TMI are $n = 10$ and $\mu = 1$ [17].

However, the relations between $\delta\hat{\Theta}$ and $\hat{E}_y$ are modified:

$$\delta\hat{\Theta}^\pm = \Theta_E \hat{E}^\pm, \quad \Theta_E = \frac{\Lambda B^e + i\omega\Gamma_{\times,2}}{-\omega^2 + m_\Theta^2 - i\omega\Gamma_m}, \tag{5.53}$$

or equivalently

$$\hat{E}_y^\pm = E_\Theta \delta\hat{\theta}^\pm, \quad E_\Theta = \frac{\omega^2\kappa\mu B^e + in^2\omega\Gamma_{\times,1}}{k_\Theta^2 - k_p^2}. \tag{5.54}$$

It can be checked that equation (5.53) and (5.54) reduce in the limit $\mathbf{\Gamma} \to 0$ to equation(5.42) and (5.43). Equation (5.53) determines now again (in complete analogy to the case without losses) the dynamical AQ field, cf. equation (5.44).

5.2.2.2 Matrix formalism for many interfaces

The solutions of the one dimensional axion-Maxwell equations in a homogeneous medium were discussed in the previous section. Here $N+1$ media, that are separated by N interfaces, are considered. To describe the layered system we use the same convention as in the matrix formalism for the particle physics axion-photon mixing in section 3.3, cf. figure 3.5. The first interface is at $z_0 = z_1$ and the last interface is at z_N. In the most general case, that we describe here, each medium is characterized by $\Theta_r, \epsilon_r, \mu_r, \mathbf{\Gamma}^r$, $r = 0, \cdots N$. As an example the matrix formalism with $N = 2$ would be suited to describe a single TMI layer that is surrounded by vacuum. The spin wave velocity v_z is set to zero in each medium and the external B-field has the same magnitude and polarization in all media $\boldsymbol{B}^e = B^e\hat{\boldsymbol{e}}_y$. In order to link the solutions in different materials to each other a matrix formalism is developed in this section. This makes it possible to compute the scattering of incoming electromagnetic radiation from a multilayer system. The simplest application is the computation of the reflection and transmission coefficients for THz radiation that hits a layer of TMI. This particular case is discussed in the following section.

The most general ansatz in medium $r = 0, \cdots, N$ is given by:

$$\begin{aligned} E_x^r &= \hat{E}_{x,r}^+ e^{ik_p^r(z-z_r)} + \hat{E}_{x,r}^- e^{-ik_p^r(z-z_r)}, \\ E_y^r &= \hat{E}_{y,r}^+ e^{ik_\Theta^r(z-z_r)} + \hat{E}_{y,r}^- e^{-ik_\Theta^r(z-z_r)}, \\ \delta\Theta^r &= \Theta_E^r \hat{E}_{y,r}^+ e^{ik_\Theta^r(z-z_r)} + \Theta_E^r \hat{E}_{y,r}^- e^{-ik_\Theta^r(z-z_r)}, \end{aligned} \tag{5.55}$$

where on top of the discussion in section 5.2.2.1 different phases are introduced. The expressions for k_p, k_Θ and Θ_E were derived already in equation (5.34), (5.38) and (5.42) for the case $\mathbf{\Gamma} = 0$ and

in equation (5.50), (5.51) and (5.53) for the lossy case $\mathbf{\Gamma} \neq 0$. Applying the interface conditions, cf. equation (5.17) and (5.20) for the electromagnetic fields at z_r yields the following system of equations

$$\boldsymbol{t}_r = \boldsymbol{M}_r^{-1} \cdot \boldsymbol{M}_{r-1} \cdot \boldsymbol{P}_{r-1} \boldsymbol{t}_{r-1}, \tag{5.56}$$

with

$$\boldsymbol{M}_r = \begin{pmatrix} 1 & 1 & 0 & 0 \\ 0 & 0 & 1 & 1 \\ \frac{k_p^r}{\omega\mu_r} & -\frac{k_p^r}{\omega\mu_r} & -\kappa_r\Theta_r & -\kappa_r\Theta_r \\ -\kappa_r\Theta_r & -\kappa_r\Theta_r & -\frac{k_\Theta^r}{\omega\mu_r} & \frac{k_\Theta^r}{\omega\mu_r} \end{pmatrix} \text{ and } \boldsymbol{t}_r = \begin{pmatrix} \hat{E}_{x,r}^+ \\ \hat{E}_{x,r}^- \\ \hat{E}_{y,r}^+ \\ \hat{E}_{y,r}^- \end{pmatrix} \tag{5.57}$$

and

$$\boldsymbol{P}_r = \mathrm{diag}(e^{i\Delta_r^p}, e^{-i\Delta_r^p}, e^{i\Delta_r^\Theta}, e^{-i\Delta_r^\Theta}). \tag{5.58}$$

The phases are defined as: $\Delta_r^\Theta := k_\Theta^r(z_{r+1} - z_r)$ and $\Delta_r^p := k_p^r(z_{r+1} - z_r)$.

The S-Matrix is defined in order to relate the incoming and outgoing field amplitudes in medium 0 and N:

$$\boldsymbol{t}_N = \boldsymbol{S} \cdot \boldsymbol{t}_0. \tag{5.59}$$

For a single interface the S matrix is given by:

$$\boldsymbol{S} = \boldsymbol{M}_1^{-1} \cdot \boldsymbol{M}_0 \cdot \boldsymbol{P}_0 \tag{5.60}$$

and for two interfaces by:

$$\boldsymbol{S} = \boldsymbol{M}_2^{-1} \cdot \boldsymbol{M}_1 \cdot \boldsymbol{P}_1 \boldsymbol{M}_1^{-1} \cdot \boldsymbol{M}_0 \cdot \boldsymbol{P}_0. \tag{5.61}$$

For N interfaces the S matrix is:

$$\boldsymbol{S} = \boldsymbol{M}_N^{-1} \cdot \boldsymbol{M}_{N-1} \cdot \boldsymbol{P}_{N-1} \cdot \boldsymbol{M}_{N-1}^{-1} \cdot \boldsymbol{M}_{N-1} \boldsymbol{P}_{N-2} \cdot \boldsymbol{M}_{N-2} \cdots \boldsymbol{M}_2^{-1} \cdot \boldsymbol{M}_1 \cdot \boldsymbol{P}_1 \boldsymbol{M}_1^{-1} \cdot \boldsymbol{M}_0 \cdot \boldsymbol{P}_0. \tag{5.62}$$

Without loss of generality it is now assumed that the electromagnetic radiation is coming into the system from medium 0. In this case $\hat{E}_{x0}^+$ and $\hat{E}_{y,0}^+$ are known and $\hat{E}_{x,N}^- = 0 = \hat{E}_{y,N}^-$. The other unknown fields can be determined from the S-matrix elements by:

$$\begin{pmatrix} \hat{E}_{x,N}^+ \\ \hat{E}_{x,0}^- \\ \hat{E}_{y,N}^+ \\ \hat{E}_{y,0}^- \end{pmatrix} = \begin{pmatrix} -1 & S_{12} & 0 & S_{14} \\ 0 & S_{22} & 0 & S_{24} \\ 0 & S_{32} & -1 & S_{34} \\ 0 & S_{42} & 0 & S_{44} \end{pmatrix}^{-1} \cdot \begin{pmatrix} -S_{11}\hat{E}_{x0}^+ - S_{13}\hat{E}_{y0}^+ \\ -S_{21}\hat{E}_{x0}^+ - S_{23}\hat{E}_{y0}^+ \\ -S_{31}\hat{E}_{x0}^+ - S_{33}\hat{E}_{y0}^+ \\ -S_{41}\hat{E}_{x0}^+ - S_{43}\hat{E}_{y0}^+ \end{pmatrix}. \tag{5.63}$$

The following section focuses on a $N = 2$ system as an application. However, note that the matrix approach here is fully capable to also describe more complicated systems which consist of more layers. One particular example could be a layered system of different topological insulators with different topological material properties.

5.2.2.3 Layer of topological magnetic insulator

In this section the reflection and transmission coefficients for a layer of TMI are calculated. In the language of the matrix formalism the system has $N = 2$ and therefore three media. Medium 0 and 2 are vacuum while medium 1 is the TMI. The THz laser radiation is coming from medium 0 and hits the layer of TMI. The reflected and transmitted fields can be calculated by using equation (5.63).

It is assumed that the laser is polarized in the y-direction (parallel to the external B-field). In this case the following reflection and transmission coefficients are obtained:

$$T_y = \frac{2i\tilde{k}}{\left(\tilde{k}^2+1\right)\sin\Delta + 2i\tilde{k}\cos\Delta} + \mathcal{O}(\kappa^2), \tag{5.64}$$

$$R_y = -\frac{\left(\tilde{k}^2-1\right)\sin\Delta}{\left(\tilde{k}^2+1\right)\sin\Delta + 2i\tilde{k}\cos\Delta} + \mathcal{O}(\kappa^2), \tag{5.65}$$

where $\tilde{k} = \frac{k_\Theta}{\omega\mu}$, $\Delta := dk_\Theta$ and $d = z_2 - z_1$ is the thickness of the layer with the topological material. The transmission and reflection coefficients are given to lowest order in κ. Note, that also $\tilde{k}$ depends on κ, however the κ dependence of the dispersion relation is ignored in the the Taylor expansion because otherwise the expansion would not be valid around the resonance. The given transmission and reflection coefficients are valid for the case with and without losses since it is assumed that all losses are bulk losses. The dispersion relation in equation (5.51) has to be used to calculate the reflection coefficients with losses. If losses are not included the dispersion relation in equation (5.38) has to be used. To lowest order in κ T_y and R_y agree with the normal transmission and reflection coefficients [58] of a dielectric disk if the coupling b of the AQ to the photon is set to zero, i.e. $k_\Theta \to \omega n$.

On the other hand R_y and T_y do not depend on Θ and κ to lowest order. However, the leading order term of R_x and T_x is at least linear in Θ and κ. Physically this is due to the fact that the incoming laser is polarized in y-direction and a mixing, which is proportional to $\kappa\Theta$, can happen only at the interface, cf. equation (5.20) and (5.57). In the following the focus is therefore on the transmission and reflection coefficients T_y and R_y, where an order one modification, with respect to the spectrum of a normal TI, is expected to arise due to the AQ and photon coupling. The effect in T_x and R_x would be much smaller and of the order $\kappa\Theta$. However, note that once the AQ is found one can also use the E_x-component to determine for example Θ of the material. Another point that can be studied with the x-components is the influence of nonlinear effects. In equation (5.24) is was shown that the laser sources nonlinearly the x-component. This effect is neglected here because the equations are linearized.

In figure 5.6 the full functions for the reflection and transmission coefficients without any losses $\mathbf{\Gamma} = 0$ are shown. The coefficients are shown for different laser frequencies ω and sample thicknesses d. In the left column it is assumed that a dynamical AQ field exists, while in the right column it is assumed that the material is just a normal TI ($\Theta = \pi$) without a dynamical AQ field. If a dynamical AQ is present the dispersion relation k_Θ becomes imaginary between m_Θ and $\omega_{LO} = \sqrt{m_\Theta^2 + b^2}$. The gap between these two frequencies is marked with the two vertical lines. The reflection and transmission coefficients for the y-components are shown in the top and middle row. For large TMI layer thicknesses d all frequencies in the gap are reflected and nothing gets transmitted. This is a direct consequence of the purely imaginary k_Θ in the gap. For small thicknesses within the gap there is no total reflection, since towards ω_{LO} the imaginary part of the dispersion relation decreases and therefore the skin depth of the material increases. When going away from the gap, the figures in the left and right columns agree more and more. This is as expected, since the dispersion relation k_Θ differs only significantly from a normal photon dispersion around the gap. In the bottom row of figure 5.6 the transmission coefficient for the x-component is shown. The difference between the case when a dynamical AQ is present (left) and no dynamical AQ is present (right), is much smaller than in the y-component. This is because due to the mixing at the interface the signal in the x-component is always proportional to $\kappa\Theta$. If no dynamical AQ field is present and the material is just an ordinary TI ($\Theta = \pi$) the transmission T_x is exactly zero. At first sight this is surprising, because also in the case of a normal TI there is mixing at the interface ($\Theta = \pi$) and therefore also a polarization rotation. However, the transmission in the

x-component is zero, since the polarization rotation at the two interfaces cancels each other.

In the figures 5.7 and 5.8 the transmission coefficient T_y including losses is shown. The focus is on the transmission coefficient T_y, since transmission measurements are easier and the effect of AQ and photon mixing is maximal in the y-component, i.e. parallel to the external B-field polarization. We want to stress that TMIs with AQs have not been established so far and therefore also the order of magnitude of the losses is not known. Nevertheless, we want to give a general discussion of magnon and photon losses in the following. Therefore we first assume relatively large losses of the order of $10^{-1} - 10^{-2}\,\mathrm{eV}$. Later we also comment on smaller losses, which – as we show in section 5.3 – will be necessary for axion dark matter detection with TMIs.

In figure 5.7 magnon losses are neglected ($\Gamma_m = 0$) while two different photon losses $\Gamma_\rho = 3 \times 10^{-2}$ (left) and $\Gamma_\rho = 3 \times 10^{-1}$ (right) are shown. In the top row the case of a dynamical AQ in a TMI is shown. In the bottom row the results are compared to the case of a normal TI ($\Theta = \pi$). For large losses Γ_ρ the transmission at large thicknesses becomes smaller independently of the resonance (top right in figure 5.7). This is due to the fact that Γ_ρ appears in the dispersion relation (5.52) as an additional term which is independent of the resonance. The skin depth is $\sim \frac{1}{\Gamma_\rho}$. Therefore the material thickness has to be thin enough such that the gap is still visible. For example by comparing the two plots in the right column of figure 5.7 ($\Gamma_\rho = 0.3\,\mathrm{meV}$) it is clear that if the sample is $d = 0.1\,\mathrm{mm}$ thick then the AQ cannot be found, since material losses make the gap indistinguishable from the outer region. As already noted before, the sample must not be too thin. This is because even in the lossles limit and for very small thicknesses the frequencies inside the gap do not all correspond to zero transmission, cf. middle left plot in figure 5.6.

In figure 5.8 photon losses are neglected ($\Gamma_\rho = 0$) and two variations of magnon losses Γ_m are considered. The larger the magnon losses, the more pronounced is the widening of the gap. This can be understood by looking at the dispersion relation in eqution (5.52). Magnon losses Γ_m introduce a Lorenzian shaped imaginary part to the dispersion relation. The width of the Lorenzian is proportional to Γ_m. Due to the Lorenzian shape of the damping imaginary part in the dispersion relation also frequencies that are not directly in the gap, but close to the gap, can become highly damped. This effect becomes more pronounced the thicker the sample is.

The reason why we investigate losses on the order of $10^{-1} - 10^{-2}\,\mathrm{eV}$ in the figures 5.7 and 5.8 is because standard layer thicknesses are on the order of $d = 0.01\,\mathrm{mm}$. For this particular thickness the effect of losses becomes visible best for the chosen loss values. Smaller losses would by eye in the plots be hard to distinguish from the lossless case. In reality the losses can be much smaller than $10^{-2}\,\mathrm{eV}$. In this case losses will not spoil the axion discovery when the thickness of the layer is on the order of $d = 0.01\,\mathrm{mm}$. One only has to take care that the minimum thickness is larger than $0.01\,\mathrm{mm}$ in order not to close the gap, cf. figure 5.6.

In practice one has to start the transmission experiments with a sample thickness on the order of $d = 0.01\,\mathrm{mm}$. As we have shown this thickness is well suited for the discovery of an AQ. Finding a gap in the transmission spectrum that scales with the external B-field as predicted, will give strong indication for the existence of an AQ that is realized in the TMI. In a second step one wants also to determine the properties of the TMI material. As we will show, one can do this by fitting the one dimensional model to future measurements of the transmission spectrum. Note that in the second step of determining the material properties a much larger layer thickness than the suggested $0.01\,\mathrm{mm}$ might be helpful, since if the losses are much smaller than the benchmark loss $10^{-2}\,\mathrm{eV}$, the transmission spectrum will be less sensitive to them. The correct characterization of the parameters of the TMI is of huge importance. In section 5.3 it is shown that a TMI can be used as dark matter axion detector. To estimate the induced photon signal from DA, AQ and photon mixing, the parameters of the TMI have to be known precisely. In the following a specific thickness d is fixed and transmission spectra for different losses and B-fields are computed to demonstrate that fitting measurements to the presented results can determine the parameters of the TMI.

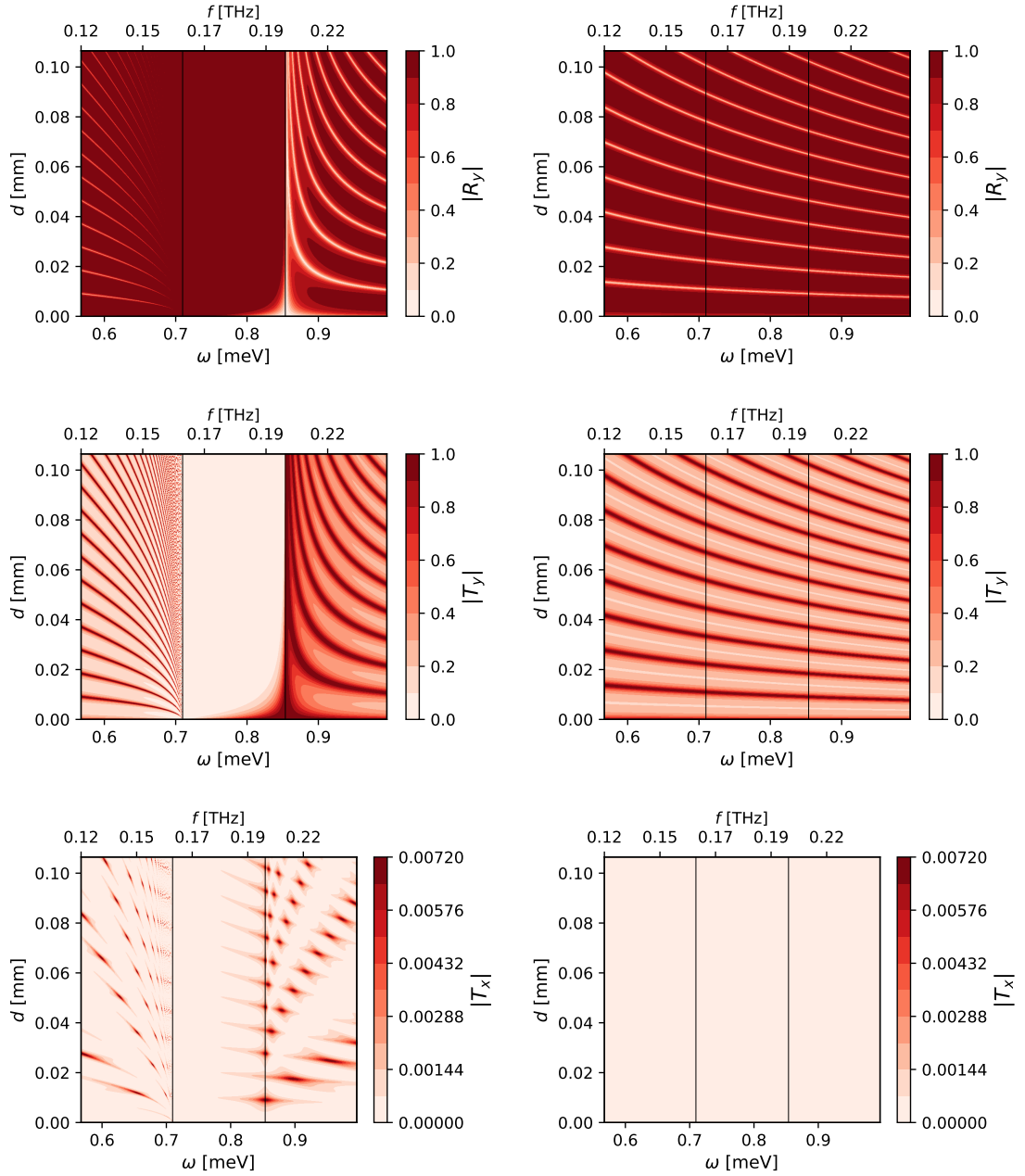

Figure 5.6: Reflection and transmission coefficients for a laser that hits a TI with (left) and without (right) a dynamical AQ field. The laser polarization is in the y-direction (parallel to the external B-field). The TI and the TMI have $\Theta = \pi$ and $n = 10, \mu = 1$ [17]. On top of that the TMI with an applied external B-field of $B^e = 2\,\mathrm{T}$ host an AQ with: $m_\Theta = 0.72\,\mathrm{meV}, b = 0.5\,\mathrm{meV}$, cf. equations (5.3)-(5.5). m_Θ and ω_{LO} are marked with the black vertical lines. The R_y/T_y coefficient is always close to one/zero inside the gap (between m_Θ and ω_{LO}) if a dynamical AQ is present. The T_x coefficient is much smaller, since a transmission in the E_x-component can only be induced via polarization rotation with non zero Θ.

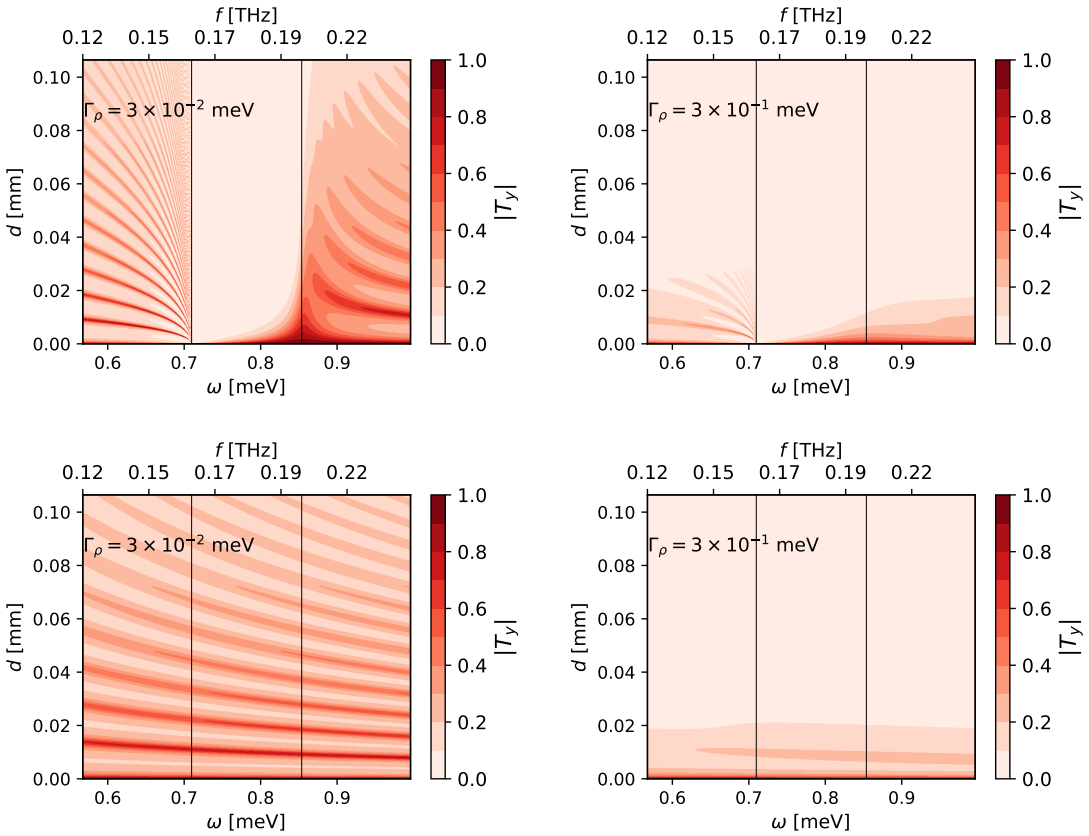

Figure 5.7: Transmission coefficients for the E_y-component (parallel to external B-field) for different losses Γ_ρ. Magnon losses Γ_m are neglected. The TI and the TMI have $\Theta = \pi$ and $n = 10, \mu = 1$ [17]. On top of that the TMI with an applied external B-field of $B^e = 2\,\mathrm{T}$ host an AQ with: $m_\Theta = 0.72\,\mathrm{meV}, b = 0.5\,\mathrm{meV}$, cf. equations (5.3)-(5.5). m_Θ and ω_{LO} are marked with the black vertical lines. In the top row a dynamical AQ is present, while in the bottom row the results for a normal TI ($\Theta = \pi$) without a dynamical AQ are shown. Large photon losses Γ_ρ make it harder to distinguish between a gapped and a non gapped spectrum. Therefore small layer thicknesses should be considered for the reflection and transmission experiments.

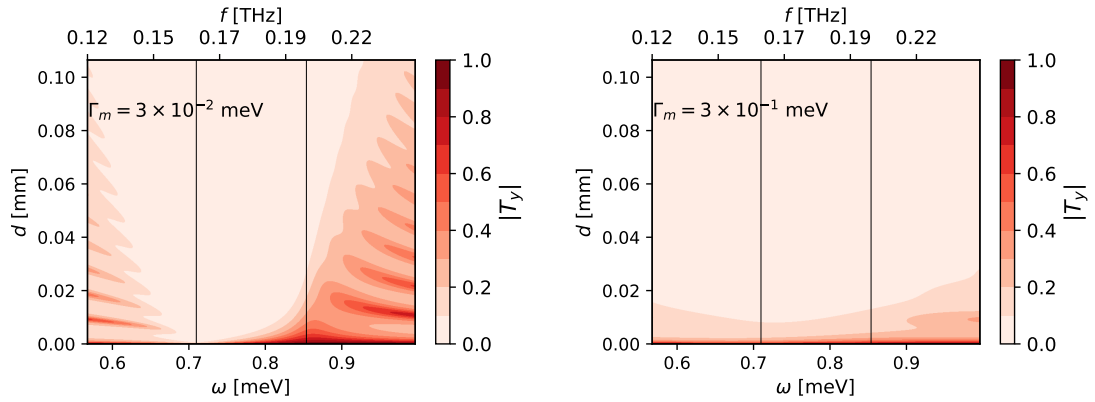

Figure 5.8: Transmission coefficients for the E_y-component (parallel to external B-field) for different losses Γ_m. Photon losses Γ_ρ are set to zero. The TI and the TMI have $\Theta = \pi$ and $n = 10, \mu = 1$ [17]. On top of that the TMI with an applied external B-field of $B^e = 2\,\mathrm{T}$ host an AQ with: $m_\Theta = 0.72\,\mathrm{meV}, b = 0.5\,\mathrm{meV}$, cf. equations (5.3)-(5.5). m_Θ and ω_{LO} are marked with the black vertical lines. Magnon losses Γ_m smear out the gap. For large enough thicknesses d and losses Γ_m it is hard to distinguish the spectrum for a spectrum where no dynamical AQ is present.

Based on the previous discussion we chose a TMI layer thickness of $d = 30\,\mu\mathrm{m}$ in the following. In figure 5.9 photon losses are varied between $\Gamma_\rho = 3 \times 10^{-4} - 3 \times 10^{-1}\,\mathrm{meV}$ and magnon losses between $\Gamma_m = 3 \times 10^{-4} - 3 \times 10^{-1}\,\mathrm{meV}$. In each figure three different external B-field strengths (different colors) are shown. The gap between m_Θ and ω_{LO} is marked with two vertical dotted lines of the corresponding color. The weaker the external B-field, the smaller is the gap, cf. b parameter as defined in equation (5.5). For a smaller B-field not only the gap size b shrinks, but also the AQ mass decreases, cf. equation (5.3).

Figure 5.9 makes clear that the larger the losses the harder it is to distinguish the case where a dynamical AQ is present (solid colored curves) from the case that no dynamical AQ (black dashed line) is present. For relatively small losses the distinction between the curves is very clear. Therefore it can be concluded that comparing these results to future measurements will give the possibility to explicitly determine the material parameters, i.e. losses, permittivity, permeability, Θ and the parameter that enter the AQ mass m_Θ and the gap size parameter b. We want to point out again that based on the order of magnitude of the losses the material characterization – by fitting the one dimensional model to future measurements – will be optimal for a certain thickness of TMI layer. Once the AQ is found it is therefore recommended to carry out this fitting procedure with different TMI layer thicknesses, since the different thicknesses will be differently sensitive to the magnon and photon losses.

In the following the resonance around ω_{LO} is investigated more, cf. figure 5.9. For each B-field configuration there are two vertical dotted lines of the same color that denote m_Θ and ω_{LO}. ω_{LO} is denoted by the vertical line that is at the higher frequency. When the losses in figure 5.9 are small the resonance frequency f_{res} corresponds to ω_{LO}. However, when the losses are increased the resonance frequency f_{res} moves to higher frequencies, i.e. $f_{\mathrm{res}} > \frac{\omega_{LO}}{2\pi}$. The width of the resonance peak is called Γ_{res} in the following. With increasing losses the resonance smears out until it vanishes completely. From figure (5.9) it can therefore be read off directly what amount of losses would be acceptable for a sample of thickness $d = 0.03\,\mathrm{mm}$ to still detect an AQ.

The resonance peaks around ω_{LO} in figure 5.9 are not symmetric. In this case Γ_{res} is defined as two times the frequency interval that ranges from the frequency of maximum resonance to the smaller frequency where half of the resonance peak value is reached. The ratio $\frac{f_{\mathrm{res}}}{\Gamma_{\mathrm{res}}}$ is called Q-

factor in the following. The Q-factor describes the quality of the resonance. Large Q-factors give rise to a well defined resonance, whereas low Q-factors show that the resonance is highly damped. In figure 5.10 the Q-factor is shown with respect to the applied external B-field for different losses. Starting from a low loss material (red) the magnon loss (blue and green) are increased. The largest Q-factor is observed at small external B-field. For larger external B-fields the difference between the red, blue and green curve becomes small. This means that the larger the external B-field the smaller is the effect of the losses on the Q-factor. If magnon losses are kept small and the photon losses Γ_ρ (pink and purple) are increased, the curves get an overall reduction, i.e. also for large external B-fields. Qualitatively this can be understood with the previous finding that Γ_ρ introduces a constant loss term (if the frequency interval is not too large) to the dispersion relation which leads to damping everywhere in the same way.

In the whole section the case, that the incoming THz laser is polarized parallel to the external B-field, was discussed. It was argued already in section 5.2.1.3 that this makes it easier to distinguish the case where an AQ is present from the case where it is not present. In the following the discussion is extended and it is argued why we focused on this case and what would happen if the external B-field is orthogonal to the THz laser field. In the case that the THz laser is in the E_x-component and $\boldsymbol{B}^e = B^e \hat{\boldsymbol{e}}_y$ it has to be taken into account that the E_x component does not directly mix with the dynamical axion field in the equations of motion. The transmission spectrum for the E_x component will therefore – to lowest order in κ – be equivalent to the transmission spectrum of a normal dielectric material without gap. However, E_x can mix indirectly with the AQs due to the interface conditions. The transmission spectrum T_x therefore has corrections of the order κ which modify the spectrum of a normal dielectric material and are unique for a TMI. However, if this case is compared to the extensively discussed case where the THz laser and external B-field are parallel, it becomes immediately clear that this effect is much smaller. Another complication, which would arise if a laser, that is orthogonal to the external B-field, was used, would be that the properties of the TMI such as permittivity, permeability and conductivity have to be known in advance. However, since no TMI has been realized yet they are not known and this will complicate to sort out the small effects that the dynamical AQ has on the transmission spectrum. All in all if the laser is polarized perpendicularly to the external B-field the effects that make it possible to distinguish between a TMI with a dynamical AQ field and a normal TI are much smaller. Therefore only the case case where the external laser is polarized parallel to the external B-field has been considered.

5.2.2.4 How to distinguish axion polariton resonance from antiferromagnetic resonance

In this section we have discussed the effect of the axion quasiparticle on the transmission and reflection spectra. We find a resonance above the upper gap frequency ω_{LO}, cf. figure 5.9. The axion polariton resonance in the transmission and reflection spectra corresponds physically to a longitudinal spin wave mode [17]. However, since the considered materials are antiferromagnets [17] in a real transmission experiment also the antiferromagnetic resonance (AFMR), which is the resonance in the transversal spin wave mode, will appear.

One way to distinguish the AFMR and the axion polariton resonance is to just turn off the external B-field. In this case the AFMR is still present (for sufficiently low temperatures). However, the axion polariton resonance disappears, since the term $\boldsymbol{E} \cdot \boldsymbol{B}^e$ vanishes and no dynamical axion field can be sourced efficiently. Another way of how to identify the AFMR in order to distinguish it from the axion polariton is to verify that the corresponding resonance frequencies follow exactly the theoretical predictions [123] for changing external B-field and laser polarization.

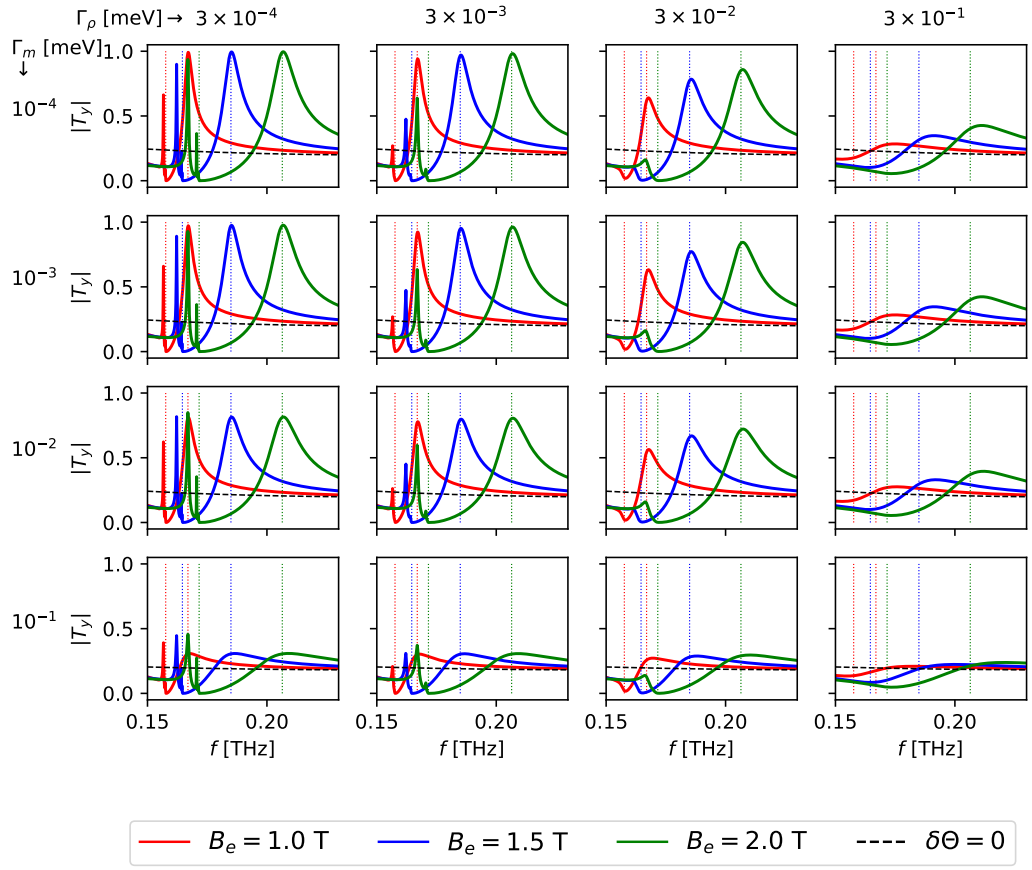

Figure 5.9: Transmission coefficient T_y for a layer of TMI with thickness $d = 0.03\,\text{mm}$. Different losses and B-field configurations (red, blue and green) are shown. Horizontally Γ_ρ is varied, while in the vertical Γ_m changes from plot to plot. The dotted vertical lines in each plot indicate the gap for each B-field configuration, i.e. the frequencies corresponding to $m_\Theta(B^e)$ and $\omega_{LO}(B^e) = \sqrt{m_\Theta^2(B^e) + b^2(B^e)}$. The B^e dependence of m_Θ and b is taken from equations (5.3) and (5.5). Further parameters of the TMI that were used are $n = 10, \mu = 1$ [17]. In each plot three different external B-fields are shown. The larger the external B-field, the larger is m_Θ and the gap between m_Θ and ω_{LO}. The dashed black line shows the result when no dynamical AQ $\delta\Theta$ is present, while the colored solid lines represent the forecasts for the case that a dynamical AQ is present. The difference between both cases is less pronounced when the losses are large. However, even for the largest loss the difference between both cases (dahsed black line and colored solid curves) is still visible. The resonant peak at ω_{LO} is approximately symmetric for low losses. For larger losses, however, the peak becomes non symmetric and the peak frequency shifts significantly away form ω_{LO}.

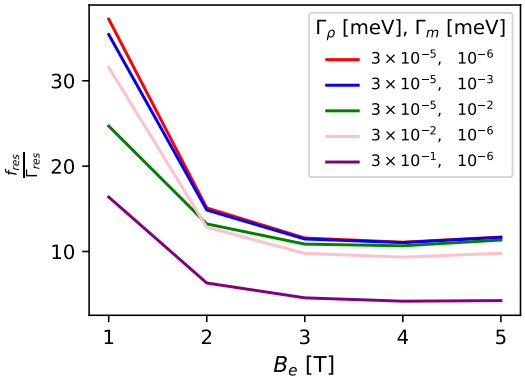

Figure 5.10: Q-factor for a transmission experiment of a layer of TMI with thickness $d = 0.03\,\text{mm}$. The Q-factor of the resonance peak around ω_{LO} is defined by the ratio of the resonant frequency divided by the width of the resonance peak, i.e. $Q = \frac{f_{\text{res}}}{\Gamma_{\text{res}}}$. For low external B-fields the Q-factor is largest. The exact value of the Q-factor for low external B-fields depends strongly on the losses. In the figure five different losses are shown in different colors. For large external B-fields the Q-factors converge to an approximate constant value. The lowest Q-factor is obtained for the largest loss $\Gamma_\rho = 3 \times 10^{-1}$ meV, $\Gamma_m = 10^{-6}$ meV. The TMI parameters are defined as in equations (5.3)-(5.5). Further parameters that were used are $n = 10, \mu = 1$ [17].

5.3 Using axion quasiparticles to find dark matter

In Ref. [19] it was proposed that dynamical axion quasiparticles in a TMI can be used to detect DAs. The idea is that the DAs can mix resonantly with the axion polariton. In comparison to Ref. [19], we work out a more detailed signal calculation for the emitted photon signal by taking into account the correct interface conditions for the photon and axion field. In the end the sensitivity reach of a TMI layer for a DA search is presented.

5.3.1 Dark axion, axion quasiparticle and photon mixing

The starting point are again the three dimensional equations of motion. After linearization, a one dimensional model (in analogy to section 5.2.1.3) is derived. In the following the one dimensional model is used to derive the photon signal that is generated by a DAs which passes trough a magnetized TMI with a dynamical AQ.

5.3.1.1 General formulation

To describe the threefold mixing between an AQs, DAs and photons, another Klein-Gordon equation for the DA, which is sourced by the electromagnetic fields, has to be added to the set of equations (5.6)-(5.10). Furthermore, additional source terms have to be added in equations (5.6)

and (5.7) that arise due to the DAs. Summarized the following equations of motions are obtained:

$$\begin{aligned}
\nabla \cdot \boldsymbol{D} &= \rho_f - \kappa \nabla(\delta\Theta + \Theta) \cdot \boldsymbol{B} - g_{a\gamma} \nabla a \cdot \boldsymbol{B}, && (5.66)\\
\nabla \times \boldsymbol{H} - \partial_t \boldsymbol{D} &= \boldsymbol{J}_f + \kappa(\boldsymbol{B}\partial_t(\delta\Theta + \Theta) - \boldsymbol{E} \times \nabla(\delta\Theta + \Theta)) \\
&\quad + g_{a\gamma}(\boldsymbol{B}\partial_t a - \boldsymbol{E} \times \nabla a), && (5.67)\\
\nabla \cdot \boldsymbol{B} &= 0, && (5.68)\\
\nabla \times \boldsymbol{E} + \partial_t \boldsymbol{B} &= 0, && (5.69)\\
\partial_t^2 \delta\Theta - v_i^2 \partial_i^2 \delta\Theta + m_\Theta^2 \delta\Theta &= \Lambda \boldsymbol{E} \cdot \boldsymbol{B}, && (5.70)\\
(\partial_t^2 - \nabla^2 + m_a^2) a &= g_{a\gamma} \boldsymbol{E} \cdot \boldsymbol{B}. && (5.71)
\end{aligned}$$

In addition to the variables that were already defined below equations (5.6)-(5.10) the following variables have been defined: a is the pseudoscalar DA field, $g_{a\gamma}$ is the DA-photon coupling and m_a is the DA mass. Analogous to equations (5.11)-(5.12), the equations (5.66)-(5.67) can be brought in the form of normal electrodynamics in matter with modified displacement field and magnetic field strength:

$$\boldsymbol{D}_{\Theta a} := \boldsymbol{D} + \kappa(\Theta + \delta\Theta)\boldsymbol{B} + g_{a\gamma} a \boldsymbol{B}, \tag{5.72}$$

$$\boldsymbol{H}_{\Theta a} := \boldsymbol{H} - \kappa(\Theta + \delta\Theta)\boldsymbol{E} - g_{a\gamma} a \boldsymbol{E}. \tag{5.73}$$

Consequently also the interface conditions (5.18) and (5.20) have to be adapted: $\boldsymbol{D}_\Theta \to \boldsymbol{D}_{\Theta a}$ and $\boldsymbol{H}_\Theta \to \boldsymbol{H}_{\Theta a}$.

In section 5.2.1.1 it was noted already that we cannot obtain an interface condition from the Klein-Gordon equation for the AQ field when we consider an interface between a region where we have a material that hosts AQs and a material that does not have them, e.g. in vacuum. However, a DA is expected to be in both media, since it is expected that dark matter is everywhere around us. Therefore, if two media, which both have DAs, are considered, the Klein-Gordon equation for the dark axion field (5.71) can be used to derive an interface condition for the a-field. The derivation of the interface condition is in complete analogy to the discussion around equation (3.40). We use that $\nabla^2 = \nabla \cdot \nabla$. Then we consider an infinitesimal volume element that lies between two media, e.g. medium 1 and 2. We integrate over the infinitesimal volume element and apply the divergence theorem. It follows that the normal derivative of the axion field between two interfaces has to be continuous:

$$\boldsymbol{n} \cdot (\nabla a_1 - \nabla a_2) = 0. \tag{5.74}$$

Furthermore it is required that the dark axion field is also continuous over the interface. This does not follow from the equations of motions and can therefore be seen as a physical assumption:

$$a_1 - a_2 = 0. \tag{5.75}$$

5.3.1.2 Linearized one dimensional model

It is assumed again that a strong and static external B-field $\boldsymbol{B}^e$ is present. Without loss of generality $\boldsymbol{B}^e$ is taken to be polarized in the y-direction $\boldsymbol{B}^e = B^e \hat{\boldsymbol{e}}_y$. Then similar steps as in section 5.2.1.2 and 5.2.1.3 lead to the following linearized equations of motions:

$$\begin{aligned}
\left(\partial_z^2 - n^2 \partial_t^2 - \sigma\mu\partial_t\right) E_y &= \mu B^e \partial_t^2 \left(\kappa\delta\Theta + g_{a\gamma} a\right), && (5.76)\\
\left(v_z^2 \partial_z^2 - \partial_t^2 - m_\Theta^2\right) \delta\Theta &= -\Lambda B^e E_y, && (5.77)\\
\left(\partial_z^2 - \partial_t^2 - m_a^2\right) a &= -g_{a\gamma} B^e E_y. && (5.78)
\end{aligned}$$

We neglect the E_x-component (orthogonal to the $\boldsymbol{B}^e$) in the following calculation. The photon signal in the E_x component, which is caused by a DA, is always an order κ smaller than the E_y-component. This is due to the fact that only the E_y-component mixes with the DA and AQ and the E_x-component can only be generated due to the mixing at the interface, which is proportional to κ. Therefore, in an axion dark matter search experiment the main photon signal is polarized parallel to the external B-field, i.e. in the y-component. Due to the κ suppression of the E_x-component it will be even more challenging to detect a signal in the E_x component. Therefore, it is well justified to drop the E_x component in the following considerations.

In addition to the assumptions that were made in section 5.2.1 it is also assumed that the non-linear terms that include the DA can be linearized. The linearization is justified due to the non-relativistic nature of the galactic axions, i.e. $\partial_t a/\partial_z a \approx 10^{-3}$.

The interface conditions for the electromagnetic fields after linearization are obtained with the linearized fields $\boldsymbol{D}_{\Theta,a} = \boldsymbol{D}+\kappa(\Theta+\delta\Theta)\boldsymbol{B}^e+g_{a\gamma}a\boldsymbol{B}^e$ and $\boldsymbol{H}_{\Theta,a} = \boldsymbol{H}-\kappa\Theta\boldsymbol{E}$. In the one dimensional model $\boldsymbol{n}\cdot(\boldsymbol{D}_{\Theta,a2}-\boldsymbol{D}_{\Theta,a1})=0$ and $\boldsymbol{n}\cdot(\boldsymbol{B}_2-\boldsymbol{B}_1)=0$ are always fulfilled, since transverse waves ($B_z = 0 = E_z$) are assumed. The only nontrivial interface conditions are:

$$\boldsymbol{n}\times(\boldsymbol{H}_{\Theta,a,2}-\boldsymbol{H}_{\Theta,a,1}) = 0, \tag{5.79}$$

$$\boldsymbol{n}\times(\boldsymbol{E}_2-\boldsymbol{E}_1) = 0, \tag{5.80}$$

where $\boldsymbol{n}=\hat{\boldsymbol{e}}_z$ and it is assumed again that no free surface charges and currents are present. Note that both $\boldsymbol{H}_{\Theta,a,1}$ and $\boldsymbol{H}_{\Theta,a,2}$ include the term $g_{a\gamma}a\boldsymbol{E}$. Now since a and the transverse $\boldsymbol{E}$ are continuous over the interface and the term $g_{a\gamma}a\boldsymbol{E}$ appears in both terms in equation (5.79) it cancels such that we can just write:

$$\boldsymbol{n}\times(\boldsymbol{H}_{\Theta,2}-\boldsymbol{H}_{\Theta,1}) = 0. \tag{5.81}$$

Including bulk losses in the one-dimensional model does not change the interface conditions. The magnon losses Γ_m, photon losses Γ_ρ, as well as mixed losses $\Gamma_{\times,1}$ and $\Gamma_{\times,2}$ are included in complete analogy to section 5.2.1.4 . The resulting equations of motions are:

$$\boldsymbol{K}\partial_t^2\boldsymbol{X}-\boldsymbol{\Gamma}\partial_t\boldsymbol{X}+\boldsymbol{M}\boldsymbol{X}=0, \tag{5.82}$$

with

$$\begin{aligned}
\boldsymbol{X} &= \begin{pmatrix} E_y \\ \delta\Theta \\ a \end{pmatrix}, \quad \boldsymbol{K} = \begin{pmatrix} 1 & \frac{\kappa B^e}{\epsilon} & \frac{g_{a\gamma}B^e}{\epsilon} \\ 0 & 1 & 0 \\ 0 & 0 & 1 \end{pmatrix}, \quad \boldsymbol{\Gamma} = \begin{pmatrix} \Gamma_\rho & \Gamma_{\times,1} & 0 \\ \Gamma_{\times,2} & \Gamma_m & 0 \\ 0 & 0 & 0 \end{pmatrix}, \\
\boldsymbol{M} &= \begin{pmatrix} \frac{k^2}{n^2} & 0 & 0 \\ -\Lambda B^e & v_z^2k^2+m_\Theta^2 & 0 \\ -g_{a\gamma}B^e & 0 & k^2+m_a^2 \end{pmatrix}.
\end{aligned} \tag{5.83}$$

No losses for the DA are included, since its lifetime [56] is much larger than the timescale that it remains in the TMI.

5.3.2 Dark matter signal calculation

In this section the linearized equations of motions, which we derived in the previous section, are solved. First, this is done for the case without losses and then we generalize the solutions to the case that includes losses. A matrix formalism is developed to calculate the emitted photons and axions from a multilayer system. In the end the matrix formalism is applied to the case of a layer of TMI surrounded by vacuum. However, the presented formalism makes it in principle possible to evaluate an emitted photon signal form a many-layer system. In future studies this can be used to boost the signal like it was proposed for the MADMAX haloscope [58]. In the following the spin wave density v_z is set to zero.

5.3.2.1 Solution of the one dimensional model

In the case without losses the dispersion relation can be obtained by transforming the set of equations (5.76)-(5.78) into Fourier space:

$$\left(k^2 - \frac{k_a^2 + k_\Theta^2}{2}\right)^2 = b_a^2 k_p^2 + \left(\frac{k_a^2 - k_\Theta^2}{2}\right)^2, \tag{5.84}$$

where $b_a^2 = \frac{g_{a\gamma}^2 (B^e)^2}{\epsilon}$ was defined in analogy to to $b^2 = \frac{\kappa \Lambda (B^e)^2}{\epsilon}$. $k_a^2 = \omega^2 - m_a^2$ is the free space axion dispersion, $k_p^2 = n^2\omega^2$ is the ordinary photon dispersion and k_Θ^2 fulfills the AQ-photon mixing dispersion in equation (5.38). The two solutions of equation (5.84) are defined as:

$$\begin{aligned}
k_+^2 &:= \frac{k_a^2 + k_\Theta^2}{2} + \begin{cases} +\sqrt{\left(\frac{k_\Theta^2 - k_a^2}{2}\right)^2 + b_a^2 k_p^2} & k_\Theta^2 \geq k_a^2 \\ -\sqrt{\left(\frac{k_a^2 - k_\Theta^2}{2}\right)^2 + b_a^2 k_p^2} & k_\Theta^2 < k_a^2 \end{cases}, \\
k_-^2 &:= \frac{k_a^2 + k_\Theta^2}{2} + \begin{cases} -\sqrt{\left(\frac{k_\Theta^2 - k_a^2}{2}\right)^2 + b_a^2 k_p^2} & k_\Theta^2 \geq k_a^2 \\ +\sqrt{\left(\frac{k_a^2 - k_\Theta^2}{2}\right)^2 + b_a^2 k_p^2} & k_\Theta^2 < k_a^2 \end{cases}.
\end{aligned} \tag{5.85}$$

The definitions in equation (5.85) guarantee that in the limit of vanishing DA-photon coupling ($b_a \to 0$) one dispersion relation is the axion polariton dispersion, c.f., equation (5.38), and the other dispersion is the free axion dispersion:

$$k_+^2 \to k_\Theta^2, \tag{5.86}$$

$$k_-^2 \to k_a^2. \tag{5.87}$$

The most general solution is now given by:

$$\begin{aligned}
E &= \hat{E}^{++} e^{ik_+ z} + \hat{E}^{+-} e^{-ik_+ z} + \hat{E}^{-+} e^{ik_- z} + \hat{E}^{--} e^{-ik_- z}, \\
\delta\Theta &= \delta\hat{\Theta}^{++} e^{ik_+ z} + \delta\hat{\Theta}^{+-} e^{-ik_+ z} + \delta\hat{\Theta}^{-+} e^{ik_- z} + \delta\hat{\Theta}^{--} e^{-ik_- z}, \\
a &= \hat{a}^{++} e^{ik_+ z} + \hat{a}^{+-} e^{-ik_+ z} + \hat{a}^{-+} e^{ik_- z} + \hat{a}^{--} e^{-ik_- z},
\end{aligned} \tag{5.88}$$

where the y index at the E-field is omitted, since the E_x-component is not taken into account in the following considerations. If the equations (5.88) are plugged into the equations of motion a lot of the constants in the ansatz (5.88) can be eliminated:

$$\begin{pmatrix} E \\ \delta\Theta \\ a \end{pmatrix} = \hat{E}^{++} \begin{pmatrix} 1 \\ \Theta_E^+ \\ a_E^+ \end{pmatrix} e^{ik_+ z} + \hat{E}^{+-} \begin{pmatrix} 1 \\ \Theta_E^+ \\ a_E^+ \end{pmatrix} e^{-ik_+ z} + \hat{a}^{-+} \begin{pmatrix} E_a^- \\ \Theta_a^- \\ 1 \end{pmatrix} e^{ik_- z} + \hat{a}^{--} \begin{pmatrix} E_a^- \\ \Theta_a^- \\ 1 \end{pmatrix} e^{-ik_- z}, \tag{5.89}$$

where the following variables were defined:

$$\Theta_E = \frac{\Lambda B^e}{m_\Theta^2 - \omega^2}, \quad a_E = \frac{g_{a\gamma} B^e}{k^2 - k_a^2}, \tag{5.90}$$

$$E_a = \frac{\omega^2 \mu g_{a\gamma} B^e}{k^2 - k_\Theta^2}, \quad \Theta_a = \Theta_E a E. \tag{5.91}$$

Note in the formulas above μ was not set to one. From equation (5.89) it becomes clear that the dynamical AQ field is completely determined when the variables $\hat{E}^{++}, \hat{E}^{+-}, \hat{a}^{-+}$ and $\hat{a}^{--}$ are known. In the next section it is shown that the unknown variables can be fully determined with the interface conditions for the electromagnetic and DA fields. Therefore, again no boundary conditions for the AQ[3] have to be applied.

[3] If we would consider a finite spin wave velocity we would get three modes $k_{1,2,3}^2$. In this case the most general ansatz would have 6 unknowns per field and we would also need boundary conditions for the AQ field. However, in our case the AQ field is completely fixed without boundary conditions.

If losses are included, the full dispersion relation $k_\pm^2$ takes a complicated form. However, in the limit $b_a \to 0$ it is found that $k_-^2 \to k_a^2$ and $k_+^2 \to k_\Theta^2$, where k_Θ^2 is given by equation (5.51). In the following sections E_a and a_E are needed also in the case of losses. a_E form equation (5.90) does not get modified in the case of losses and E_a has the same form as in equation (5.91), however now k_Θ from equation (5.51) has to be used in the equation for E_a.

5.3.2.2 Matrix formalism

In the previous section the solution of the linearized equations in a homogeneous medium (all material properties are constant) was described. Here the solutions for the fields in a multilayer system which consists of $N+1$ media, c.f. figure 3.5, is discussed. To label the media the same convention as in section 5.2.2.2 is used. There are $N+1$ interfaces which are labeled by $r = 0, \cdots N$. The first interface is at $z_0 = z_1$ and the last interface is at z_N. Each medium is characterized by $\epsilon_r, \mu_r, \Theta_r, \boldsymbol{\Gamma}_r,\ r = 0, \cdots N$. The external B-field B^e is the same in all media and is polarized in the y-direction.

The ansatz in medium r is given by equation (5.89) by putting an index r to all variables which depend on the medium. On top of that a phase similar to the case of AQ-photon mixing is introduced in the ansatz, c.f., equation (5.55). Applying the interface conditions for the electromagnetic fields, cf. equation (5.81) and (5.80), and for the DA field, cf. equation (5.74) and (5.75), at z_r between medium $r-1$ and r we obtain the following system of equations:

$$\boldsymbol{t}_r = \boldsymbol{M}_r^{-1} \cdot \boldsymbol{M}_{r-1} \cdot \boldsymbol{P}_{r-1} \boldsymbol{t}_{r-1}, \tag{5.92}$$

with

$$\boldsymbol{M}_r = \begin{pmatrix} 1 & 1 & E_{a,r}^- & E_{a,r}^- \\ k_+^r & -k_+^r & k_-^r E_{a,r}^- & -k_-^r E_{a,r}^- \\ a_{E,r}^+ & a_{E,r}^+ & 1 & 1 \\ k_+^r a_{E,r}^+ & -k_+^r a_{E,r}^+ & k_-^r & -k_-^r \end{pmatrix} \text{ and } \boldsymbol{t}_r = \begin{pmatrix} \hat{E}_r^{++} \\ \hat{E}_r^{+-} \\ \hat{a}_r^{-+} \\ \hat{a}_r^{--} \end{pmatrix} \tag{5.93}$$

and

$$\boldsymbol{P}_r = \mathrm{diag}(e^{i\Delta_r^+}, e^{-i\Delta_r^+}, e^{i\Delta_r^-}, e^{-i\Delta_r^-}). \tag{5.94}$$

The phases are defined as follows: $\Delta_r^\pm := k_\pm^r (z_{r+1} - z_r)$ and $k_\pm^r$ fulfills the equation (5.85).

In complete analogy to section 5.2.2.2 the S-matrix is defined. The S-matrix relates the states in medium 0 and N with each other

$$\boldsymbol{t}_N = \boldsymbol{S} \cdot \boldsymbol{t}_0. \tag{5.95}$$

The expressions for one, two and N interfaces are the same as in equations (5.60)-(5.62) .

We are in particular interested in DAs coming onto a system of TMIs. Without loss of generality it can therefore be assumed that the axions are coming in from medium 0. The amplitude of the incoming axions is known and within the used convention given by $\hat{a}_0^{-+}$. The unknown fields can be calculated from the S-matrix as follows:

$$\begin{pmatrix} \hat{E}_N^{++} \\ \hat{E}_0^{+-} \\ \hat{a}_N^{-+} \\ \hat{a}_0^{--} \end{pmatrix} = -\hat{a}_0^{-+} \begin{pmatrix} -1 & S_{12} & 0 & S_{14} \\ 0 & S_{22} & 0 & S_{24} \\ 0 & S_{32} & -1 & S_{34} \\ 0 & S_{42} & 0 & S_{44} \end{pmatrix}^{-1} \cdot \begin{pmatrix} S_{13} \\ S_{23} \\ S_{33} \\ S_{43} \end{pmatrix}. \tag{5.96}$$

The emitted E-field in medium N, that propagates in the positive z-direction, i.e. in the direction of the incoming axions, is called $\hat{E}_N^{++}$. The emitted E-field in the direction opposed to the incoming axions, i.e. in the negative z-direction, is called $\hat{E}_0^{+-}$. The same naming convention applies also

to the DA fields. $\hat{a}_0^{-+}/\hat{a}_0^{--}$ are the incoming/reflected axions and $\hat{a}_N^{-+}$ are the transmitted axions in medium N. After writing down the most general solution in the following sections we focus on the case of two interfaces and in particular on the case that there is a layer of TMI with an AQ. The layer is surrounded by vacuum.

5.3.2.3 Layer of topological magnetic insulator

In this section we consider the situation that DAs hit a layer of TMI. With the convention of the matrix formalism there are two interfaces ($N = 2$). Medium 0 and 2 are vacuum and medium 1 is a TMI of thickness d. The TMI has constants $n^2 = \epsilon, \mu = 1, \Theta = \pi$ and losses $\mathbf{\Gamma}$. The external B-field is present in all media. Incoming DAs have the amplitude $\hat{a}_0^{-+}$, which is determined by the dark matter density.

Due to the mixing between DAs, AQs and photons a detectable photon signal, which propagates away from the TMI layer, can be produced. The emitted E-fields in medium 0 and 2 are denoted by $\hat{E}_0^{+-}$ and $\hat{E}_2^{++}$. $\hat{E}_0^{+-}$ is the E-field amplitude that is emitted in the opposite direction to the incoming axions and $\hat{E}_2^{++}$ is the emitted photon signal in medium 2 that is emitted in the direction of the incoming axions. Note that the incoming axions have a very small velocity. In the zero velocity limit there will be no preferred direction and the magnitudes of $\hat{E}_2^{++}$ and $\hat{E}_0^{+-}$ are the same. In the following $\hat{E}_2^{++}$ is investigated more closely; however it is noteworthy to point out that the evaluation of $\hat{E}_0^{+-}$ would lead to similar results in the small velocity limit for DAs.

First, the lossless case is investigated. Losses are introduced later on in this section. The full formula for $\hat{E}_2^{++}$ from the matrix formalism is quite longish. Therefore, the result is given in the zero velocity limit ($\omega = m_a$)[4] and to first order in the DA-photon coupling:

$$\hat{E}_2^{++} = -\hat{a}_0^{-+} \frac{\sin(\Delta/2)\left(k_\Theta^2 - \omega^2\right)}{k_\Theta\left(k_\Theta \sin(\Delta/2) + i\omega\cos(\Delta/2)\right)} g_{a\gamma} B^e + \mathcal{O}((g_{a\gamma}B^e)^2), \tag{5.97}$$

where the phase depth $\Delta = dk_\Theta$ was defined. Later on in this section the influence of velocity effects is also discussed with the full result from the matrix formalism. On top of that it is also shown later on that the expansion up to linear order in the DA-photon coupling covers all essential features. From now on the term '$\mathcal{O}((g_{a\gamma}B^e)^2)$' is neglected to simplify the expressions, but one should keep in mind that the equation is strictly true only up to linear order. We define an effective refractive index $k_\Theta = n_\Theta \omega$ and normalize the emitted E-field to the axion induced field in vacuum:

$$\frac{\hat{E}_2^{++}}{g_{a\gamma}B^e\hat{a}_0^{-+}} = \frac{\sin(\Delta/2)\left(1 - n_\Theta^2\right)}{n_\Theta\left(n_\Theta \sin(\Delta/2) + i\cos(\Delta/2)\right)}. \tag{5.98}$$

Equation (5.98) is the same as the boost factor of a single dielectric [2, 58] disc with the defined effective refractive index n_Θ instead of a normal refractive index of a dielectric material. However, note that this statement is not trivial and with the matrix formalism that was introduced in section 5.3.2.2 and the above expansion we have shown this here explicitly.

From equation (5.98) it can be seen directly that a resonance occurs if

$$\Delta = \Delta_j = n_\Theta(\omega_j)\omega_j d = (2j+1)\pi,\ j \in \mathbb{N}_0, \tag{5.99}$$

where ω_j are the different resonance frequencies. More explicitly the resonance frequencies are located at:

$$\omega_j^2 = \frac{\omega_{LO}^2}{2} + \sqrt{\frac{\omega_{LO}^4}{4} + \Delta_j^2 \frac{b^2}{n^2 d^2}} = \omega_{LO}^2 + \frac{\Delta_j^2 b^2}{n^2 d^2 \omega_{LO}^2} + \mathcal{O}\left(\frac{4\Delta_j^2 b^2}{n^2 d^2 \omega_{LO}^4}\right). \tag{5.100}$$

[4] $E_{a,0}^- = -g_{a\gamma}B^e, E_{a,1}^- = -g_{a\gamma}B^e \frac{m_a^2}{k_\Theta^2}, a_{E,0} = \frac{g_{a\gamma}B^e}{m_a^2}$ and $a_{E,1} = \frac{g_{a\gamma}B^e}{k_\Theta^2}$ are used according to equation (5.90) and (5.91). For the dispersion relations the coupling between DA and AQ is neglected: $k_+^0 = m_a, k_+^1 = k_\Theta, (k_-^0)^2 = -(g_{a\gamma}B^e)^2, (k_-^1)^2 = -(g_{a\gamma}B^e)^2/n^2, \Delta_1^- = 0, \Delta_1^+ = dk_\Theta$. Note that because we take the zero velocity limit we cannot set $k_-^2 = 0$, but we have to expand until the first non-vanishing order in the DA-photon coupling. The variables for medium 2 are exactly the same as the variables for medium 0.

From equation (5.100) it becomes evident that the resonance frequencies are always larger than ω_{LO}: $\omega_{LO} < \omega_0 < \omega_1 \cdots$. Only in the infinite medium limit ($d \to \infty$) they converge $\omega_j \to \omega_{LO}$. In the following it can also be understood why the frequencies, which were defined in equation (5.99), are the resonance frequencies. If equation (5.99) is fulfilled $\cos \Delta_j = 0$ and therefore the emitted E-field is $\hat{E}_2^{++} \sim \frac{1-n_\Theta^2}{n_\Theta^2}$. Therefore, for a pronounced resonance a small n_Θ is needed. From figure 5.3 is becomes immediately clear that this will happen the closer ω_j is to ω_{LO}. Looking again at equation (5.100) it can be concluded that the resonance is more pronounced for large sample thickness d of a fixed material. The higher modes are further away from ω_{LO} and have therefore a less pronounced resonance value. The largest maximal value of $\hat{E}_2^{++}$ is obtained for ω_0 while ω_1 leads to to a less pronounced resonance and so on. In the following the resonances are investigated in more detail. Analytical expressions for the widths and the maximum values of the resonances are derived. The statements that were made before about the maximum values at the resonance frequencies ω_j are illustrated for specific examples.

Around the resonances equation (5.98) reduces to:

$$\frac{\hat{E}_2^{++}}{gB^e \hat{a}_0^{-+}} = \frac{\left(1 - n_\Theta^2\right)}{n_\Theta^2 - \frac{i}{2} n_\Theta \left(\Delta - \Delta_j\right)}. \tag{5.101}$$

where we have expanded the cos() and sin() to lowest non vanishing order. If d is large enough then $n_\Theta^2(\omega_j) \ll 1$. Furthermore it is used that $\Delta - \Delta_j \approx \frac{n^2 \omega_j d}{2b^2 n_\Theta(\omega_j)}(\omega^2 - \omega_j^2) + \cdots$. Equation (5.101) can then be written as:

$$\frac{\hat{E}_2^{++}}{g_{a\gamma} B^e \hat{a}_0^{-+}} = \frac{i A_j}{i\gamma_j \omega_j + (\omega^2 - \omega_j^2)}, \tag{5.102}$$

with

$$\gamma_j = \frac{d}{4} \frac{\omega_j^2 - \omega_{LO}^2}{\omega_j^2} \approx \frac{4\Delta_j^2 b^2}{n^2 d^3 \omega_{LO}^4} \tag{5.103}$$

and

$$A_j = \frac{4b^2}{n^2 \omega_j d} \approx \frac{4b^2}{n^2 \omega_{LO} d}, \tag{5.104}$$

where it was used that in a resonant case ω_j is close to ω_{LO}. In the following the quantity of interest is the power boost factor, which is defined as follows:

$$\beta^2 = \left| \frac{\hat{E}_2^{++}}{g_{a\gamma} B^e \hat{a}_0^{-+}} \right|^2. \tag{5.105}$$

If β is not squared we call this quantity the power boost amplitude in the following. This naming convention is taken over from [58]. The FWHM of β^2 around the resonance ω_j is given by γ_j and the highest value at the resonance ω_j by

$$\frac{A_j^2}{\gamma_j^2 \omega_j^2} \approx \left(\frac{d\omega_{LO}}{\Delta_j} \right)^4. \tag{5.106}$$

With equation (5.106) it now becomes explicitly clear that the higher modes have a lower maximum resonance value, since $\Delta_j < \Delta_{j+1}$. Also large layer thicknesses d increase the maximal value of the resonance. Therefore, to achieve a certain amount of signal boost from one layer of TMI a relatively large layer thickness d is needed. Equation (5.103) tells us the necessary information about the width of the resonance. First, note that going to larger modes j or larger b will increase the FWHM γ_j. Relatively thick TMI layers, i.e. large d, have a very narrow resonance. Therefore, a good balance for d has to be found. On the one hand d should be large to reach a high resonance

value. On the other hand d should not be too large, because otherwise the FWHM γ_j becomes smaller than the axion linewidth. A large refractive index n does not increase the maximum value of the resonance, cf. equation (5.106). Large n, however, make the FWHM γ_j very small. We therefore conclude that it is advantageous to have low n materials, such that the resonances are more broadband resonances.

In figure 5.11 the boost amplitude β is shown for different layer thicknesses (top left: $d = 0.2\,\mathrm{mm}$, top right: $d = 5\,\mathrm{mm}$, bottom left: $d = 10\,\mathrm{mm}$ and bottom right: $d = 20\,\mathrm{mm}$). Each plot shows the full result from the matrix formalism for a DA dark matter velocity $v_{DM} = 10^{-3}$ (blue) and $v_{DM} = 0$ (black). In red the result from equation (5.98), which is based on an expansion in $g_{a\gamma}B^e$ and assumes $v_{DM} = 0$, is shown. In all figures we see that the red curves perfectly match the black curves. This confirms that the expansion in equation (5.98) is correct and can describe all relevant features around the resonance.

In the top left plot in figure 5.11 we show the case $d = 0.2\,\mathrm{mm}$. No clear enhancement of the boost factor is reached, since for this relatively small thickness we obtain a resonance frequency ω_0 (dashed vertical line) that is too far away from ω_{LO} (solid vertical line) such that $n_\Theta(\omega_0)$ is not much smaller than one. In conclusion no resonance is observed. In the top right plot the case $d = 5\,\mathrm{mm}$ is shown. We can now see clearly that we have a resonance at ω_0 (dashed vertical line), i.e. $n_\Theta(\omega_0) \ll 1$ for the chosen d. Velocity effects do not influence the resonance very much, since the resonance is not very pronounced. In the bottom left figure the case $d = 10\,\mathrm{mm}$ is shown. The vertical solid line again indicates the position of ω_{LO} while this time two dashed vertical lines indicate the position of two resonance frequencies ω_0 and ω_1. From the previous discussion it is expected that if we take an even larger layer thickness of $d = 10\,\mathrm{mm}$, we then get an even higher peak at ω_0. In particular from equation (5.106) we expect that the peak at ω_0 is now $(10/5)^2$ times higher in comparison to the peak at ω_0 in the top right figure. Comparing the top right and bottom left figures we can verify this explicitly. Furthermore, by comparing both figures it becomes clear that the width of the peak around ω_0 shrinks drastically by going from $d = 5\,\mathrm{mm}$ to $10\,\mathrm{mm}$. From equation (5.103) we can directly read off that the width shrinks by a factor $(5/10)^3$. A larger width, but with a lower maximum value, is realized at the second resonance peak ω_1 in the bottom left figure. According to equation (5.103) the width of the resonance around ω_1 should be broader than the resonance width around ω_0 by a factor of $\left(\frac{\Delta_1}{\Delta_0}\right)^2 = 9$. A comparison of the two peaks in the bottom left plot confirms this. Finally, in the bottom right figure the most resonant case with $d = 20\,\mathrm{mm}$ is shown. Here only the first resonance peak at ω_0 is shown. As we expect it is again much narrower than the other examples that were discussed already. In particular now the linewidth of β is narrower than the axion linewidth $10^{-6}m_a$. Therefore, the discussion of the example $d = 20\,\mathrm{mm}$ is more academic and probably not very useful for a real DA search. Another interesting observation is that now velocity effects start to play a role when it comes to the determination of the resonance frequency. This agrees with the naive understanding that in general disturbances of resonant systems are more pronounced the more resonant the system is. Nevertheless, in the case that is described here, the finite axion velocity leads only to a shift of the resonance frequency and does not destroy the resonance.

Summarized we found that it requires large TMI layer thicknesses d to build a resonant system. However, the larger the TMI, the more important are material losses as was already shown in section 5.2.2.3 for the transmission and reflection coefficients. To include losses we first notice that we have neglected the DA-photon mixing in the k_+ dispersion relation to derive equation (5.98). We can therefore also in the case of losses say that $k_+^2 \approx k_\Theta^2$, where k_Θ^2 fulfills equation (5.51). Mixed losses are neglected in the following and therefore k_Θ^2 is more precisely given by the first part of equation (5.51) only. In the case of losses a_E has the same form as in equation (5.91), however the appearing k_Θ^2 now includes losses. In conclusion equation (5.98) can also be used to

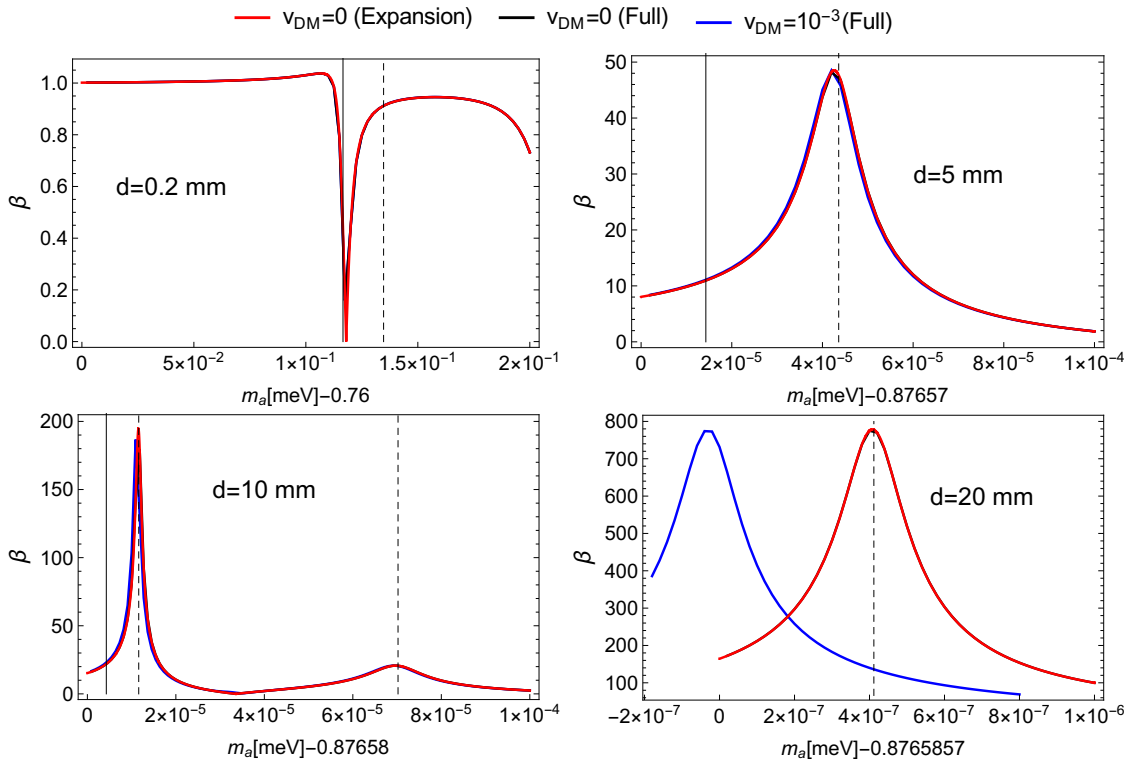

Figure 5.11: Power boost amplitude β for a TMI layer. Each plot shows the results for different TMI layer thicknesses: top left 0.2 mm, top right 5 mm, bottom left 10 mm, bottom right: 20 mm. The results from the full matrix formalism formulas (section 5.3.2.2) for zero DA velocity are drawn in black while the case of a DA velocity $v_{DM} = 10^{-3}$ is drawn in blue. In red we show the result from the lowest order expansion, cf. equation (5.98). The expanded result assumes zero DA velocity ($v_{DM} = 0$). The solid vertical black line marks ω_{LO} and the dotted vertical lines the resonance frequencies ω_j. Only in the case of $d = 10$ mm we show two resonance peaks ω_0 and ω_1. In all the other cases only ω_0, i.e. the main resonance peak, is shown. Typical material values for a TMI with an external B-field of $B^e = 2$ T are used: $m_\Theta = 0.72$ meV, $b = 0.5$ meV, cf. equations (5.3)-(5.5). Furthermore we use $n = 10, \mu = 1$ [17]. The black and red curves agree in all cases, what illustrates that the expansion in equation (5.98) is correct and covers all important features. In the $d = 0.2$ mm case we do not find a resonance, since $d = 0.2$ mm is not large enough for ω_0 to be close enough to ω_{LO} in order the make $n_\Theta(\omega_0)$ small. If we, however increase the thickness d we observe resonant structures around ω_j. The resonance is more pronounced the thicker the material is. Velocity effects become important only in very resonant configurations. In the case of $d = 20$ mm the system is the most resonant. However, the signal linewidth is already smaller than the DA linewidth of $10^{-6} m_a$.

compute the power boost factor in the lossy case (for $v_{DM} = 0$) when losses are included into the effective refractive index:

$$n_\Theta^2 = n^2 \left(1 + \frac{b^2}{m_\Theta^2 - \omega^2 - i\omega\Gamma_m} + i\frac{\Gamma_\rho}{\omega}\right). \tag{5.107}$$

In figure 5.12 the boost factor β around the resonances for two different layer thicknesses $d = 5\,\text{mm}$ (top) and $d = 10\,\text{mm}$ (bottom) is shown. The results now also include losses. In each plot ω_{LO} is indicated by the solid vertical line. For $d = 5\,\text{mm}$ only the first resonance frequency ω_0 is shown (dashed vertical line). However, for the $d = 10\,\text{mm}$ the first three resonance frequencies ω_0, ω_1 and ω_2 are shown in order to see the effect of losses on the higher resonances. In the left column magnon losses Γ_m are varied while photon losses Γ_ρ are neglected. In the right column we neglect magnon losses and vary photon losses. For both shown thicknesses magnon losses have a slightly larger effect on the resonant peaks than photon losses Γ_ρ. However, both magnon and photon losses, lead to the same order of boost factor reduction. Magnon losses Γ_m enter the resonance directly, cf. equation (5.107), while photon losses Γ_ρ only enter via an additional term that is added to the other terms of the dispersion relation.

Furthermore, from figure 5.12 (bottom left) it becomes clear that magnon losses have a bigger effect on the low frequency resonance peaks, i.e. the resonance ω_0 is damped more than the resonance ω_1 and the resonance at ω_1 is damped more than the resonance at ω_2. This can be understood by looking at the AQ-photon dispersion, cf. figure 5.5. Magnon losses introduce an imaginary damping part to the dispersion relation that peaks around m_Θ and falls off for larger and smaller frequencies. Since $m_\Theta < \omega_{LO} < \omega_j < \omega_{j+1}$ it is clear that the resonance around ω_j experiences more damping than the resonance around ω_{j+1}. We conclude that losses may lead to a scanning strategy that uses in the end a higher mode resonance $j > 0$, since these resonances are less damped and more broadband. However, the final scanning strategy can only be given when the losses for the material are determined by reflection and transmission experiments.

The two benchmark thicknesses in figure 5.12 are chosen since a reasonable boost factor is obtained for them in the lossless limit. Acceptable losses Γ_m, Γ_ρ should be smaller than $10^{-5}\,\text{meV}$. It is interesting to compare this to other DA search experiments such as MADMAX. In MADMAX a loss tangent $\tan\delta < 10^{-5}$ is required for the disk materials. In our case the conditions $\Gamma_m, \Gamma_\rho < 10^{-5}\,\text{meV}$ gives the same condition, since Γ_ρ/ω is the loss tangent for sufficiently small losses.

Finally we estimate the sensitivity reach of one layer of TMI for a DA search. Here, the sensitivity is estimated without taking into account the losses and can therefore be seen as the best case sensitivity. Losses will mitigate the estimated sensitivity, what could be compensated by a longer measurement time in each frequency interval. Under the assumption that no significant signal over background is found the signal rate n_s is smaller than $n_s < \frac{1}{\tau} + 2\sqrt{\frac{n_b}{\tau}}$ [78–80], where n_b is the background rate and τ the measurement time. We assume $n_b = 10^{-3}$ Hz which has been demonstrated in the THz regime at a temperature of 0.05 K [124]. Background domination can only be assumed if the measurement time is longer than $\tau = \frac{1}{4n_b} = 250\,\text{s}$. However, because the bandwidth of the resonance is very narrow we assume that the measurement time for one single configuration is shorter. In this case the measurements are not background dominated: $n_s < \frac{1}{\tau}$. The signal rate follows from the power P as: $n_s = \frac{P}{\omega}$. The power is calculated from the time averaged pointing vector S as: $P = SA$, where A (without a subscript j) is the surface area of the TMI layer. Putting everything together we obtain the sensitivity estimate:

$$g_{a\gamma} > 9.9 \times 10^{-10} \frac{1}{\text{GeV}} \left(\frac{2\,\text{T}}{B^e}\right) \left(\frac{1\ \text{mm}^2}{A}\right)^{\frac{1}{2}} \left(\frac{300\frac{\text{MeV}}{\text{cm}^3}}{\rho_a}\right)^{\frac{1}{2}} \left(\frac{100}{\beta}\right) \left(\frac{m_a}{2\,\text{meV}}\right)^{\frac{3}{2}} \left(\frac{60\,\text{s}}{\tau}\right)^{\frac{1}{2}}. \tag{5.108}$$

Using the maximum peak value from equation (5.106) to eliminate β in the previous equation we

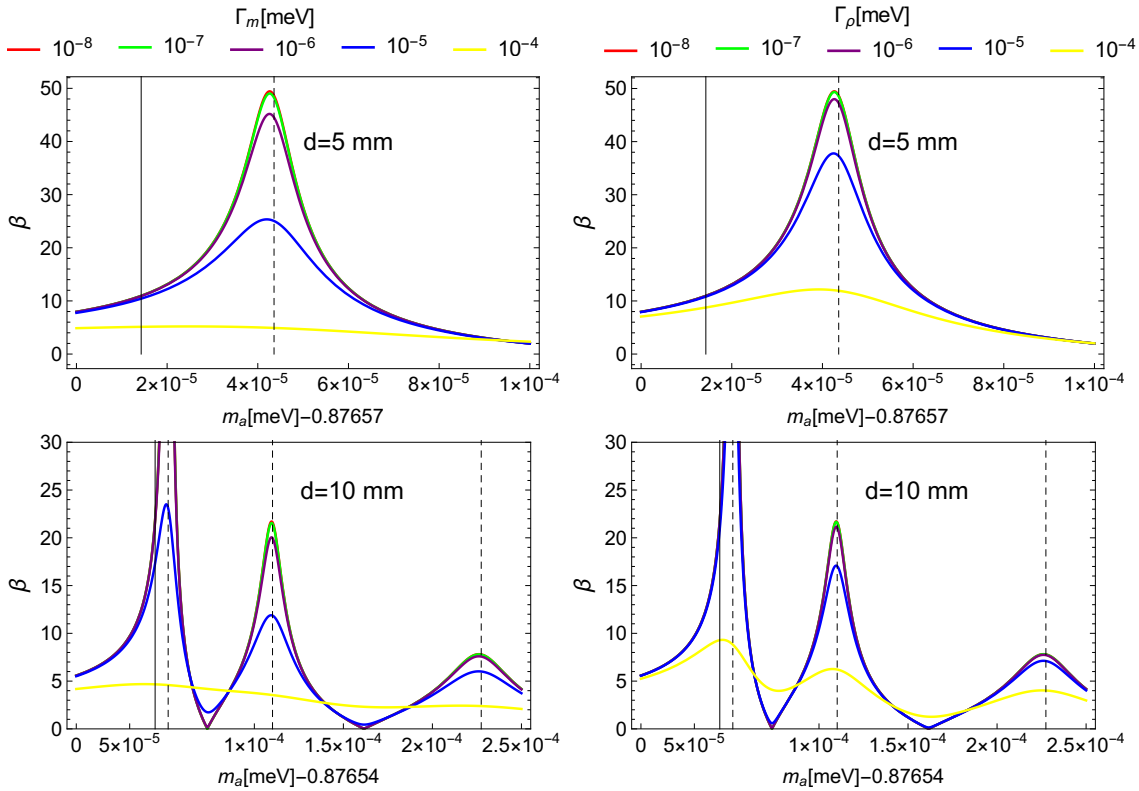

Figure 5.12: Power boost amplitude β for a TMI layer. DAs are assumed to have zero velocity and produce via mixing a detectable photon signal that propagates away from the TMI layer. We show the power boost amplitude for two different TMI layer thicknesses d. Top row: $d = 5\,\text{mm}$, bottom row $d = 10\,\text{mm}$. The solid vertical line signifies the position of ω_{LO} while the dashed lines mark the position of the resonance frequencies ω_j. In the $d = 5\,\text{mm}$ case only the main resonance frequency ω_0 is shown. However, in the case $d = 10\,\text{mm}$ the first three resonance peaks ω_0, ω_1 and ω_2 are shown. In the left column we vary magnon losses Γ_m, while photon losses Γ_ρ are set to zero. The right column shows the variation of photon losses while magnon losses are neglected. Typical material values for a TMI with an external B-field of $B^e = 2\,\text{T}$ are used: $m_\Theta = 0.72\,\text{meV}, b = 0.5\,\text{meV}$, cf. equation (5.3)-(5.5). Furthermore, we use $n = 10, \mu = 1$ [17]. Magnon losses Γ_m have a larger effect on the resonances than photon losses Γ_ρ. However, they lead to a smaller reduction of higher resonant mode peaks. This is because the imaginary damping part originating from Γ_m peaks around m_Θ and falls off for larger frequencies, cf. figure 5.5.

obtain:

$$g_{a\gamma} > 2.4 \times 10^{-9} \frac{1}{\mathrm{GeV}} \left(\frac{2\,\mathrm{T}}{B^e}\right) \left(\frac{1\ \mathrm{mm}^2}{A}\right)^{\frac{1}{2}} \left(\frac{300\frac{\mathrm{MeV}}{\mathrm{cm}^3}}{\rho_a}\right)^{\frac{1}{2}} \left(\frac{2\,\mathrm{meV}}{m_a}\right)^{\frac{1}{2}} \left(\frac{\Delta_j}{\pi}\right)^2 \left(\frac{2\,\mathrm{mm}}{d}\right)^2 \left(\frac{60\,\mathrm{s}}{\tau}\right)^{\frac{1}{2}}. \tag{5.109}$$

Note that the strength of the AQ-photon coupling b and the refractive index n do not explicitly appear, since only the maximum value of the resonance, cf. equation (5.106) enters the sensitivity.

In figure 5.13 the sensitivity for a layer of $(Bi_{1-x}Fe_x)Se_3$ is shown. The left figure shows the case of a $d = 2\,\mathrm{mm}$ thick TMI layer, while the right figure shows the case of a $d = 5\,\mathrm{mm}$ thick layer. In each figure we show the sensitivity reach (above the blue lines) in the DA mass-DA coupling range for a different layer surface areas A. The QCD axion band is shown in yellow. In the most optimistic case ($A = 100\ \mathrm{m}^2$ and $d = 5\,\mathrm{mm}$) the sensitivity reaches a large fraction of the QCD band. However, in the case that the layer surface area is much smaller ($d = 1\,\mathrm{mm}^2$) the sensitivity does not reach down to the QCD band. A good compromise would be the case $A = 1\,\mathrm{m}^2$, since for this surface area large parts of the QCD band can be reached and it is possible to have a magnet with tunable B-field strength over $A = 1\,\mathrm{m}^2$. The sensitivity estimate in figure 5.13 assumes that only the resonance around ω_0 is used. However, once the losses Γ_m and Γ_ρ are determined it might be useful to use higher resonant modes $j > 0$. Note that for $B^e \to 0$ we also have $\gamma_j \to 0$ and therefore at some point γ_j will be smaller than the axion linewidth. To avoid this case the sensitivity estimate starts with an external B-field of $B^e = 0.5\,\mathrm{T}$.

The sensitivity estimate in the figures 5.13 does not take into account losses. However, our results point out that the exact values of the losses will decide finally if the DA search can be performed or not. In the case that the losses reduce the boost factor by orders of magnitude the QCD band might not be reached. We therefore conclude that after finding the axion quasiparticles in TMI, it is of huge importance for a DA search to determine the magnon and photon losses in these materials. In section 5.2.2.3 we have described how this works. One has to fit the measured transmission spectra to our model such that one can extract the precise values for the losses.

5.4 Summary

Besides in particle physics, axions were proposed very recently to exist also as quasiparticles in condensed matter systems such as TMIs [17]. The main difference between axions in TMIs and axions in particle physics is that the axions in TMIs are quasiparticles while the axions in particle physics are real particles. AQs and axions from particle physics have the same interaction with the electromagnetic fields, what explains the name of the quasiparticles. For this reason it is very appealing for particle physicists to study AQs in order to learn more about the so far elusive axions in particle physics.

Until today AQs in TMIs have not been found in experiments. In section 5.2 of this chapter we discussed therefore how this could be achieved in the future. One way to detect AQs in TMIs is via THz spectroscopy. A layer of TMI is exposed to electromagnetic radiation in the THz regime. If AQs exists, the transmission spectrum should be gapped at a specific frequency range, which corresponds to the AQ mass. For a detection in the future it is very important to have a detailed signal calculation such that experimentalists know what they should expect and look for. Therefore, in section 5.2 of this chapter we presented a novel signal calculation for a THz transmission experiment. The calculation takes into account the correct interface conditions for the electromagnetic fields and includes magnon as well as photon losses. We demonstrated that for varying external B-fields the axion-polariton resonance frequency as well as the gap size of the transmission spectrum changes. We showed that by fitting upcoming transmission measurements

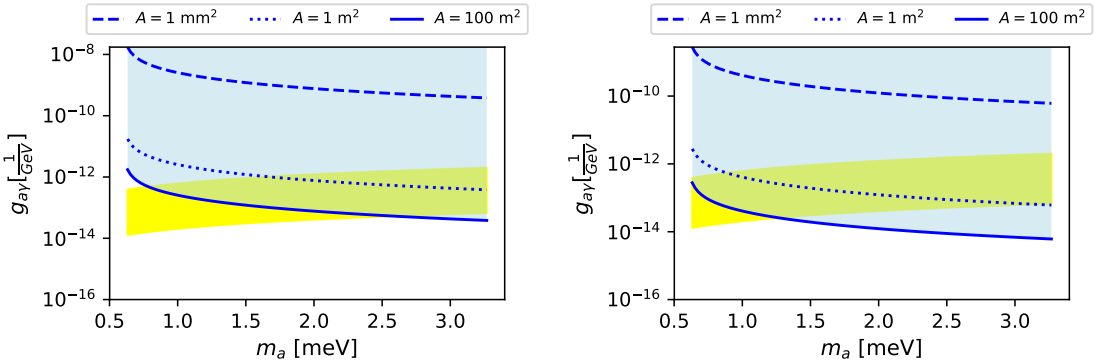

Figure 5.13: Sensitivity estimate for the DA-photon coupling $g_{a\gamma}$ with respect to the DA mass. The DAs, AQs and photons mix resonantly inside the TMI such that a detectable photon signal proagates away from the TMI. Two different TMI layer thicknesses $d = 2\,\mathrm{mm}$ (left) and $d = 5\,\mathrm{mm}$ (right) are shown. The external B-field varies from 0.5 T to 10 T and material values for $(Bi_{1-x}Fe_x)Se_3$, cf. equations (5.3)-(5.5) are used. The refractive index is $n = 10$ while the permeability is $\mu = 1$ [17]. In each plot the sensitivity estimate for different surface areas A is shown. In the case $d = 2\,\mathrm{mm}$ only the most optimistic case with a surface area of $A = 100\ \mathrm{m}^2$ covers a significant fraction of the QCD band (yellow). In the case of a $d = 5\,\mathrm{mm}$ thick TMI layer also the $A = 1\ \mathrm{m}^2$ case can exclude a significant fraction of the QCD band. The QCD band in this plot is defined by $C_{a\gamma}$ ranging from 0.1 to 3.

to the presented signal calculation the material properties of the TMI, i.e. the refractive index, the magnon and photon losses and the parameters that enter the AQ mass m_Θ and the gap size b, can be determined. The knowledge of these parameters will be crucial for applications. One of these applications was discussed in the second part of this chapter.

In section 5.3 of this chapter we showed that AQs – if realized in novel materials – can also be used for DA detection. DAs, AQs and photons can resonantly mix in TMIs and therefore produce an enhanced photon signal that leaves the TMI. For the first time we explicitly calculated the photon signal, which such a mixing phenomenon would create. Our calculation takes into account the correct interface conditions for all fields and also includes material losses.

In particular we found that the emitted photon signal from a layer of TMI has a Lorentzian shape. The amplitude enhancement of emitted E-field compared to the amplitude of the axion induced E-field in vacuum is specified through the boost factor β. We calculated the width and hight of β analytically around the resonances.

For the case without material losses we found that the width scales as d^{-3} and the maximum of the Lorentzian curve as d^2, where d is the thickness of the TMI layer. This tells us that the TMI should have a certain thickness in order to achieve a large enough boost factors. However, the thickness should not be too large because then the width of the Lorentzian curve becomes extraordinarily small. Furthermore the width scales with the refractive index as n^{-2}, while the maximum is not affected by the refractive index. Therefore – contrary to axion haloscopes such as MADMAX – large refractive indices are highly disfavored for DA detection with a layer of TMI.

We showed that TMI layers with a thickness of a few mm and surface area of around $1\,\mathrm{m}^2$ are able to reach down to the QCD axion band in the region between $0.7 - 3.5\,\mathrm{meV}$. Future advances in material science, with axion polariton resonances in different frequency regimes, can extend the mass range for DA searches. The sensitivity estimate for two benchmark thicknesses $d = 2\,\mathrm{mm}$ and $d = 5\,\mathrm{mm}$ is shown in figure 5.13.

The influence of losses on the emitted signal, i.e. the boost factor β, was also evaluated. In

the lossless case we see that making the TMI layer thicker increases the maximum boost factor β. However, when taking into account losses we cannot increase the maximum β arbitrarily, since the thicker we make the TMI, the larger the influence of the losses becomes. We found that for a benchmark TMI thickness of 5 mm, magnon and photon losses $\Gamma_m, \Gamma_\rho \leq 10^{-5}$ meV are acceptable.

Chapter 6

Overall Summary and Outlook

Axions in particle physics can solve two main problems of modern physics. They can account for the dark matter relic density in the universe and solve the strong CP problem of the SM. Particle physics axions have not been detected so far. However, due to the good theoretical and phenomenological motivation the search for axions is getting more and more attention recently. The fact that other dark matter candidates have not been found yet reinforces this trend. In the first part of this thesis (chapter 3 and 4) several possibilities to directly detect axions are considered. The second part (chapter 5) focuses on axion quasiparticles, which could be present in condensed matter systems such as topological magnetic insulators. The quasiparticles are also called axions, since they interact with the electromagnetic fields exactly as the particle physics axions do. First, we consider how the AQs can be detected in TMIs. Then we point out how AQs can be used for dark matter axion detection. In the following we give a short summary of the three chapters of this thesis, which contain the main results.

A generalized matrix formalism and the application to light shining through a wall experiments

In chapter 3 we solved the axion-Maxwell equations in the presence of an external B-field to all orders in the axion-photon coupling and for arbitrary axion velocities. We classified the solutions into a weak and strong mixing regime. Our computation is valid for materials of arbitrary permittivity, permeability and conductivity. On the basis of this we developed a matrix formalism that describes the axion-photon mixing in multi layer systems. The matrix formalism is obtained by applying appropriate interface conditions for the axion and photon fields at each layer interface. A multi layer system can for example be multiple magnetized dielectric layers or successive magnetized and non-magnetized regions. The matrix formalism that is presented here is more general than that of previous studies [58, 59], since it is valid for arbitrary, not just small, axion velocities. We applied the developed matrix formalism to the case of relativistic axions. As a validation we first reproduced the well known axion-photon conversion formulas. Then we used the matrix formalism to study light shining through a wall experiments. In ordinary LSW experiments axions are produced in a magnetized generation region. The generated axions then travel through a wall and are reconverted into measurable photons. In chapter 3 we investigated in particular how the LSW sensitivity can be increased with dielectric layers, placed inside the magnetized regions of the (re)generation regions. We found that the layers can be configured in a resonant and a transparent configuration.

In the transparent configuration the layers are transparent to all electromagnetic radiation and therefore the radiation that is coming from each layer can be coherently added. The transparent configuration can increase the LSW sensitivity with respect to an ordinary LSW setup (without

dielectric layers) only in the high mass region, where the axion and photon wavelengths start to differ significantly. An advantage of the dielectric layers in LSW setups is that – contrary to ordinary LSW setups – one can achieve the greater sensitivity at a specific axion mass interval. The interval can be tuned by varying the distance between the dielectric layers. This can be useful for confirming or excluding hints from astrophysics or other Earth based experiments at a specific axion mass. However, dielectric layers in LSW experiments are not useful for scanning large mass ranges, since the number of layers would have to be changed constantly. As a specific example we considered the ALPS II setup. With dielectric layers the sensitivity can be increased starting for axion masses that are larger than $10^{-4}\,\mathrm{eV}$. The estimated sensitivity reach in the m_a-$g_{a\gamma}$ plane is visualized in figure 6.1 and labeled as 'ALPS dielectric'. We demonstrated that the dielectric layers have to be manufactured with high precision. For example for a 200 dielectric layer setup which enhances axion masses around $m_a \approx 1\,\mathrm{meV}$ the layer surface precision has to be on the order $10\,\mathrm{nm}$. A practical realization therefore seems challenging but not impossible. The precision with which the layers have to be positioned is much less important and for $m_a \approx 1\,\mathrm{meV}$ on the order of cm. A sensitivity reduction due to imprecisely manufactured layers is already incorporated in the 'ALPS dielectric' sensitivity forecast in figure 6.1. Although the 'ALPS' dielectric' sensitivity range in figure 6.1 is already excluded by CAST it could be relevant, since it was recently shown that the CAST limits can be relaxed due to the suppression of ALP production in a dense astrophysical plasma [125].

Another new finding of this thesis is that the magnetized dielectric layers can also be used in a resonant configuration to boost LSW experiment sensitivities. We pointed out that this could be an alternative to the cavities, that usually surround the (re)generation regions. However, future studies have to confirm if it is really possible to beat the cavity approach from a technological point of view, since the dielectric layers also have to be positioned with high precision. Our presented matrix formalism is perfectly suited to carry out these future studies.

Three dimensional effects in open axion haloscopes

Open axion haloscopes, such as dielectric haloscopes and dish antennas, search for axions from the dark matter halo. Dish antennas are magnetized conductors which convert the axion induced electric field into propagating (photon-like) radiation. Dielectric haloscopes consist of a magnetized conductor as well as of magnetized dielectric disks [1] which all emit photon-like radiation. The dielectric disks can be configured so that the dielectric haloscope is sensitive to a specific axion mass interval. Contrary to axion cavity searches, dielectric haloscopes and dish antennas are open systems. In order to make realistic sensitivity estimates it is important to study the three dimensional effects, that can arise in these systems.

In this thesis we established two efficient techniques for calculating the electromagnetic fields in open axion haloscopes in three dimensions. Our advanced techniques are necessary since straightforward three dimensional finite element calculations are computationally very expensive. One of the presented methods relies on a two dimensional FEM solution and is capable of calculating three dimensional solutions for a radial symmetric geometry even in the case where a linearly polarized external B-field breaks the radial symmetry (2D3D approach). The second method recursively constructs the three dimensional solution by propagating the emitted electromagnetic fields inside the systems. For the propagation one can use vector diffraction or scalar diffraction equations (recursive Fourier propagation approach).

With the developed methods we study axion velocity effects in dish antennas, such as the BRASS experiment [87]. The diffraction pattern of the emitted electromagnetic radiation and the influence of axion velocity effects are computed. For wavelengths large than $0.1\,\mathrm{cm}$ ($m_a < 120\,\mu\mathrm{eV}$)

[1] Here we use the word 'disk', however conceptually a dielectric disk and a dielectric layer are the same.

the width of the diffraction pattern is greater than the shift of the diffraction pattern due to axion velocity effects. On the other hand if $\lambda < 0.1\,\mathrm{cm}$ ($m_a > 120\,\mu\mathrm{eV}$) the width of the diffraction maximum is smaller than the shift and therefore velocity effects become more pronounced.

With the developed three dimensional methods we also investigated the feasibility of the MADMAX axion haloscope. Among the studied effects are diffraction, disk tiling and waveguide surroundings. Diffraction effects only lead to a reduction between $30\% - 40\%$ when the coupling to an antenna is considered. A surrounding waveguide would have almost no influence on the emitted electromagnetic radiation. In the most extreme cases that were studied in this thesis there would be a combined reduction by a factor of 2 from the diffraction and disk tiling effects. Motivated by our studies the MADMAX sensitivity is reduced by a factor of 2 – compared to an idealized one dimensional estimate – in figure 6.1. The reduction by a factor of 2 is not severe since the axion-photon coupling is shown on a logarithmic scale and the QCD band can still be reached. We therefore conclude that none of the studied 3D effects reduces the sensitivity of the MADMAX haloscope so much that they can be regarded as a show stopper.

A potential future study would be to consider tiled disks with hexagonal tiles instead of radial symmetric tiles that were used in this chapter. Hexagonally tiled disks are foreseen in the upcoming MADMAX experiment. However, since the radial symmetric tiles approximate the hexagonal structure well no further significant sensitivity reduction, on top of the one that was obtained here, is expected. Another future study would be to investigate if the disk distances, which are currently optimized within a one dimensional model, can be optimized such that three dimensional losses are minimized.

Axion quasiparticles and the quest for dark matter

In the second part of this thesis we investigated axion quasiparticles in condensed matter systems such as topological magnetic insulators. Axions in TMIs are quasiparticles that physically correspond to magnetic fluctuations. AQs were proposed in the 2010s [17] much later than axions in particle physics. Until today AQs in TMIs have not been found. Therefore, the first part of chapter 5 discusses how one could find AQs in TMIs while in the second part we considered how those can be used to search for dark matter axions.

One idea how to detect AQs in TMIs is via THz transmission experiments. This is because the transmission spectrum has a gap (zero transmission) in the presence of AQs [17]. The gap is around the AQ mass that is predicted to be in the meV (THz) range. Here we have performed for the first time an explicit transmission spectrum calculation for one layer of TMI. We discussed the correct interface conditions and included magnon as well as photon losses. We found that in order to detect the AQ in THz transmission experiments the thickness of the layer should be on the order of 0.01 mm. If the thickness is too large then the gap in the spectrum cannot be identified anymore, since the losses dominate. However, if the layer is too thin, the gap in the spectrum also partly disappears.

Once AQs in TMIs are found, we demonstrated that by fitting our signal calculation to future measurements of the transmission spectrum we can determine the material properties of the TMI. It will be advantageously to compare the future measurements to our calculation for different layer thicknesses since the exact order of magnitude of the losses is not known beforehand and different thicknesses are differently sensitive to magnon and photon losses. The knowledge of the material properties, i.e. the refractive index, the magnon and photon losses and the parameters that enter the AQ mass m_Θ and the gap size b, is important for future applications. One of these is the use of TMIs with established AQs as axion dark matter detector.

In TMIs, photons, AQs and DAs can mix resonantly such that the signal from weakly interacting DAs is enhanced sufficiently for detection. In this thesis we considered a single TMI layer that is magnetized by an external B-field and hosts AQs. Scanning different axion masses can be achieved

by changing the strength of the external B-field, i.e. the axion quasiparticle mass. Contrary to previous signal estimates [19], we performed for the first time a full calculation that takes into account the interface conditions for the axion and photon fields as well as material losses.

For the description of the emitted photon signal from the TMI we used the boost factor β as a quantity that describes the enhancement of the emitted signal E-field compared to the axion induced E-field in vacuum. In our calculation we found that the resonance of the boost factor follows a Lorentzian shape. The width of the resonances scales with the refractive index as n^{-2} while the maximal value at the resonance does not increase for larger or smaller refractive indices. Therefore an important finding is that TMIs with a small refractive index are highly favored for a DA search. The width of the boost factor scales with the thickness of the layer as d^{-3}, while the maximal peak value of β scales as d^2. Therefore, a good compromise for the thickness has to be found. It should not be too thick so that the width of the resonance becomes smaller than the axion linewidth. However, it should also not be too thin, since then the amount of power enhancement is too small to reach the QCD axion band. We showed that for two benchmark thickness of $d = 2\,\mathrm{mm}$ and $d = 5\,\mathrm{mm}$ the QCD axion band for axion masses between $m_a = 0.7 - 3.5\,\mathrm{meV}$ can be reached if the TMI material has a surface area of $A = 1\,\mathrm{m}^2$. The sensitivity reach of a TMI layer with thickness $d = 5\,\mathrm{mm}$ and surface area $A = 1\,\mathrm{m}^2$ is shown in figure 6.1 and labeled as 'TOORAD' (Topological Resonant Axion Detection).

Magnon as well as photon losses may further reduce the sensitivity of the DA search. For our benchmark thicknesses the magnon and photon losses have to be smaller than $\Gamma_m, \Gamma_\rho < 10^{-5}\,\mathrm{meV}$. Our results are relevant for the design of TMI materials that would be suited for DA detection.

Our work illustrates how advances in material science can boost the progress in axion dark matter direct detection. Having at hand materials containing AQs of larger or smaller masses would, in turn, allow one to search for DAs in an even wider mass range. Another possibility is to investigate other quasiparticles such as phonons. Studies in this direction have been done in Ref. [126] but could eventually be extended to wider axion mass ranges.

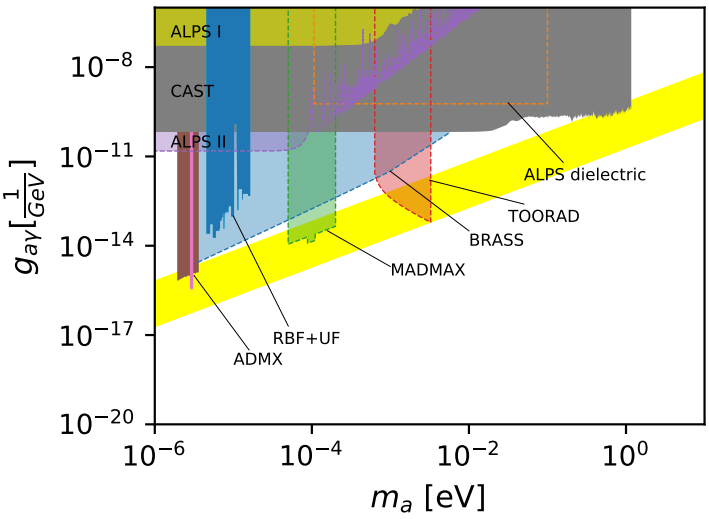

Figure 6.1: Overview of different direct detection approaches for particle physics axions. We show the axion-photon coupling $g_{a\gamma}$ over the axion mass m_a. The QCD axion band is shown in yellow and corresponds to values $C_{a\gamma} = 3 \cdots 0.1$. All colored regions, which are transparent and boxed by dashed lines, are projected sensitivities for upcoming experiments. We show only approaches that have been considered in this thesis. The TOORAD sensitivity was calculated in chapter 5 of this thesis. Due to three dimensional effects the MADMAX [86, 112] sensitivity was decreased by a factor 2 in comparison to an idealized one dimensional calculation. We discussed the three dimensional effects in chapter 4. For the BRASS haloscope [87] we have considered axion dark matter velocity effects in chapter 4. The ALPS dielectric sensitivity was derived in chapter 3 with a generalized matrix formalism. As a comparison we also show the ALPS II sensitivity [11]. The non transparently colored regions are already excluded by experiments. We show the regions that are excluded by ADMX [13, 14, 127, 128], RBF [15], UF [16], CAST [12] and ALPS I [129]. For better visibility we do not show small excluded regions from the experiments ORGAN [130], HAYSTAC [131, 132], QUAX [133], CAPP-8TB [134]. The sensitivity forecast of the upcoming or upgraded experiments ABRACADABRA [135], ADMX [136], KLASH [137], LAMPOST [138], ORGAN [130] Plasma Haloscope [139] IAXO [140] are not shown here, since the plot serves as a summary plot of this thesis.

Acknowledgements

I would like to express my deepest gratitude to Andreas Ringwald who has supervised me now for three years. Andreas always supported my work and most importantly gave me the freedom to conduct my own independent research. I really enjoyed our discussions and the questions that he raised. I also want to thank Erika Garutti for the discussions on MADMAX. Erikas broad knowledge on the MADMAX setup really increased the level of reality of the MADMAX related calculations. Thanks also to Geraldine Servant, Dieter Horns and Günter Sigl for agreeing to be in the committee for my defense.

I also enjoyed to work together with David J.E. Marsh on how to detect dark matter axions with axion quasiparticles. It was a lot of fun to work on this very interdisciplinary topic which was guided by Davids excellent physical intuition. I also would like to thank Alexander Millar, Akihiko Sekine, Erik Lentz, Libor Smejkal, Sebastian Hoof, Nicolo Crescini and Mazhar Ali for working together on the TOORAD project.

It was also fun to work together with Stefan Knirck on the calculations and simulations for the MADMAX experiment. In addition I would also like to thank Javier Redondo, Frank Steffen, Alexander Schmidt and Christoph Krieger for useful comments on the MADMAX calculations and simulation.

I also want to thank all people from DESY with whom it was always fun to chat during lunch or to discuss any kind of physics related questions. Thanks to: Daniel Meuser, Ivan Sobolev, Philipp Englert, Yoshiyuki Tatsuta, Gleb Kotousov, Thomas Biekötter, Pablo Quilez and Anton Sokolov! I also have to thank you guys for proof reading parts of my thesis and any kind of social activities like watching Champions League or going to Schanze.

From the good old times in Aachen I want to thank my friends Thorben Quast and Fabian Lux. I have to thank Thorben for his wise advice (although the beard is missing) and for proof reading a part of my thesis. I also have to acknowledge Fabians support when we chatted about axion quasiparticles and topological magnetic insulators on Sunday evenings.

Finally, I want to thank my parents Rosa and Jürgen for supporting me in any kind of situation in life. Your support has given me strength to go my own way in life. I also have to thank Alejandra for her support especially in the end phase of my thesis.

Appendix A

Appendix for chapter 3

A.1 Further cases for the single interface

Here we compute the emitted fields from one single surface. In the case for incoming axions we consider a surface at which the permeability jumps from one value to another value. In the case of incoming axions we consider a permittivity and permeability discontinuity.

A.1.1 Incoming axions

A.1.1.1 Permeability discontinuity

In this section we assume that the two media have the permeabilities μ_0 and μ_1. Furthermore we require $\epsilon_0 = 1 = \epsilon_1$ and the loss in the media is neglected $\sigma_0 = 0 = \sigma_1$. We give again the solution for the fields in the weak mixing region:

$$\begin{pmatrix} \hat{E}_0^{+-} \\ \hat{a}_0^{--} \\ \hat{E}_1^{++} \\ \hat{a}_1^{-+} \end{pmatrix} = \begin{pmatrix} \frac{\hat{E}^a_{L,0}\left(k_a \frac{\mu_1}{\mu_0} - k_p^1\right) + \hat{E}^a_{L,1}(k_p^1 - k_a)}{k_p^0 \frac{\mu_1}{\mu_0} + k_p^1} \\ 0 \\ \frac{\hat{E}^a_{L,0}(k_a + k_p^0) - \hat{E}^a_{L,1}\left(k_a \frac{\mu_0}{\mu_1} + k_p^0\right)}{k_p^0 + k_p^1 \frac{\mu_0}{\mu_1}} \\ \hat{a}_0^{-+} \end{pmatrix} + \mathcal{O}(\tilde{x}^2), \tag{A.1}$$

with $k_p^{0/1} = \sqrt{\mu_{0/1}}\omega$. Note again that for low velocity axions the whole weak mixing region coincides with almost the entire range for the oscillatory couplings $g_{a\gamma}$. The permeability discontinuities produce detectable photon-like radiation similar to the case of a dielectric interface. One can combine many permeability discontinuities to enhance the photon-like signal as it was already suggested for many dielectric surfaces in a dielectric haloscope [58]. We leave the investigation of a permeability axion haloscopes for future studies.

A.1.2 Incoming photons

A.1.2.1 Permittivity Discontinuity

Medium 0 has refractive index $n_0^2 = \epsilon_0$ and medium 1 $n_1^2 = \epsilon_1$. The weak mixing regime is then determined by $\min(n_0^2 - 1, n_1^2 - 1)$. We find explicitly in the weak mixing regime for the unknown fields:

$$\begin{pmatrix} \hat{E}_0^{+-} \\ \hat{a}_0^{--} \\ \hat{E}_1^{++} \\ \hat{a}_1^{-+} \end{pmatrix} = \begin{pmatrix} \hat{E}_0^{++} \frac{n_0 - n_1}{n_0 + n_1} \\ \frac{1}{2}\left(1 - \frac{k_p^1}{k_a}\right)\left(\hat{a}^p_{L,1} - \hat{a}^p_{L,0} \frac{2n_0}{n_0 + n_1}\right) \\ \hat{E}_0^{++} \frac{2n_0}{n_0 + n_1} \\ \frac{1}{2}\left(1 + \frac{k_p^1}{k_a}\right)\left(\hat{a}^p_{L,0} \frac{2n_0}{n_0 + n_1} - \hat{a}^p_{L,1}\right) \end{pmatrix} + \mathcal{O}(\tilde{x}^2). \tag{A.2}$$

The reflected and transmitted E-fields are up to linear order in $\tilde{x}$ given by the ordinary reflection and transmission coefficients for a dielectric interface. The axion fields that travel in the positive and negative z-direction can be understood again with a continuity argument. The total axion field between both media has to be continuous and therefore axions, that are radiated off the interface, are generated. Due to the similarity to the incoming axion case we do not show again a figure that illustrates this behavior. Let us stress that in the limit $m_a \ll \omega$ and $n \to 1$ the axions that propagate in the opposed direction to the incoming photons are suppressed by the factor $1 - \frac{k_p^1}{k_a} \ll 1$.

A.1.2.2 Permeability discontinuity

Here we have $\epsilon_0 = 1 = \epsilon_1$, but both media have a different permeability μ_0 and μ_1 ($n_0 = \sqrt{\mu_0}$, $n_1 = \sqrt{\mu_1}$). In the following we give the formulas for the unknown field amplitudes in the weak mixing regime:

$$\begin{pmatrix} \hat{E}_0^{+-} \\ \hat{a}_0^{--} \\ \hat{E}_1^{++} \\ \hat{a}_1^{-+} \end{pmatrix} = \begin{pmatrix} \hat{E}_0^{++} \frac{\mu_1 n_0 - \mu_0 n_1}{\mu_0 n_1 + \mu_1 n_0} \\ \hat{a}_{L,0}^p \left(\frac{k_p^1}{k_a} - \frac{\mu_1}{\mu_0}\right) (\frac{\mu_1}{\mu_0} + \frac{n_1}{n_0})^{-1} + \frac{1}{2}\hat{a}_{L,1}^p \left(1 - \frac{k_p^1}{k_a}\right) \\ \hat{E}_0^{++} \frac{2 n_0 \mu_1}{n_0 \mu_1 + n_1 \mu_0} \\ \hat{a}_{L,0}^p \left(\frac{k_p^1}{k_a} + \frac{\mu_1}{\mu_0}\right) (\frac{\mu_1}{\mu_0} + \frac{n_1}{n_0})^{-1} - \frac{1}{2}\hat{a}_{L,1}^p \left(\frac{k_p^1}{k_a} + 1\right) \end{pmatrix} + \mathcal{O}(\tilde{x}^2). \tag{A.3}$$

We do not investigate the effect of permeability discontinuities further. However, the results will be useful for further studies on axion haloscopes with materials of nontrivial permeability. Note that the coefficients for the photon-like E-fields in equation (A.3) are not modified by axion interactions to lowest order.

A.2 Matrix formalism in the weak coupling regime

The interface conditions at interface z_j are described by equation (3.53). We rephrase the equation as:

$$\boldsymbol{t}_j = \boldsymbol{S}_{j,j-1} \boldsymbol{t}_{j-1}, \quad \text{with } \boldsymbol{S}_{j,j-1} := \boldsymbol{M}_j^{-1} \boldsymbol{M}_{j-1} \boldsymbol{P}_{j-1}. \tag{A.4}$$

In the following we divide the 4×4 matrices of the matrix formalism into 2×2 block matrices:

$$\boldsymbol{M}_j = \begin{pmatrix} \boldsymbol{A}_j & \boldsymbol{B}_j \\ \boldsymbol{C}_j & \boldsymbol{D}_j \end{pmatrix}, \quad \boldsymbol{P}_j = \begin{pmatrix} \boldsymbol{E}_j^+ & 0 \\ 0 & \boldsymbol{E}_j^- \end{pmatrix}, \tag{A.5}$$

where $\boldsymbol{B}_j$ and $\boldsymbol{C}_j$ are of the order $\tilde{x}$. We are interested in :

$$\boldsymbol{S}_{j,j-1} = \begin{pmatrix} \boldsymbol{A}_j^{-1} \boldsymbol{A}_{j-1} & \boldsymbol{A}_j^{-1} \boldsymbol{B}_{j-1} - \boldsymbol{A}_j^{-1} \boldsymbol{B}_j \boldsymbol{D}_j^{-1} \boldsymbol{D}_{j-1} \\ -\boldsymbol{D}_j^{-1} \boldsymbol{C}_j \boldsymbol{A}_j^{-1} \boldsymbol{A}_{j-1} & \boldsymbol{D}_j^{-1} \boldsymbol{D}_{j-1} \end{pmatrix} \begin{pmatrix} \boldsymbol{E}_{j-1}^+ & 0 \\ 0 & \boldsymbol{E}_{j-1}^- \end{pmatrix} + \mathcal{O}(\tilde{x}^2). \tag{A.6}$$

In the section about single interfaces we saw, that reflected axions are always zero up to linear order. Therefore we get:

$$\begin{pmatrix} \hat{E}_j^{++} \\ \hat{E}_j^{+-} \end{pmatrix} = \begin{pmatrix} S_{j,j-1}^{(1,1)} & S_{j,j-1}^{(1,2)} \\ S_{j,j-1}^{(2,1)} & S_{j,j-1}^{(2,2)} \end{pmatrix} \begin{pmatrix} \hat{E}_{j-1}^{++} \\ \hat{E}_{j-1}^{+-} \end{pmatrix} + \hat{a}_{j-1}^{-+} \begin{pmatrix} S_{j,j-1}^{(1,3)} \\ S_{j,j-1}^{(2,3)} \end{pmatrix} + \mathcal{O}(\tilde{x}^2). \tag{A.7}$$

Explicitly we have:

$$\begin{pmatrix} S_{j,j-1}^{(1,1)} & S_{j,j-1}^{(1,2)} \\ S_{j,j-1}^{(2,1)} & S_{j,j-1}^{(2,2)} \end{pmatrix} = \boldsymbol{A}_j^{-1} \boldsymbol{A}_{j-1} \boldsymbol{E}_{j-1}^+ =: \boldsymbol{G}_{j-1} \boldsymbol{E}_{j-1}^+, \tag{A.8}$$

with

$$\boldsymbol{G}_{j-1} = \frac{1}{2 k_p^j \mu_{j-1}} \begin{pmatrix} k_p^j \mu_{j-1} + k_p^{j-1} \mu_j & k_p^j \mu_{j-1} - k_p^{j-1} \mu_j \\ k_p^j \mu_{j-1} - k_p^{j-1} \mu_j & k_p^j \mu_{j-1} + k_p^{j-1} \mu_j \end{pmatrix} \tag{A.9}$$

and

$$\bar{\boldsymbol{K}}_{j-1} := \hat{a}_{j-1}^{-+} \begin{pmatrix} S_{j,j-1}^{(1,3)} \\ S_{j,j-1}^{(2,3)} \end{pmatrix} = \hat{a}_{j-1}^{-+} \frac{e^{i\Delta_-^{j-1}}}{2k_p^j} \begin{pmatrix} -\delta_j \omega \mu_j (k_a + k_p^j) + \delta_{j-1} \omega (k_a \mu_j + k_p^j \mu_{j-1}) \\ \delta_j \omega \mu_j (k_a - k_p^j) + \delta_{j-1} \omega (k_p^j \mu_{j-1} - k_a \mu_j) \end{pmatrix}, \tag{A.10}$$

where all appearing quantities are understood to be up to linear order in $\tilde{x}$.

Summarized we get at z_j:

$$\begin{pmatrix} \hat{E}_j^{++} \\ \hat{E}_j^{+-} \end{pmatrix} = \boldsymbol{G}_{j-1} \boldsymbol{E}_{j-1}^{+} \begin{pmatrix} \hat{E}_{j-1}^{++} \\ \hat{E}_{j-1}^{+-} \end{pmatrix} + \bar{\boldsymbol{K}}_{j-1} + \mathcal{O}(\tilde{x}^2), \quad j = 1, \cdots, N. \tag{A.11}$$

When we apply the formulas recursively we end up with:

$$\begin{pmatrix} \hat{E}_N^{++} \\ \hat{E}_N^{+-} \end{pmatrix} = \boldsymbol{T}_0^N \begin{pmatrix} \hat{E}_0^{++} \\ \hat{E}_0^{+-} \end{pmatrix} + \sum_{s=1}^{N} \boldsymbol{T}_s^N \bar{\boldsymbol{K}}_{s-1}, \tag{A.12}$$

with $\boldsymbol{T}_b^a = \boldsymbol{G}_{a-1} \boldsymbol{P}_{a-1} \cdots \boldsymbol{G}_b \boldsymbol{P}_b$ and $\boldsymbol{T}_N^N := \mathbf{1}$ and $\boldsymbol{P}_0 = \mathbf{1}$. Note that up to leading order $\hat{a}_j^{-+} e^{-ik_- z_j} = \hat{a}_0^{-+}$ and therefore a common factor can be pulled out of the sum in equation (A.12). We have chosen here a convention very similar to [58] and [59], where a matrix formalism for zero and small axion velocities is presented. Our results generalize these results to arbitrary axion velocities.

If there are no incoming E-fields ($\hat{E}_0^{++} = 0$ and $\hat{E}_N^{+-} = 0$) the field amplitudes leaving the system to the left and right are:

$$\hat{E}_0^{+-} = -\frac{\bar{Q}_2}{T_{2,2}}, \tag{A.13}$$

$$\hat{E}_N^{++} = \bar{Q}_1 - \frac{T_{1,2}}{T_{2,2}} \bar{Q}_2, \tag{A.14}$$

where we have defined:

$$\bar{\boldsymbol{Q}} = \sum_{s=1}^{N} \boldsymbol{T}_s^m \bar{\boldsymbol{K}}_{s-1} \text{ and } \boldsymbol{T} := \boldsymbol{T}_0^N. \tag{A.15}$$

The matrix formalism that was derived here is valid for axions with arbitrary velocity. It is easy to see in our notation that in the zero velocity limit the equations reduce to the matrix formalism that was derived in [58].

The power emitted by the system to both sides in the z-direction under the assumption that medium $r = 0$ and $r = N$ are vacuum are:

$$P_z^L = \frac{A}{2} |\hat{E}_0^{+-}|^2 \tag{A.16}$$

$$P_z^R = \frac{A}{2} |\hat{E}_N^{++}|^2 \tag{A.17}$$

where A is the surface of the interfaces that emit the photon-like radiation.

A.3 Violation of energy conservation?

In section 3.4 we have seen that the outgoing fields can be enhanced in the strong mixing region by a factor $\frac{1}{\Delta n}$. In this section we investigate if this effect is physical. We do this by investigating if energy conservation is guaranteed. We do the calculation for the case of incoming axions $\hat{a}_0^{-+}$ on a magnetized region of length ℓ, cf. figure A.1. The amplitude of the axions that are transmitted and reflected are called $\hat{a}_2^{-+}$ and $\hat{a}_0^{--}$ respectively. The generated photons have the amplitude $\hat{E}_0^{+-}$ and $\hat{E}_2^{++}$.

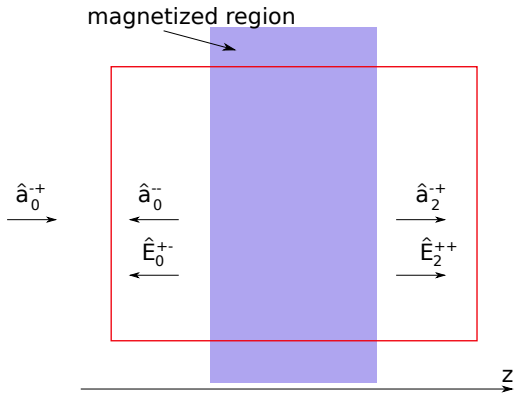

Figure A.1: Axions $\hat{a}_0^{-+}$ coming onto a magnetized region (blue). As a consequence there are reflected axions $\hat{a}_0^{--}$ and photons $\hat{E}_0^{+-}$ and also transmitted axions $\hat{a}_2^{-+}$ and generated photons $\hat{E}_2^{++}$.

To check if energy conservation holds we have to calculate the energy momentum tensor. Since we are interested only in the incoming and outgoing axion and photon fields we can calculate the energy momentum tensor under the assumption that the axions and photons are not mixed, i.e. we are in a region without external B-field. Furthermore we calculate everything in the massless limit $m_=0$, since in this limit the effect the Δn enhancement is visible best.

The energy momentum tensor of free massless axions with $\mathcal{L}_a = \frac{1}{2}\partial_\mu \partial^\mu a$ is given as:

$$T_a^{\mu\nu} = \frac{\partial \mathcal{L}}{\partial \partial_\mu a}\partial^\nu a - \eta^{\mu\nu}\mathcal{L} = \begin{pmatrix} \frac{1}{2}(\partial_t a)^2 & 0 & 0 & -\partial_t a \partial_z a \\ 0 & 0 & 0 & 0 \\ 0 & 0 & 0 & 0 \\ -\partial_t a \partial_z a & 0 & 0 & \frac{1}{2}(\partial_z a)^2 \end{pmatrix}, \tag{A.18}$$

where we have used that a just depends on z and time t. $w_a = T_a^{00}$ is the energy density and $S_a^i = T_a^{0i}$ is the energy flux.

The electromagnetic energy momentum tensor in perfect vacuum, which is derivable from the Lagrangian $\mathcal{L} = -\frac{1}{4}F_{\mu\nu}F^{\mu\nu}$, is:

$$T_{\mathrm{EM}}^{\mu\nu} = \begin{pmatrix} w_{\mathrm{EM}} & \boldsymbol{S}_{\mathrm{EM}}^T \\ \boldsymbol{S}_{\mathrm{EM}} & \sigma_{\mathrm{EM}}^{ij} \end{pmatrix}, \tag{A.19}$$

where $w_{\mathrm{EM}} = \frac{1}{2}(E^2 + B^2)$ is the energy density, $\boldsymbol{S}_{\mathrm{EM}} = \boldsymbol{E} \times \boldsymbol{B}$ the pointing vector and $\sigma_{\mathrm{EM}}^{ij}$ the Maxwell stress tensor, that is not further specified here. Including matter, the energy density and pointing vector become:

$$w_{\mathrm{EM}} = \frac{1}{2}(\boldsymbol{E}\cdot\boldsymbol{D} + \boldsymbol{B}\cdot\boldsymbol{H}), \tag{A.20}$$

$$\boldsymbol{S}_{\mathrm{EM}} = \boldsymbol{E}\times\boldsymbol{H}. \tag{A.21}$$

In our case we have plane waves that propagate in z-direction. Furthermore we can assume linear constitutive relations: $\boldsymbol{H} = \boldsymbol{B}$ and $\boldsymbol{D} = \epsilon\boldsymbol{E}$. The E-field is polarized in y-direction and the B-field in x-direction. In this case we get:

$$w_{\mathrm{EM}} = \frac{1}{2}(\epsilon E^2 + B^2), \tag{A.22}$$

$$\boldsymbol{S}_{\mathrm{EM}} = \hat{\boldsymbol{e}}_z n E^2. \tag{A.23}$$

The total energy momentum tensor is the sum $T^{\mu\nu} = T_a^{\mu\nu} + T_{\mathrm{EM}}^{\mu\nu}$. We have $\partial_\mu T^{\mu\nu} = 0$ and for $\nu = 0$ we get energy conservation:

$$\partial_0 w + \nabla\cdot\boldsymbol{S} = 0. \tag{A.24}$$

We focus now on the case that we have a single magnetized region of finite length, cf. figure A.1. We integrate equation (A.24) over the volume of the red box that is shown in figure A.1 and apply the divergence theorem:

$$\partial_t W + \int d\boldsymbol{A} \cdot \boldsymbol{S} = 0. \tag{A.25}$$

$W = \int dV w$ is the total energy in the red box. Note that we cannot determine W with the energy momentum tensor that we have derived since we have only determined the energy momentum tensor in the region without external B-field and one would also have to integrate over a magnetized region in order to determine W explicitly. However, we do not need to determine W explicitly. We take the time average of equation (A.25) and since the time average of the change of the total energy vanishes $\langle \partial_t W \rangle = 0$ we obtain:

$$\int d\boldsymbol{A} \cdot \langle \boldsymbol{S} \rangle = 0. \tag{A.26}$$

In the following we compute the time average pointing vectors $\langle S_z^a \rangle$ and $\langle S_z^{\mathrm{EM}} \rangle$. We use that the physical fields are that are given by the real part. We can write:

$$\begin{aligned} S_z^{\mathrm{EM}} &= n\Re(E(z)e^{-i\omega t})\Re(E(z)e^{-i\omega t}) = n\frac{1}{2}(E(z)e^{-i\omega t} + E^*(z)e^{i\omega t})\frac{1}{2}(E(z)e^{-i\omega t} + E^*(z)e^{i\omega t}) && \text{(A.27)} \\ &= \frac{n}{4}\left(2|E(z)|^2 + 2\Re(E(z)e^{-2i\omega t})\right). && \text{(A.28)} \end{aligned}$$

After performing the time average we obtain:

$$\langle S_z^{\mathrm{EM}} \rangle = \frac{n}{2}|E(z)|^2 \tag{A.29}$$

We can play the same game with the axion energy flux:

$$\begin{aligned} S_z^a &= -\partial_t \Re(a)\partial_z \Re(a) = -\Re(\partial_t a)\Re(\partial_z a) = -\Re(-i\omega a(z)e^{-i\omega t})\Re(e^{-i\omega t}\partial_z a(z)) && \text{(A.30)} \\ &= \frac{1}{4}(i\omega a(z)e^{-i\omega t} - i\omega a^*(z)e^{i\omega t})(e^{-i\omega t}\partial_z a(z) + e^{i\omega t}\partial_z a^*(z)) && \text{(A.31)} \\ &= \frac{1}{4}(i\omega a(z)e^{-2i\omega t}\partial_z a(z) + i\omega a(z)\partial_z a^*(z) - i\omega a^*(z)\partial_z a(z) - i\omega a^*(z)e^{2i\omega t}\partial_z a^*(z)) && \text{(A.32)} \end{aligned}$$

After performing the time average we get:

$$\langle S_z^a \rangle = -\frac{\omega}{2}\Im(a(z)\partial_z a^*(z)) \tag{A.33}$$

In the case that $a(z) = \hat{a}e^{i\omega z}$ we have $\langle S_z^a \rangle = \frac{\omega^2}{2}|\hat{a}|^2$ and in the case that $a(z) = \hat{a}_+ e^{i\omega z} + \hat{a}_- e^{-i\omega z}$ we get $\langle S_z^a \rangle = \frac{\omega^2}{2}\left(|\hat{a}_+|^2 - |\hat{a}_-|^2\right)$.

We can now evaluate equation (A.26) for the situation that is shown in figure A.1:

$$-\frac{\omega^2}{2}|\hat{a}_0^{-+}| + \frac{\omega^2}{2}|\hat{a}_0^{--}| + \frac{n}{2}|\hat{E}_0^{+-}|^2 + \frac{n}{2}|\hat{E}_2^{++}|^2 + \frac{\omega^2}{2}|\hat{a}_2^{-+}|^2 = 0. \tag{A.34}$$

To quantify if equation (A.34) is satisfied we define

$$\Omega = -1 + \left|\frac{\hat{a}_0^{--}}{\hat{a}_0^{-+}}\right|^2 + n\left|\frac{\hat{A}_0^{+-}}{\hat{a}_0^{-+}}\right|^2 + n\left|\frac{\hat{A}_2^{++}}{\hat{a}_0^{-+}}\right|^2 + \left|\frac{\hat{a}_2^{-+}}{\hat{a}_0^{-+}}\right|^2 \tag{A.35}$$

with $\hat{E} = \omega\hat{A}$. If the energy flux is conserved then we should find $\Omega = 0$.

In the weak mixing region we obtain:

$$\Omega = 0 + \mathcal{O}(\tilde{x}^2). \tag{A.36}$$

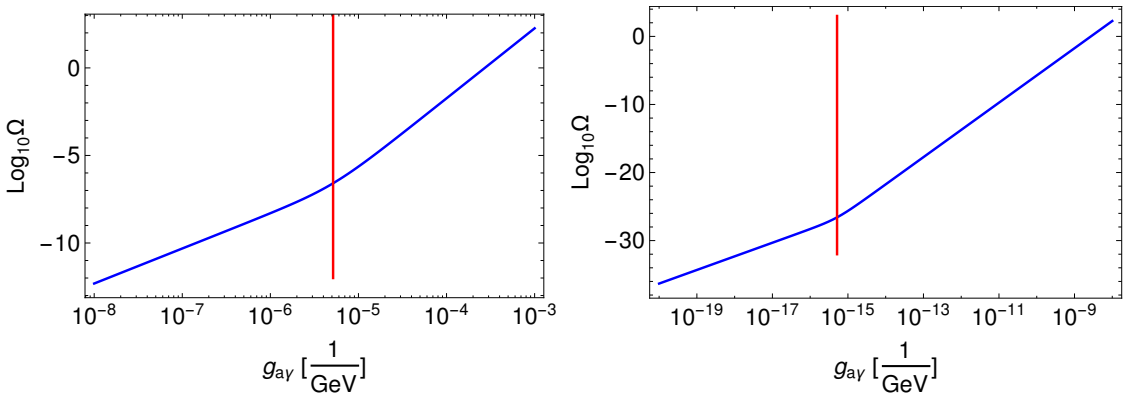

Figure A.2: Energy flux violation parameter in the massless limit for axions that come in onto a magnetized region. We show two different vacuum configurations: $\Delta n = 10^{-12}$ (left) and $\Delta n = 10^{-22}$ (right). The red line depicts the border between strong and weak mixing regions. In the weak mixing region Ω, which describes the amount of energy flux non-conservation, is always small. However, in some parts of the strong mixing regime Ω can become of order one.

In the strong mixing region we can however get larger values for Ω. In the strong mixing region all emitted fields, that are emitted off the magnetized region, are proportional to ζ^{-1} and therefore we consider $\Omega\zeta^2$ here:

$$\Omega\zeta^2 = -\zeta^2 + \frac{1}{2}\sin^2\left(\frac{q\ell}{2}\right) + \frac{\chi^2}{64}\left|-2 + e^{2i\kappa_-} + e^{2i\kappa_+}\right|^2 + \zeta\frac{3}{4}\sin^2\left(\frac{q\ell}{2}\right) + \mathcal{O}(\chi^3, \zeta^3) \tag{A.37}$$

It becomes directly evident that the leading order of $\Omega\zeta^2$ is not necessarily zero. The term $-\zeta^2$ does not necessarily cancel with the term $\frac{1}{2}\sin^2\left(\frac{q\ell}{2}\right)$ that can become order one for large enough couplings. Therefore in the strong mixing region energy flux conservation can be maximally violated and the multilayer approach is not adequate to describe the axion proton mixing in this region.

In figure A.2 we plot Ω for different vaccum refractive indices Δn in the zero mass limit. The left figure shows the case that $\Delta n = 10^{-12}$ while the right figure shows $\Delta n = 10^{-22}$. The red vertical line is g_{sw}, i.e. the border between weak and strong mixing regimes. As expected from the previous analytical discussion Ω is always small in the weak mixing region, but can become large in the strong mixing region. However, note that Ω is not maximally violated in the strong mixing region (above the red line). Order one violations happen at $g_{a\gamma} = 10^{-4}\frac{1}{\text{GeV}}$ in the case $\Delta n = 10^{-12}$ and for $g_{a\gamma} = 10^{-8}\frac{1}{\text{GeV}}$ in the case $\Delta n = 10^{-22}$.

To enforce energy flux conservation, one can replace the condition for continuity of the axion field, cf. equation (3.41), with an energy flux conserving condition. One would replace the continuity condition for the axion field, since it is the only interface condition that does not follow from the equations of motion and is put in by hand. Instead of the continuity condition for the axion one would replace the equation with one that is similar to equation (A.34). However, one would do this at every interface and hence one would have to compute the energy momentum tensor also in the regions where the axions and photons are mixed, i.e. where an external B-field exists. This alternative strategy comes with the difficulty that one would get quadratic equations, where in the existing matrix formalism all interface conditions are linear. Therefore enforcing energy flux conservation at each interface with a new interface condition would practically be very difficult, since it results in a system with not only linear equations.

Appendix B

Appendix for chapter 4

B.1 Derivation of Fourier propagation formula for circular emitting surface

We start with the three dimensional Fourier transformation of the electric field. In general we have

$$E(x,y,z) = \int \frac{d^3k}{(2\pi)^3} \hat{E}(k_x,k_y,k_z) e^{i\boldsymbol{k}\cdot\boldsymbol{x}}, \tag{B.1}$$

where we have omitted the time dependence $e^{-i\omega t}$.

The following calculation is valid for all three E-field components. However, we drop the index, since it goes through the same way fro each polarization component. For open axion haloscopes the propagation equation is used mostly for the E-field component that is parallel to the external B-field, i.e. to the axion induced E-field.

Plugging equation (B.1) into the scalar wave equation (4.40) yields the three dimensional photon dispersion relation:

$$\omega^2 = k_x^2 + k_y^2 + k_z^2. \tag{B.2}$$

Here we consider a radial symmetric geometry and therefore it is advantageous to do further calculations with cylindrical coordinates:

$$k_x = k_r \cos(\psi), \tag{B.3}$$
$$k_y = k_r \sin(\psi), \tag{B.4}$$
$$k_z = k_z. \tag{B.5}$$

Equation (B.1) becomes after the transformation

$$E'(r,\phi,z) := E(r\cos(\phi), r\sin\phi, z) = \int \frac{dk_r d\psi dk_z k_r}{(2\pi)^3} \hat{E}'(k_r,\psi,k_z) e^{irk_r\cos(\psi-\phi)} e^{ik_z z}. \tag{B.6}$$

Due to the symmetry of the problem the function E' cannot depend on ϕ. According to this argument $\hat{E}'$ can also not depend on the conjugated variable ψ:

$$E'(r,\phi,z) = E'(r,z), \tag{B.7}$$

$$\hat{E}'(k_r,\psi,k_z) = \hat{E}'(k_r,k_z). \tag{B.8}$$

Equation (B.6) becomes:

$$E'(r,z) = \int_0^\infty \frac{dk_r k_r}{2\pi} \int \frac{dk_z}{2\pi} \hat{E}'(k_r,k_z) e^{ik_z z} \int_0^{2\pi} \frac{d\psi}{2\pi} e^{irk_r\cos(\psi-\phi)}. \tag{B.9}$$

The ψ integral can be evaluated:

$$\int_0^{2\pi} \frac{d\psi}{2\pi} e^{irk_r \cos(\psi-\phi)} = \int_0^{2\pi} \frac{d\psi}{2\pi} e^{irk_r \cos(\psi)} = \int_0^{2\pi} \frac{d\psi}{2\pi} e^{-irk_r \sin(\psi)} = \int_{-\pi}^{\pi} \frac{d\psi}{2\pi} e^{-irk_r \sin(\psi)} = J_0(rk_r). \tag{B.10}$$

Then equation (B.9) becomes:

$$E'(r,z) = \int_0^\infty \frac{dk_r k_r}{2\pi} \int \frac{dk_z}{2\pi} \hat{E}'(k_r,k_z) e^{ik_z z} J_0(rk_r). \tag{B.11}$$

The dispersion relation can be incorporated with the following relation:

$$\hat{E}'(k_r,k_z) =: 2\pi \hat{E}''(k_r)\delta(k_z \mp \sqrt{\omega^2 - k_r^2}), \tag{B.12}$$

where the $-$ stands for a wave which propagates in positive z direction and the $+$ for a wave which propagates into negative z direction. Therefore we can evaluate the k_z integration in (B.11) and obtain:

$$E'(r,z) = \int_0^\infty \frac{dk_r k_r}{2\pi} \hat{E}''(k_r) e^{\pm i\sqrt{\omega^2-k_r^2}z} J_0(rk_r) \tag{B.13}$$

Finally from the requirement

$$E'(r, z=0, t) \stackrel{!}{=} E_0(r)\Theta(R-r) \tag{B.14}$$

we get

$$\int_0^\infty \frac{dk_r k_r}{2\pi} \hat{E}''(k_r) J_0(rk_r) = E_0(r)\Theta(R-r), \tag{B.15}$$

where $E_0(r)$ is the radial symmetric field that is propagated from a radial syfrace of radius R. Now we multiply both sides of (B.15) with $\int_0^\infty dr r J_0(ru)$, $u \in \mathbb{R}^+$ and use the relation of Bessel functions

$$\int_0^\infty dx J_n(ux) J_n(vx) x = \frac{1}{u}\delta(u-v) \tag{B.16}$$

we end up with

$$\frac{1}{2\pi}\hat{E}''(u) = \int_0^\infty dr\ r E_0(r) J_0(ru)\Theta(R-r). \tag{B.17}$$

Plugging this result into (B.13) we obtain:

$$E'(r,z) = \int_0^\infty dk_r\ k_r \int_0^R dr'\ r' E_0(r') J_0(r'k_r) e^{\pm i\sqrt{\omega^2-k_r^2}z} J_0(rk_r). \tag{B.18}$$

If $E_0(r) = \text{const.}$ we have $\frac{1}{2\pi}\hat{E}''(u) = E_0 \frac{R}{u} J_1(Ru)$ and therefore equation (B.18) simplifies to:

$$E'(r,z) = E_0 \int_0^\infty dk_r R e^{\pm i\sqrt{\omega^2-k_r^2}z} J_0(rk_r) J_1(Rk_r). \tag{B.19}$$

After introducing the dimensionless variables

$$\tilde{k}_r = k_r R, \quad \tilde{r} = \frac{r}{R}, \quad \tilde{z} = \frac{z}{R}, \quad \tilde{\omega} = \omega R \tag{B.20}$$

we end up with

$$\frac{E_i'(r,z)}{E_{0i}} = \int_0^\infty d\tilde{k}_r e^{\pm i\sqrt{\tilde{\omega}^2-\tilde{k}_r^2}\tilde{z}} J_0(\tilde{r}\tilde{k}_r) J_1(\tilde{k}_r). \tag{B.21}$$

The $+$ sign in (B.21) is for a circular surface that sits at $z=0$ and emits in positive z direction. The minus sign is for a wave which is emitted in negative z direction. This argument is directly evident, because otherwise the integral will diverges. If the emitting surface is located at z_s we get:

$$\frac{E'(r,z)}{E_{0i}} = e^{-i\omega t} \int_0^\infty d\tilde{k}_r e^{\pm i\sqrt{\tilde{\omega}^2-\tilde{k}_r^2}|\tilde{z}-\tilde{z}_s|} J_0(\tilde{r}\tilde{k}_r) J_1(\tilde{k}_r). \tag{B.22}$$

B.2 Details of the finite element simulation

This section is written in order to give more details on the FEM solutions that were done in COMSOL Multiphysics ® [95]. With the FEM we solve the vectorized Helmholtz equation 4.29. In this thesis the wave optics module in COMSOL was used to solve equation (4.29) explicitly with the source term included. In section B.2.1 two methods in incorporating the external axion current are given. In section B.2.2 the 2D3D method, which effectively solves three dimensional problems in two dimensions, is discussed.

B.2.1 Backgroundfield method vs. external current method

COMSOL's wave optics module offers the possibility to solve the vectorized Helmholtz equation (4.29) directly in three dimensions. There are two ways to incorporate the external current $\boldsymbol{E}_a$ in COMSOL. The first method is to use the 'Polarization' node in COMSOL. In this way the source term $\boldsymbol{E}_a$ can be directly incorporated. The second possibilityis to use the 'Scattered field' formulation. The total E-field is divided into a scattered and background field:

$$\boldsymbol{E} = \boldsymbol{E}_r + \boldsymbol{E}_b. \tag{B.23}$$

We refer to the Scattered field formulation as *Background field* method in the following. Plugging this into the vectorized Helmhotz equation of classical electromagnetism, i.e. without axion source term, yields:

$$\nabla \times (\mu^{-1}\nabla \times (\boldsymbol{E}_r + \boldsymbol{E}_b)) - \omega^2\tilde{\epsilon}(\boldsymbol{E}_r + \boldsymbol{E}_b) = 0. \tag{B.24}$$

COMSOL computes the solution of this equation for a given $\boldsymbol{E}_b$. We choose $\boldsymbol{E}_b = \frac{1}{\tilde{\epsilon}\omega^2}\boldsymbol{E}_a$. Now if the external B-field, that appears in $\boldsymbol{E}_a$ varies on scales much larger than the photon wavelength we have $\nabla \times (\mu^{-1}\nabla \times \boldsymbol{E}_b) \ll \omega^2\tilde{\epsilon}\boldsymbol{E}_b$ and the vectorized Helmholtz equation becomes:

$$\nabla \times (\mu^{-1}\nabla \times \boldsymbol{E}_r) - \omega^2\tilde{\epsilon}(\boldsymbol{E}_r) = \boldsymbol{E}_a, \tag{B.25}$$

what is equation (4.29).

It was checked that both described approaches give similar results. In figure B.1 the full three dimensional simulations using the background field method (BF) and the external current density (EC) directly are shown for the case of a dielectric disk. The small deviations in the different components E_x (left), E_y (center) and E_z (right) are du to the fact that in the background field method the double curl term is dropped. However, we can see here that this leads only to a small difference between both methods. In very resonant systems this difference is not visible at all.

B.2.2 Validation of 2D3D method

In section 4.3.1 it was shown that if the geometry of the setup is radial symmetric and the external B-field is linearly polarized, then the full three dimensional solution can be computed by solving a two dimensional problem. The approach was names 2D3D approach. Here we explicitly compare the 2D3D approach for a simple setups with a full three dimensional solution.

In figure B.2 the difference between the 2D3D solution and the solution of a full three dimensional simulation is shown for the E_x (left), E_y (center) and E_z (right) components. In all shown cases the results agree very well up to numerical noise, which is on the order of 10% of the original computed values.

In the 2D3D solution in figure B.2 a further simplification was used. As it was pointed out in section 4.3.1 two two dimensional computations for the modes $m = \pm$ have to be done in the 2D3D approach in order to obtain the full three dimensional solution. However, it turns out that this can

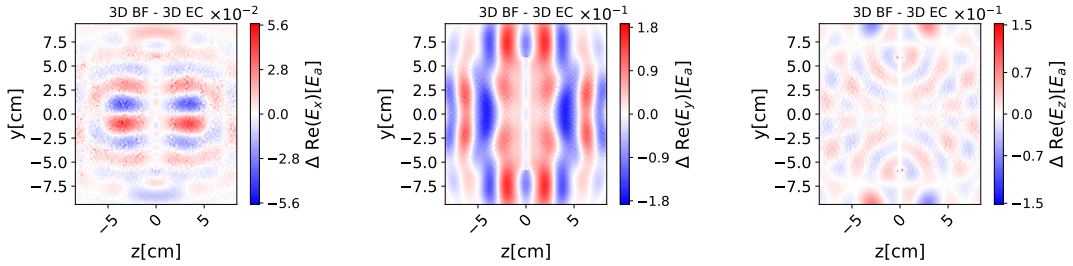

Figure B.1: E-field solutions for a dielectric disk with an external B-field and a homogeneous axion dark matter background. The dielectric disk is placed at the coordinate origin and it's surface is in the xy-plane. The external B-field polarization is in the y-direction. The disk has a radius of $R = 6\,\mathrm{cm}$, thickness $d = 0.5\,\mathrm{cm}$ and refractive index of $n = 3$. The frequency is $f = 10\,\mathrm{GHz}$. There are two ways to incorporate the axion source term in the vectorized Helmholtz equation into COMSOL. One can use an external current density (EC) or the background field method (BF). The difference of the results are shown in the figures for all three polarizations. The resulting difference is due to the neglected double curl in the background field method. However, the difference is small compared to the axion induced E-field. The slice plot is shown at $x = -1.5\,\mathrm{cm}$.

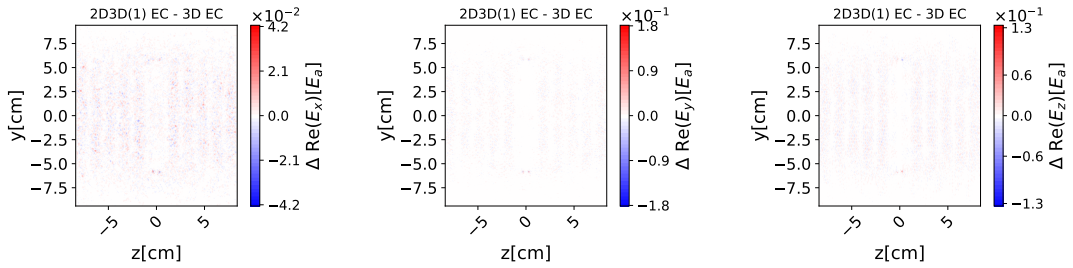

Figure B.2: E-field solutions for a dielectric disk with an external B-field and a homogeneous axion dark matter background. The dielectric disk is placed at the coordinate origin and it's surface is in the xy-plane. The external B-field polarization is in the y-direction. The disk has a radius of $R = 6\,\mathrm{cm}$, thickness $d = 0.5\,\mathrm{cm}$ and refractive index of $n = 3$. The frequency is $f = 10\,\mathrm{GHz}$. The slices are shown at $x = -1.5\,\mathrm{cm}$. We compare the 2D3D method with the relations (B.26)-(B.28) (2D3D(1)) with a standard three dimensional solution. In both cases the axion source was incorporated with an external current (EC) in COMSOL. The slices show the difference between both approaches. We confirm explicitly the they both give the same result up to numerical noise.

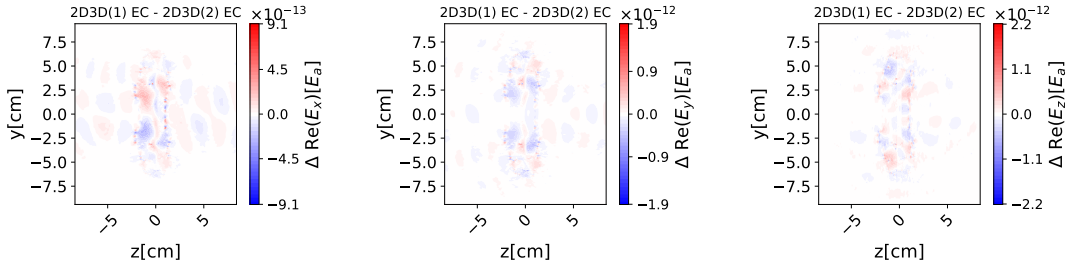

Figure B.3: E-field solutions for a dielectric disk with an external B-field and a homogeneous axion dark matter background. The dielectric disk is placed at the coordinate origin and it's surface is in the xy-plane. The external B-field polarization is in the y-direction. The disk has a radius of $R = 6\,\text{cm}$, thickness $d = 0.5\,\text{cm}$ and refractive index of $n = 3$. The frequency is $f = 10\,\text{GHz}$ and the slices are shown at $x = -1.5\,\text{cm}$. We compare the 2D3D method which uses the relations (B.26)-(B.28) (2D3D(1)) with the 2D3D method which does not use these relations, but computes the two modes $m = \pm$ explicitly. For both cases the same mesh, boundary conditions and solver was used. We find tremendouly good agreement and therefore conclude that the relations (B.26)-(B.28) can be used.

be simplified further if the source term of the vectorized Helmholtz equation is linearly polarized. After solving explicit examples with two modes we see that the following relations between the $m = \pm$ modes hold:

$$\tilde{E}_r^- = -\tilde{E}_r^+, \tag{B.26}$$

$$\tilde{E}_\phi^- = \tilde{E}_\phi^+, \tag{B.27}$$

$$\tilde{E}_z^- = -\tilde{E}_z^+. \tag{B.28}$$

In the title of figure B.2 '2D3D(1)' was written in order to clarify that the relations (B.26)-(B.28) were used, i.e. only one two dimensional calculation had to be done in order to get the full three dimensional solution.

In figure B.3 the 2D3D approach with two two dimensional computations (2D3D(2)) for the $m = \pm$ modes and the 2D3D approach, which computes only one mode in a two dimensional computation (2D3D(1)) and the uses (B.26)-(B.28), are compared for the E_x (left), E_y (center) and E_z (right) components. In this specific case all settings (mesh, solver, boundary conditions) are exactly the same. We obtain in all three cases in figure B.3 a tremendously good agreement what gives us confidence that the relations (B.26)-(B.28) have to hold in our case.

Bibliography

[1] Stefan Knirck, Jan Schütte-Engel, et al. "A first look on 3D effects in open axion haloscopes". **Journal of Cosmology and Astroparticle Physics** 2019.08 (Aug. 2019), pp. 026–026. DOI: 10.1088/1475-7516/2019/08/026.

[2] Alexander J. Millar David J. E. Marsh and Jan Schütte-Engel. "Axion Quasiparticles for Axion Dark Matter Detection". **in preparation** (2020).

[3] Stefan Knirck, Jan Schütte-Engel, et al. "Dielectric Haloscopes to Search for Axion Dark Matter: 3D Effects". **in preparation** (2020).

[4] Jan Schütte-Engel. "Simulation studies for the MADMAX axion direct detection experiment". **14th Patras Workshop on Axions, WIMPs and WISPs (AXION-WIMP 2018) (PATRAS 2018) Hamburg, Germany, June 18-22, 2018**. 2018. arXiv: 1811.00493 [hep-ph].

[5] Peter W. Higgs. "Broken Symmetries and the Masses of Gauge Bosons". **Phys. Rev. Lett.** 13 (16 Oct. 1964), pp. 508–509. DOI: 10.1103/PhysRevLett.13.508.

[6] F. Englert and R. Brout. "Broken Symmetry and the Mass of Gauge Vector Mesons". **Phys. Rev. Lett.** 13 (9 Aug. 1964), pp. 321–323. DOI: 10.1103/PhysRevLett.13.321.

[7] R. D. Peccei and Helen R. Quinn. "CP Conservation in the Presence of Pseudoparticles". **Phys. Rev. Lett.** 38 (25 June 1977), pp. 1440–1443. DOI: 10.1103/PhysRevLett.38.1440.

[8] F. Wilczek. "Problem of Strong P and T Invariance in the Presence of Instantons". **Phys. Rev. Lett.** 40 (5 Jan. 1978), pp. 279–282. DOI: 10.1103/PhysRevLett.40.279.

[9] Steven Weinberg. "A New Light Boson?" **Phys. Rev. Lett.** 40 (4 Jan. 1978), pp. 223–226. DOI: 10.1103/PhysRevLett.40.223.

[10] Peter Svrcek and Edward Witten. "Axions in string theory". **Journal of High Energy Physics** 2006.06 (June 2006), pp. 051–051. DOI: 10.1088/1126-6708/2006/06/051.

[11] R Bähre, B Döbrich, et al. "Any light particle search II — Technical Design Report". **Journal of Instrumentation** 8.09 (Sept. 2013), T09001–T09001. DOI: 10.1088/1748-0221/8/09/t09001.

[12] V. Anastassopoulos, S. Aune, et al. "New CAST limit on the axion-photon interaction". **Nature Physics** 13.6 (2017), pp. 584–590. ISSN: 1745-2481.

[13] S. J. Asztalos, G. Carosi, et al. "SQUID-Based Microwave Cavity Search for Dark-Matter Axions". **Phys. Rev. Lett.** 104 (4 Jan. 2010), p. 041301. DOI: 10.1103/PhysRevLett.104.041301.

[14] T. Braine, R. Cervantes, et al. "Extended Search for the Invisible Axion with the Axion Dark Matter Experiment". **Phys. Rev. Lett.** 124 (10 Mar. 2020), p. 101303. DOI: 10.1103/PhysRevLett.124.101303.

[15] S. DePanfilis, A. C. Melissinos, et al. “Limits on the abundance and coupling of cosmic axions at 4.5<m_a<5.0 μeV”. **Phys. Rev. Lett.** 59 (7 Aug. 1987), pp. 839–842. DOI: 10.1103/PhysRevLett.59.839.

[16] C. Hagmann, P. Sikivie, et al. “Results from a search for cosmic axions”. **Phys. Rev. D** 42 (4 Aug. 1990), pp. 1297–1300. DOI: 10.1103/PhysRevD.42.1297.

[17] R. Li, J. Wang, et al. “Dynamical axion field in topological magnetic insulators”. **Nature Physics** 6 (Apr. 2010), pp. 284–288. DOI: 10.1038/nphys1534. arXiv: 0908.1537 [cond-mat.other].

[18] D L Mills and E Burstein. “Polaritons: the electromagnetic modes of media”. **Reports on Progress in Physics** 37.7 (July 1974), pp. 817–926. DOI: 10.1088/0034-4885/37/7/001.

[19] David J. E. Marsh, Kin Chung Fong, et al. “Proposal to Detect Dark Matter using Axionic Topological Antiferromagnets”. **Phys. Rev. Lett.** 123 (12 Sept. 2019), p. 121601. DOI: 10.1103/PhysRevLett.123.121601.

[20] David Tong. **Gauge Theory**. 2018.

[21] Luca Di Luzio, Maurizio Giannotti, et al. “The landscape of QCD axion models” (Mar. 2020). arXiv: 2003.01100 [hep-ph].

[22] David J.E. Marsh. “Axion cosmology”. **Physics Reports** 643 (2016). Axion cosmology, pp. 1–79. ISSN: 0370-1573. DOI: https://doi.org/10.1016/j.physrep.2016.06.005.

[23] Ken’ichi Saikawa. “Axion as a non-WIMP dark matter candidate”. **PoS** EPS-HEP2017 (2017). Ed. by Paolo Checchia et al., p. 083. DOI: 10.22323/1.314.0083. arXiv: 1709.07091 [hep-ph].

[24] A.A. Anselm and A.A. Johansen. “Can the electroweak Theta-term be observable?” **Nuclear Physics B** 412.3 (1994), pp. 553–573. ISSN: 0550-3213. DOI: https://doi.org/10.1016/0550-3213(94)90392-1.

[25] Pavel Fileviez Pérez and Hiren H. Patel. “The electroweak vacuum angle”. **Physics Letters B** 732 (2014), pp. 241–243. ISSN: 0370-2693. DOI: https://doi.org/10.1016/j.physletb.2014.03.064.

[26] A.M. Polyakov. “Compact gauge fields and the infrared catastrophe”. **Physics Letters B** 59.1 (1975), pp. 82–84. ISSN: 0370-2693. DOI: https://doi.org/10.1016/0370-2693(75)90162-8.

[27] A.A. Belavin, A.M. Polyakov, et al. “Pseudoparticle solutions of the Yang-Mills equations”. **Physics Letters B** 59.1 (1975), pp. 85–87. ISSN: 0370-2693. DOI: https://doi.org/10.1016/0370-2693(75)90163-X.

[28] G. ’t Hooft. “Symmetry Breaking through Bell-Jackiw Anomalies”. **Phys. Rev. Lett.** 37 (1 July 1976), pp. 8–11. DOI: 10.1103/PhysRevLett.37.8.

[29] G. ’t Hooft. “Computation of the quantum effects due to a four-dimensional pseudoparticle”. **Phys. Rev. D** 14 (12 Dec. 1976), pp. 3432–3450. DOI: 10.1103/PhysRevD.14.3432.

[30] C.G. Callan, R.F. Dashen, et al. “The structure of the gauge theory vacuum”. **Physics Letters B** 63.3 (1976), pp. 334–340. ISSN: 0370-2693. DOI: https://doi.org/10.1016/0370-2693(76)90277-X.

[31] R. Jackiw and C. Rebbi. “Vacuum Periodicity in a Yang-Mills Quantum Theory”. **Phys. Rev. Lett.** 37 (3 July 1976), pp. 172–175. DOI: 10.1103/PhysRevLett.37.172.

[32] Maxim Pospelov and Adam Ritz. “Theta vacua, QCD sum rules, and the neutron electric dipole moment”. **Nuclear Physics B** 573.1 (2000), pp. 177–200. ISSN: 0550-3213. DOI: https://doi.org/10.1016/S0550-3213(99)00817-2.

[33] P. G. Harris, C. A. Baker, et al. "New Experimental Limit on the Electric Dipole Moment of the Neutron". **Phys. Rev. Lett.** 82 (5 Feb. 1999), pp. 904–907. DOI: 10.1103/PhysRevLett.82.904.

[34] Cumrun Vafa and Edward Witten. "Parity Conservation in Quantum Chromodynamics". **Phys. Rev. Lett.** 53 (6 Aug. 1984), pp. 535–536. DOI: 10.1103/PhysRevLett.53.535.

[35] R. D. Peccei and Helen R. Quinn. "Constraints imposed by CP conservation in the presence of pseudoparticles". **Phys. Rev. D** 16 (6 Sept. 1977), pp. 1791–1797. DOI: 10.1103/PhysRevD.16.1791.

[36] Jihn E. Kim. "Weak-Interaction Singlet and Strong CP Invariance". **Phys. Rev. Lett.** 43 (2 July 1979), pp. 103–107. DOI: 10.1103/PhysRevLett.43.103.

[37] M.A. Shifman, A.I. Vainshtein, et al. "Can confinement ensure natural CP invariance of strong interactions?" **Nuclear Physics B** 166.3 (1980), pp. 493–506. ISSN: 0550-3213. DOI: https://doi.org/10.1016/0550-3213(80)90209-6.

[38] Michael Dine, Willy Fischler, et al. "A simple solution to the strong CP problem with a harmless axion". **Physics Letters B** 104.3 (1981), pp. 199–202. ISSN: 0370-2693. DOI: https://doi.org/10.1016/0370-2693(81)90590-6.

[39] A.R. Zhitnitsky. "On Possible Suppression of the Axion Hadron Interactions. (In Russian)". **Sov. J. Nucl. Phys.** 31 (1980), p. 260.

[40] Marco Gorghetto and Giovanni Villadoro. "Topological susceptibility and QCD axion mass: QED and NNLO corrections". **Journal of High Energy Physics** 2019.3 (2019), pp. 33–. ISSN: 1029-8479.

[41] David J. Gross, Robert D. Pisarski, et al. "QCD and instantons at finite temperature". **Rev. Mod. Phys.** 53 (1 Jan. 1981), pp. 43–80. DOI: 10.1103/RevModPhys.53.43.

[42] S. Borsanyi, Z. Fodor, et al. "Calculation of the axion mass based on high-temperature lattice quantum chromodynamics". **Nature** 539.7627 (2016), pp. 69–71. ISSN: 1476-4687.

[43] Giovanni Grilli di Cortona, Edward Hardy, et al. "The QCD axion, precisely". **JHEP** 01 (2016), p. 034. DOI: 10.1007/JHEP01(2016)034. arXiv: 1511.02867 [hep-ph].

[44] John Preskill, Mark B. Wise, et al. "Cosmology of the invisible axion". **Physics Letters B** 120.1 (1983), pp. 127–132. ISSN: 0370-2693. DOI: https://doi.org/10.1016/0370-2693(83)90637-8.

[45] L.F. Abbott and P. Sikivie. "A cosmological bound on the invisible axion". **Physics Letters B** 120.1 (1983), pp. 133–136. ISSN: 0370-2693. DOI: https://doi.org/10.1016/0370-2693(83)90638-X.

[46] Michael Dine and Willy Fischler. "The not-so-harmless axion". **Physics Letters B** 120.1 (1983), pp. 137–141. ISSN: 0370-2693. DOI: https://doi.org/10.1016/0370-2693(83)90639-1.

[47] P. Sikivie. "Axions, Domain Walls, and the Early Universe". **Phys. Rev. Lett.** 48 (17 Apr. 1982), pp. 1156–1159. DOI: 10.1103/PhysRevLett.48.1156.

[48] R.L. Davis. "Cosmic axions from cosmic strings". **Physics Letters B** 180.3 (1986), pp. 225–230. ISSN: 0370-2693. DOI: https://doi.org/10.1016/0370-2693(86)90300-X.

[49] Vincent B. Klaer and Guy D. Moore. "How to simulate global cosmic strings with large string tension". **Journal of Cosmology and Astroparticle Physics** 2017.10 (Oct. 2017), pp. 043–043. DOI: 10.1088/1475-7516/2017/10/043.

[50] Vincent B.. Klaer and Guy D.. Moore. "The dark-matter axion mass". **JCAP** 1711.11 (2017), p. 049. DOI: 10.1088/1475-7516/2017/11/049. arXiv: 1708.07521 [hep-ph].

[51] Andreas Ringwald and Ken'ichi Saikawa. "Axion dark matter in the post-inflationary Peccei-Quinn symmetry breaking scenario". **Phys. Rev.** D93.8 (2016). Addendum: Phys. Rev.D94,no.4,049908(2016), p. 085031. DOI: 10.1103/PhysRevD.93.085031, 10.1103/PhysRevD.94.049908. arXiv: 1512.06436 [hep-ph].

[52] Marco Gorghetto, Edward Hardy, et al. "More Axions from Strings" (July 2020). arXiv: 2007.04990 [hep-ph].

[53] Paola Arias, Davide Cadamuro, et al. "WISPy cold dark matter". **Journal of Cosmology and Astroparticle Physics** 2012.06 (June 2012), pp. 013–013. DOI: 10.1088/1475-7516/2012/06/013.

[54] Ann E. Nelson and Jakub Scholtz. "Dark light, dark matter, and the misalignment mechanism". **Phys. Rev. D** 84 (10 Nov. 2011), p. 103501. DOI: 10.1103/PhysRevD.84.103501.

[55] Eduard Massó, Francesc Rota, et al. "Planck-scale effects on global symmetries: Cosmology of pseudo-Goldstone bosons". **Phys. Rev. D** 70 (11 Dec. 2004), p. 115009. DOI: 10.1103/PhysRevD.70.115009.

[56] M. Tanabashi *et al.* [Particle Data Group]. "Review of Particle Physics". **Phys. Rev. D** 98 (3 Aug. 2018), p. 030001. DOI: 10.1103/PhysRevD.98.030001.

[57] Michael S. Turner. "Periodic signatures for the detection of cosmic axions". **Phys. Rev. D** 42 (10 Nov. 1990), pp. 3572–3575. DOI: 10.1103/PhysRevD.42.3572.

[58] Alexander J. Millar, Georg G. Raffelt, et al. "Dielectric haloscopes to search for axion dark matter: theoretical foundations". **Journal of Cosmology and Astroparticle Physics** 2017.01 (Jan. 2017), pp. 061–061. DOI: 10.1088/1475-7516/2017/01/061.

[59] Alexander J. Millar, Javier Redondo, et al. "Dielectric haloscopes: sensitivity to the axion dark matter velocity". **JCAP** 1710.10 (2017). [Erratum: JCAP1805,no.05,E02(2018)], p. 006. DOI: 10.1088/1475-7516/2017/10/006, 10.1088/1475-7516/2018/05/E02. arXiv: 1707.04266 [hep-ph].

[60] Georg Raffelt and Leo Stodolsky. "Mixing of the Photon with Low Mass Particles". **Phys. Rev.** D37 (1988), p. 1237. DOI: 10.1103/PhysRevD.37.1237.

[61] Stephen L. Adler, J. Gamboa, et al. "Axions and "light shining through a wall": A detailed theoretical analysis". **Annals of Physics** 323.11 (2008), pp. 2851–2872. ISSN: 0003-4916. DOI: https://doi.org/10.1016/j.aop.2008.02.001.

[62] P. Sikivie. "Experimental Tests of the "Invisible" Axion". **Phys. Rev. Lett.** 51 (16 Oct. 1983), pp. 1415–1417. DOI: 10.1103/PhysRevLett.51.1415.

[63] Luca Di Luzio, Federico Mescia, et al. "Window for preferred axion models". **Phys. Rev.** D96.7 (2017), p. 075003. DOI: 10.1103/PhysRevD.96.075003. arXiv: 1705.05370 [hep-ph].

[64] R. Abela, A. Aghababyan, et al. **XFEL: The European X-Ray Free-Electron Laser - Technical Design Report**. Hamburg: DESY, 2006, pp. 1–646. ISBN: 978-3-935702-17-1. DOI: 10.3204/DESY-06-097.

[65] Alexandra Dobrynina, Alexander Kartavtsev, et al. "Photon-photon dispersion of TeV gamma rays and its role for photon-ALP conversion". **Phys. Rev. D** 91 (8 Apr. 2015), p. 083003. DOI: 10.1103/PhysRevD.91.083003.

[66] A. M. Hillas. "The Origin of Ultra-High-Energy Cosmic Rays". **Annual Review of Astronomy and Astrophysics** 22.1 (1984), pp. 425–444. DOI: 10.1146/annurev.aa.22.090184.002233.

[67] P.A. Redhead. **Ultrahigh and Extreme HTechnology in Foundations of Vacuum Science and Technology**. Ed. by J. M. Lafferty. Wiley, 1998.

[68] P A Redhead. “Extreme high vacuum”. OPEN-2000-281 (1999). DOI: 10.5170/CERN-1999-005.213.

[69] C. Benvenuti. “Extreme High Vacuum Technology for Particle Accelerators (Invited)”. **Conf. Proc.** C0106181 (2001). [,602(2001)], pp. 602–606.

[70] Stephen L Adler. “Photon splitting and photon dispersion in a strong magnetic field”. **Annals of Physics** 67.2 (1971), pp. 599–647. ISSN: 0003-4916. DOI: https://doi.org/10.1016/0003-4916(71)90154-0.

[71] Javier Redondo and Andreas Ringwald. “Light shining through walls”. **Contemporary Physics** 52.3 (2011), pp. 211–236. DOI: 10.1080/00107514.2011.563516.

[72] K. Van Bibber, N. R. Dagdeviren, et al. “Proposed experiment to produce and detect light pseudoscalars”. **Phys. Rev. Lett.** 59 (7 Aug. 1987), pp. 759–762. DOI: 10.1103/PhysRevLett.59.759.

[73] E. I. Guendelman. “Photon and Axion Splitting in an Inhomogeneous Magnetic Field”. **Phys. Lett.** B662 (2008), pp. 445–448. DOI: 10.1016/j.physletb.2008.03.050. arXiv: 0802.0311 [hep-th].

[74] Eduardo I. Guendelman, Idan Shilon, et al. “Photon Production From The Scattering of Axions Out of a Solenoidal Magnetic Field”. **JCAP** 1006 (2010), p. 031. DOI: 10.1088/1475-7516/2010/06/031. arXiv: 0906.2537 [hep-ph].

[75] Javier Redondo. “Photon-Axion conversions in transversely inhomogeneous magnetic fields”. **Proceedings, 5th Patras Workshop on Axions, WIMPs and WISPs (AXION-WIMP 2009): Durham, UK, July 13-17, 2009**. 2010, pp. 185–188. DOI: 10.3204/DESY-PROC-2009-05/redondo_javier. arXiv: 1003.0410 [hep-ph].

[76] Stefan Knirck, Jan Schütte-Engel, et al. “A First Look on 3D Effects in Open Axion Haloscopes”. **JCAP** 1908 (2019), p. 026. DOI: 10.1088/1475-7516/2019/08/026. arXiv: 1906.02677 [physics.ins-det].

[77] Adrian Ayala, Inma Dominguez, et al. “Revisiting the Bound on Axion-Photon Coupling from Globular Clusters”. **Phys. Rev. Lett.** 113 (19 Nov. 2014), p. 191302. DOI: 10.1103/PhysRevLett.113.191302.

[78] Paola Arias, Joerg Jaeckel, et al. “Optimizing light-shining-through-a-wall experiments for axion and other weakly interacting slim particle searches”. **Phys. Rev. D** 82 (11 Dec. 2010), p. 115018. DOI: 10.1103/PhysRevD.82.115018.

[79] S. I. BITYUKOV and N. V. KRASNIKOV. “NEW PHYSICS DISCOVERY POTENTIAL IN FUTURE EXPERIMENTS”. **Modern Physics Letters A** 13.40 (1998), pp. 3235–3249. DOI: 10.1142/S0217732398003442.

[80] S.I. Bityukov and N.V. Krasnikov. “On the observability of a signal above background”. **Nucl. Instrum. Meth. A** 452 (2000), pp. 518–524. DOI: 10.1016/S0168-9002(00)00454-X.

[81] Joerg Jaeckel and Andreas Ringwald. “Extending the reach of axion-photon regeneration experiments towards larger masses with phase shift plates”. **Phys. Lett.** B653 (2007), pp. 167–172. DOI: 10.1016/j.physletb.2007.07.066. arXiv: 0706.0693 [hep-ph].

[82] F Hoogeveen and T Ziegenhagen. “Production and detection of light bosons using optical resonators”. **Nuclear Physics B** 358.1 (1991), pp. 3–26. ISSN: 0550-3213. DOI: https://doi.org/10.1016/0550-3213(91)90528-6.

[83] Yukio Fukuda, Toshiro Kohmoto, et al. “Production and detection of axions by using optical resonators”. **Progress in Crystal Growth and Characterization of Materials** 33.1 (1996), pp. 363–366. ISSN: 0960-8974. DOI: https://doi.org/10.1016/0960-8974(96)83672-2.

[84] Igor G. Irastorza and Javier Redondo. “New experimental approaches in the search for axion-like particles”. **Progress in Particle and Nuclear Physics** 102 (2018), pp. 89–159. ISSN: 0146-6410. DOI: https://doi.org/10.1016/j.ppnp.2018.05.003.

[85] Dieter Horns, Joerg Jaeckel, et al. “Searching for WISPy Cold Dark Matter with a Dish Antenna”. **JCAP** 1304 (2013), p. 016. DOI: 10.1088/1475-7516/2013/04/016. arXiv: 1212.2970 [hep-ph].

[86] Allen Caldwell, Gia Dvali, et al. “Dielectric Haloscopes: A New Way to Detect Axion Dark Matter”. **Phys. Rev. Lett.** 118 (9 Mar. 2017), p. 091801. DOI: 10.1103/PhysRevLett.118.091801.

[87] **BRASS website**. http://www.iexp.uni-hamburg.de/groups/astroparticle/brass/brassweb.htm. Apr. 6, 2019.

[88] Stefan Knirck. “How To Search for Axion Dark Matter with MADMAX”. PhD thesis. 2020.

[89] R. H. Dicke. “The Measurement of Thermal Radiation at Microwave Frequencies”. **Review of Scientific Instruments** 17.7 (1946), pp. 268–275. DOI: 10.1063/1.1770483.

[90] Joerg Jaeckel and Javier Redondo. “Resonant to broadband searches for cold dark matter consisting of weakly interacting slim particles”. **Phys. Rev. D** 88 (11 Dec. 2013), p. 115002. DOI: 10.1103/PhysRevD.88.115002.

[91] Younggeun Kim, Dongok Kim, et al. “Effective approximation of electromagnetism for axion haloscope searches”. **Physics of the Dark Universe** 26 (2019), p. 100362. ISSN: 2212-6864. DOI: https://doi.org/10.1016/j.dark.2019.100362.

[92] Olgierd Cecil Zienkiewicz, Robert Leroy Taylor, et al. **The finite element method**. Vol. 36. McGraw-hill London, 1977.

[93] Jianming Jin. **Finite Element Electromagnetic**. John Wiley & Sons, 2014.

[94] Jean-Pierre Berenger. “A perfectly matched layer for the absorption of electromagnetic waves”. **Journal of Computational Physics** 114.2 (1994), pp. 185–200. ISSN: 0021-9991. DOI: https://doi.org/10.1006/jcph.1994.1159.

[95] **COMSOL Multiphysics® v. 5.3.a COMSOL AB, Stockholm, Sweden**.

[96] Walter Frei. URL: https://www.comsol.de/blogs/using-perfectly-matched-layers-and-scattering-boundary-conditions-for-wave-electromagnetics-problems/.

[97] **COMSOL: Corrugated Circular Horn Antenna**.

[98] Frank Pedrotti. **Introduction to optics**. Englewood Cliffs, N.J: Prentice Hall, 1993. ISBN: 0130169730.

[99] John David Jackson. **Classical electrodynamics**. 3rd ed. New York, NY: Wiley, 1999. ISBN: 9780471309321.

[100] J. Goodman. **Introduction to Fourier Optics**. Roberts and Company Publishers, 2016.

[101] Allen Caldwell, Gia Dvali, et al. “Dielectric Haloscopes: A New Way to Detect Axion Dark Matter”. **Phys. Rev. Lett.** 118.9 (2017), p. 091801. DOI: 10.1103/PhysRevLett.118.091801. arXiv: 1611.05865 [physics.ins-det].

[102] P. Brun, A. Caldwell, et al. “A new experimental approach to probe QCD axion dark matter in the mass range above 40 μeV”. **The European Physical Journal C** 79.3 (2019), pp. 186–. ISSN: 1434-6052.

[103] Jonathan Ouellet and Zachary Bogorad. “Solutions to axion electrodynamics in various geometries”. **Phys. Rev. D** 99 (5 Mar. 2019), p. 055010. DOI: 10.1103/PhysRevD.99.055010.

[104] G. B. Airy. “On the Diffraction of an Object-glass with Circular Aperture”. **Transactions of the Cambridge Philosophical Society.** 5 (1833-1835), pp. 283–291.

[105] Joerg Jaeckel and Stefan Knirck. “Directional Resolution of Dish Antenna Experiments to Search for WISPy Dark Matter”. **JCAP** 1601 (2016), p. 005. DOI: 10.1088/1475-7516/2016/01/005. arXiv: 1509.00371 [hep-ph].

[106] Joerg Jaeckel and Stefan Knirck. “Dish Antenna Searches for WISPy Dark Matter: Directional Resolution Small Mass Limitations”. **Proceedings, 12th Patras Workshop on Axions, WIMPs and WISPs (PATRAS 2016): Jeju Island, South Korea, June 20-24, 2016**. 2017, pp. 78–81. DOI: 10.3204/DESY-PROC-2009-03/Knirck_Stefan. arXiv: 1702.04381 [hep-ph].

[107] D. Veberič et al. “Search for hidden-photon dark matter with the FUNK experiment”. **PoS** ICRC2017 (2018), p. 880. DOI: 10.22323/1.301.0880. arXiv: 1711.02958 [hep-ex].

[108] Stefan Knirck, Takayuki Yamazaki, et al. “First results from a hidden photon dark matter search in the meV sector using a plane-parabolic mirror system”. **JCAP** 1811.11 (2018), p. 031. DOI: 10.1088/1475-7516/2018/11/031. arXiv: 1806.05120 [hep-ex].

[109] Joerg Jaeckel and Javier Redondo. “An antenna for directional detection of WISPy dark matter”. **JCAP** 1311 (2013), p. 016. DOI: 10.1088/1475-7516/2013/11/016. arXiv: 1307.7181 [hep-ph].

[110] J.A. Stratton. **Electromagnetic Theory**. New York: Mc Graw-Hill, 1941.

[111] A. Partsch. “Investigation of Loss Effects Influencing the Sensitivity of the Magnetized Disc and Mirror Axion Experiment - MADMAX”. MA thesis. Max Planck Institute for physics, Munich, 2018.

[112] S. Beurthey et al. “MADMAX Status Report” (Mar. 2020). arXiv: 2003.10894.

[113] J. Gooth, B. Bradlyn, et al. “Axionic charge-density wave in the Weyl semimetal (TaSe4)2I”. **Nature** 575.7782 (2019), pp. 315–319. ISSN: 1476-4687.

[114] Xiao-Liang Qi, Taylor L. Hughes, et al. “Topological field theory of time-reversal invariant insulators”. **Phys. Rev. B** 78 (19 Nov. 2008), p. 195424. DOI: 10.1103/PhysRevB.78.195424.

[115] Xiao-Liang Qi, Taylor L. Hughes, et al. “Erratum: Topological field theory of time-reversal invariant insulators [Phys. Rev. B 78, 195424 (2008)]”. **Phys. Rev. B** 81 (15 Apr. 2010), p. 159901. DOI: 10.1103/PhysRevB.81.159901.

[116] Sergio M. Rezende, Antonio Azevedo, et al. “Introduction to antiferromagnetic magnons”. **Journal of Applied Physics** 126.15 (2019), p. 151101. DOI: 10.1063/1.5109132.

[117] Akihiko Sekine and Kentaro Nomura. “Axionic Antiferromagnetic Insulator Phase in a Correlated and Spin–Orbit Coupled System”. **Journal of the Physical Society of Japan** 83.10 (2014), p. 104709. DOI: 10.7566/JPSJ.83.104709.

[118] F. Keffer, H. Kaplan, et al. “Spin Waves in Ferromagnetic and Antiferromagnetic Materials”. **American Journal of Physics** 21.4 (1953), pp. 250–257. DOI: 10.1119/1.1933416.

[119] Jian-Min Zhang, Wenguang Zhu, et al. "Tailoring Magnetic Doping in the Topological Insulator Bi_2Se_3". **Phys. Rev. Lett.** 109 (26 Dec. 2012), p. 266405. DOI: 10.1103/PhysRevLett.109.266405.

[120] Jian-Min Zhang, Wenmei Ming, et al. "Stability, electronic, and magnetic properties of the magnetically doped topological insulators Bi_2Se_3, Bi_2Te_3, and Sb_2Te_3". **Phys. Rev. B** 88 (23 Dec. 2013), p. 235131. DOI: 10.1103/PhysRevB.88.235131.

[121] Heon-Jung Kim, Ki-Seok Kim, et al. "Topological Phase Transitions Driven by Magnetic Phase Transitions in $Fe_xBi_2Te_3$ ($0 \leq x \leq 0.1$) Single Crystals". **Phys. Rev. Lett.** 110 (13 Mar. 2013), p. 136601. DOI: 10.1103/PhysRevLett.110.136601.

[122] S. J. Pickart, M. F. Collins, et al. "Spin-Wave Dispersion in KMnF3". **Journal of Applied Physics** 37.3 (1966), pp. 1054–1055. DOI: 10.1063/1.1708332.

[123] F. Keffer and C. Kittel. "Theory of Antiferromagnetic Resonance". **Phys. Rev.** 85 (2 Jan. 1952), pp. 329–337. DOI: 10.1103/PhysRev.85.329.

[124] S. Komiyama, O. Astafiev, et al. "A single-photon detector in the far-infrared range". **Nature** 403.6768 (2000), pp. 405–407. ISSN: 1476-4687.

[125] Gautham Adamane Pallathadka, Francesca Calore, et al. "Reconciling hints on axion-like-particles from high-energy gamma rays with stellar bounds" (Aug. 2020). arXiv: 2008.08100 [hep-ph].

[126] Andrea Mitridate, Tanner Trickle, et al. "Detectability of Axion Dark Matter with Phonon Polaritons and Magnons" (May 2020). arXiv: 2005.10256 [hep-ph].

[127] N. Du, N. Force, et al. "Search for Invisible Axion Dark Matter with the Axion Dark Matter Experiment". **Phys. Rev. Lett.** 120 (15 Apr. 2018), p. 151301. DOI: 10.1103/PhysRevLett.120.151301.

[128] C. Boutan, M. Jones, et al. "Piezoelectrically Tuned Multimode Cavity Search for Axion Dark Matter". **Phys. Rev. Lett.** 121 (26 Dec. 2018), p. 261302. DOI: 10.1103/PhysRevLett.121.261302.

[129] Klaus Ehret, Maik Frede, et al. "New ALPS results on hidden-sector lightweights". **Physics Letters B** 689.4 (2010), pp. 149–155. ISSN: 0370-2693. DOI: https://doi.org/10.1016/j.physletb.2010.04.066.

[130] Ben T. McAllister, Graeme Flower, et al. "The ORGAN experiment: An axion haloscope above 15 GHz". **Physics of the Dark Universe** 18 (2017), pp. 67–72. ISSN: 2212-6864. DOI: https://doi.org/10.1016/j.dark.2017.09.010.

[131] L. Zhong, S. Al Kenany, et al. "Results from phase 1 of the HAYSTAC microwave cavity axion experiment". **Phys. Rev. D** 97 (9 May 2018), p. 092001. DOI: 10.1103/PhysRevD.97.092001.

[132] K.M. Backes et al. "A quantum-enhanced search for dark matter axions" (Aug. 2020). arXiv: 2008.01853 [quant-ph].

[133] D. Alesini, C. Braggio, et al. "Galactic axions search with a superconducting resonant cavity". **Phys. Rev. D** 99 (10 May 2019), p. 101101. DOI: 10.1103/PhysRevD.99.101101.

[134] S. Lee, S. Ahn, et al. "Axion Dark Matter Search around 6.7 μeV". **Phys. Rev. Lett.** 124 (10 Mar. 2020), p. 101802. DOI: 10.1103/PhysRevLett.124.101802.

[135] Yonatan Kahn, Benjamin R. Safdi, et al. "Broadband and Resonant Approaches to Axion Dark Matter Detection". **Phys. Rev. Lett.** 117 (14 Sept. 2016), p. 141801. DOI: 10.1103/PhysRevLett.117.141801.

[136] I. Stern. "ADMX Status". **PoS** ICHEP2016 (2016), p. 198. DOI: 10.22323/1.282.0198. arXiv: 1612.08296 [physics.ins-det].

[137] David Alesini, Danilo Babusci, et al. "The KLASH Proposal" (July 2017). arXiv: 1707.06010 [physics.ins-det].

[138] Masha Baryakhtar, Junwu Huang, et al. "Axion and hidden photon dark matter detection with multilayer optical haloscopes". **Phys. Rev. D** 98 (3 Aug. 2018), p. 035006. DOI: 10.1103/PhysRevD.98.035006.

[139] Matthew Lawson, Alexander J. Millar, et al. "Tunable Axion Plasma Haloscopes". **Phys. Rev. Lett.** 123 (14 Oct. 2019), p. 141802. DOI: 10.1103/PhysRevLett.123.141802.

[140] I. Shilon, A. Dudarev, et al. "Conceptual Design of a New Large Superconducting Toroid for IAXO, the New International AXion Observatory". **IEEE Transactions on Applied Superconductivity** 23.3 (2013), pp. 4500604–4500604.

Selbständigkeitserklärung

Hiermit versichere ich an Eides statt, die vorliegende Dissertationsschrift selbst verfasst und keine anderen als die angegebenen Hilfsmittel und Quellen benutzt zu haben. Die eingereichte schriftliche Fassung entspricht der auf dem elektronischen Speicher- medium. Die Dissertation wurde in der vorgelegten Form oder einer ähnlichen Form nicht schon einmal in einem früheren Promotionsverfahren angenommen oder als ungenügend beurteilt.

Hamburg, den October 30, 2020